Fall 2013

Characterization of nano-scaled metal-hydrides confined in nano-porous carbon frameworks

David Edward Peaslee

Department: Physics

CHARACTERIZATION OF NANO-SCALED METAL-HYDRIDES CONFINED IN NANO-POROUS CARBON FRAMEWORKS

by

DAVID EDWARD PEASLEE

A DISSERTATION

Presented to the Faculty of the Graduate School of the

MISSOURI UNIVERSITY OF SCIENCE AND TECHNOLOGY

and

UNIVERISTY OF MISSOURI – ST. LOUIS

In Partial Fulfillment of the Requirements for the Degree

DOCTOR OF PHILOSOPHY

in

PHYSICS

2013

Approved by

Eric H. Majzoub, Advisor
George D. Waddill, Co-Advisor
Phil Fraundorf
Bin Chen
Alexey Yamilov

PUBLICATION DISSERTATION OPTION

Part of this dissertation has been prepared in publication format. Papers II, III, and IV have been previously published in scientific journals. Papers I and V have been formatted for publication in a scientific journal and are awaiting final review before submission. Although the formatting of these sections follows that of this dissertation, the text has not been changed from the original publications. Therefore, references cited in these papers appear at the end of each section. The only exception is for figure captions; they do not follow the general numbering format of this dissertation, and where figures have been changed to grey scale italicized notes have been made.

PAPERS:

Paper I, pages 64-77, "A Study of the Heat and Pressure Induced S105 Phase in $NaAlH_4$", D. Peaslee, G. Wang, D. Zhao, E. Sorte, S. Hayes, M. Conradi, B. Bowman, and E. H. Majzoub *Awaiting Publication,* 2013.

Paper II, pages 78-101, "Controlling the decomposition pathway of $LiBH_4$ via confinement in highly ordered nanoporous carbon", Xiangfeng Liu, David Peaslee, C.Z. Jost, and E.H. Majzoub, *J. Phys. Chem. C*, 2010, 114 (33), 14036–14041.

Paper III, pages 102-123, "Systematic pore size effects of nanoconfinement of $LiBH_4$: Elimination of diborane release and tunable behavior for hydrogen storage applications", X. Liu, C. Jost, D. Peaslee, T. Baumann, E.H. Majzoub, *Chemistry of Materials*, 2011, 23 (5), 1331–1336.

Paper IV, pages 124-145, "Tailoring the hydrogen storage properties of $Li_4BN_3H_{10}$ by confinement into highly ordered nanoporous carbon", X. Liu, D. Peaslee, E.H. Majzoub, *J. Mater. Chem. A*, 2013, 1 (12), 3926-3931.

Paper V, pages 146-165, "Decomposition Behaviors of Eutectic $LiBH_4$-$Mg(BH_4)_2$ and Confinement Effects in Ordered Nanoporous Carbon", D. Peaslee, X. Liu, T. P. Sheehan, and E. H. Majzoub, *Awaiting Publication,* 2013.

ABSTRACT

Metal hydrides are currently being studied to provide hydrogen for use in fuel cells and for transportation applications. Hydrogen can be stored in chemical compounds at higher density and lower volume than liquid H_2 or compressed gas. Thermodynamic properties of metal hydrides differ between bulk and nano-sized particles. Many metal hydrides with useful volumetric and gravimetric capacities have high decomposition temperatures, but when placed in nano-sized frameworks (or templates) desorption and adsorption temperatures can be fine-tuned to meet engineering requirements for real-world systems. Additionally, some metal hydrides have shown a change in the decomposition pathway when infiltrated into these frameworks, thereby reducing the amount of unwanted byproducts, and potentially improving the cyclability of the material.

The Temperature Programmed Decomposition Mass Spectrum Residual Gas Analyzer can be used to characterize gas desorption, decomposition temperatures, picogram changes in mass, and ionization energies for a variety of materials and gasses. The goal of the system is to characterize desorption of the hydrogen (including byproduct gasses) and the decomposition of the metal hydrides. The experimental apparatus is composed of four main components: the residual gas analyzer (RGA), the low temperature stage quartz crystal microbalance (QCM), the high temperature heating stage, and two vacuum chambers separated by a small flow hole which allows a direct line-of-site to the RGA.

ACKNOWLEDGMENTS

I would like to thank Dr. Eric Majzoub for taking me on as a graduate student. His style of teaching, learning, and doing have helped me accomplish so much while I have worked with him.

I would also like to thank Dr. Bruce Wilking for helping me navigate through life as an undergraduate (and now graduate) student at the University of Missouri – St. Louis. I appreciate all that the faculty of the physics department has taught me and helped me accomplish.

The members of my research group; Dr. Xiangfeng Liu, Patrick Sheehan, Dr. Timothy Mason, Dongxue Zhao, and Gang Wang have all provided invaluable contributions to this work. Additionally, B. A. Burkeen and Wayne Garver provided the experience and support to create the equipment necessary for this research.

Dr. Bin Chen has provided me with exceptional experience working in a lab, and I owe my last few years as a graduate to her. I am also indebted to the NASA - Harriett G. Jenkins Predoctoral Fellowship Project for supporting me as a graduate student since 2011.

I would like to thank my committee members; Dr. George Waddill, Dr. Alexey Yamilov, and especially Dr. Phil Fraundorf who has always given me something to think about when it comes to different methods of teaching and learning.

I'd especially like to thank my family and friends for keeping me sane during the last 10 years of school. My parents and brothers have provided the caring and understanding while my friends have provided the much needed distractions.

TABLE OF CONTENTS

Page

PUBLICATION DISSERTATION OPTION iii

ABSTRACT iv

ACKNOWLEDGMENTS v

LIST OF ILLUSTRATIONS xii

LIST OF TABLES xvii

SECTION

1. INTRODUCTION 1

1.1. THE FUTURE OF ENERGY STORAGE 1

1.2. HYDROGEN ENERGY STORAGE CONCERNS 3

1.2.1. Hydrogen Production and Storage Systems. 4

1.2.2. Metal Hydrides as Hydrogen Storage Materials. 5

1.2.2.1 $NaAlH_4$ 5

1.2.2.2 $LiBH_4$ 5

1.2.2.3 $LiMg(BH_4)_3$ 6

1.2.2.4 $Li_4BN_3H_{10}$ 6

1.3. NANOSCALED MATERIALS IN POROUS FRAMEWORKS 6

1.3.1. Frameworks. 7

1.3.2. Decomposition Pathways. 7

1.4. MEASURING THE EFFICIENCY OF HYDROGEN STORAGE MATERIALS 8

1.5. OUTLINE OF WORK 9

2. TEMPERATURE PROGRAMMED DECOMPOSITION IN THE DIRECT LINE-OF-SIGHT MASS SPECTRUM RESIDUAL GAS ANALYZER..... 10

2.1. INTRODUCTION 10

2.2. CONSTRUCTION..... 16

2.2.1. Chamber Systems. 16

2.2.2. Pumping System. 21

2.2.3. Heating and Cooling Systems. 22

2.2.3.1 Turbo pumps. 22

2.2.3.2 Chamber heaters.....22

2.2.3.3 Sample stages. 22

2.2.4. Electrical Control Systems. 23

2.2.4.1 RGA. 23

2.2.4.2 QCM. 25

2.2.4.3 Electromechanical valves.....27

2.2.4.4 Pressure gauge controller. 27

2.2.4.5 Data logger.....27

2.3. OPERATION..... 28

2.3.1. Pumping Down..... 28

2.3.2. Bake Out..... 30

2.3.3. Sample Preparation, Removal, and Insertion 31

2.3.3.1 Temperature controlled decomposition 31

2.3.3.2 Sample gas preparation.....33

2.3.4. TPD and Data Acquisition 34

2.3.4.1 RGA 34

2.3.4.2 Temperature controller.....36

2.3.4.3 Pressure gauge controller..... 38

2.3.4.4 Data logger..... 39

2.3.4.5 QCM..... 39

2.3.5. Measuring Sample Gases..... 39

2.3.6. Shut Down..... 42

2.3.7. Cleaning..... 42

2.4. ANALYSIS OF DATA..... 43

2.4.1. TPD..... 43

2.4.2. Sample Gases..... 45

3. HIGHLY ORDERED NANOPOROUS CARBON POWDERS..... 51

3.1. INTRODUCTION..... 51

3.2. EXPERIMENTAL METHODS..... 52

3.3. RESULTS AND DISCUSSION..... 55

3.3.1. NPC Precursors..... 55

3.3.2. Analysis of NPC by TEM Imaging and BET/BJH Adsorption Isotherms..... 57

3.3.3. TEM and X-ray Diffraction of NPC..... 60

3.4. MODIFICATIONS TO PREPARATION AND FURTHER WORK..... 62

3.5. CONCLUSIONS..... 63

PAPER

I. A Study of the Heat and Pressure-induced S105 Phase in $NaAlH_4$..... 64

INTRODUCTION..... 64

EXPERIMENTAL SECTION..... 65

RESULTS AND DISCUSSION..... 67

The First Principles Study of the Decomposition of $NaAlH_4$. 67

Experimental Evidence for the Reaction Pathways. 70

CONCLUSION 76

ACKNOWLEDGEMENTS 76

REFERENCES 77

II. Controlling the Decomposition Pathway of $LiBH_4$ via Confinement in Highly Ordered Nanoporous Carbon 78

Introduction 79

Experimental Methods 80

Results and Discussion 83

Conclusion 99

Acknowledgment. 99

References and Notes 100

III. Systematic Pore-Size Effects of Nanoconfinement of $LiBH_4$: Elimination of Diborane Release and Tunable Behavior for Hydrogen Storage Applications 102

ABSTRACT 102

INTRODUCTION 103

EXPERIMENTAL SECTION 105

RESULTS AND DISCUSSION 107

CONCLUSION 117

ACKNOWLEDGMENT. 118

REFERENCES. 119

SUPPORTING INFORMATION 121

IV. Tailoring the hydrogen storage properties of $Li_4BN_3H_{10}$ by confinement into highly ordered nanoporous carbon 124

Introduction 125

Experimental section 126

Results and discussion 127

Conclusion 137

Acknowledgements 138

References 139

Supporting information 142

V. Decomposition Behaviors of Eutectic $LiBH_4$-$Mg(BH_4)_2$ and Confinement Effects in Ordered Nanoporous Carbon 146

ABSTRACT 146

INTRODUCTION 147

EXPERIMENTAL SECTION 149

RESULTS AND DISCUSSION 150

The Phase Formation of Dual-cation Borohydride $Li/Mg(BH_4)_3$. 150

The Decomposition Behavior and Diborane/Triborane Release of the Dual-cation Borohydride $Li/Mg(BH_4)_3$ 152

The Effects of Nanoconfinement on the Decomposition and H_2 / Diborane Releases of $Li/Mg(BH_4)_3$. 157

CONCLUSION 161

ACKNOWLEDGMENT. 162

REFERENCES 163

SECTION

4. CONCLUSIONS 166

APPENDICES

A. THERMODYNAMIC APPROXIMATIONS FOR THE MS-RGA SYSTEM... 168

B. TEMPERATURE CALIBRATION OF THE HIGH TEMPERATURE SAMPLE STAGE 171

C. OUTLINE OF MATLAB CODE FOR ANALYSIS OF MS-RGA DATA 176

D. OUTLINE OF VISUAL BASIC CODE FOR RECORDING PRESSURE FROM XGS -600 196

E. DRAWINGS OF MS-RGA PARTS AND ASSOCIATED TOOLS 210

REFERENCES 217

VITA 220

LIST OF ILLUSTRATIONS

Page

SECTION

Figure 1.1. Ragone plot of small scale energy storage systems 2

Figure 2.1. Flow chart of primary systems for Temperature Programmed Decomposition Mass Spectrum Residual Gas Analyzer 11

Figure 2.2. MS-RGA with working systems on the left and controlling systems on the right. 12

Figure 2.3. The arrangement of the sample stages with respect to the RGA head 13

Figure 2.4. A time series chart showing the background partial pressure of hydrogen, which has been fitted with an exponential curve. 15

Figure 2.5. Use of the glove bag 17

Figure 2.6. The high temperature sample stage with 2 thermocouples connected for temperature calibration, with heater power wires 18

Figure 2.7. Drawing of the glove bag seals 20

Figure 2.8. Electrical components. 24

Figure 2.9. FFT (primary axis) of RGA data taken at sample interval of 16 seconds and 27 seconds, displayed with the time series data (secondary axis) showing instability of pressure signal. 26

Figure 2.10. Tools for carrying, removing, and transporting samples 32

Figure 2.11. The layout of UHV variable leak valve and its components. 33

Figure 2.12. Chart showing time of flight approximations, using 5” as the traveled distance and various potentials set up between the focus plate and the anode. 41

Figure 2.13. The RGA Analysis program can generate background subtracted bargraphs. 44

Figure 2.14. The RGA Analysis program can generate line plots of correlated data using its peak finding algorithm 44

Figure 2.15. Background subtracted analog scans at various electron energies 46

Figure 2.16. Surface plot of ionization energy scans from 30 to 100 eV 47

Figure 2.17. Efficiency curves for argon (top) and hydrogen (bottom). 48

Figure 2.18. Ionization efficiency curves for the primary mass fragments of diborane 50

Figure 3.1. Microtome sample preparation. 54

Figure 3.2. Microtomed sample of precursors on copper grid (left), and TEM image at 6000 x magnification (right). 55

Figure 3.3. TEM images of precursors at 59,000 x magnification (left), and at 150,000 x magnification (right) 56

Figure 3.4. TEM images of NPC precursors at 150,000 x magnification; raw image (left), and "Enhanced Contrast" (right). 57

Figure 3.5. 240,000 x magnification showing overlapping planes of columns (left), and 43,000 x magnification showing curved channels (right). 58

Figure 3.6. Geometric Structure of the NPC 59

Figure 3.7. Pore Size Determination 59

Figure 3.8. Inverse SAED with 1200mm camera length and overlay of rings with ImageJ. 61

Figure 3.9. Diffraction Data 62

PAPER I

Figure 1. GSAS crystal structure representation of $NaAlH_4$ 65

Figure 2. Preparation and crystal growth of high purity $NaAlH_4$ 65

Figure 3. Rietveld Refined X-Ray Diffraction Pattern 66

Figure 4.(a). (Left) The calculated reaction enthalpies as a function of temperature. 68

Figure 4.(b). (Right) The phase diagram of $NaAlH_4$. 68

Figure 5.(a). (Left) The free energies of $(NaAlH_4)_{(1-x)}(NaOH)_x$. 69

Figure 5.(b). (Right) The changes of free energies. 69

Figure 6.(a). (Left) The solubility of NaOH into $NaAlH_4$ with temperature. 70

Figure 6.(b). (Right) Molar solution enthalpies of $(NaAlH_4)_{(1-x)}(NaOH)_x$ 70

Figure 7. MS-RGA measurements of the thermal decomposition of $NaAlH_4$ showing increase in important masses during the second step of decomposition. 71

Figure 8.(a). MS-RGA measurements of the thermal decomposition at various ramp rates for bulk $NaAlH_4$ 73

Figure 8.(b). MS-RGA measurements of the thermal decomposition at various ramp rates for high H_2 pressure N97 74

Figure 8.(c). MS-RGA measurements of the thermal decomposition at various ramp rates for the high temperature/pressure phase "S105" N98. 75

PAPER II

Figure 1. SAXS pattern of the NPC with columnar pores packed in a hexagonal geometry 84
Figure 2. TEM images for NPC of columnar pores packed in a hexagonal geometry 84
Figure 3. X-ray diffraction 85
Figure 4. Nitrogen sorption isotherms 87
Figure 5. FT-IR spectra 88
Figure 6. DSC traces 89
Figure 7. DSC traces of physical mixtures of $LiBH_4$/NPC at different heating ramps 92
Figure 8. DSC traces of physical mixtures of $LiBH_4$/NPC when the scan was stopped and cooled (a) just following the melting point and (c) just following gas escape 94
Figure 9. TGA traces 96
Figure 10. B_2H_6 and H_2 release with increasing temperature 97
Figure 11. Mass spectra for the decomposition of (a) bulk $LiBH_4$, (b) physically mixed $LiBH_4$/NPC, and (c) premelted $LiBH_4$@NPC 98

PAPER III

Figure 1. TEM images of columnar pores packed in a hexagonal geometry 108
Figure 2. Pore-size distributions of NPC-4 nm, CA-9 nm, and CA-15 nm 109
Figure 3. DSC plots of bulk $LiBH_4$ and nanoconfined $LiBH_4$@NPC or $LiBH_4$@CA 111
Figure 4. Pore-size dependence of dehydrogenation temperature of nanoconfined $LiBH_4$ in different carbon templates with a loading of 10 wt % 112
Figure 5. Comparisons of DSC plots for $LiBH_4$@NPC-4 nm with different filling degree 113
Figure 6. Desorption curves of nanoconfined $LiBH_4$@NPC-4 nm with an initial loading of 20 wt % 115
Figure 7. B_2H_6 and H_2 release with increasing temperature for $LiBH_4$@NPC-4 nm, $LiBH_4$@CA-9 nm, and $LiBH_4$@CA-15 nm 116
Figure S1. Nitrogen sorption isotherms 121
Figure S2. X-ray diffraction patterns 122
Figure S3. FT-IR spectra of pre-melted $LiBH_4$@NPC-4nm (20 wt%) 123

Figure S4. The DSC and TGA plots of $LiBH_4$@NPC-4nm 123

PAPER IV

Figure 1. (a) Nitrogen adsorption isotherms of neat NPC (b) pore size distribution of neat NPC and pre-melted $Li_4BN_3H_{10}$@NPC..... 128

Figure 2. X-ray diffraction of (a) as prepared $Li_4BN_3H_{10}$, and (b) pre-melted $Li_4BN_3H_{10}$@NPC. 129

Figure 3. DSC curves of bulk $Li_4BN_3H_{10}$ and nanoconfined $Li_4BN_3H_{10}$@NPC..... 130

Figure 4. Temperature-programmed desorption (TPD) curves of as prepared $Li_4BN_3H_{10}$ and pre-melted $Li_4BN_3H_{10}$@NPC with an initial loading of 20 wt% 131

Figure 5. (a) RGA analyses of ammonia in bulk $LiNH_2$ and $Li_4BN_3H_{10}$ samples and (b) the cracking pattern of the sample at the main ammonia peaks with the published ammonia cracking pattern..... 132

Figure 6. (a) Normalized RGA traces of diborane in bulk $LiBH_4$ and $Li_4BN_3H_{10}$ samples and (b) the cracking pattern of the sample at the main diborane peaks with published diborane cracking pattern 134

Figure 7. RGA-MS traces showing H_2, NH_3, and B_2H_6 release with increasing temperature for as prepared $Li_4BN_3H_{10}$ and nanoconfined $Li_4BN_3H_{10}$@NPC 136

Figure 8. RGA-MS traces showing H_2, NH_3, and B_2H_6 releases with increasing temperature for the rehydrided $Li_4BN_3H_{10}$@NPC. 137

Figure S1. Direct line-of-sight RGA cracking patterns and gas evolution of $LiBH_4$ 142

Figure S2. Direct line-of-sight RGA cracking patterns and gas evolution of $LiNH_2$ 143

Figure S3. Direct line-of-sight RGA cracking patterns and gas evolution of $Li_4BN_3H_{10}$..... 144

Figure S4. Direct line-of-sight RGA cracking patterns and gas evolution of $Li_4BN_3H_{10}$@NPC 145

PAPER V

Figure 1. XRD patterns of as received $LiBH_4$ (a), as received $Mg(BH_4)_2$ (b), heat-treated $Mg(BH_4)_2$ (c), ball milled mixture of $LiBH_4$/$Mg(BH_4)_2$ (d), and ball milled/heat-treated $LiBH_4$/$Mg(BH_4)_2$ (e)..... 152

Figure 2. Desorption curves of as received $LiBH_4$ (a), as received $Mg(BH_4)_2$ (b), and Li/$Mg(BH_4)_3$ (c)..... 153

Figure 3. H_2, diborane and triborane release of as received $LiBH_4$, $Li/Mg(BH_4)_3$, and heat treated $Mg(BH_4)_2$, respectively. 154

Figure 4. The cracking patterns of heated $Li/Mg(BH_4)_3$ at the B_2H_6 release peak (359°C) with the published diborane cracking pattern..... 156

Figure 5. The standard cracking pattern of B_2H_6 shown with those of $Mg(BH_4)_2$ at 377°C, indicating species larger than B_2H_6, and decomposition at 382°C, where only B_2H_6 is evident. 156

Figure 6. The cracking patterns of heated $LiBH_4$ at the B_2H_6 release peak at 386°C with the published diborane cracking pattern 157

Figure 7. Inset (a) nitrogen sorption isotherms of neat NPC with a surface area and pore volume of 1012 m^2/g and 0.65 cm^3/g respectively, and nanoconfined $Li/Mg(BH_4)_3$@NPC with a surface area and pore volume of 461 m^2/g and 0.32 cm^3/g, respectively; (b) pores size distribution of neat NPC and pre-melted $Li/Mg(BH_4)_3$@NPC. 158

Figure 8. X-ray diffraction patterns of $Li/Mg(BH_4)_3$ before and after infiltration into NPC. 159

Figure 9. FT-IR spectra of pre-melted $LiBH_4$@NPC 159

Figure 10. Desorption curves of as prepared $Li/Mg(BH_4)_3$ and the pre-melted $Li/Mg(BH_4)_3$@NPC with an initial loading of 20wt%. 160

Figure 11. H_2, diborane and triborane release with increasing temperature for as prepared $Li/Mg(BH_4)_3$ and nanoconfined $Li/Mg(BH_4)_3$@NPC..... 161

LIST OF TABLES

Page

SECTION

Table 1.1. U.S. DOE Hydrogen Storage System Performance Targets from 2006 and 2012. 2015 and 2017 goals are for one-time-use systems, while 2020 and beyond goals are for rechargeable systems. 4

Table 2.1. Temperature Parameters for Calibrated Ramp Rates 38

Table 2.2. RGA Parameters for Ionization Potential Experiments with Ion Energy of 12 Volts 41

Table 3.1. Diffraction Data 60

PAPER I

Table 1. Theoretical and Experimental Enthalpies at 1 atm. 67

Table 2. DSC Experimentally Calculated Enthalpies. 72

PAPER III

Table 1. Surface Areas and the Total Pore Volumes of Different Carbon Templates 107

1. INTRODUCTION

1.1. THE FUTURE OF ENERGY STORAGE

There are many aspects of our daily life that could be greatly enhanced by advanced energy storage systems (ESS). From the power supplied to our homes, the transportation systems that take us where we need to go, and the pocket sized personal computers that we have come to rely on; all these could benefit from advances to storage technologies. A major breakthrough in ESS technology would revolutionize the energy dependant society that we have created.

These systems range from the very small, batteries and capacitors; to the immense, as in hydroelectric reservoirs. Each of these systems is best suited for a particular application, and very few ESS have the ability to cross over into other applications. For example, rechargeable batteries are the current standard for hybrid vehicles, for mobile and backup computing, and anywhere low power densities are needed. Batteries, due to cycling capacity and charge leakage, are inefficient at providing energy for large scale needs. The energy needed for backup and supplemental power for the transmission and distribution (TD) grids in our cities and communities cannot yet be met by batteries. Hydroelectric reservoirs are ideally suited for this application. Similar to hydroelectric dams, these are small reservoirs in which water is pumped into the reservoir during times of low electrical demand and released into hydroelectric generators during time of peak power usage. These systems are useful only in geographically favorable locations, and the applications typically only apply to TD power requirements.

The larger the application's energy supply and demand is, the more it will benefit from a unique combination of different storage technologies. Figure 1.1 presents a Ragone plot of the different ESS arranged by energy density versus power density of the systems. An all electric transportation system is an example of a large scale supply and demand application that requires a variety of compact storage systems. For recharging the vehicles, the system will need a very large power and energy density storage bank. The vehicles themselves will need a large energy storage system for long range driving, or a large power supply for commercial vehicles. For efficiency, the vehicles will need a mix

of power and energy storage systems for capturing lost thermal or kinetic energy (i.e. regenerative breaking) [1,2].

Another large scale application is the current electrical TD network. This system has large inefficiencies which could be addressed with local storage facilities. The fluctuations in power demand could be met with large local power banks installed at sub-stations or even with small scale systems installed in homes and businesses. Renewable energy supplies fluctuate greatly during the day or by the time of the year. The ESS systems could address these issues with systems installed at the power generating facilities. The hydroelectric reservoir can address the seasonal energy storage requirements, whereas large scale fuel cells or compressed liquid/gas systems can address the daily power storage requirements [1].

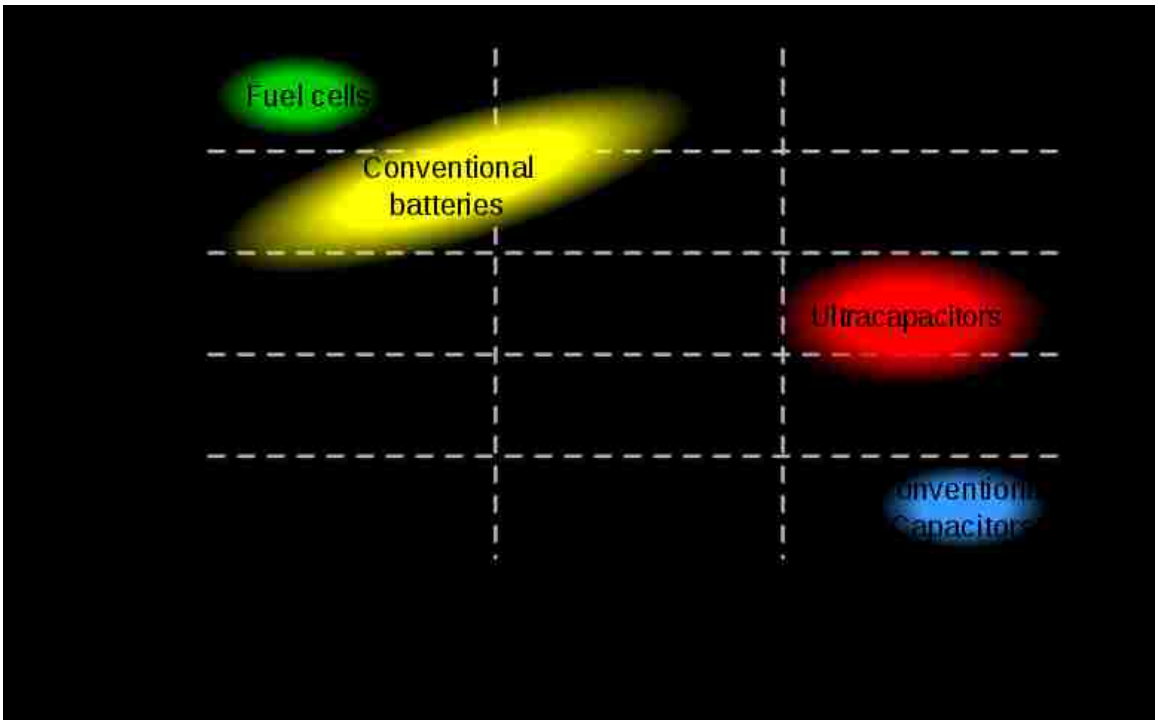

Figure 1.1. Ragone plot of small scale energy storage systems. For comparison, a 25 Ton, 1000 kW portable diesel generator provides a power density of 44 W/kg and an energy density of 570 Wh/kg and would lie between fuel cells and conventional batteries [4].

One system that has the benefit of delivering either high energy or high power is a hydrogen fueled system. An electric fuel cell can deliver a high energy density by way of proton exchange, while a hydrogen combustion engine can supply a high power density by way of thermodynamic expansion. As storage systems for TD grids, hydrogen fuel cells have been installed that have up to 10 kW of available power. These systems will become more prevalent as renewable energy generation plants become more economically viable [3].

More information on EES as well as current research and development need can be found through the Department of Energy's (DOE) website [5]. Individual government research projects are organized by the Office of Science's Basic Energy Sciences (BES) [1] and the Office of Electricity Delivery & Energy Reliability (OE) [6].

1.2. HYDROGEN ENERGY STORAGE CONCERNS

There are many methods for the generation of hydrogen, such as through electrolysis of water or as a byproduct in chemical manufacturing. For a particular H_2 fueled system, the production and storage of H_2 depends on the mobility of the system. For instance, if the application of the fuel cell is to provide energy storage for a renewable power plant, then a pressurized tank can be installed and the generation and consumption of H_2 is local to the system. On the other hand, in transportation applications, hydrogen fuel cells are primarily H_2 consumers since the energy it takes to split pure H_2O with hydrolysis makes it infeasible in most cases to install a reversible fuel cell. The U. S. Government has set up the National Hydrogen Storage Project with performance targets through 2020 [7-9]. Some of this information is shown in Table 1. When this data is compared to technologies in Figure 1, it can be seen that these goals are well above existing technologies.

For transportation applications safety is the number one issue regarding hydrogen fueled systems. The current methods for storage of H_2 can be separated into 3 categories: pressurized gas (high pressure to low pressure), cryogenic liquid, and chemical storage systems.

Table 1.1. U.S. DOE Hydrogen Storage System Performance Targets from 2006[1] [7] and 2012[2] [9]. 2015 and 2017 goals are for one-time-use systems, while 2020 and beyond goals are for rechargeable systems.

	2007[1]	2010[1]	2015[2]	2017[2]	2020[2]	Ultimate[2]
Specific Energy kWh/kg	1.5	2	.7	1.8	1	2.5
Mass % of H_2 to System	4.5 %	6 %	2.0 %	5.5%	3%	7.5 %

1.2.1. Hydrogen Production and Storage Systems. Pressurized H_2 can be stored either in high pressure tanks for immediate use, or it can be mixed with nanoporous materials for adsorption onto or absorption into engineered materials. High pressure storage is inherently dangerous for transportation applications, and the systems have to be over-engineered, adding much weight into the system. Advances in carbon fiber technologies may mitigate this issue, but high pressure H_2 would still be too dangerous for the end user to handle [9]. The low pressure storage systems usually take the form of high surface area, nano-engineered materials. High surface area nanoporous carbons (NPC) and metal organic frameworks (MOF) are currently being investigated as materials for physical storage systems [7, 10]. As fuel is needed small changes in pressure or temperature may release the H_2 for consumption. The lower pressure storage options provide a safer method for storage and transportation, but typically have a low H_2 storage capacity (2 – 6%).

The liquid storage option requires that the system be cooled to below 33K, and the cryogenic system requirements make this an infeasible option for most transportation applications. For transportation of massive amounts of H_2 this may be an option, but local generation of H_2 is advanced enough that this isn't necessary.

Chemically storing the hydrogen is quickly becoming the preferred method for portable H_2 fuelled systems. Theoretically, some of the systems have a very high storage capacity, and in most cases chemical storage is a safer alternative to physical storage systems. Chemical storage can further be separated into chemical decomposition and

thermal decomposition materials [7, 11]. Chemical decomposition systems cannot be regenerated with hydrogen overpressure alone. These systems usually involve catalysts for the release of H_2 and must be regenerated in complex multistep chemical reactions. On the other hand, metal hydrides decompose with an increased temperature, and in many cases can be regenerated with a high hydrogen pressure and temperature. Some of the few drawbacks to this option are the poor cycling ability and the high decomposition temperatures needed for the release of H_2.

1.2.2. Metal Hydrides as Hydrogen Storage Materials. Complex metal hydrides are materials which are formed from a metal and a complex such as a borohydride (BH_4), an alanate (AlH_4), or an amide (N_2). These species can form materials that have a high hydrogen capacity, but generally the hydrogen is released in multiple steps during decomposition. This could make recharging the material a complicated procedure, especially if the intermediate products phase separate, or are removed from the system if converted to a gaseous form [11].

1.2.2.1 $NaAlH_4$. Sodium alanate has a theoretical hydrogen capacity of 7.4%. This material goes through at least the 3 step decomposition process below and can be complicated by the reaction of $NaAlH_4$ with Na_3AlH_6. Improvements to the decomposition temperature have been made with confinement in nanoporous carbons and high surface area foam Al [12 -13].

$$NaAlH_4 \longleftrightarrow \tfrac{1}{3} Na_3AlH_6 + \tfrac{2}{3} Al + H_2 \quad (1)$$

$$Na_3AlH_6 \longleftrightarrow 3NaH + Al + \tfrac{3}{2} H_2 \quad (2)$$

$$NaH \longleftrightarrow Na + \tfrac{1}{2} H_2 \quad (3)$$

1.2.2.2 $LiBH_4$. This metal borohydride has a very high theoretical hydrogen capacity of 18.2%. $LiBH_4$ decomposes in at least two steps; the first step (equation 4 below) occurs around 370 °C and has a theoretical capacity of only about 13.6%. The decomposition of LiH (equation 5) occurs above 600 °C. The drawback to this material is its high decomposition temperature [14] and production of the gas diborane (B_2H_6), a toxic byproduct [15]. The fact that the byproduct is toxic is incidental, in that when the

diborane is produced some of the hydrogen and the boron is lost to this gas (equation 6). When mixed with other borohydrides the decomposition temperature has been reduced considerably, but the production of diborane still occurs [16-19].

$$LiBH_4 \longleftrightarrow LiH + B + \tfrac{3}{2} H_2 \quad (4)$$

$$LiH \longleftrightarrow Li + \tfrac{1}{2} H_2 \quad (5)$$

$$LiBH_4 \longleftrightarrow \tfrac{1}{2} B_2H_6 + LiH \quad (6)$$

1.2.2.3 $LiMg(BH_4)_3$. This is a physical mixture of 2 borohydrides; $LiBH_4$ and $Mg(BH_4)_2$. This composition has a theoretical hydrogen capacity of 15.8%. These materials when combined have a lower decomposition temperature [16, 17], but the structure and phase are highly dependent on the preparation methods for synthesizing the material.

1.2.2.4 $Li_4BN_3H_{10}$. This is another amalgamation of 2 hydrides. $LiBH_4$ is mixed with $LiNH_2$ and then annealed to form a new phase $Li_4BN_3H_{10}$. This material has a theoretical hydrogen content of 11.0%. The individual precursors both generate toxic gasses when decomposing, and unfortunately so does this material. NH_3 and B_2H_6 are both products during decomposition [18, 19].

1.3. NANOSCALED MATERIALS IN POROUS FRAMEWORKS

These materials have been studied extensively in their bulk form. When scaled down to the nano-size, these materials behave quite differently. By creating nano-sized particles of a metal hydride the thermodynamics can be favorably tuned by the use of surface interaction effects or the increased particle surface area to volume ratio. An additional benefit to the nanoconfinement is the effect it has on phase separation and in some cases the crystal structure of the material. For example: when $LiBH_4$ decomposes, if the B is phase separated and spatially distant from the LiH, then the reverse reaction would require much more energy to bring the materials back together. On the other hand,

if the B and LiH are physically constrained to limit phase separation then less energy is required for the reverse reaction to occur [23].

This research is centered on the effects that nanoconfinement has on the decomposition and subsequent rehydriding of metal hydrides. These effects stem from the high surface area of the metal hydride nanoparticle as well as the complicated surface interactions with the porous frameworks. This work studies the decomposition pathways, particle size, cycleability, and decomposition temperature of the previously described metal hydrides. The goal of this research is to design the ideal hydrogen storage system to meet the demands of a hydrogen economy. These goals are met by fitting the right metal hydride to the right framework to produce an ideal decomposition pathway.

1.3.1. Frameworks. The NPC mentioned before have pore diameters on the order of 1 ~ 15 nm. For the widely available carbon black (activated carbon), specific surface areas range from 500 – 1500 m^2/g. For amorphous carbon aerogels, pore sizes of 9 – 15 nm, surface areas of ~ 675 m^2/g, and pore volumes of ~2 ml/g have been achieved. A more ordered nanoporous carbon has been synthesized with a pore size of ~ 5.5 nm, a surface area of ~ 1000 m^2/g, and a pore volume of ~0.75 ml/g [24]. These materials give a range of potential sizes for a nanoscaled metal hydride.

This last material is a highly ordered hexagonally packed nanoporous carbon. It is synthesized by organic-organic self assembly from phenol and triblock co-polymer. The uniformity of the columnar pores should provide full access for infiltration of the NPC volume.

To get the hydrides into the pores, the material is physically mixed with the NPC and then melted under a H_2 overpressure to prevent decomposition. To enable the wetting of the hydride into the pore the surface tension must be sufficiently low. Once the material has been decomposed in the NPC, theoretically a high H_2 pressure and temperature should reverse the decomposition pathway [12, 15].

1.3.2. Decomposition Pathways. As previously mentioned, the decomposition of some metal hydrides is complicated by reactions that generate unwanted and potentially dangerous gases. By changing the thermodynamics of the metal hydride, it is possible

that the release of these gasses can be mitigated, or altogether eliminated [12]. This can occur through nanoconfinement, by mixing hydrides, or by a combination of these effects. To confirm the change in decomposition it is essential that the decomposition products be carefully and thoroughly characterized.

1.4. MEASURING THE EFFICIENCY OF HYDROGEN STORAGE MATERIALS

There are many experimental techniques that can be used for the characterization of these hydrogen storage materials. X-ray diffraction (XRD) can provide information on the crystal structure of materials before and after decomposition. This can provide insight into the decomposition pathway by correctly identifying the materials in the reaction. Thermogravimetric analysis (TGA) and differential scanning calorimetry (DSC) both provide information on the energy required for decomposition. TGA characterizes the mass change, while DSC can provide information on phase transitions such as melting, decomposition, and crystal realignment.

For characterizing NPC, electron microscopy techniques can give insight on the physical structure, while nitrogen adsorption isotherms can provide details of the pore size and volume of the material. These characterization techniques help determine the amount of hydride material that has infiltrated the pore structures.

Measuring the amount of gas produced and adsorbed can be accomplished using a high temperature fixed-volume Sievert's type instrument, but identifying the species of the gas produced requires a more complicated system. A mass spectrum analyzer can identify species down to ~10 amu, but a residual gas analyzer can identify species down to 2 amu (the mass of H_2). Instrumentation has been developed which can identify and characterize the gas formed during decomposition [25]. Part of the work presented here is conducted with a similar instrument to that outlined by R. Behrens, but this instrument is assembled from mostly off the shelf components. This instrument, the Temperature Programmed Decomposition Mass Spectrum Residual Gas Analyzer will help characterize the exact decomposition pathway that these materials take.

1.5. OUTLINE OF WORK

The following section outlines the work accomplished here while researching the hydrogen production characteristics of nanoconfined metal hydrides.

Section 2 outlines the construction and use of the Temperature Programmed Decomposition Mass Spectrum Residual Gas Analyzer (MS-RGA). This device is the heart of the work presented here.

Section 3 outlines the synthesis and characterization of the hexagonally packed nano-porous carbons (NPC). These carbons are used in subsequent sections to control the decomposition of metal hydrides. By melt infiltrating the hydrides into the carbon's nanopores we have shown that the decomposition products can be controlled, and that in most cases the release of unwanted by product gases can be reduced.

Paper I presents some recent studies of $NaAlH_4$ as a hydrogen storage material. The hydrides presented in this section have been prepared in various environments, and these preparation techniques are discussed and compared.

Paper II presents previously published work on $LiBH_4$ as a hydrogen storage material. This work covers the nanoconfinement effects on $LiBH_4$ as well as the suppression on the release of diborane.

Paper III presents previously published work and continues the studies of $LiBH_4$. This section discuses the pore-size effect on the decomposition of $LiBH_4$ and presents experimental data on the reduction of decomposition temperature and the reversibility of the decomposition pathway.

Paper IV also presents previously published work on the metal hydride: $Li_4BN_3H_{10}$. The decomposition and structure of this material is compared with that of the precursors: $LiBH_4$ and $LiNH_2$. The production of ammonia, as well as other intermediate species is discussed here.

Paper V presents previously unpublished work done on the mixed metal hydride $LiBH_4$-$Mg(BH_4)_2$. Characteristics of this hybrid material, including the cycling capacity and its decomposition temperature are compared with its precursors: $LiBH_4$ and $Mg(BH_4)_2$.

2. TEMPERATURE PROGRAMMED DECOMPOSITION IN THE DIRECT LINE-OF-SIGHT MASS SPECTRUM RESIDUAL GAS ANALYZER

2.1. INTRODUCTION

Section 2 outlines the construction and use of the Temperature Programmed Decomposition Mass Spectrum Residual Gas Analyzer (MS-RGA). This system was funded in part by the U.S. Department of Energy in the Hydrogen, Fuel Cells, and Infrastructure Technologies Program through the office of Energy Efficiency and Renewable Energy under Contract DE-AC04-94AL85000.

Mass spectroscopic analysis is performed with a quadrupole residual gas analyzer (SRS RGA200, Stanford Research Systems) and a high-temperature sample stage. The system is separated into a high vacuum (HV) (10^{-8}-10^{-5} Torr) sample chamber and an ultra high vacuum (UHV) (10^{-9}-10^{-7} Torr) gas analysis chamber. Because of the low pressure in the system, molecular interactions are assumed to be negligible (calculations for mean free path can be found in Appendix A). Thus, the decomposing sample and the geometries of the system create a beam of molecules. The RGA maintains a line of sight with the sample through a small flow hole to produce the best possible molecular beam signal.

The sample is placed into the system using hermetically sealed Tzero pans. An argon (Ar) filled glovebag serves as an ante-chamber for the RGA system. The sample holder is placed into the Ar-filled glovebag at which time a small hole is punctured for the later release of gases. Figure 2.1 shows a flow chart outlining the most important systems. Figure 2.2 is the image of the system with the working parts on the left and the controlling parts on the right.

The system is equipped with two temperature stages in the HV chamber. The low temperature stage is fitted with a quartz crystal microbalance and can be heated and cooled from an arbitrary low temperature to 100 °C. The low temperature is determined by the fluid or gas pumped through the head of the QCM. To accurately determine a change in mass down to the picogram scale, the sample must be physically deposited on the quartz crystal. Figure 2.3 (by E. H. Majzoub) shows the arrangement of the two

temperature stages with respect to the RGA head. The high temperature stage must be removed in order to use the QCM low temperature stage.

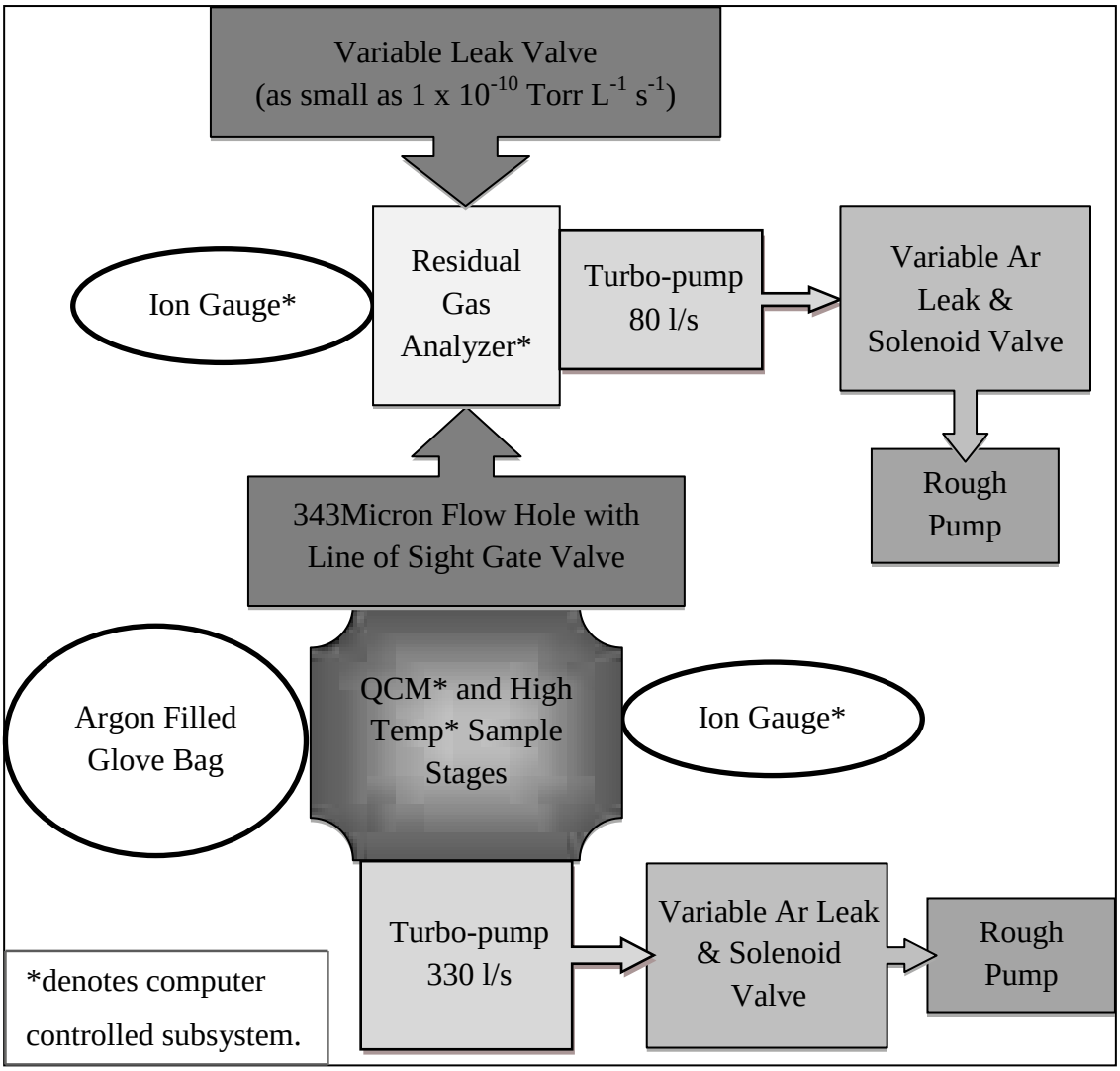

Figure 2.1. Flow chart of primary systems for Temperature Programmed Decomposition Mass Spectrum Residual Gas Analyzer

On the high temperature stage the samples are heated from room temperature (RT) to a maximum of 450 °C at multiple ramping rates. Calibration of the sample temperature was performed using a sample holder filled with glass beads, and the

reference thermocouple is placed in the center of the beads away from the aluminum pan wall. The estimated error between the sample holder temperature and the indicated sample temperature is ~15 °C.

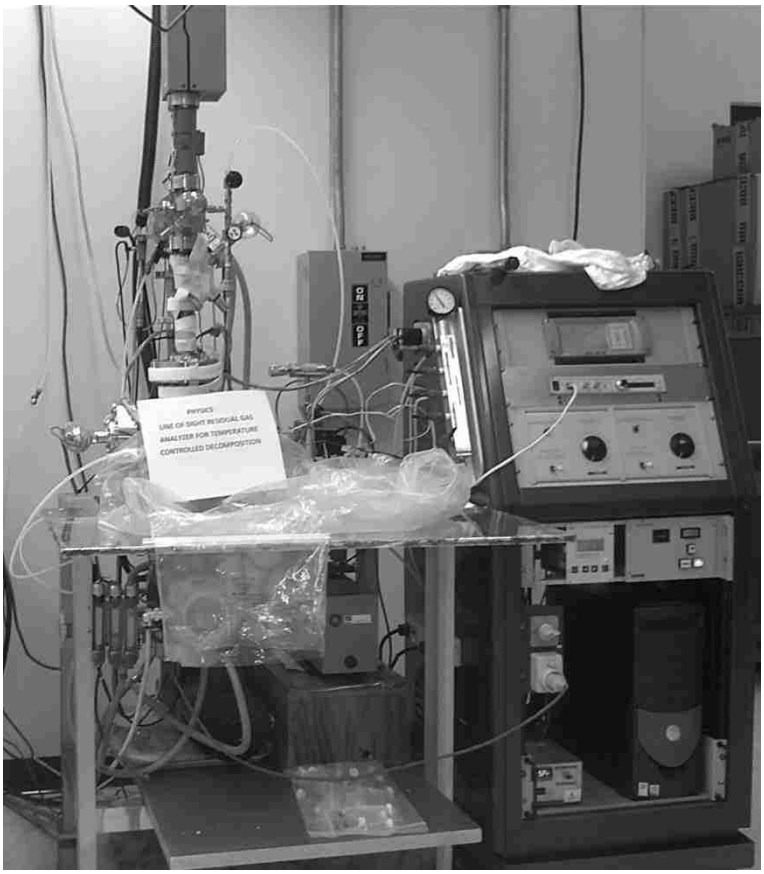

Figure 2.2.MS-RGA with working systems on the left and controlling systems on the right.

The maximum partial pressure sensitivity of the RGA using the electron multiplier is 8.8×10^{-7} Torr. At times, the mass to charge ratio (m/z = 2) of the hydrogen pressure is estimated by using m/z = 1 when this partial pressure is exceeded. Cracking-pattern histograms were used to identify the presence of gasses desorbing from the sample. As a general outline the gas molecules enter the ionization chamber, and are bombarded by electrons whereby they become the ion source. A potential set up between

the repeller cage and the focus plate cause the newly formed ions to travel into the quadrupole mass filter. The mass filter uses RF voltage to oscillate the trajectory of the ions; only ions with a stable oscillating trajectory will make it through the filter. The ions are detected either at the faraday cup or the electron multiplier (CDEM). The metallic faraday cup provides electrons for neutralizing the ions. The demand of the electrons is measured and is assumed to be equal to the incoming ion current. For the SRS RGA 200, the minimum partial pressure for this detector is ~ 10^{-9} Torr. The electron multiplier uses a high negative voltage power supply to attract the ions away from the faraday cup. The impact of the ions into the CDEM creates a cascade of secondary electrons which are measured as a current. This current is assumed to be proportional to the incoming ion current. Since the number of electrons leaving the CDEM may be as high as 10^{7} for every positive ion striking it, partial pressures as low as 10^{-13} Torr can be measured. The physics describing the operating principles of a quadrupole mass spectrometer can be found in most mass spectrometry books [26-28]. More information on this particular RGA can be found in the Operating Manual and Program Reference for the SRS RGA200 Residual Gas Analyzer [29].

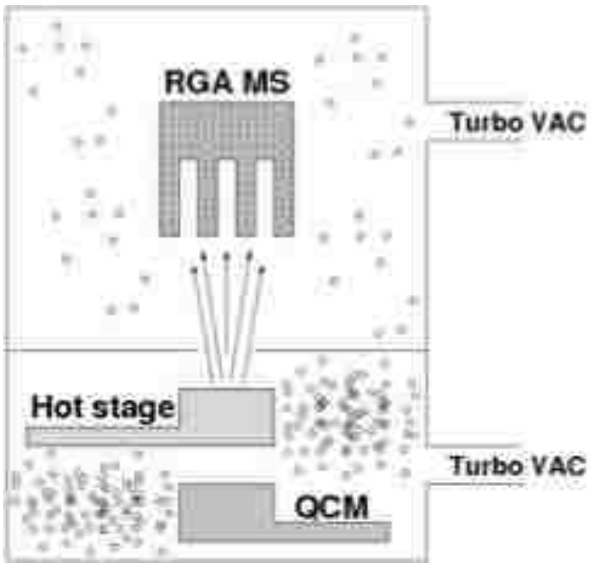

(a)

Figure 2.3. The arrangement of the sample stages with respect to the RGA head. (a) The schematic of the arrangement. (b) An image of the sample stages of the HV side of the MS-RGA. Heat tape is shown which is part of the glove bag seal.

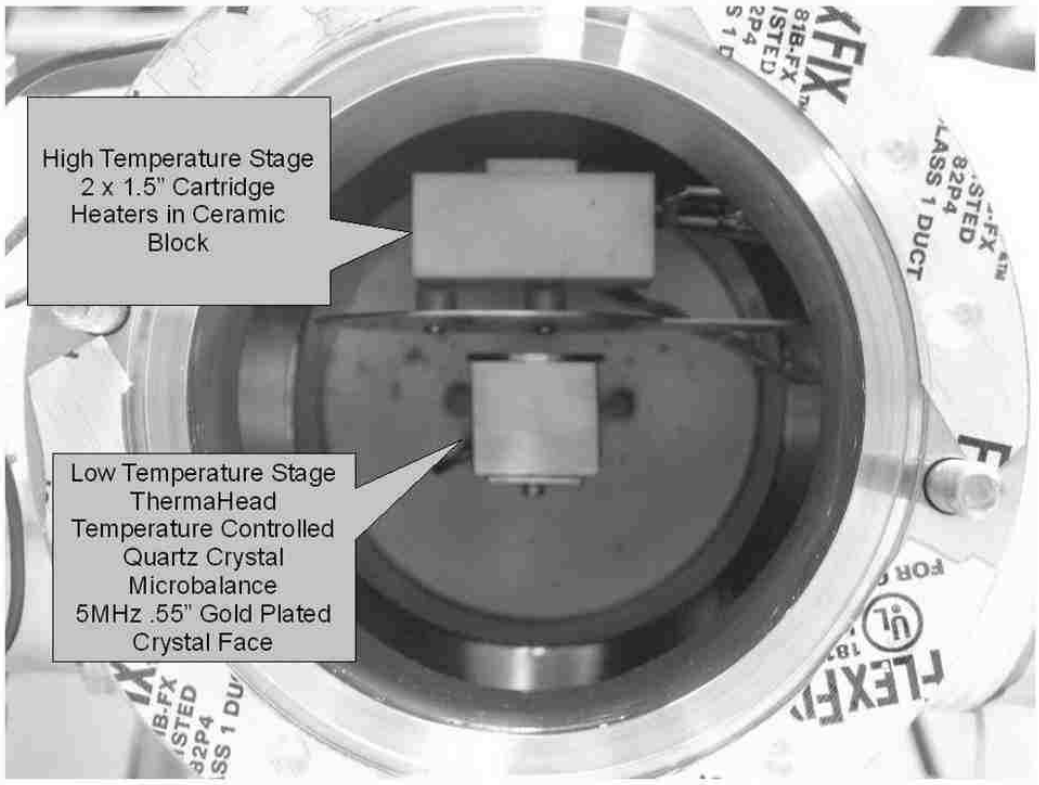

(b)

Figure 2.3. The arrangement of the sample stages with respect to the RGA head. (a) The schematic of the arrangement. (b) An image of the sample stages of the HV side of the MS-RGA. Heat tape is shown which is part of the glove bag seal.
(cont.)

The data collected from the RGA is time correlated with the data from the temperature controller and the systems pressure gauges. The correlated data sets are presented as the increase in partial pressures from temperatures in the range of room temperature to ~ 450 °C. The pressure data can be presented in a histogram chart for a range of masses at a particular temperature, line plots for the temperature dependence of a particular mass to charge ratio (m/z), or as a three dimensional surface for examining the temperature dependence of a range of m/z.

It is important to keep in mind that pressures measured by the RGA are obtained in a differentially pumped system. Therefore, an increase in pressure represents an increase in the rate of generation of a particular gas while the decrease in pressure

represents a decrease of the rate of generation for a particular gas. Figure 2.4 shows an example of the time series analysis for $NaAlH_4$. During decomposition of a sample, if hydrogen ions are created in the ionizer the partial pressure will start to increase starting from the background (which can be estimated in some situations). As the hydrogen generation slows down/ceases, it is gradually pumped out by the 2 turbo pumps. The measured pressure will then decrease until the signal returns to the estimated base line. The base line of the pressure for a particular gas species is due either to virtual leaks in the system (residual oil from a fingerprint) or leaks through the seals of the chamber. The base line is not constant during temperature programmed decomposition (TPD). Although the chambers are separated by a copper plate (thereby reducing radiative heat transfer), energy is still transferred to the top chamber kinetically. As the temperature of the top chamber increases, there is expected to be an increase in the measured partial pressures.

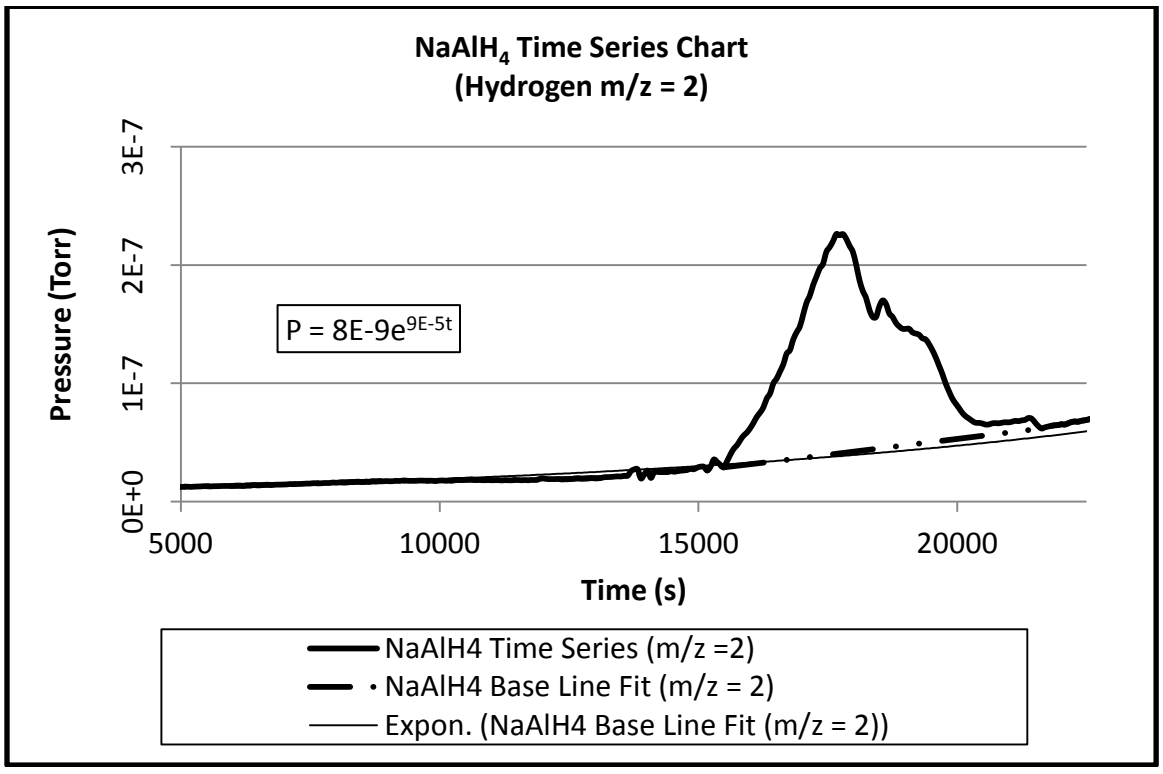

Figure 2.4. A time series chart showing the background partial pressure of hydrogen, which has been fitted with an exponential curve.

It is difficult to determine the exact amount of a particular species generated, but some thermodynamic calculations and estimations can be found in Appendix A.

2.2. CONSTRUCTION

Here the construction of the MS-RGA is broken into 4 parts: (2.2.1) chamber systems, (2.2.2) pumping and Ar supply systems, (2.2.3) heating and cooling, and (2.2.4) electrical control systems. Figure 2.5 and Figure 2.2 are images of the system. The vacuum chamber and pump systems are installed in an aluminum frame work which supports the working parts of the system (as opposed to the controlling parts). The control interfaces are housed in a rolling rack mount cabinet.

2.2.1. Chamber Systems. The HV sample chamber is composed of a stainless steel 6” (DN 100) 6-way cross with ConFlat flanges (CFF) purchased from Pfeiffer Vacuum (part number 420RKD100). Both the low temperature QCM and high temperature sample stages are mounted to 6” CFF feedthroughs attached to 2 of the ports. Drawings of the 2 sample stages and their associated parts can be found in Appendix E. The QCM sample stage is supported by the welded cooling lines to the 6” CFF plate and has electrical feedthroughs for the thermocouple, the QCM control, and the wires for the cartridge heater. The high temperature stage is bolted to the 6” CFF plate with vented allen bolts, and has feedthroughs for 2 thermocouples and for the wires for the cartridge heaters. As can be seen in Figure 2.6, the mounting plate for the sample and heater block also serves as a heat shield to keep the radiant heat from heating the sensitive feedthroughs of the thermocouple wires.

Figure 2.5. Use of the glove bag. Electrical feedthroughs for thermocouples and high temperature stage heater, heat tape for top and bottom chambers, and aluminum frame for supporting the system and glove bag are shown.

A DN-100 ISO K to 6” CFF adaptor connects the Pfeiffer Vacuum TPH 330 l/s turbo pump to the bottom port of the 6 way cross. A 6” to 2.75” CFF reducing flange connects the Agilent 571 Series Bayard-Alpert Type Hot Ionization Gauge (ion gauge) to a side port of the 6-way cross. The front port is used for viewing, inserting, and removing the sample and is a 6” CFF glass viewport. The 6” metal compression seals are all silver plated copper rings. The viewport and the TPH 330 turbo pump seals are Buna O-rings on a centering ring.

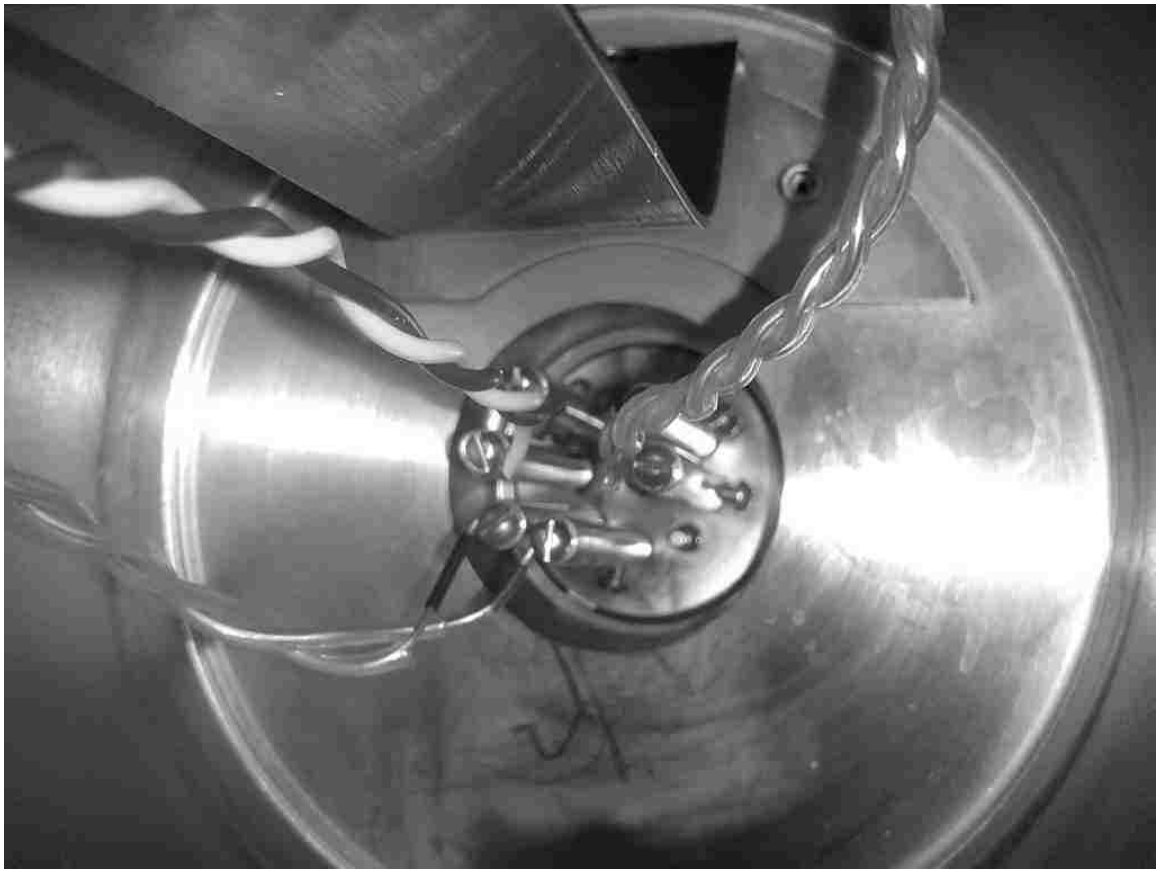

Figure 2.6. The high temperature sample stage with 2 thermocouples connected for temperature calibration, with heater power wires. All wires are twisted pairs to reduce electromagnetic interference.

The glove bag is attached to the chamber using a large diameter hose clamp and a rubber insulating ring. Figure 2.7 is a schematic of the seal between the glove bag and the sample chamber.

The top flange of the 6-way cross is fitted with a 6” to 2.75” CFF reducer and a 3” extension CFF nipple. The seal between the reducer and the nipple is a solid copper plate with a centered 343 micron drilled hole, therefore components above this plate are in the UHV side of the system. Above the nipple, a bellows in line gate valve (part number 9515052, Varian Vacuum) is installed, which has a line of sight cross sectional diameter of 0.91 inches. Attached to the auxiliary port of the valve is the UHV ion gauge. This valve is normally closed during sample changing, or when using UHV chamber for testing gas samples as described in the operations section.

Above the valve is a 2.75” CFF cross. Fitted to the cross is the RGA head, a bakeable variable UHV leak valve (part number 951-5106, Varian Vacuum), and the 80 l/s UHV turbo pump (Hi-Pace 80, Pfeiffer Vacuum).

The bakeable variable leak valve is used to introduce and analyze specific gas samples. The valves compression flare port is connected to a removable convection gauge acting as a gas sample holder. This gas reservoir can be pumped out before use via the HV rough pump and manual valves. A description for the use of this system can be found in the operation section below.

All connections on the high pressure side of the turbo pumps are done using DN 40 KwikFlange (KF) fittings and stainless steel flexible metal vacuum tubing. All connections to the Ar gas supply are made with ¼” compression fittings and adapters, with the gas supplied through polypropylene, stainless steel or copper tubing.

After it was fully assembled, the system was pumped out to 10^{-7} Torr, and vacuum leak checked by a helium leak detector (Ultratest F, Leybold-Heraeus).

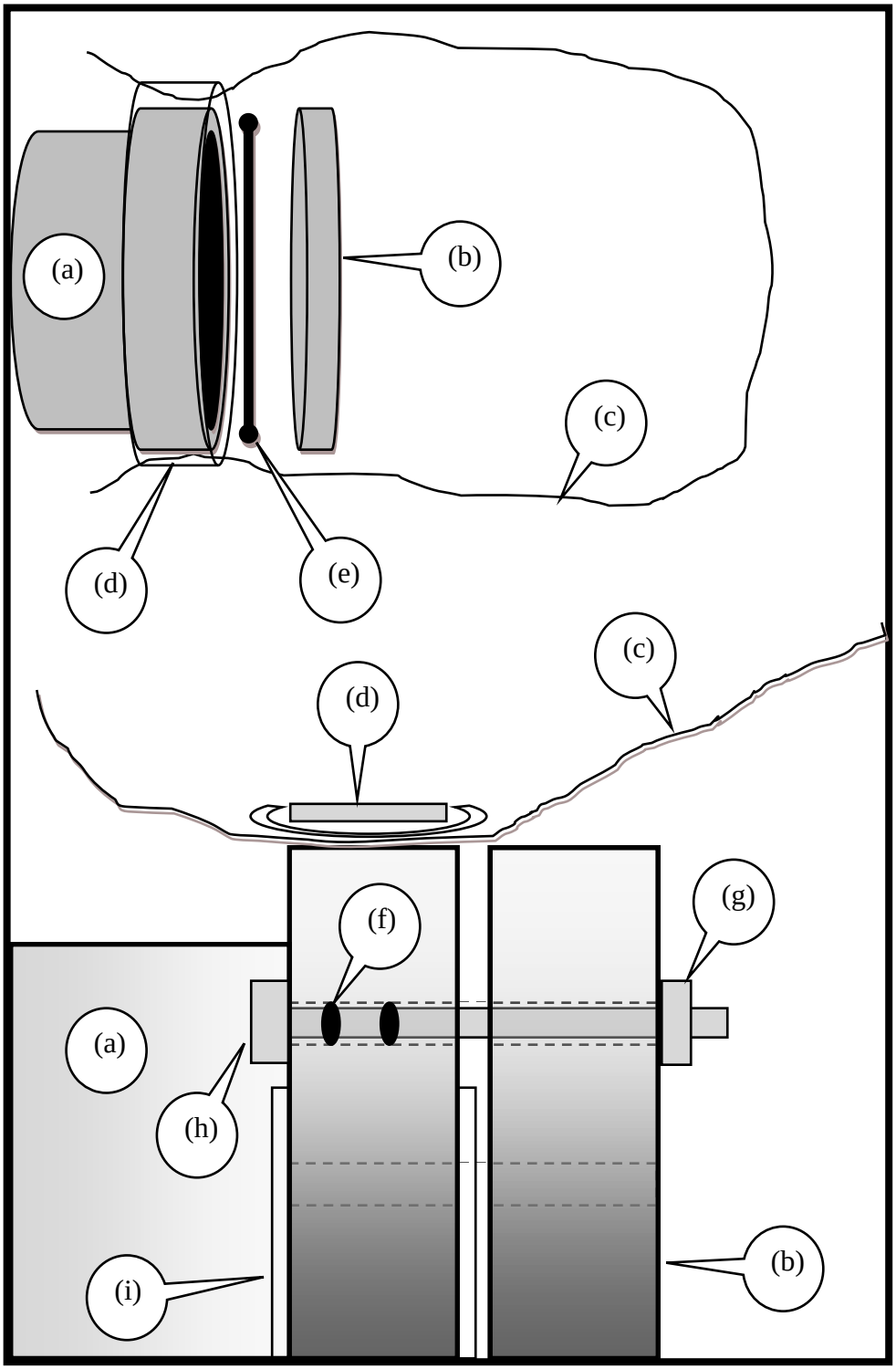

Figure 2.7. Drawing of the glove bag seals. a) HV chamber side, b) glass viewport in 6" CFF plate, c)glove bag, d) hose clamp and rubber gasket, e) O-ring and retaining ring, f) O-rings on hex head bolt, g) hex nut, h) hex head bolt with machined grooves for O-rings, i) heat tape for sealing unused bolt holes.

2.2.2. Pumping System. The HV turbo pump is a rebuilt Pfeiffer TPH 330 turbo molecular pump. It is a dual vane water cooled pump, and has a heating jacket for baking the system. The HV chamber reaches a base pressure of ~ 10^{-7} Torr. There is a screen in the turbo pump to catch parts which might fall from the sample stage. The backing pump for the turbo pump is the first Alcatel dual stage mechanical pump which provides a vacuum of ~ 10^{-4} Torr. A manual valve separates the turbo pump from the fore line pump. This valve is closed when the sample is being changed, or when the system is not being used to prevent contamination by the high grade pump oil.

There are 2 venting lines on the HV side of the system. Both of these lines are fed from an Ar tank leading into a manifold. One of these lines is attached by a manual valve to the turbo pump itself and is used for bringing the sample chamber to an atmospheric pressure of Ar. The other line is attached to the rough backing pump through a manual variable leak valve. Its primary purpose is to create a stream of Ar, preventing hydrogen and hydrocarbons from returning to the system, thereby reducing the partial pressure of hydrogen in the system.

The UHV side of the system is pumped down to ~ 10^{-8} Torr by the single vane turbo pump. There is an electromechanical KF valve separating the turbo pump from the second Alcatel dual stage mechanical backing pump. This valve is controlled by the UHV turbo pump controller, and is set to close during a power failure or as soon as the pump speed slows down. The Ar venting of this turbo pump is also automated by the turbo pump controller. It is designed to allow Ar into the pump when the speed of the pump has dropped below 40% of the maximum speed either after a power failure, or when turned off. There is also an Ar variable leak valve between the backing pump and the electromechanical valve. The purpose is the same as that of the variable leak valve on the HV side of the system.

The UHV and HV sides of the system are backed by separate mechanical vane pumps in order to prevent gases from entering the UHV side through the fore lines. Each mechanical roughing pump is vented into the house vacuum system.

Ar has been chosen as the inert gas for the MS-RGA. The Ar is supplied through a standard high pressure regulator (part number PRS20123311-580, PraxAir). The Ar is fed at around 5 PSI to a manifold with a vacuum/pressure gauge which has mechanical

on/off switches for each of the Ar subsystems. There are 5 connections here: 2 variable leak valves (as mentioned above), 2 turbo pump venting valves (as mentioned above), and one connection for the glove bag. The connection for the glove bag is made through a 3 way gas switch. The switch is also connected to the house vacuum in order to purge the glove bag and back fill it with Ar during sample insertion.

2.2.3. Heating and Cooling Systems. The following outlines the systems which provide ambient and sample temperature control.

2.2.3.1 Turbo pumps. The UHV and HV turbo pumps are cooled by water pumped through the system by the house refrigeration lines. The house water enters a manifold on the system where it is separated into 3 fluid flow meters. The UHV system runs on 8 gallons per hour, while the HV system runs on 10 gallons per hour. The water is then circulated back into the house cooling return lines. The flow of the water is increased while baking out the system. The UHV cooling block was machined from aluminum.

The HV also has a self regulating heating jacket which is powered by 220 V, and is turned on at the control panel during system bake out.

2.2.3.2 Chamber heaters. Heat tape wraps the main sample chamber, the 2.75" CFF nipple, and the inline valve. The heaters are used for baking out the system. Control of the heaters is accessed through the backing pump and heater control panel. The heat tape is powered by 220 VAC and monitored by thermocouples. The main chamber and the inline valve are on separate controls, and the temperature can be regulated independently from RT to 220 °C.

The quadrupole (as seen in Figure 2.6) of the RGA also has a heating jacket (not shown) which is used during bake out. It is self regulating and is powered on using a 120 V power strip.

2.2.3.3 Sample stages. Both the high temperature and low temperature sample stages use the same heater controller (CAL 3300 Single Loop Controller, CAL Controls). The CalControl 3300 temperature controller monitors and controls the temperature using a type K thermocouple (+/- yellow/red). The controller has been modified so that the voltage supply to the heater can be switched from the front of the controller. The QCM

cartridge heater is a 48 VAC heater, while the cartridge heaters for the high temperature stage are two .25” diameter, 1.5” long, 120 VAC, 100 W cartridge heaters (part number E1J40-L12, Watlow) wired in parallel. Therefore the total maximum power is 200 Watts. Power is delivered to the heaters via a solid state relay, controlled by the temperature controller. The high temperature stage (Figure E.1) is machined from stainless steel, and is electrically insulated from the rest of the system (in case of heater burnout and shorting). The temperature controller is connected to the serial expansion port of the computer via an RS232 cable. More information on the temperature controller as well as instructions for programming can be found in the Cal Control operations manual [30]. To test the heaters, disconnect the heater power from the back of the temperature controller, and measure the resistance between the heater power feedthroughs on the CFF. The resistance should read near 70 Ohms since the heaters are wired in parallel. To check for a shorted heater element, ensure there is no continuity between the chamber and either of the heater’s electrical feedthroughs.

The low temperature QCM sample stage is plumbed into the 3rd fluid flow meter of the refrigerated water manifold. The heater when combined with the cooling lines should allow for precise control of the QCM temperature as well as immediate temperature response.

2.2.4. Electrical Control Systems. Figure 2.8 shows the stack of electrical component interfaces mounted in version 1 of the cabinet. The final arrangement of the components can be seen in the right of the image of Figure 2.2

2.2.4.1 RGA. The RGA is powered through a 120 VAC isolator, to reduce transient signals in the system. The RGA is controlled directly by the computer, and is wired via a RS232 cable connected to a serial port expansion card in the computer. The RGA is controlled directly from the Windows software.

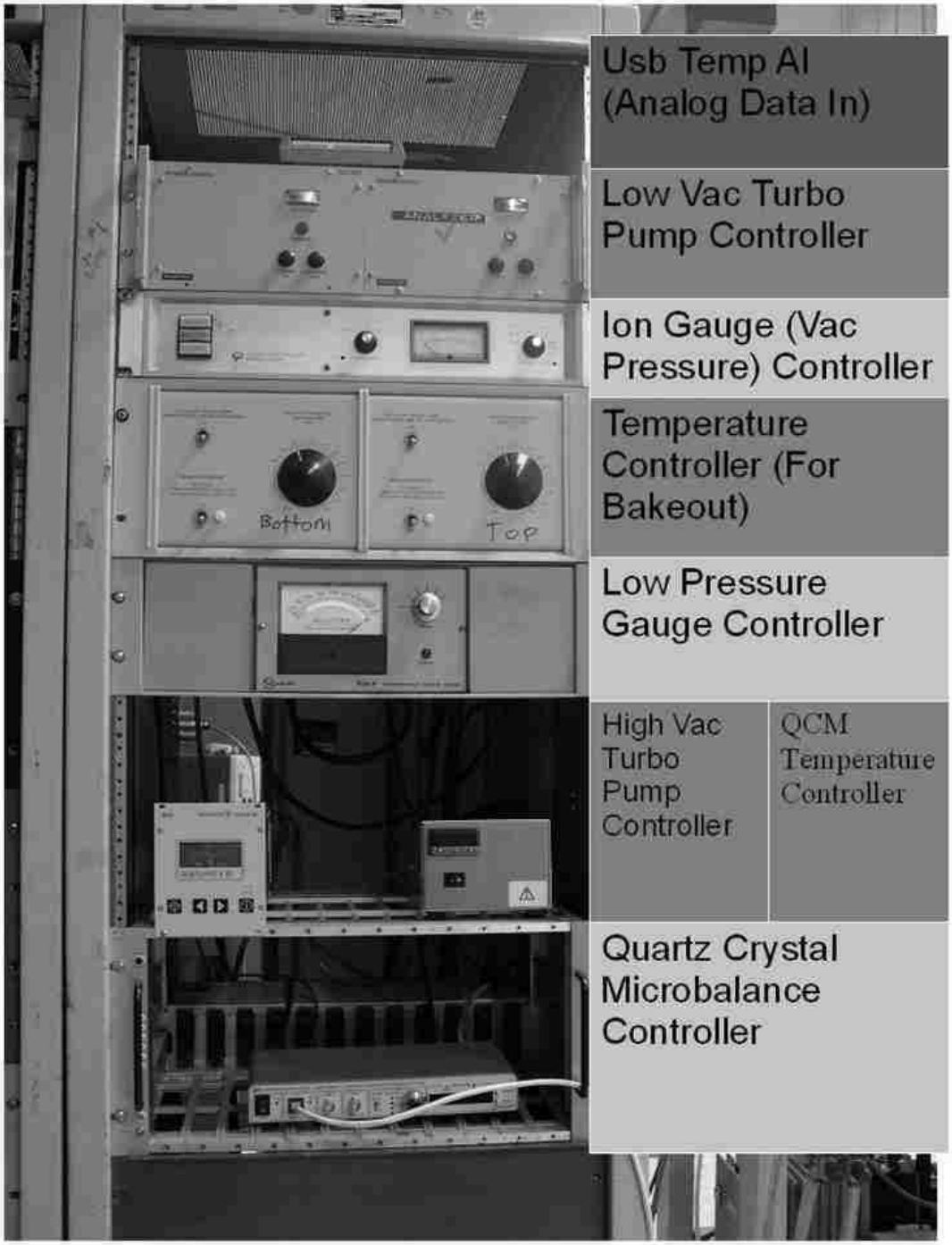

Figure 2.8. Electrical components.

Even with the voltage isolation there is a cyclic noise in the signal. This signal can be reduced by picking appropriate scan speeds to try to minimize the effects of the cycling behavior. Figure 2.9 shows 2 charts where FFT analysis has been performed in order to determine the cause of the oscillations. Unfortunately, the source of the noise in the signal cannot be determined due to the low frequencies of the scan speeds. The oscillations tend to go away with a slower scan speed and a longer wait time between scans (e.g. 64 seconds per scan trigger or 0.94 scans per minute). Oscillations in the power of the heater do not correlate with the oscillations in the pressure.

2.2.4.2 QCM. The QCM is controlled by the QCM controller mounted in the control rack. The controller is powered by 120 VAC, and can be remotely controlled from the Windows software. Data acquisition is performed by the computer or by the USB analog to digital data logger (USB Temp-AI, Measurement Computing). A BNC cable connects the QCM to the data logger which records the frequency of the QCM crystal. The analog voltage is ±10 VDC and is linearly related to the Relative Frequency display of the QCM controller in the selected scale. A RJ45 cable connects the QCM head to the controller and a RS232 cable connects the controller to the serial expansion port of the computer. More information on the operating principles can be found in the SRS QCM200 manual [31].

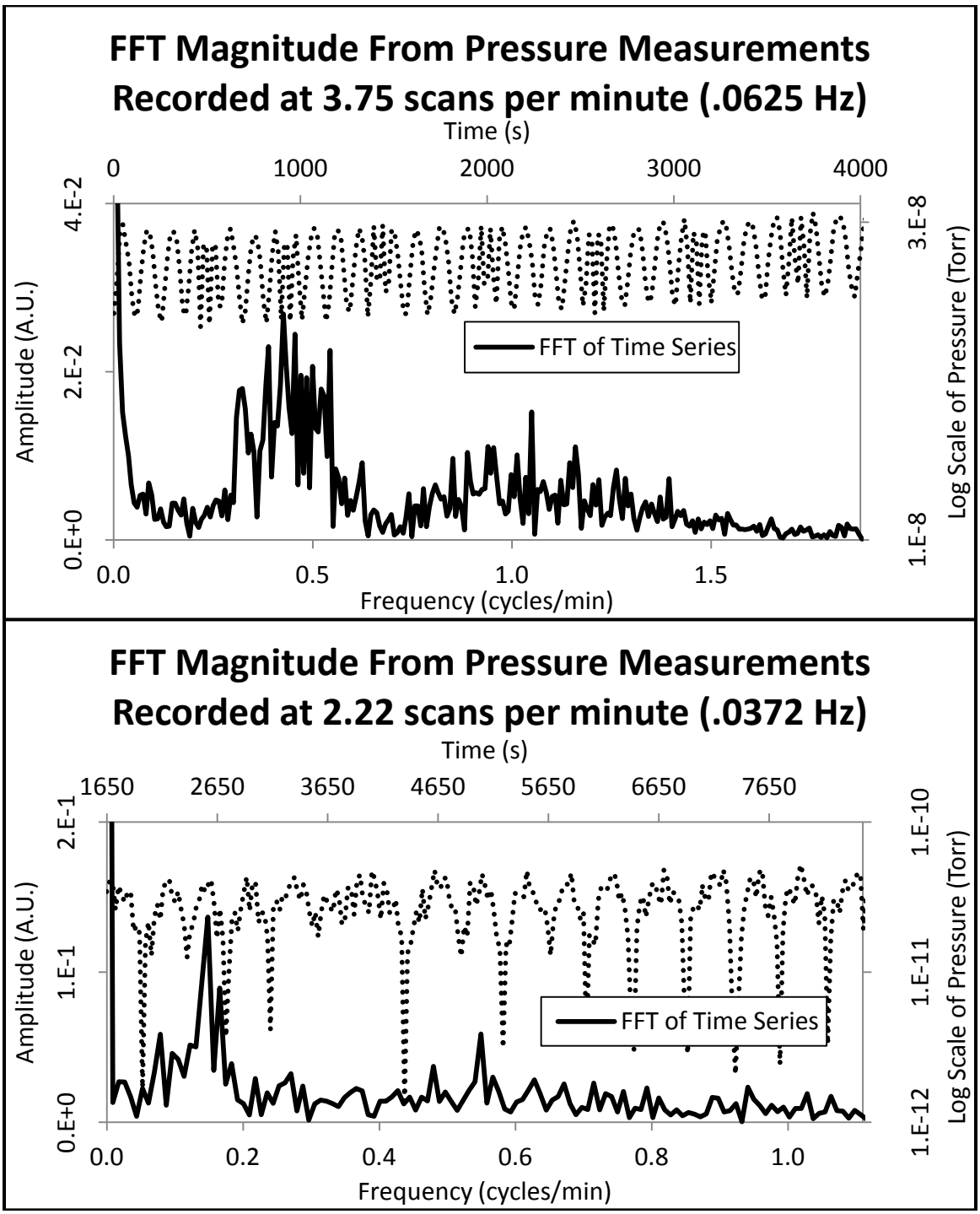

Figure 2.9 FFT (primary axis) of RGA data taken at sample interval of 16 seconds(top) and 27 seconds (bottom), displayed with the time series data (secondary axis) showing instability of pressure signal.

2.2.4.3 Electromechanical valves. There are 2 electromechanical valves on the system. The fore line valve between the 80 l/s UHV turbo pump and the mechanical backing pump is powered by the 120 VAC power strip. This valve is controlled by the turbo pump controller via a connection to the body of the turbo pump itself. The venting valve for this turbo pump is also connected to the body, but is powered by the pump itself. Both valves can be controlled through the turbo pump controller. These valves are installed for the health and safety of the turbo pump.

2.2.4.4 Pressure gauge controller. The pressure gauge controller (XGS 600 Gauge Controller, Varian Vacuum) is powered by 120 VAC, and is installed in the control rack. There are 4 pressure gauges; 2 ion gauges (571 ionization gauge tube, Varian Vacuum) and 2 convection gauges (531 or 536 Thermocouple Gauge, Varian Vacuum). Each gauge is wired into the gauge controller with its own gauge cable. During normal operation the convection gauges measure the pressure of the mechanical pumps, and the ion gauges measure the pressure of the turbo pumps and chambers. The gauge controller can be controlled manually or through the Windows software. The controller is connected to the serial expansion port of the computer via an RS232 cable. There is an analog output for the gauges and data for each gauge is sent to the USB data logger using 2 modified FireWire (IEEE 1394) cables. The analog output is 0-10 VDC and the output voltage equals Log(Pressure) + 11. More information on the operation of the XGS controller can be found in the operating manual [32].

2.2.4.5 Data logger. To reiterate, the USB Temp-AI data logger records analog data of the gauges from the pressure controller. It also records temperature measurements from the QCM head and the reference thermocouple attached to the high temperature sample stage. This can be especially useful if the system crashes during an experiment. The data logger is connected via a USB-B cable to the computer, and is controlled by the Windows software. The gauges are connected to the USB-Temp-AI logger using the software selected differential mode on the voltage input terminals. More information on the operation of the USB Temp-AI can be found in the operation manual [33].

2.3. OPERATION

The following sections outline the basic parameters and steps to properly characterize gas desorption, decomposition temperatures, picogram changes in mass, and ionization energies for a variety of materials systems. For the various components there are some settings that do not get changed, but none the less have been determined through trial and error. Where applicable these settings are noted here.

2.3.1. Pumping Down. The system can be set to run in a few different configurations. Pumping down the chambers should be performed with the inline valve closed. To close this valve tightly, use a torque wrench set to 25 ft. lbs. Before pumping down the system it is assumed the samples have been inserted, and the chambers have been sealed. If the operating configuration is for gas sample analysis, the UHV inline valve between the chambers will remain closed, and the lower turbo pump (HV) will not be used.

1. To set the water cooling flow rates: first, completely open the return valve for the house refrigerated water lines (on the wall). Next, open the supply valve only enough to match the pressure gauge on the return gauge, (about 1/8 of a turn on the ¼ turn ball valve). Adjust the flow on the turbo pump meters so that the lower pump is supplied with more than 4 gallons per minute, and the upper pump is supplied with more than 20 gallons per hour. Check for water leaks around the system.
2. Check that the venting valve on the lower turbo pump is closed, and then turn on the rough backing pumps. These pumps are controlled from switches at the control panel by the temperature dials. The manual valve between the lower pump (HV) and its backing pump should now be opened.
3. Power ON the pressure gauge controller (switch on back), and optionally run the Windows software for the XGS – 600 controller. Once the controller has warmed up, the convection pressure should be visible on the panel. Ideally, the pressure should be below 10^{-3} Torr before turning on the turbo pumps. The turbo pumps should never be turned on if the backing pressures are above 10^{-2} Torr.
4. Turn on and check the pressure on the Argon supply tank. The pressure supplied to the system should be about 5 P.S.I. at the Ar manifold of the system. This is well

below the limit for the turbo pumps (20 P.S.I.). Open the switches for the upper chamber, the lower chamber and the leak valves. Check that the leak valves are off. The switch for the glove bag should be off and/or the purging valve should be set to vacuum or off.

5. Power ON the turbo pumps' controllers (switches on back). Set the top (UHV) turbo pumps to run (run/stop buttons on front of controller). This should immediately open the electromechanical valve between the top pump and its roughing pump. Check that the LED light on the valve is green. **If it is red, immediately stop the turbo pump (press the run/stop button) and troubleshoot the valve**. Next, set the lower turbo pump to run. Once the UHV pump is up to speed, the controller should show an arrow above the rightmost symbol. Once the HV pump is up to speed, the analog indicator should point to max. **Wait until these pumps are up to speed before proceeding!**
6. If the operating configuration is for temperature controlled decomposition, the inline valve can now be opened using the torque wrench. If the operation is for gas sample analysis, the valve can be left closed and proceed to step 8.
7. The ion gauges should only be used when performing temperature controlled decomposition experiments. Power ON the ion gauges, either by the controller or by the XGS – 600 software (Explained in section: "**TPD and Data Acquisition"**).
8. The convection gauges should show a pressure near 10^{-4} Torr. The variable Ar leak valves can now be turned on (the lower valve is not used in gas sample analysis). Slowly open the valves so that the pressure on the convection gauges is **no higher** than $1x10^{-2}$ Torr.

The system is now pumping down. Typically, the system will not reach a base pressure for about 4-8 hours. Before leaving and before sample runs, **double check**:

- Water flow is constant.
- Pumps are running.
- Ar and vacuum pressures are not fluctuating, and there is enough pressure in the Ar tank.
- The electromechanical valve shows a green light.

2.3.2. Bake Out. The bake out of the system is an important step after the system has been idle for an amount of time, or after any runs have possibly contaminated the system. The bake out described here brings the vacuum chamber and sample stages to 200 °C, thereby removing any water that has adsorbed to the surface. This temperature is high enough to loosen some oils or other contaminants, but the maximum temperature is limited by O-rings and the electronics in the turbo pumps.

1. **IMPORTANT**! Remove the control unit (ECU) of the RGA.
2. Remove the glove bag, and secure any hoses and wires away from the chambers and heating tape. Replace the viewport O-ring with a used O-ring if needed.
3. Pump out the system as described in section 2.3.1. Open inline valve after pumping down is complete.
4. Set both turbo pump controllers to heating. The lower pump has a button on the face of the controller, while the upper pump has to be set manually. To set:
    a. Using the left and right arrows on the controller find “heating”.
    b. Press both arrows together to select this setting.
    c. Using the arrows select “on”.
    d. Press both arrows together to select this setting.
5. Once the system is at a base pressure, increase the flow of the water cooling lines for the turbo pumps to just below their maximum flow rate.
6. At the chamber heater control panel, set the dials to 200 °C, and then turn on the top and bottom heaters.
7. Turn on the heating jacket for the lower turbo pump. This switch is located on the bottom of the control panel above the orange cord leading to the pump.
8. Plug in the heating jacket for the RGA. The power for this heater comes from the power strip on the frame.
9. On the sample stage controller run a ramp rate program with max temperature 200 °C, ramp rate of 50 °C per hour, and soak time of 8 hours. Instructions for this can be found in the “**TPD and Data Acquisition**” section below.
10. Let the system bake for 8 hours, or overnight.

When the bake out is complete reverse procedures 8 - 4, and leave the turbo pumps running. Replace the RGA controller and check that the high temperature sample

stage is returning to RT. The lower turbo pump can be set to standby by pressing the "standby" switch on the controller.

2.3.3. Sample Preparation, Removal, and Insertion. The following outlines the process for correctly preparing the samples for measurement.

2.3.3.1 Temperature controlled decomposition. Samples are normally prepared using a hermetically sealed Tzero sample pan, the same pan used in DSC and TGA analysis (901697.901 and 901698.901, TA Instruments). The pan is loaded with the sample and then sealed closed using the TA Instruments Sample Press or hammered closed using the punch and die set shown in Figure E.5. Alternatively, the bulk sample can be loaded into a sample holder and carefully carried in the sample holder container pictured in Figure 2.10. Sample preparation of air and oxygen sensitive materials is done in a glove box, and appropriate measures are taken when transporting the sample from the glove box to the systems glove bag.

The following steps outline removing the sample holder and inserting the new sample. This should be done with the UHV inline valve closed, the manual valve between the HV turbo pump and its rough pump closed, and the lower chamber venting valve open. This ensures the sample chamber is at or above 0 P.S.I with Ar. The process for inserting a sample for the low temperature stage is essentially the same as outlined here. Tools that are required in the glove bag are: the sample removal tool shown in Figure 2.10, a perforation tool (in an open bottle to prevent punctures of the bag), and a new O-ring for the viewport if needed.

1. Check that all switches (except the glove bag) on the Ar manifold are off and that there is Ar pressure at the manifold.
2. The Ar switch next to the glove bag should be set to "Vacuum" until completely empty. Next, set to "Fill" until the bag is half full, i.e. not stretching the seams of the bag. Repeat this process 3 times.

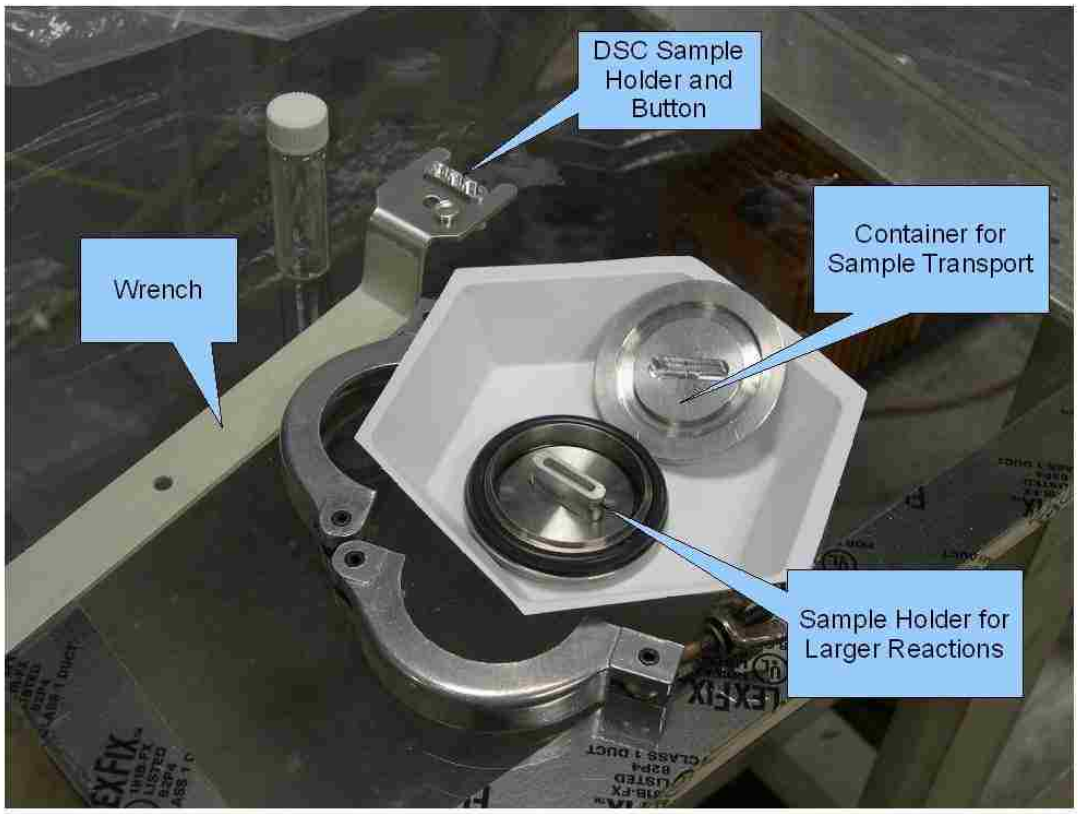

Figure 2.10. Tools for carrying, removing, and transporting samples. The transport device is machined from 2 KF-40 blanking flanges and is sealed with the sample inside a glove box.

3. Making sure the lower chamber is vented, remove the 4 nuts holding the 6" CFF viewport with the wrench end of the sample removal tool. Do not remove the bolts from the chamber as these provide a seal for the glovebag.
4. Using the sample removal tool, remove the sample holder (also shown in Figure 2.10) from the high temperature heater block (Figure 2.3(b)).
5. Place the new sample in the sample holder, and carefully put a small hole in the lid with the perforation tool.
6. Using the sample removal tool, place the sample holder back in the heater block.

7. Replace the viewport (with a new O-ring if necessary), and tighten the nuts back onto the bolts with the wrench end of the sample removal tool. After pumping down the system, recheck these nuts.
8. Turn off the venting valve on the lower turbo pump and pump the system down according to section "**Pumping Down**" above.

2.3.3.2 Sample gas preparation. Figure 2.11 outlines a flow chart for the variable leak gas sampling system. For measuring a gas sample directly from the UHV variable leak valve, it is assumed that the UHV inline valve and the variable leak valve are closed and that the top chamber is pumped down with the ion gauges off. The rough pump for the bottom chamber is used in this application to evacuate the gas sample holder/convection gauge (GSH) and variable leak valve.

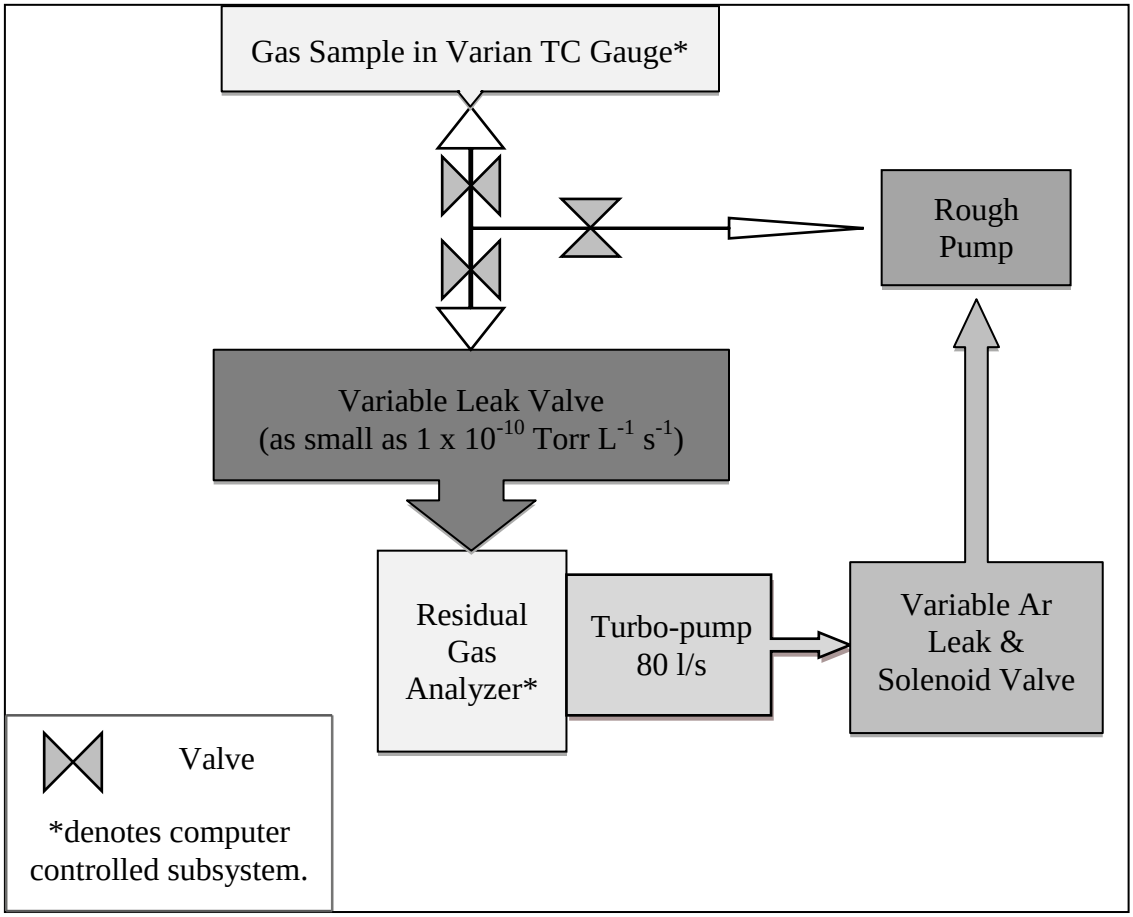

Figure 2.11. The layout of UHV variable leak valve and its components.

1. With the GSH attached to the tee, open the three valves leading to the rough pump, GSH and UHV variable leak valve.
2. After a sufficient amount of time (30 minutes or more), close the 3 valves and remove the GSH from the bottom of the tee.
3. Connect the GSH to the gas sample supply after purging the supply where appropriate. The pressure of the gas supply needs to be close to STP in order to correctly measure the pressure of the GSH. Completely open then close the valve on the GSH. Remove the GSH from the gas sample supply.
4. After reattaching the GSH to the system, open only the valves to the vacuum line and the variable leak and let the system come to equilibrium (30 minutes or more).
5. Close the valve to the vacuum system and open the valve to the GSH.
6. Connect the convection gauge to the vacuum gauge controller using either gauge cable.
7. Turn the RGA on and monitor the total pressure as described in the sections "**Measuring Sample Gasses**" and "**RGA**" below.
8. Purge the variable leak valve by opening it until the RGA total pressure reads no more than 10^{-5} Torr. Purging should take up to 30 minutes, but is complete when the pressure on the convection gauge starts to drop considerably.

2.3.4. TPD and Data Acquisition. This section describes the procedures for preparing and running samples in the MS-RGA. It covers the basics of the Windows software including naming formats and some variable settings. For settings not covered here, refer to the specific sections' user manual. Proper naming conventions are necessary for the analysis of the data using the Data Analysis Tool (Appendix C). Troubleshooting should always start with "*Is the device turned on?*" followed by "*Is the device plugged into the computer?*" In the following sections buttons or menu items are indicated with italics.

2.3.4.1 RGA. The RGA can only be controlled through the computer and the RGA software (RGA v3.213, Stanford Research Systems). Power ON the RGA and open the software. *Connect* to the RGA head using the *Connector List Setup. Toggle Filament On*, then start *Degas* through the *Head* menu. Choose *Calibrate Detector* through the

same menu. Next, select *Total Pressure* under the *Utilities menu.* This will display the total pressure for rough measurement and not function when making low pressure measurement using the CDEM. This method is used for the purging the variable leak valve for measuring sample gasses.

Scan Logging needs to be set under the *File* menu. Save every scan and *Enable* advanced logging. The log directory also needs to be set. After selecting *Histogram Mode* select the clock icon and the wrench icon. These are the settings that need to be enabled to correlate the temperature and pressure data. Unfortunately, the software has bugs that can be avoided by selecting the right *Stop Mas*s and *Scan Speed* for the particular *Triggered + Scan Period*. To start and stop taking measurements, use the *Start Scan* and *Stop at End* buttons.

Here is an example of some settings used during an arbitrary experiment with a scan speed of 6 and a scan period of 64 seconds:

Histogram Scan Setup

- Data Points in Scan: 193
- Units: Torr
- Noise Floor: 4
- CEM Status: OFF
- Points Per AMU: 1
- Scan Start Mass: 1 amu
- Scan Stop Mass: 193 amu
- Focus Voltage: 90 Volts
- Ion Energy: HIGH
- Electron Energy: 70 eV
- CEM Voltage: 1000 Volts
- CEM Gain: 1.00E+006
- Sensitivity Factor: 1.00E-004
- Filament Current: 1.00 mAmps

After running a measurement, the data needs to be converted to text files for analysis. First, *Open Scan Logs* and select the file. Next, *Save Scan Logs As* ASCII data named "RGAText" (no space). This creates a folder named "RGAText" with the time stamped text files (a few hundred .txt files). The data is now ready to be analyzed using *InputGui.m* for the RGA analysis MATLAB program. When finished with the experiments, toggle OFF the CDEM and the filament. Then *Disconnect* the RGA head using the *Connector List Setup*. Finally, power OFF the RGA.

2.3.4.2 Temperature controller. The controller regulates using the PID method (proportional (P), integral (I), derivative (D)). These parameters are listed in Apendix B. **Do not start the heating cycle until the device is communicating with the computer, all of the initial parameters are set, and the chart is logging. Do not change the set point during a run, as the temperature will become unstable.**

To avoid burning out several heaters, it is a better idea to start with a smaller power level limit (*PL.1*; % of power supplied during a set cycle time) and cycle time of 0.2 seconds (*CyC.t*; proportional cycle time or P from PID). The number of complete cycles provided is the product of the AC frequency (60Hz), the cycle time, and the power level percentage (*l*). Since the solid state relay provides complete AC cycles, a simple calculation (1) gives the power *P* input into the system as a function of the power limit *l* at a particular time.

$$P(t) = l(t) \times P_{Average} = l(t) \times \frac{V_{RMS}^2}{R} \tag{1}$$

CalGrafix is a bare bone interface for the CalControl 3300 temperature controller. Most of the settings are not self-explanatory. To get started select the *CalGrafix* shortcut. Next, select the *New Instrument Tab* from the picture tool bar. If the device, in this case the Cal3300, is not automatically listed there is a problem with the communications of the controller. Check that the manual settings on the controller are set correctly, and if necessary, reset the controller and restart the computer. The controller reset is under *level 3* (*rSET*). The settings for the CalControl 3300 can be reset using the controller interface. After resetting the controller, one must manually configure the communications settings.

After selecting the instrument and its type, a box should appear which mimics the controller face. A right click on the controller allows you to change the settings of the heater using the *Settings* tab. The settings depend on the application, and the type of heater being used. For example in a vacuum; a 100W 120V AC heater, (1/4" x 1"), will require a power limit of 40% and a cycle time of 0.2 seconds to reach a temperature of 400 °C. These settings can be made under the *setpoint 1* tab of the properties. Don't forget to set the toggle switch to 120V on the temperature controller.

To create a chart of the temperature and other data ranges, select *New Chart* from the picture tool bar. Next select the file name and sample frequency. The default is 5 seconds, but it needs to be **set to the same sampling frequency as the RGA**. Then add the data field that you want to measure. The most important is the temperature; it can be displayed by selecting *Device.../Display/ProcessValue*. Input the name of the trace, and select the units to be used. The settings cannot be selected correctly after this point. The temperature set point *set_point1* and the power *Set_Point1_Power* are two other relevant traces. The traces are arranged in the file system according to the level from which they can be manually accessed. Note that this is different from the arrangement which can be remotely set. Change the time scale to include the time and date. Ex: 20 30 40 [Date] where date is in 03/02/01 format. After creating the graph it can be modified from the properties with a right click on the graph. As mentioned before, the name and units cannot be changed.

To set the properties for the run, click on the controller interface and change the parameters. 4 heating ramp rates have been calibrated (Appendix B): 60, 120, 240 and 480 °C per hour. The ramp rates and soak times are set under the *Programmer* header. The *Setpoint value* (set in *Setpoint 1*) should be set to no more than 500 °C. *Power level* (set in *Setpoint 1*) is the ON/OFF switch for the system and should be set to no higher than 50%. For the calibrated ramp rates, chose the wait time according to Table 2.1. Before confirming (*OK* or *Apply*) the rest of the systems must be running.

When ready to start the run set the *Power level* to 10% and the *Programmer* to OFF then apply the changes. Wait the specified time and then switch the *Power level* from the initial limit of 10% to the final limit of 50%, set the *Programmer* to ON and then apply the changes.

When the run is finished, the power limit must be reset to 0 in *Setpoint 1* and the program should be set to OFF in *Programmer*. Saving a chart is done by selecting the chart and then saving as "TempChart.csv". The .csv can be loaded into the *RGA Analysis* MATLAB program, or imported into a spread sheet later.

Table 2.1. Temperature Parameters for Calibrated Ramp Rates

°C/hr	Wait time (minutes)	Curve Fitting Equations (T_S is the estimated sample temperature and T_C is the recorded controller temperature)
60	0	$T_S = 3.6x10^{-9} T_C^4 – 5.1x10^{-6} T_C^3 + 2.7x10^{-4} T_C^2 + 1.5x10^{-2} T_C + 15.3$
120	2.5	$T_S = 6.1x10^{-9} T_C^4 - 8.8x10^{-6} T_C^3 + 4.5x10^{-3} T_C^2 - 2.1x10^{-1} T_C + 24.9$
240	5.0	$T_S = -4.5x10^{-9} T_C^4 + 1.5x10^{-6} T_C^3 + 1.9x10^{-3} T_C^2 - 1.35x10^{-1} T_C + 25.2$
480	7.5	$T_S = -8.9x10^{-9} T_C^4 + 8.1x10^{-6} T_C^3 - 8.6x10^{-4} T_C^2 + 9.2x10^{-2} T_C + 20.5$

2.3.4.3 Pressure gauge controller. The XGS-600 Windows software (written by D. Peaslee and T. Mason in MS Visual Studio 2010) emulates the pressure controller and allows for data logging. The code and screens are outlined in Appendix D. Once the pressure controller is powered ON (from the back), and the communications established; the software provides the same functionality as the controller. The convection gauges can be calibrated, and the ion gauges can be turned on/off and degassed from the buttons on the software's interface.

1. Select the correct communications port under *Edit/Comm Set Up*.
2. Select the file location under *File/Save As* and save the file as "Pressure".
3. Select the *frequency* (seconds per scan) under *Edit/Start-Stop*, to match that of the RGA logging.
4. Start data logging by selecting *Edit/Start-Stop*. Once the logging has started, the Varian logo will turn green. If the recording is stopped the logo will turn red.
5. Ensure the gauges are on. If a gauge is on, its *ON/OFF* button will turn yellow. Also, if it is degassing, its degas button will turn yellow.

6. The XGS-600 is now ready for a sample run. The data does not need to be saved again, as it updates the file after every scan.
7. When finished with the measurement; stop the logging (select *Edit/Start-Stop*), turn off the gauges (click on the *ON/OFF* buttons of the gauges) and exit the program.

2.3.4.4 Data logger. The USB Temp-AI software (TracerDaq Pro, Measurement Computing) has many steps to set up correctly. Once the device has been set up, the software opens the last saved settings and is then somewhat intuitive. This data is not used in the RGA Analysis MATLAB program, and so can have a much higher scan rate (a scan rate of 1 or 0.1 Hz is adequate). This data logger is used to watch the temperatures and pressures in real time.

1. Open the TracerDaq program and select *Strip Chart*.
2. If needed, select the scan rate and time span from the *Edit/Scan Rate-Trigger Settings* menu. The settings must be chosen so that the recording will not end before the measurement is finished.
3. Start the recording with the *play* button.
4. When finished, press the *stop* button.

The file needs to be exported (not just saved) to a .csv file for analysis in MS Excel. The naming conventions are not as important here, but using "TDData.csv" is best. After saving the data, simply close the program when done.

2.3.4.5 QCM. The windows software for the RSR QCM200 has the requirement that the QCM is *Running* before the logging file can be started or named. After clicking on the *Running* button the log file path can be named. This is done in the window under the SRS logo. After naming the file, select the *Logging* button. The program saves as a .txt file as it collects the data. Before starting an experiment the relative frequency needs to be zeroed (*Zero Rel F* button).

2.3.5. Measuring Sample Gases. The RGA is the only instrument used when studying sample gases. After preparing the sample as outlined in the above section "Sample Gas Preparation", the RGA can be used in the *Analog Scan* mode. This mode is useful for studying characteristics such as ionization potentials and possibly the recombination or stability of ions in the gas. It is essential to run a few scans to warm up

the system, and capture a background measurement. Scans should run at a slow speed for maximum resolution. The scans must be converted to ASCII .txt files for importing data into MS Excel. Refer to the section "RGA" above for this procedure.

The settings that are most useful in this application are the *Electron Energy* (ionization energy) and the *Focus Voltage* (related to the velocity of the ion entering the mass filter). These settings can be found in the *Head/Ionizer Settings* menu. The focus voltage (FV) is the negative potential set up between the ground and the focus plate and is equal to the ion energy (IE) minus the electron energy (EE). The electron energy (absolute value) is equal to the potential between the anode and the repeller. It is recommended that the focus voltage be at least 30 V more negative than the repeller voltage (RV) in order to reduce electron leakage into the mass filter.

The time of flight *TOF* of the ions of mass to charge ratio (*m/z*) as they pass through the mass filter is related to the distance between the detector and the focus plate ($d \approx 5$" or .127 meters) and the potential between the focus and anode plates (V = IE - FV). This calculation does not take into account external components and geometry of the ionizer, the deceleration by the quadrupole filter, or the acceleration due to the CDEM. It is an estimation based on ionization at the center of the RGA ionizer. Additionally, this is the lower limit of the *TOF* since the particles will have an initial velocity attributed to thermal and kinetic energy inherited from the sample. Table 2.2 gives some values of the settings used in a measurement of diborane. Figure 2.12 is a plot of *TOF* as a function of *V* and *m/z*. These approximations indicate that the time of flight of ions in the system is probably of the order 10^{-5} seconds; hence only metastable ions with lifetimes greater than this will be detected.

$$TOF = \frac{d}{v_{average}} = \frac{d}{\sqrt{V(q/M)}} = d \times \frac{\sqrt{1.04 \times 10^{-8} \cdot (m/z)}}{\sqrt{V}} \qquad (2)$$

Table 2.2. RGA Parameters for Ionization Potential Experiments with Ion Energy of 12 Volts. (*Default Values*)

Electron Energy (EE)	Focus Voltage (FV)	Voltage of Repeller (RV)	RV - FV	V = IE - FV	Average TOF (seconds)
100	-120	-88	32	108	1.18E-05
90	-110	-78	32	98	1.24E-05
80	-100	-68	32	88	1.30E-05
(70)	(-90)	(-58)	(32)	(78)	1.39E-05
60	-80	-48	32	68	1.48E-05
50	-70	-38	32	58	1.61E-05
40	-60	-28	32	48	1.77E-05
30	-50	-18	32	38	1.98E-05
25	-45	-13	32	33	2.13E-05

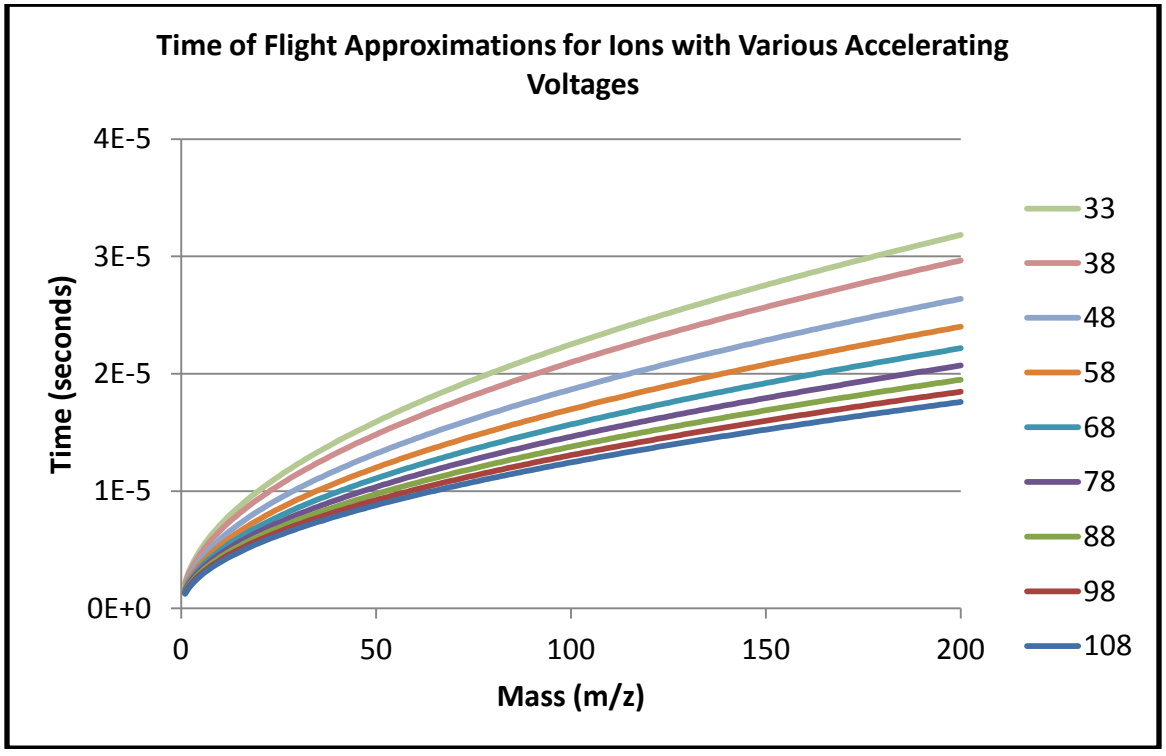

Figure 2.12. Chart showing time of flight approximations, using 5" as the traveled distance and various potentials set up between the focus plate and the anode.

2.3.6. Shut Down. The system can be shut down completely, or set in a standby state. The steps for shutting down the subsystems can be found in the sections above. To reiterate:

- The temperature controller must be set to a power level of 0%.
- The ion gauges must be powered OFF.
- The RGA ionizer and CDEM must be powered OFF.
- The inline gauge must be tightly closed with the torque wrench.
- The UHV variable leak valves must be closed.
- There must be pressure in the Ar manifold, the supply to the glove bag must be OFF, and the supply to the variable leak valves and top and bottom chambers must be ON.

To set the system in standby, first press the Standby/Reset button on the HV turbo pump controller. Next, set the UHV turbo pump to standby; using the arrows scroll to *Standby* (002), then select, change and confirm by pressing both arrows. Be sure that the water is still running at the recommended flow rates. With the system in this state, one or both turbo pumps can be shut off completely.

When shutting off the top UHV chamber, the venting process is automatic and starts as soon as the *run/stop* button is pressed. When shutting off the bottom HV chamber: first, be sure to shut the manual valve between the turbo and rough pump. Next, press the power button on the turbo pump controller, and after 10 minutes (the green LED will fade out) open the Ar venting valve on the side of the turbo pump. After the pressure on the manifold returns to STP, close the vent valve and power OFF the rough pumps and completely open the 2 variable leak valves for 10 minutes (this vents the rough pumps). Finally, the supply and return valves for the cooling lines need to be closed. Power down any systems that remain on, including the RGA controller.

2.3.7. Cleaning. If the system needs to be cleaned, solvents such as acetone and trichloroethylene should be used to reduce the amount of adsorbed liquids on vacuum surfaces. Gloves should be worn whenever handling parts that see the inside of the vacuum system, including samples and sample holders.

2.4. ANALYSIS OF DATA

2.4.1. TPD. Data analysis is performed using the RGA Analysis tool (written by T. P. Sheehan and D. Peaslee in MATLAB). The program imports the data, collates the time stamps, and outputs a .m file containing the ion gauge pressures, temperature and RGA partial pressures. More information about the program can be found in Appendix C.

After running a TPD experiment this program needs 2 files and 1 folder. The files are: Pressure.csv and TempChart.csv. The folder will be the collection of "Mon_DD_YYYY_ _HH-MM-SS_AM/PM.txt" files generated by the RGA Windows software. The names must be in this format for importing the data.

1. In MATLAB run: inputGUI.m
2. Select *Add File(s)* and select all and open the .txt files in the RGAText folder.
3. *Read Data* and follow the instructions, including selecting the appropriate scan rate and temperature ramp rate.

The data is now correlated and saved as a .m file. The data can be opened again by running viewerGUI.m and selecting the sample's .m file. The data can also be exported as a .csv file for analysis in MS Excel. Analysis tools included in this program are:

- Normalizing pressure by mass.
- Smoothing data.
- Removing data recorded after the experiment ended.
- Plotting histograms, including background subtraction.
- Multiple line plots of temperature vs. pressure.
- Comparing pressure data from other TPD measurements.
- Peak finding algorithms that enable the RGA mass series to be correlated and grouped according to common peaks in the pressures.

An example of an outputted figure from the peak finding algorithm is shown in Figure 2.14, where there is a strong correlation in masses from decomposing $NaAlH_4$ at 184 °C. The corresponding background subtracted bargraph is shown in Figure 2.13.

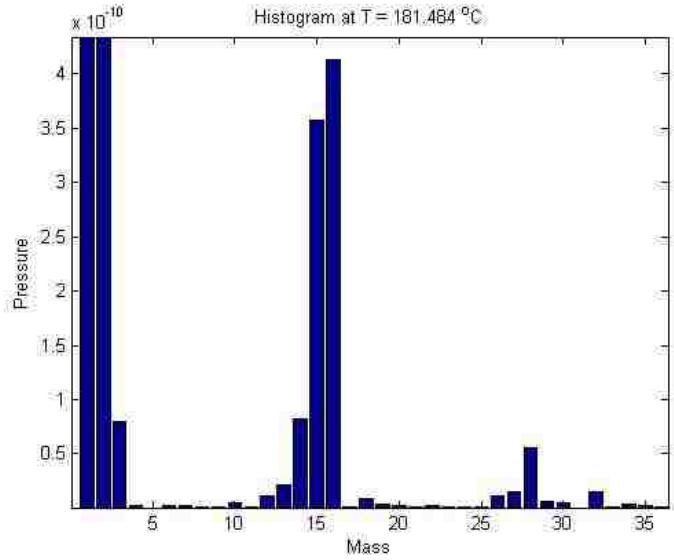

Figure 2.13. The RGA Analysis program can generate background subtracted bargraphs. This data is from $NaAlH_4$ decomposing at 180 °C during a TPD run of 120 °C per hour. This temperature highlights the masses from Figure 2.14 where displayed masses (m/z) are: 15, 14, 13, and 12.

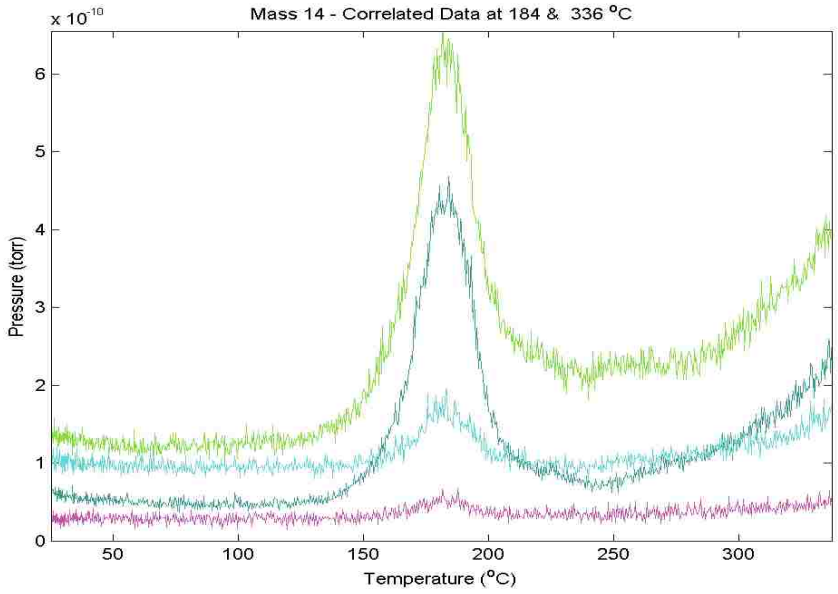

Figure 2.14. The RGA Analysis program can generate line plots of correlated data using its peak finding algorithm. This data is from $NaAlH_4$ decomposing at 180 °C during a TPD run of 120 °C per hour. From top peak to bottom peak the masses (m/z) are: 15, 14, 13, and 12.

2.4.2. Sample Gases. The RGA can be useful for studying species of gases that have not been previously reported. By introducing a sample gas into the system the cracking pattern can also be used to calibrate the RGA detector. For instance, if diborane is suspected to be released during the decomposition of a borohydride, a sample of diborane gas can be analyzed and compared to the unknown substance.

Figure 2.15 and Figure 2.16 are the analog scans of a known gas sample of diborane in a mixing gas of Hydrogen (5.66% diborane by volume). The top of Figure 2.17 shows just the background subtracted RGA data with an overlay of the NIST mass spectrum for diborane [34].The bottom of the figure shows the mass peaks as they fall with the decreasing ionization energy (EE or electron energy). The RGA was operated in analog scan mode, and the resolution is .1 amu. This figure is presented with the background pressure data of the UHV chamber subtracted from the various EE traces. This sample was a few years old, but it is evident that the gas still maintained a high level of diborane.

It is important to have a strong understanding of what the data represents before studying the ionization efficiency curves. A chapter on ionizing molecules will be useful to the reader [27]. There are 3 main parts to the ionization efficiency curve. The nonlinear part of the curve occurs when EE $\leq$ the ionization potential (IP) of the molecule. This is indicative of the wide range of thermal energies in the ionizing electrons. The linear part begins when the EE is greater than the IP and increases until it reaches a peak. This peak is an indication of the beginning of the second ionization. As the electron's energy reaches the second ionization potential and doubly charged ions form, there will be less singly charged ions for the detector to measure. As an example, in the diborane sample above, there was a strong signal for hydrogen H_2^+ and argon Ar^+ and Ar^{++}. The efficiency curves are shown in Figure 2.17. The 1^{st} ionization curve for Ar^+ has a visible peak just before 60 eV, where the 2^{nd} curve starts to increase. The Ar^{++} efficiency curve shows the nonlinear tail before 50 eV. When the linear segment is interpolated to the 0 Torr intercept, a value of 21 eV for Ar^+, and a value of 53 eV for Ar^{++} are obtained as the upper limits for the ionization potential. A search in the literature confirms that these results have been obtained in other experimental designs [35]. The 1^{st} and 2^{nd} ionization potentials for Ar are 15.8 and 27.6 eV respectively [36].

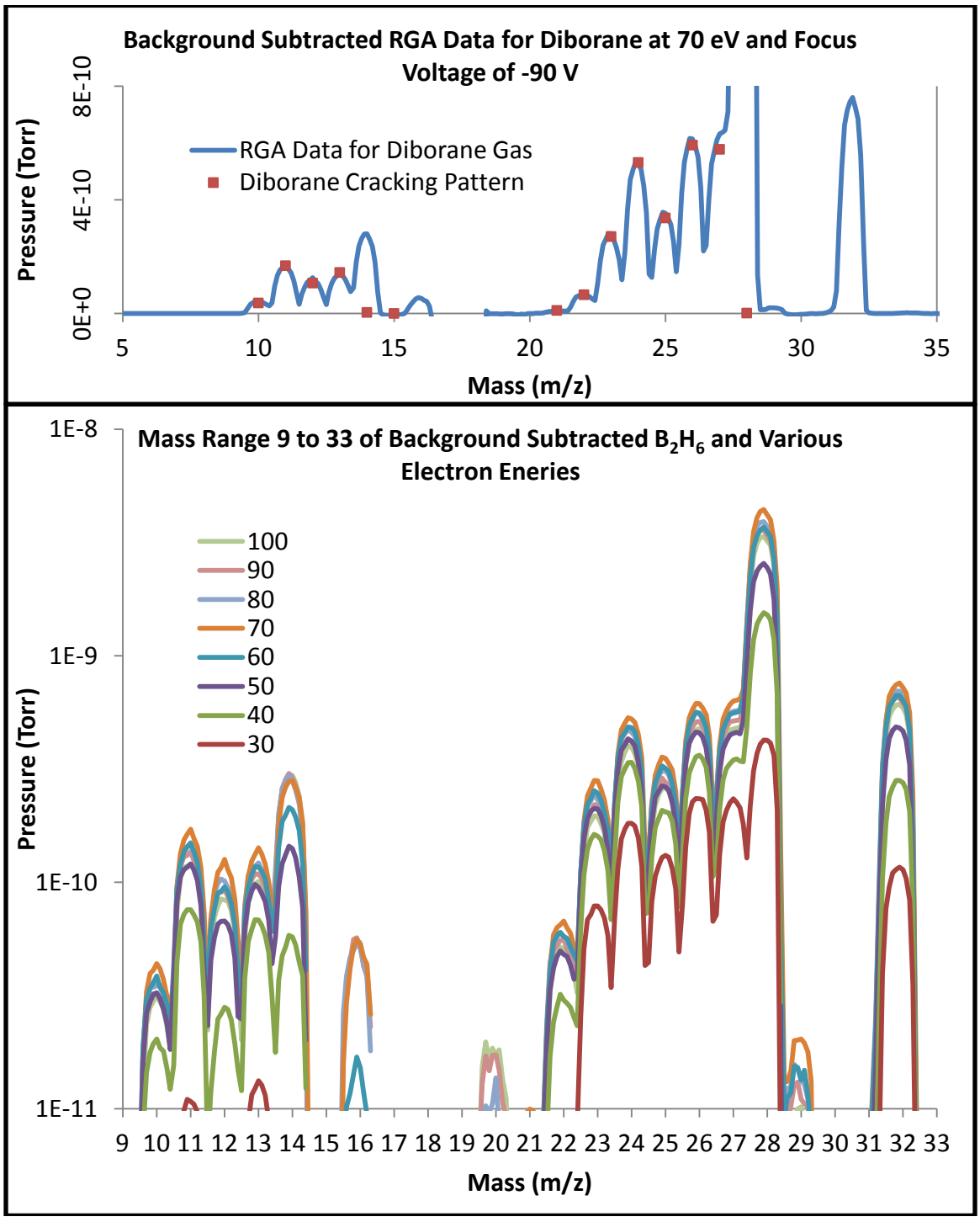

Figure 2.15. Background subtracted analog scans at various electron energies. The top figure is of the RGA Data with an overlay of the diborane mass spectrum from the NIST database. The bottom figure is the mass range (m/z) of 9 – 33 showing the primary peaks of diborane. Mass (m/z) of 32 probably represents N_2H_4 or another contaminant present in the gas sample.

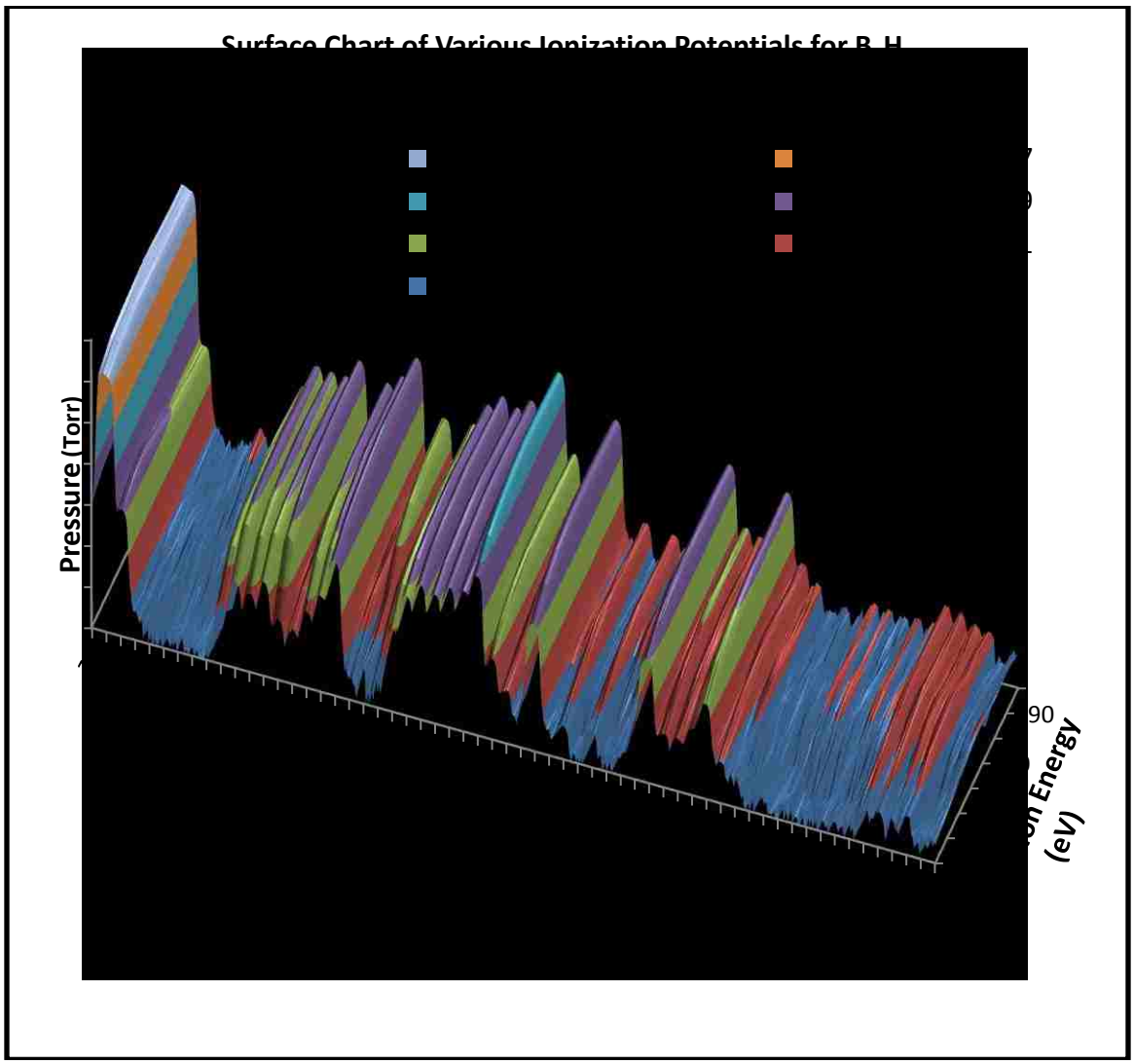

Figure 2.16. Surface plot of ionization energy scans from 30 to 100 eV. The pressure is reported here in log scale.

Another aspect of ionization potentials is the electron impact cross section σ_i. The pressure measured of a mass (m/z) is directly related the ionization cross section. This is simply the probability that a molecule will be ionized by electron bombardment from an electron with a certain energy (EE). The bottom of Figure 2.17 shows the H_2^+ ion efficiency curve with the overlay of the cross section curve [37]. These curves are well correlated, and the extrapolated IP is 16 eV for the cross section IP and 22 eV for the RGA measured IP. The reported IP for H_2 is 13.6 eV [36].

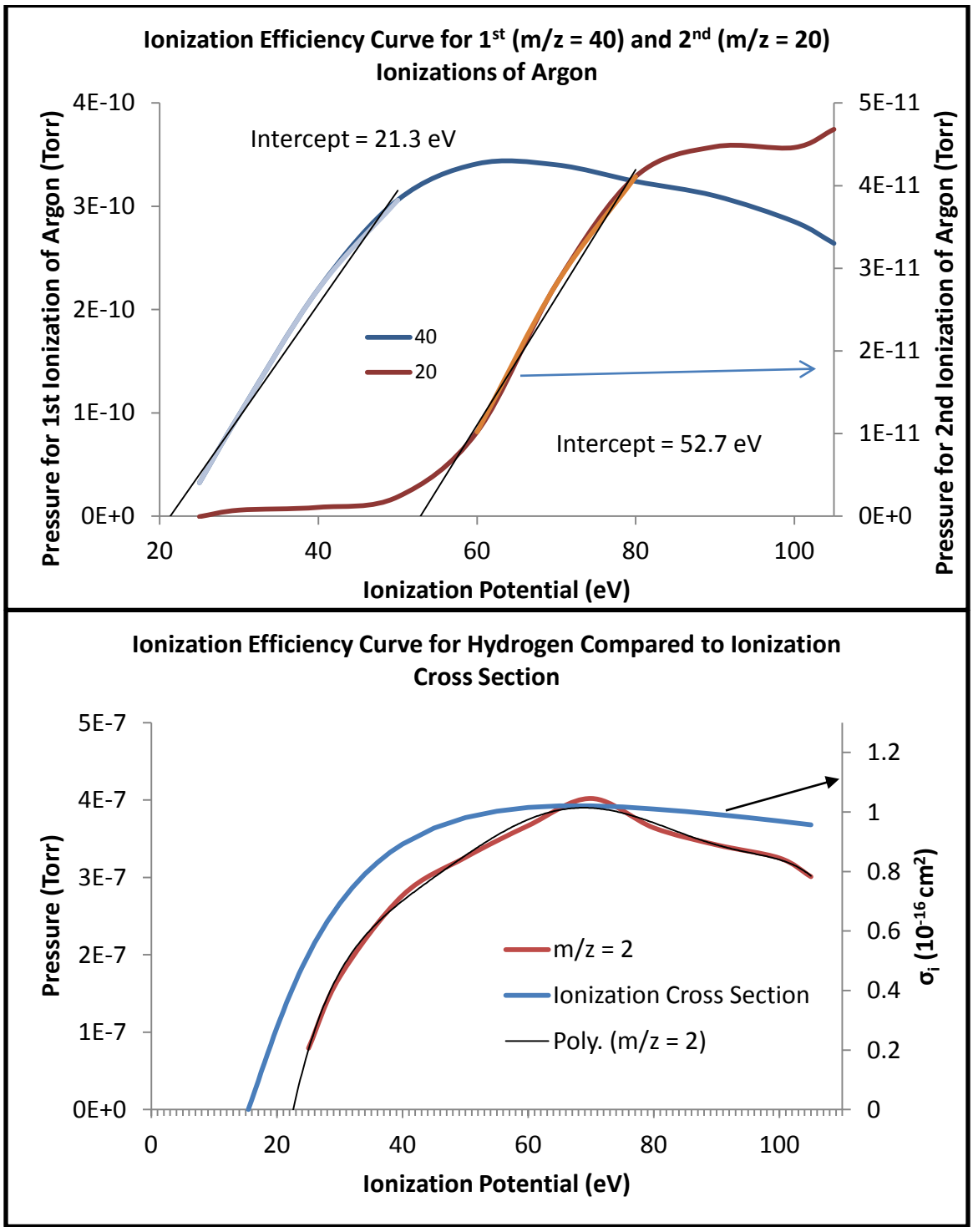

Figure 2.17. Efficiency curves for argon (top) and hydrogen (bottom). The top figure shows the 1st and 2nd ionizations of Ar (m/z = 40 and 20, respectively) with the extrapolated intercepts for estimated ionization potential. The bottom figure presents the experimental hydrogen efficiency curve and the theoretical H_2 ionization cross section [37].

Once the meaning of the ionization efficiency curve is clear, other hypotheses can be tested. For instance, with the mass cracking pattern of diborane, it is unclear whether the lower mass fragments are doubly ionized, or are simply smaller fragments. For example: $^{11}B_2H_6$ can be ionized to $B_2H_2^+$ with a mass of 24 and ionized again for a mass (m/z) of 12. But it is also possible that $^{11}B_2H_6$ could be fragmented to form $^{11}BH^+$ and $^{11}BH_4^-$. When examining Figure 2.18 it is evident that there are 2 groups of curves: those with an extrapolated IP of more than 25 eV, and those with an IP of less than 25 eV. The upper part of the figure contains the low mass elements (m/z = 10, 11, 12, 13, 14) of the diborane cracking pattern. These show the distinct tail of the efficiency curve near the IP. On the other hand the lower part of the figure contains the high mass elements (m/z = 23, 24, 25, 26, 27). These series do not show a tail pattern. It is probable that none of these series represent a double ionization. The peaks of the high mass curves do not match the tails of the low mass curves, and so it is more likely that the low mass series represent smaller fragments as opposed to double ionizations. A comparison to the cross section measurements of B_2H_6 reveals the linear portions of the curves occur at similar electron energy ranges [38].

Future experiments may benefit from this application, and more detailed experiments may lead to a greater understanding of the physics behind the cracking patterns of mass spectrometry.

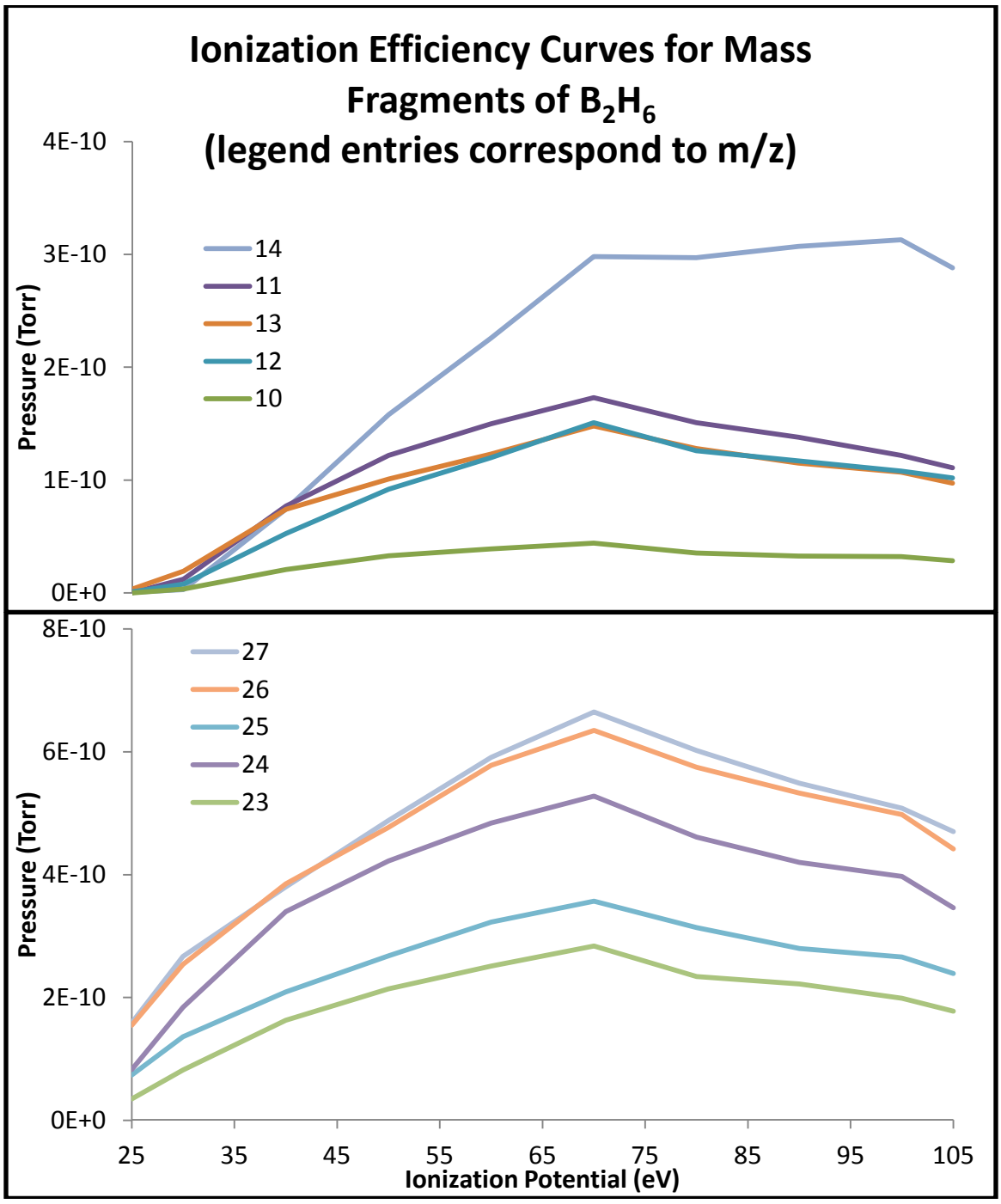

Figure 2.18. Ionization efficiency curves for the primary mass fragments of diborane. The top figure has been grouped by curves already in their tail end of ionization, as the potential decreases. In the bottom figure; the curves are still in the linear portion of the efficiency curve as the potential decreases.

3. HIGHLY ORDERED NANOPOROUS CARBON POWDERS

3.1. INTRODUCTION

Porous carbon has many uses in the fields of chemical and power storage. Porous carbons can be used for gas and chemical sequestration, to remove toxic materials from the environment, and as filters in processes [38]. In power storage porous carbons have shown to improve hydrogen desorption kinetics for fuel cells [39], and increase capacitance as a material for electrodes in supercapacitors [40]. The ability to tune the characteristics in these carbons will lead to systems enhanced by nano-engineering. Properties such as pore-size distribution, ordering of the pores, and uniformity of the pores curvature, all have an effect on the design of the carbon system. For instance, a 15 nm carbon aerogel may have a large surface area and volume density but will have a high size distribution about this value as it is a randomly oriented network of connected pockets. Alternatively, as a hydrogen storage medium the highly ordered 4 nm hexagonally packed nanoporous carbon is more efficient than the carbon aerogel because of its small pore size distribution, and uniform surface effects, even though it has a lower volume density [40].

Ideally a porous carbon system will be designed around the material that it will interact with. The International Union of Pure & Applied Chemistry adopted the following standards for pore sizes [41]:

Micropores: have widths smaller than 2 nm.

Mesopores: have widths between 2 and 50 nm.

Macropores have: widths larger than 50 nm.

Using this standard, the nanoporous carbons (NPC) studied here are micro/meso-pores.

For porous carbon there are two primary ways to measure the pore size, the surface area and the volume of a particle. The first is by direct measurement through microscopy and/or X-ray diffraction (XRD) spectra. The second indirect method is by measuring the amount of substance that can be absorbed into the carbon. The measurement technique used is highly dependent on the range of pore sizes that are

expected to be measured. In this report TEM analysis gives insight into the morphology of the NPC, as well as the structure of the carbon precursors. Additionally X-ray diffraction, and surface area & pore size analysis confirm these results.

The methods for creating highly ordered NPC's using the organic-organic assembly of copolymers PEO-PPO-PEO with resols via evaporation induced self-assembly has been well established by Zhao's group [42]. Earlier work in our group has shown that these NPC's can be easily tuned to pore-size distributions of between 2 and 15 nm [43].

Our nanoporous carbon produced from phenolic resins and amphiphilic triblock copolymers have been shown to contain highly ordered cavities. These cavities or tubular columns have a hexagonal packing structure as well as a well defined pore size. TEM analyses of the cross linked polymer precursor show that the ordered structure may be a result of the thermo-polymerization of the precursor following the evaporation of ethanol. Images also suggest a polymer arrangement parallel to the surface. TEM analysis of the final nanoporous carbon shows that the carbon powder may have a column spacing of about 9nm. Pore size analysis shows that the diameter of the pores is between 4 nm and 5 nm. TEM diffraction images as well as X-ray diffraction confirm that the carbon is amorphous but has polycrystalline properties.

3.2. EXPERIMENTAL METHODS

Nanoporous carbon was prepared by using phenolic resins as carbon precursors and amphiphilic triblock copolymers as soft templates according to the referenced literature [42]. Briefly, phenolic resins were first prepared from phenol and formaldehyde with NaOH as the catalyst and dissolved in ethanol after the removal of water. Triblock copolymer F127 (Mw = 12,600; EO_{106}-PO_{70}-EO_{106}, Aldrich) dissolved in ethanol was mixed with the above ethanol solution of phenolic resin. The 1 : 2 : 0.1 : 0.012 molar ratio of phenol/formaldehyde/NaOH/F127 was used. The mixed ethanol solution was poured into dishes, and the ethanol evaporated. The dishes were then put into an oven for thermopolymerization at 100 °C for 24 hours.

The powdered products scraped from the dishes were calcinated in a tubular furnace with a 97.5% nitrogen/ 2.5% oxygen mixture (flow rate: 105 cc/min). The furnace was first heated to 100 °C at a rate of 10 deg/min and then to 350 °C at a rate of 1 deg/min. It was kept at this temperature for 2 hours to remove the triblock copolymer template. It was heated to 600 °C with a rate of 1 deg/min then to 800 °C at 5 deg/min and kept at this temperature for 2 ½ hours to carbonize. By increasing the oxygen content in the N/O gas mixture the pore size can be increased [43]. Cleaning the carbon can be accomplished by heating to 600 °C for 2 hours.

For hydrogen storage applications, metal hydrides are physically mixed with the carbons in an inert environment and then heated to the melting point of the hydrides. Surface tension and other physical properties (discussed in subsequent sections) cause the materials to be wetted into the pores. This heating can take place either in an inert gas or under a hydrogen pressure.

For energy storage applications, the NPC can be formed into electrodes using a pellet press. Drawings for such a press can be found in Appendix E. E. H. Majzoub recommend that the walls of the press be a graphite material to prevent carbon adhesion to metal.

For TEM analysis a small amount of the NPC powder mixed with ethanol was placed in a sonic bath (sonicator). A single drop of the ethanol mixture was suspended on a holy carbon covered copper grid, and the ethanol was allowed to evaporate. Powder X-ray diffraction (XRD) was performed on a Rigaku Ultima IV multipurpose X-ray diffraction (XRD) system with Cu Kα radiation source ($\lambda = 1.54$Å). For surface area, pore size distribution, and volume analysis; nitrogen adsorption isotherms were measured at 77 K by an SA3100 analyzer (Coulter). Before analysis, the sample of nanoporous carbon was outgassed for 1 h at 300 °C under vacuum. The Brunauer-Emmett-Teller (BET) method was used to calculate the specific surface areas (SBET) using adsorption data in a relative pressure range from 0.05 to 0.2 bar. The total pore volume was estimated from the adsorbed amount at a relative pressure P/P_0 of 0.98 based on the Barrett-Joyner-Halenda (BJH) calculation model.

A crosslinked sample was prepared by a similar method as the above carbon precursor but instead of scraping into a powder, the flakes were removed from the dishes in pieces. The thicknesses of the flakes are about 100 μm.

Thin films sections of the crosslinked (thermopolymerized) material were microtomed and suspended on 3 mm copper grids. 20 ml of medium hardness embedding resin was prepared by the following mixture: Resin 11.6g; DDSA (anhydride) 6.4g; NMA (anhydride) 5.72g; BDMA (accelerator) 0.7g. The sample was prepared for the microtome by embedding flakes in this hand mixed resin and allowing the sample to cure in a mold at 60 °C in an oven overnight.

In an attempt to limit the contact of the resin to the surface of the materials, several pieces were stacked together as seen in the left image of Figure 3.1. The Figures 3.1 and 3.2 show the arrangement of the flakes in relation to the thin films that were prepared. Essentially, the microtome sample is prepared so that the TEM view is parallel to the liquid surface of the sample as the ethanol is evaporated. The thin film sections have a thickness of about 50 ~ 60 nm.

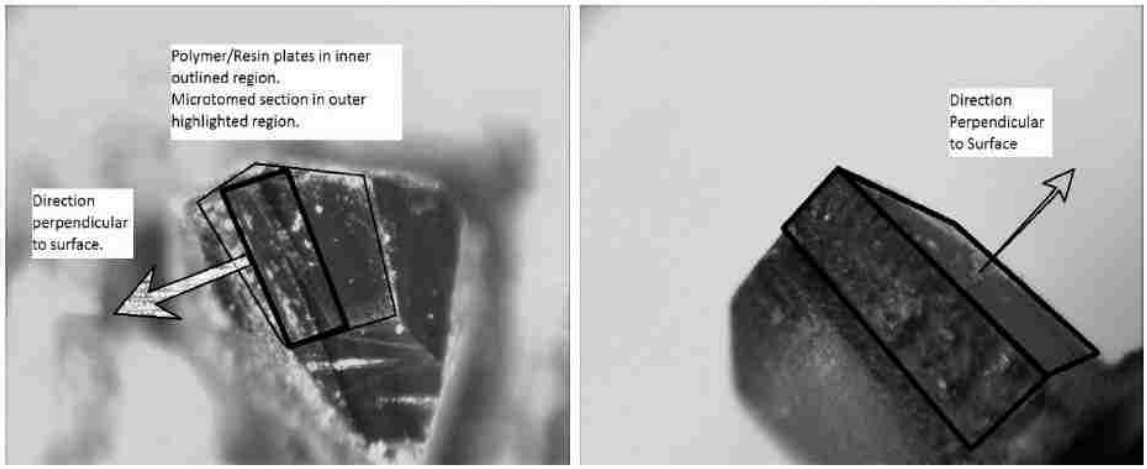

Figure 3.1. Microtome sample preparation.

3.3. RESULTS AND DISCUSSION

3.3.1. NPC Precursors. TEM analysis of the carbon precursors shows a mostly amorphous structure at the smaller magnifications. These images were taken at a rougher portion of the microtomed sample, and higher magnifications are centered on a defect which could be a bubble suspended in the polymer/resin precursor. The right image of Figure 3.3 is a high resolution image showing a thinned region; but at low magnifications (left of Figure 3.3 and right of Figure 3.2) this seems to be a clear hole in the sample. In this image no other details are evident. However, in the raw image of Figure 3.4 (left) the detail is not clear until image manipulation with ImageJ [46] highlights the speckling of the same image (right of Figure 3.4). These images were scanned at 1200 dpi, for higher detail. The methods used in ImageJ were “Smooth” and “Enhance Contrast”.

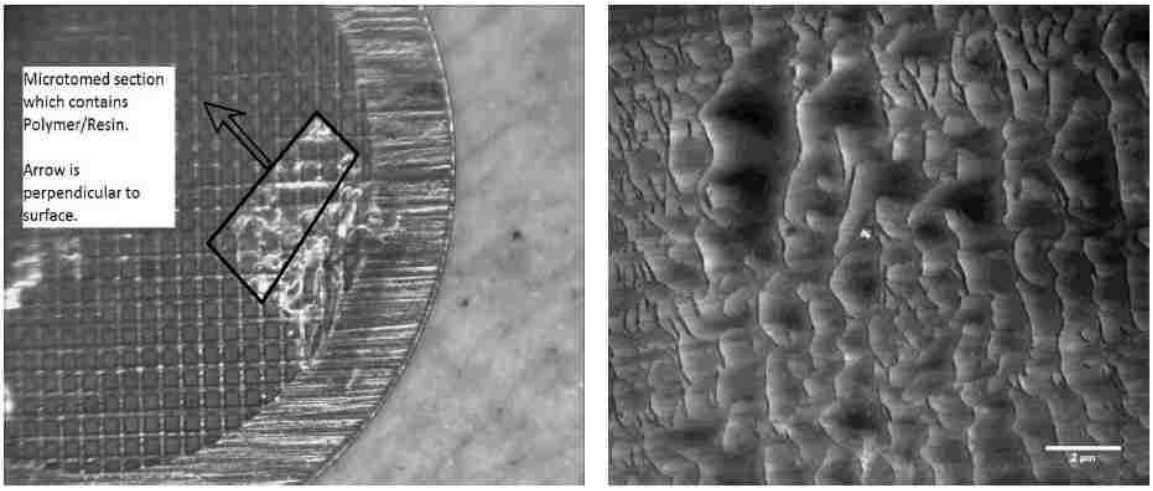

Figure 3.2. Microtomed sample of precursors on copper grid (left), and TEM image at 6000 x magnification (right).

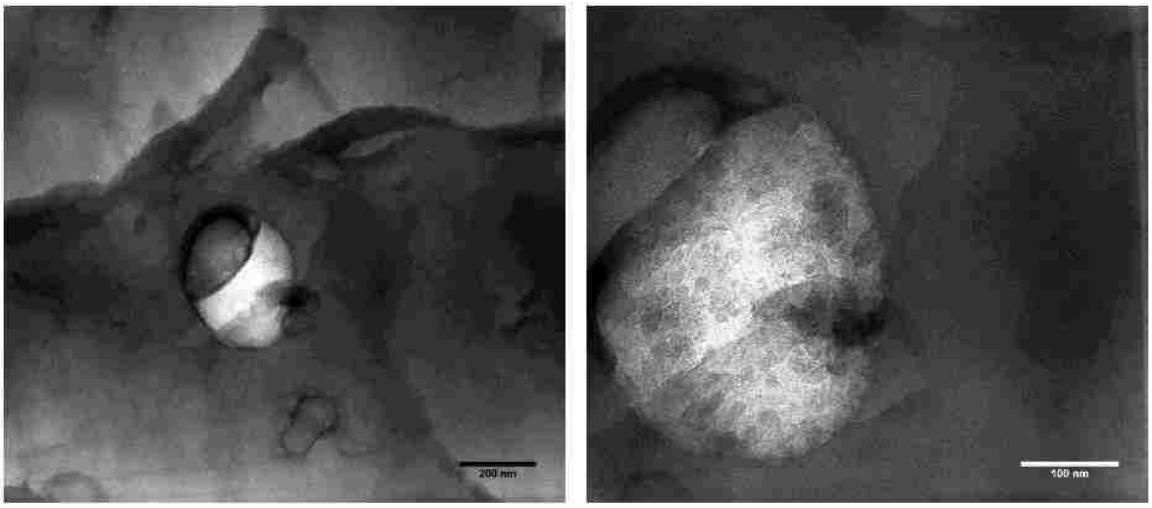

Figure 3.3. TEM images of precursors at 59,000 x magnification (left), and at 150,000 x magnification (right).

From the enhanced image of Figure 3.4 there are evidently spots which could represent the triblock copolymers. These spots have a spacing of roughly 11 nm between them, but are not arranged in an obvious hexagonal pattern. For comparison the spacing between the nearest neighbor columns in the final NPC is about 10.4 nm. There is stripping evident on a larger scale, and this striping may be an indicator of strain in the sample, or it may be an indicator of layering of the copolymers. It is clear that the microtome section cuts the polymer chains and this may be evidence that the polymers lay flat in the carbon template.

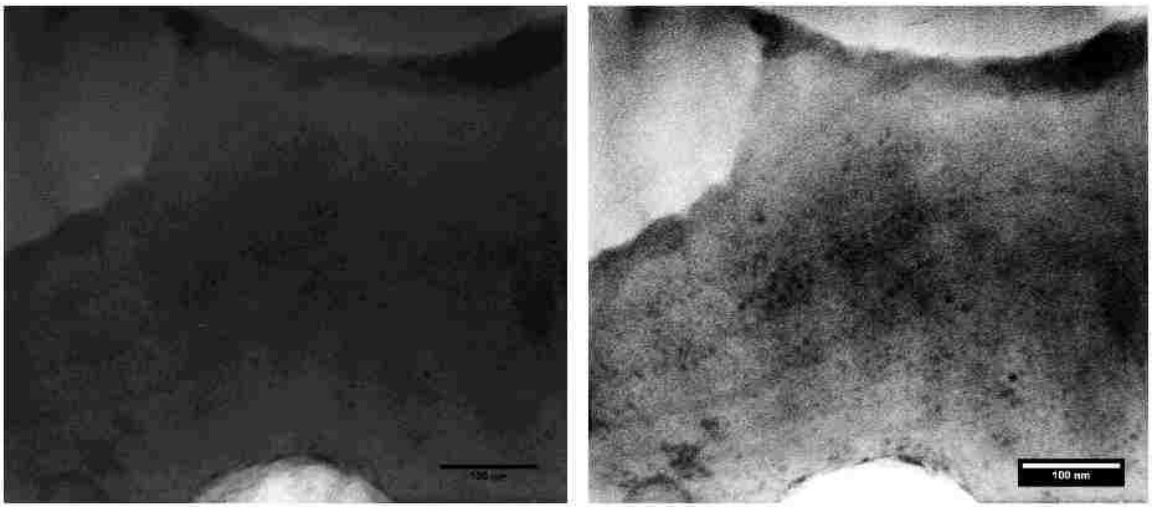

Figure 3.4. TEM images of NPC precursors at 150,000 x magnification; raw image (left), and "Enhanced Contrast" (right).

Much work has been done to arrange the polymers in the direction perpendicular to the surface; however it may be easier to take thin films of the precursor in this orientation and then bake the films for carbonization. In this way one may obtain a thin film with columns perpendicular to the surface.

3.3.2. Analysis of NPC by TEM Imaging and BET/BJH Adsorption Isotherms.

TEM images of NPC powder particles readily show rows of evenly spaced structures at a low magnification of 43,000 x. While most linear features are straight channels there are structures where the channels curve, and other regions of intersecting channels. These intersecting regions may be overlapping structures in a single grain, or grains which bonded together during the firing processes. The most interesting features are shown in the images of Figure 3.5.

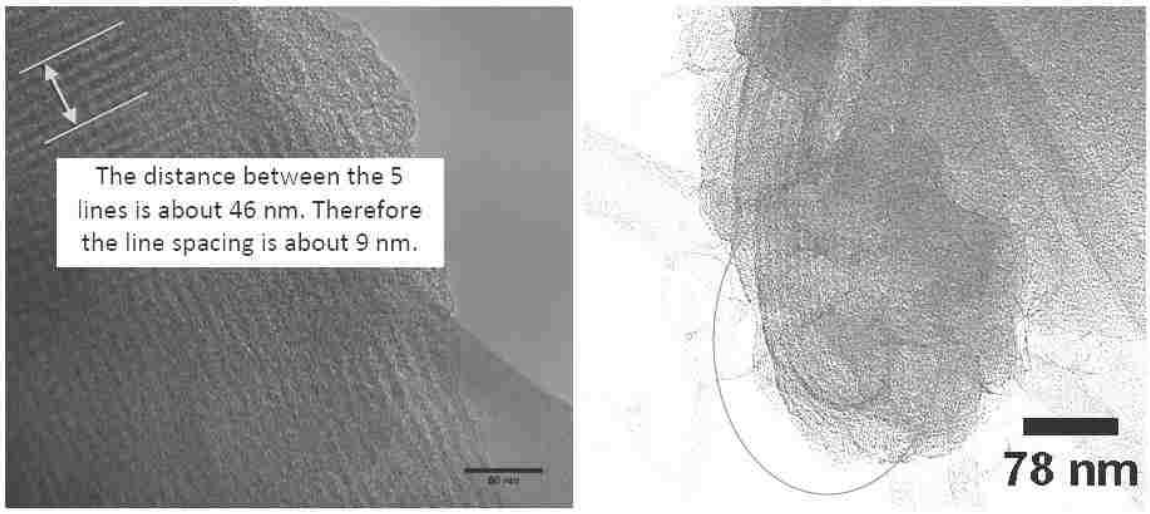

Figure 3.5. 240,000 x magnification showing overlapping planes of columns (left), and 43,000 x magnification showing curved channels (right).

The left image of Figure 3.5 is also used to measure the spacing of the columns. An image of the pore openings could not be obtained from this sample, and so the geometry will be analyzed below using the observed stripe separation of 9 nm.

Figure 3.6 represents the estimated geometry of the NPC sample. Using the indirect measurement of nitrogen adsorption isotherms (Figure 3.7) the pore size distribution is determined to be tightly centered on 4.5 nm. This along with the observed separation gives the estimated geometry of Figure 3.6.

When viewed perpendicular to the pores the image will be stripes aligned to each other. The 9 nm spacing may represent the view in the (0, 1, 0, 0) direction relative to a hexagonal arrangement, which has been previously reported [39]. This arrangement will allow for equal areas of optically thin and thick regions (4.5 nm each), owing to the geometry.

The additional direction of (0, 1, 1, 0) would not provide as much contrast, as the bands will have a separation of only 5.2 nm, with the optically thick portion only .7nm wide, hence these bands may not be visible in the TEM images.

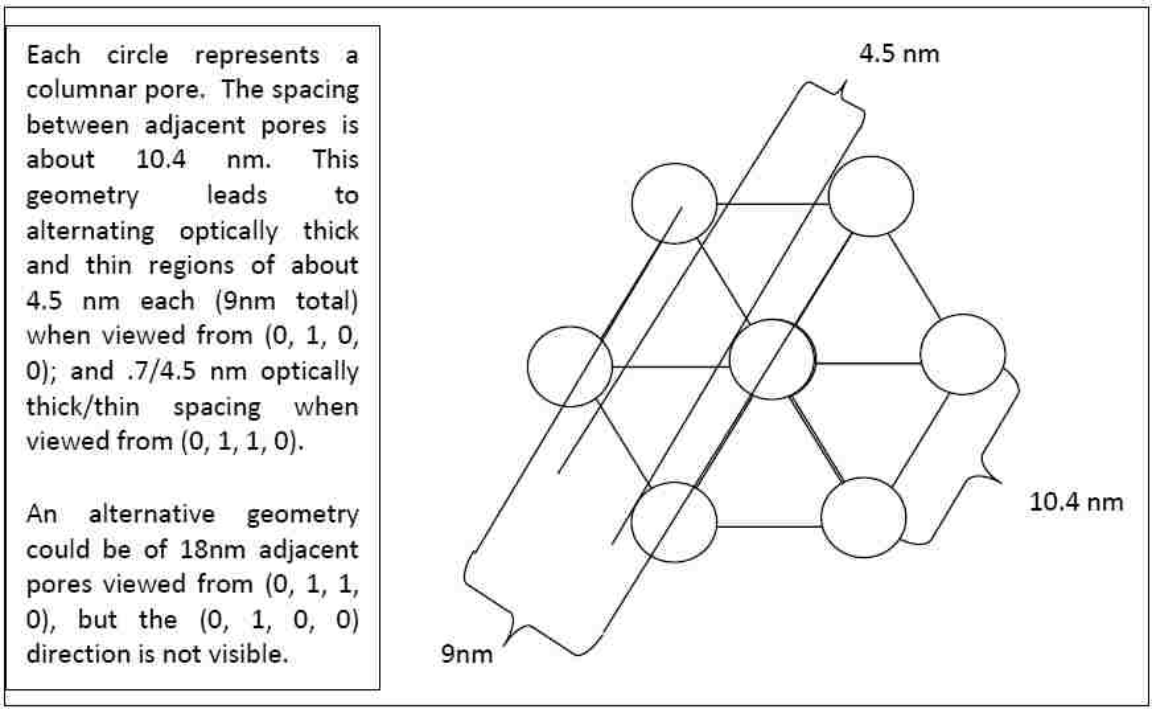

Figure 3.6. Geometric Structure of the NPC

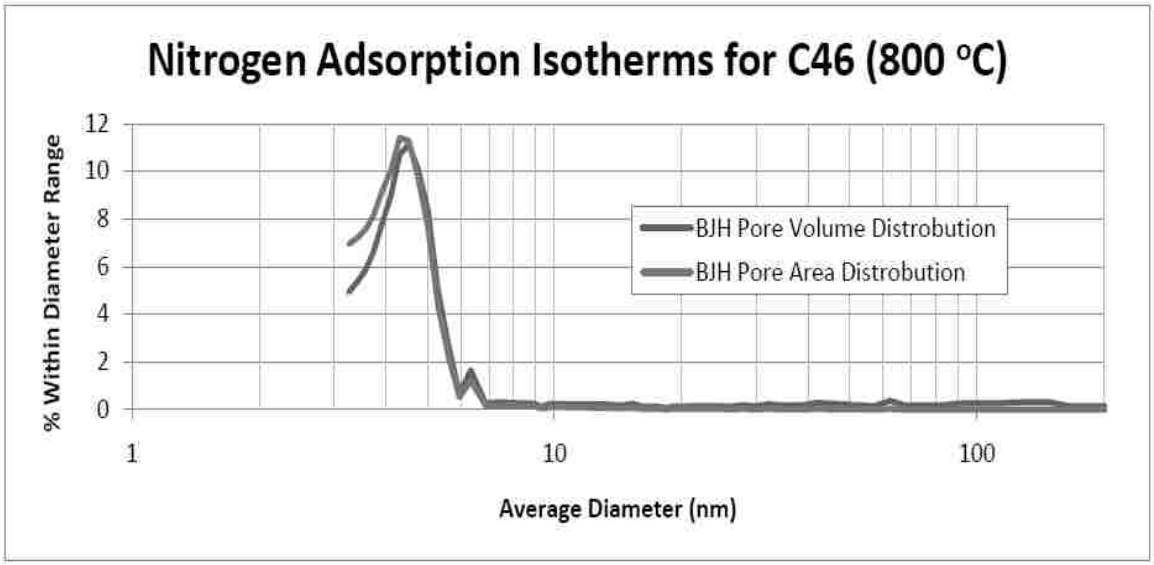

Figure 3.7. Pore Size Determination

3.3.3. TEM and X-ray Diffraction of NPC. A diffraction image was taken with a camera length of 1,200 mm over a selected area of the image on the left of Figure 3.5. The following equations were used for the diffraction analysis.

$$\tan(2\theta) = R_{hkl} \Big/ L \tag{1}$$

$$\frac{4\sin^2(\theta)}{\lambda^2} = \frac{1}{d^2} = \frac{h^2 + k^2 + l^2}{a^2} \tag{2}$$

The data from Table 3.1 shows a similar trend for both the X-ray diffraction data and the analysis of the TEM diffraction image. Using "Plot Profile" in ImageJ the intensity of the diffraction image of Figure 3.8 is plotted against the XRD data in Figure 3.9. Both data sets show two peaks and the corresponding d-spacing differs by only a factor of 1.7. This could be attributed to error in the camera length or in the wavelength of the TEM beam. The supposedly amorphous nature of the NPC should lead to no diffraction pattern in either data set, but there is obviously some ordering, which is apparent in the bulk powder sample for the XRD and as well as the single grain in the selected area electron diffraction (SAED).

Table 3.1. Diffraction Data

	λ (Å)	$\theta_{Peak\ 1}$	$\theta_{Peak\ 2}$	$\sin(\theta_{Peak\ 1})$	$\sin(\theta_{Peak\ 2})$	d_1(Å)	d_2(Å)
XRD	1.54E+00	1.11E+01	2.19E+01	1.93E-01	3.73E-01	3.99E+00	2.07E+00
SAED	1.97E-02	2.52E-01	4.58E-01	4.41E-03	7.99E-03	2.24E+00	1.23E+00

The d-spacing is an order of magnitude different than the column's lattice spacing; therefore the SAED image is consistent with random orientation of a 3-D crystal structure, and not of a 2-D structure. In a paper by Cao et al., carbon nanotubes show a similar XRD pattern when the tubes are well aligned straight nanotube arrays [44].

Their XRD data (same wavelength) shows a similar broad peak at the 2θ angle of 22 and 44 degrees.

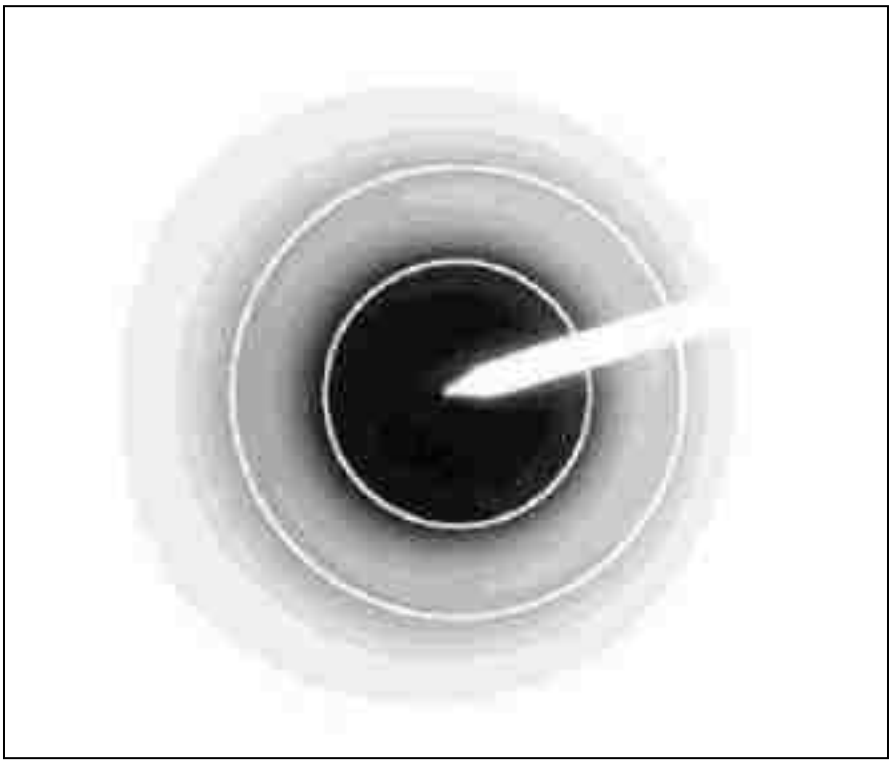

Figure 3.8. Inverse SAED with 1200mm camera length and overlay of rings with ImageJ.

From the SAED data the 1/2.24 Å peak could be indexed to {100} and the 1/1.23 Å spacing indexed to {110}. The third peak visible in the SAED data of Figure 3.9 could be attributed to a 1/3.4 Å band which may be layering seen in poorly crystallized carbon. This spacing of the {002} may not be visible in XRD data due to instrumental broadening.

According to the one online XRD data base [45], Chaoite (C) may be a match (3% error) if there are other peaks ($2\theta < 10°$) not recorded in this measurement. Alternatively graphite is a match with a 20% error, and diamond with 9% error.

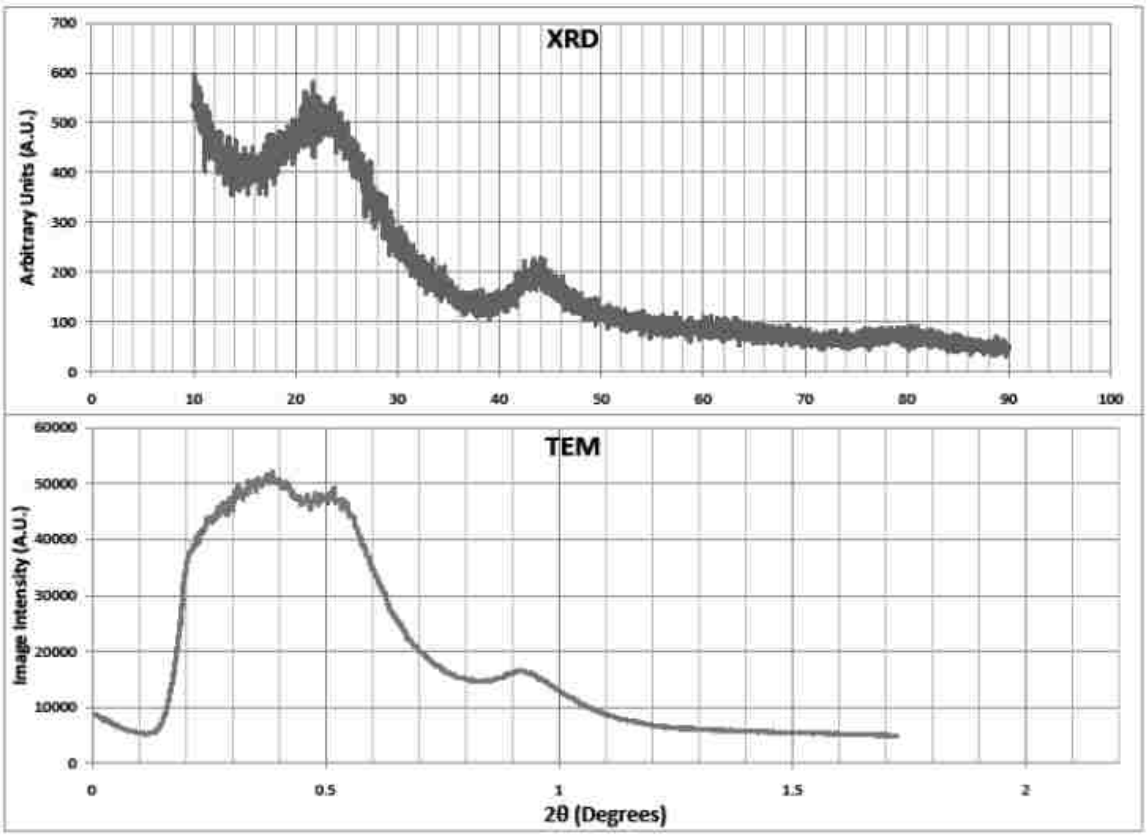

Figure 3.9. Diffraction Data

3.4. MODIFICATIONS TO PREPARATION AND FURTHER WORK

Modifications to the carbon preparation have been performed in order to increase the batch yield. Much material was lost when scraping the glass petri dishes. In order to remove all the material silicon ice cube trays were used in the evaporation and thermopolymerization process. The thermopolymerized material was easily removed from the flexible silicon trays. Next the hardened material was placed into an electric coffee bean grinder a ground into a fine powder. With the glass scraping method described above, it was essential that the powder was a fine powder as opposed to chunks or shards of the precursor material. If the particle size is too large, the triblock copolymer does not get completely removed in the first stage of the carbonization process, and it has been shown that the hexagonal structure is not formed. With the grinding method the

powder is fine enough to produce a final carbon product with similar surface area and pore size as the material described above.

Future studies include the effects of nano-confinement in NPC on hydrogen storage materials, and on electrolytes for battery and suppercapacitor applications. The NPC diffraction pattern is a very interesting problem. As the signal is very weak, the material is assumed to be amorphous, but this may not be the case. By designing a method to arrange the columns perpendicular to a surface, thin films could be designed as filters in fluidic devices, or as membranes in small fuel cells. Finally, methods to functionalize the NPC materials may also improve characteristics in energy systems, by adding catalytic sites in the framework.

3.5. CONCLUSIONS

The TEM analysis of hexagonally packed nanoporous carbons, along with X-ray diffraction and BET/BJH adsorption isotherms confirm the structure as nanoporous and well ordered. The hexagonal packing is not confirmed in this report, but previous studies have determined the structure [39]. Additionally, the carbon precursors, specifically the arrangement of triblock copolymers suspended in a phenolic resin has been identified. The arrangement of the copolymers seems to be parallel to the top and bottom surfaces. The long range arrangement is not as clear, for instance, the image in Figure 3.5 shows a curling of the pores. This could arise from curling in the ethanol solution, or from the carbonization process. The hexagonal packing is not evident in the precursors, but there is an apparent layering in the material.

Diffraction in SAED images as well as in the XRD data show that even though the materials are amorphous there is some underlying structure, both in the bulk powder and in individual grains. Perhaps this diffraction pattern is arising from similarities between the nanotube walls and the column walls of NPC.

PAPER

I. A Study of the Heat and Pressure-induced S105 Phase in $NaAlH_4$

David Peaslee[a], Gang Wang[a], Dongxue Zhao[a], Eric Sorte[b], Sophia Hayes[c], Mark Conradi[b], Bob Bowman[c], and Eric Majzoub[a]

[a]*Center for Nanoscience and Department of Physics and Astronomy, University of Missouri-St. Louis*

[b]*Department of Physics Washington University*

[c]*Department of Chemistry Washington University*

[d]*Oak Ridge National Laboratory*

INTRODUCTION

Hydrogen is an efficient and pollution-free energy carrier. The current barrier of entry for hydrogen in the energy market is a low cost and reliable storage method. Complex anionic hydrides such as sodium aluminum hydride ($NaAlH_4$) are promising storage materials due to their high hydrogen storage capacities (about 5-6 wt.%), and reasonable reaction temperatures (around 100 °C using a catalyst).

Here, we present a study of the decomposition of a high purity bulk $NaAlH_4$ (crystal structure shown in Figure 4.1) with a new phase created under a high hydrogen pressure (200 bar) and high temperature (near 180 °C). Recent NMR studies have found a highly mobile Al-species (the "S105 phase") in heat and pressure-treated $NaAlH_4$ [1, 2]. By studying the decomposition pathways with a high temperature direct line-of-sight mass spectrum residual gas analyzer (MS-RGA) approximation can be made on the decomposition energy and reaction rates of the bulk material.

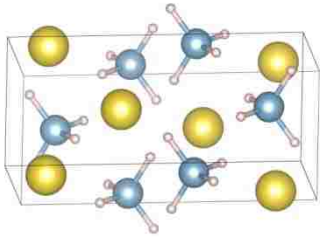

Figure 1. GSAS crystal structure representation of $NaAlH_4$ [3].

EXPERIMENTAL SECTION

Figure 2 shows how the high purity bulk $NaAlH_4$ crystals were synthesized using the evaporation crystallization method. Three samples have been created to determine some of the properties of this phase.

- Pure $NaAlH_4$: synthesized in our lab.
- N97 (no S105): Heated to just below melting temperature under high H_2 pressure.
- N98 (S105): Heated to just above melting temperature under high H_2 pressure

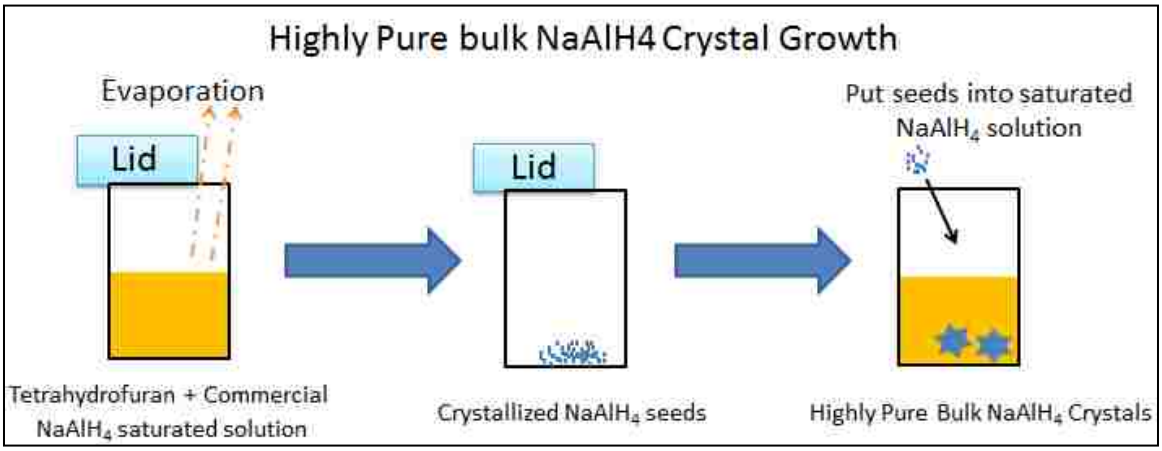

Figure 2. Preparation and crystal growth of high purity $NaAlH_4$

Powder X-ray diffraction (XRD) was performed on a Rigaku Ultima IV X-ray diffraction (XRD) system with Cu Kα radiation. The XRD data is analyzed using the Rietveld refinement method. The refined pattern with optimized structure is shown in Figure 3. The criterion of the refinement fit is determined by whole pattern residuals (*Rp*) and weighted residuals (*wRp*).

$$Rp = \frac{\sum |I_O - I_C|}{\sum I_O} \tag{1}$$

$$wRp = \frac{\sum w \cdot |I_O - I_C|^2}{\sum w \cdot I_O{}^2} \tag{2}$$

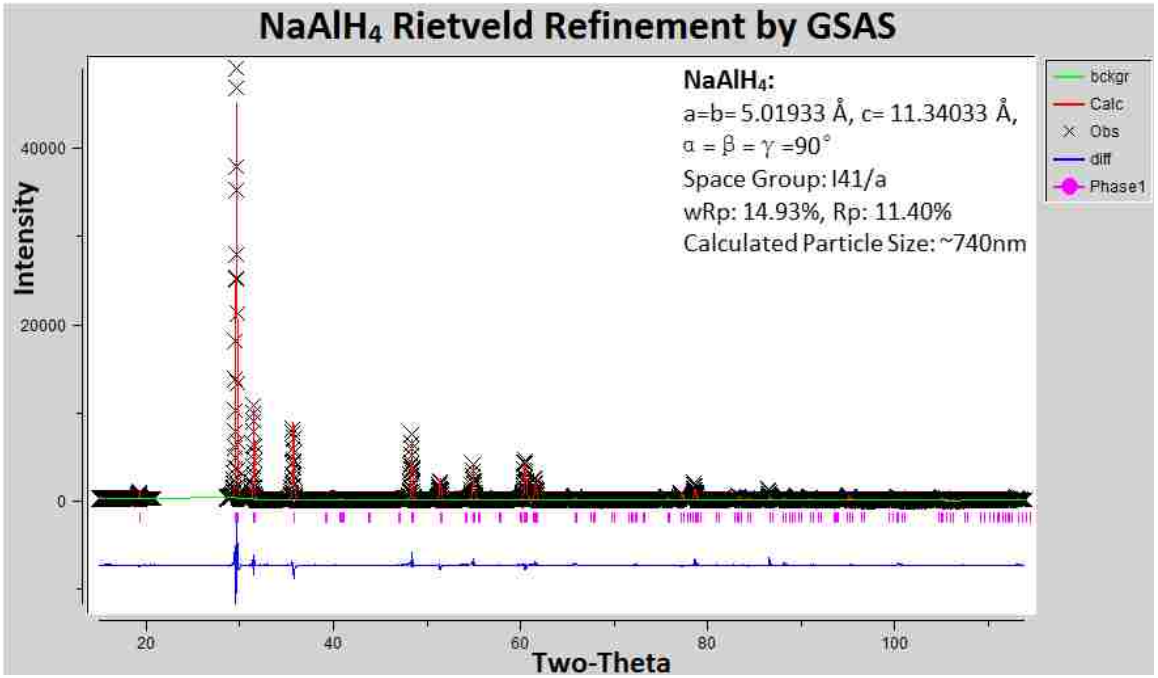

Figure 3. Rietveld Refined X-Ray Diffraction Pattern

Here I_O is the XRD observed intensity, and I_C is the calculated intensity. The calculated particle sizes range is given by the Debye–Scherrer Equation (3).

$$D = 0.94 \times \frac{\lambda}{\mathrm{FWHM} \cdot \cos\theta} \tag{3}$$

We can clearly see that the pattern is well fitted with optimized structure constants by the whole pattern Rietveld Refinement method. From Figure 3, *wRp* is 14.93, *Rp* is 11.40%, and the calculated coherence length is 740 nm.

RESULTS AND DISCUSSION

The First Principles Study of the Decomposition of $NaAlH_4$. $NaAlH_4$ decomposes by 3 steps:

$$NaAlH_4 \longleftrightarrow \tfrac{1}{3}Na_3AlH_6 + \tfrac{2}{3}Al + H_2 \text{ (Reaction 1)} \tag{4}$$

$$Na_3AlH_6 \longleftrightarrow 3NaH + Al + \tfrac{3}{2}H_2 \text{ (Reaction 2)} \tag{5}$$

$$NaH \longleftrightarrow Na + \tfrac{1}{2}H_2 \text{ (Reaction 3)} \tag{6}$$

Experimentally, the 3 decomposition steps occur in bulk material at 230, 265 and 660 °C [4]. By first-principles calculations of the thermodynamic free energy, at 1 atm of H_2 and ignoring kinetic barriers, they occur at -50.1, -19.15 and 591.85 °C.

Table 1. Theoretical and Experimental Enthalpies at 1 atm.

	ΔH [4]		ΔH (calc.)		ΔH (exp.)	
	°C	kJ/mol H_2	°C	kJ/mol H_2	°C	kJ/mol H_2
Reaction 1	230	25	-50	23	249.5	52.6
Reaction 2	265	39	-19	37		
Reaction 3	660	76	592	78	434.41	66.3

The melting temperature of $NaAlH_4$ was about 183 °C, the experimental heat of fusion of which was 1.5 kJ/mol. The calculated enthalpy of the first two reactions are 64 kJ/mol H_2, which is greater than the experimental value of about 52.6 kJ/mol H_2. The difference may be caused by the crystallization of Na_3AlH_6, from molten $NaAlH_4$, when the first decomposition proceeds to produce Na_3AlH_6, which has a melting temperature of 252 °C.

The reacting enthalpies are shown in Figure 4(a). They show the same trend as the experimental enthalpies show. They increase at the beginning, reach a peak and then decrease with the increase of temperature.

The phase diagram (pressure vs. temperature) has also been investigated as illustrated in Figure 4(b). The black, red and green boundaries clearly mark the edges of the three phase regions. In the first region, there is only $NaAlH_4$. In the second region, $NaAlH_4$ decomposes into Na_3AlH_6 and Al to release H_2. The temperature of the phase boundaries increases with the increase of H_2 pressure.

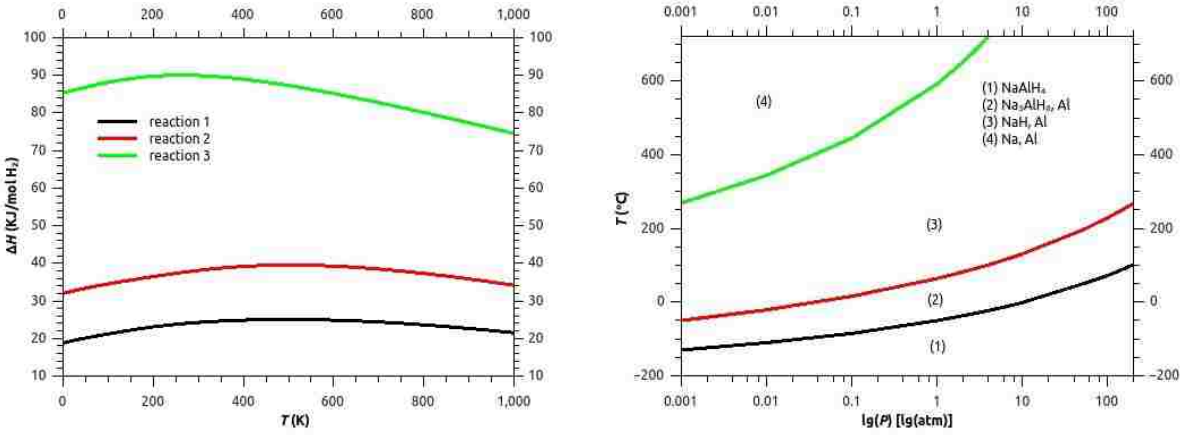

Figure 4.(a). (Left) The calculated reaction enthalpies as a function of temperature.
Figure 4.(b). (Right) The phase diagram of $NaAlH_4$.

Oxidized $NaAlH_4$ was also investigated using supercell first-principles calculations. $[AlH_4]^-$ was replaced with OH^- to inspect the solubility of NaOH in $NaAlH_4$, which can be determined by the difference of free energy between $(NaAlH_4)_{(1-x)}(NaOH)_x$ and $NaAlH_4$+NaOH by the equation:

$$\Delta F = F[(NaAlH_4)_{(1-x)}(NaOH)_x] - (1-x)\cdot F(NaAlH_4) - x\cdot F(NaOH) \qquad (7)$$

Figure 5(a) illustrates the calculated free energies of $(NaAlH_4)_{(1-x)}(NaOH)_x$. This clearly shows that the free energy increases with the increase of NaOH concentration up to the free energy of NaOH. The changes of free energies can be deduced from the data as shown in Figure 5(b). Within the temperature zone $0 < T < 1000$ K, the changes of the free energies gradually decrease, becoming favorable. The exception is for x=0.4375, which becomes favorable beyond 1000 K. This data clearly indicates that NaOH is soluble in $NaAlH_4$ over a wide composition range.

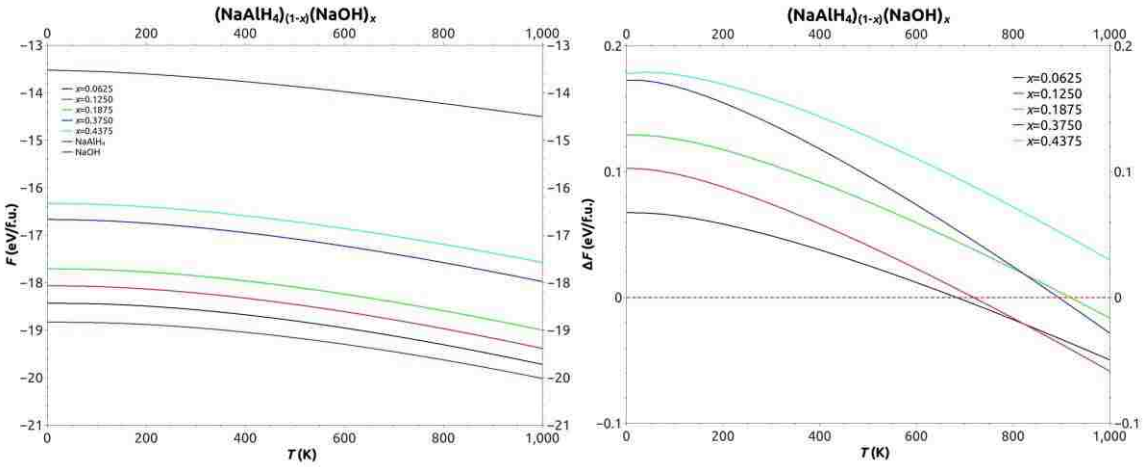

Figure 5.(a).(Left) The free energies of $(NaAlH_4)_{(1-x)}(NaOH)_x$.
Figure 5.(b).(Right) The changes of free energies. For a particular concentration x, OH- is soluble when $\Delta F<0$. As x increases ΔF at 0 K also increase.

Figure 6(a) was derived from the changes of free energies of $(NaAlH4)_{(1-x)}(NaOH)_x$ at the points ΔF just below 0, which illustrate the saturated concentrations of NaOH in $NaAlH_4$ at various temperatures. Furthermore, the solubility occurs above 650 K (400 °C). However, $NaAlH_4$ decomposes before this temperature, which implies that NaOH cannot dissolve into $NaAlH_4$ at 1 atm. The solubility might be observed at high H_2 overpressures where $NaAlH_4$ is prevented from decomposing. The solution enthalpies of $(NaAlH_4)_{(1-x)}(NaOH)_x$ have also been investigated.

Figure 6(b) shows the calculated enthalpies in a wide temperature range. The meaningful ones are above the temperatures at which solubility occurs. The figure shows that the reaction enthalpies increase with the increase of temperature, becoming more favorable.

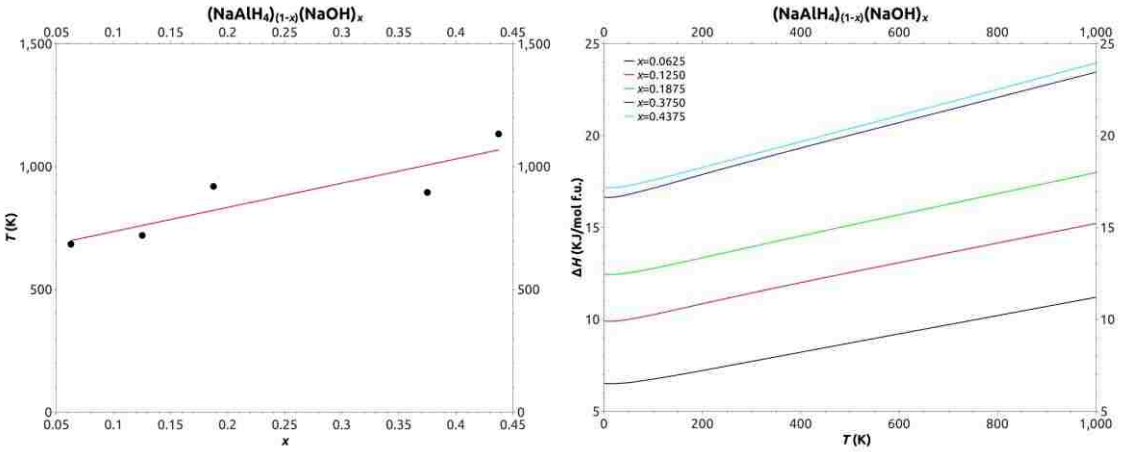

Figure 6.(a). (Left) The solubility of NaOH into $NaAlH_4$ with temperature.
Figure 6.(b). (Right) Molar solution enthalpies of $(NaAlH_4)_{(1-x)}(NaOH)_x$. As x increases the enthalpies also increase.

Experimental Evidence for the Reaction Pathways. Mass spectroscopy measurements during the decomposition of these materials reveal some important clues to their reaction pathways. Figure 7 outlines the decomposition of bulk $NaAlH_4$. Under ultra high vacuum, a mass spectrum residual gas analyzer (MS-RGA) detects that the bulk material melts at 180 °C, and begins to release H_2 at about 200 °C (blue/black boxes

in Figure 8). This reaction reaches its peak rate at 245 °C, and in some cases, a second round of H_2 emission precedes the decomposition of Na_3AlH_6 (at 280 °C) into NaH, Al, and H_2 (yellow/grey boxes in Figure 8). In Figures 7 and 8, the mass (m/z) of 23 may represent the fracturing of NaH into the ions Na^+ and H^- implying that NaH is lost as a gas. Small amounts of other ions are detected in the MS-RGA, which indicate that other gases are present in the H_2 stream. These gasses may be forming from oxygen impurities in the sample.

We use a Differential Scanning Calorimetry (DSC) instrument to measure the experimental decomposition enthalpies for pure $NaAlH_4$, N97 and N98. The enthalpies for the materials heated at 1 °C/minute are listed in Table 2.

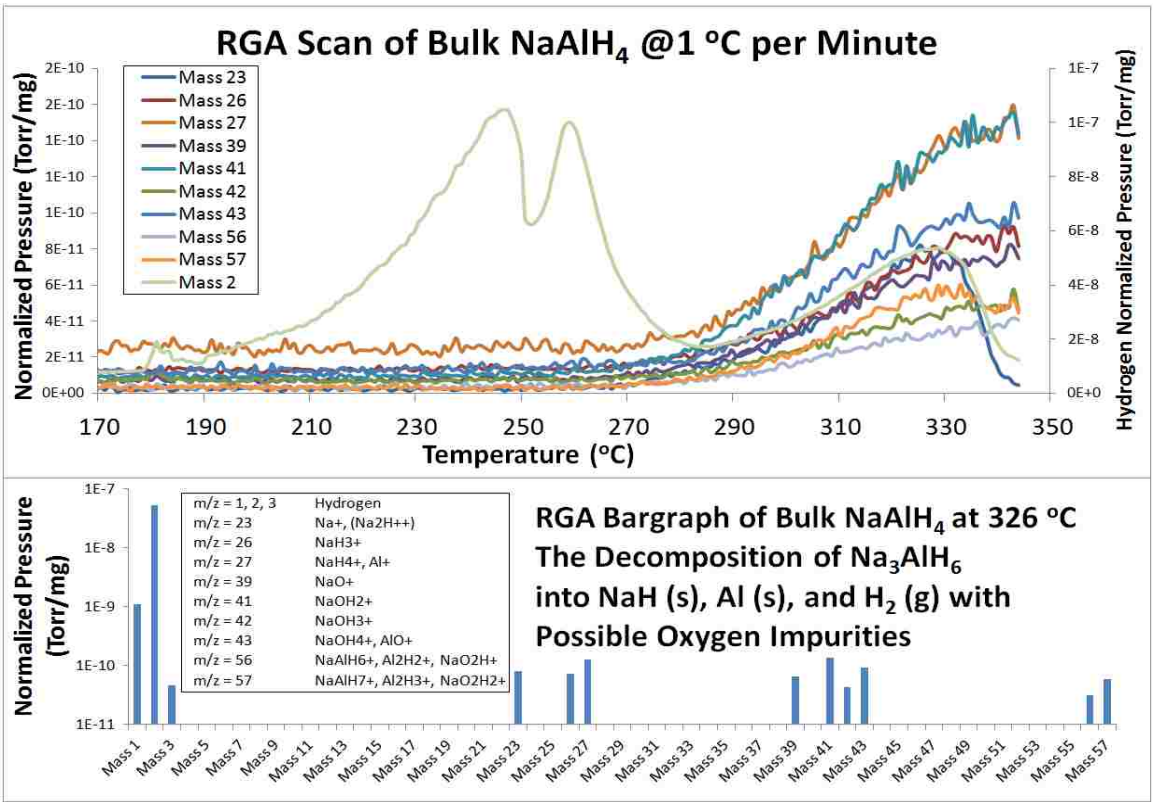

Figure 7. MS-RGA measurements of the thermal decomposition of $NaAlH_4$ showing increase in important masses during the second step of decomposition.

These DSC measurements are plotted along with the RGA data and most of the results have a strong correlation. The results of the MS-RGA show that all 3 samples decompose through the same reaction pathways, but N97 and N98 decompose at a lower temperature than the bulk material. Additionally, N98 in the S105 phase shows a smaller temperature range for reaction 2 to complete.

Table 2. DSC Experimentally Calculated Enthalpies.

	Bulk		N97		N98 (S105 phase)	
	°C	J/g	°C	J/g	°C	J/g
Reaction 1	183	273	179	315	179	166
Reaction 2	250	487	250	333	234	434
Reaction 3	434	614	402	801	391	802

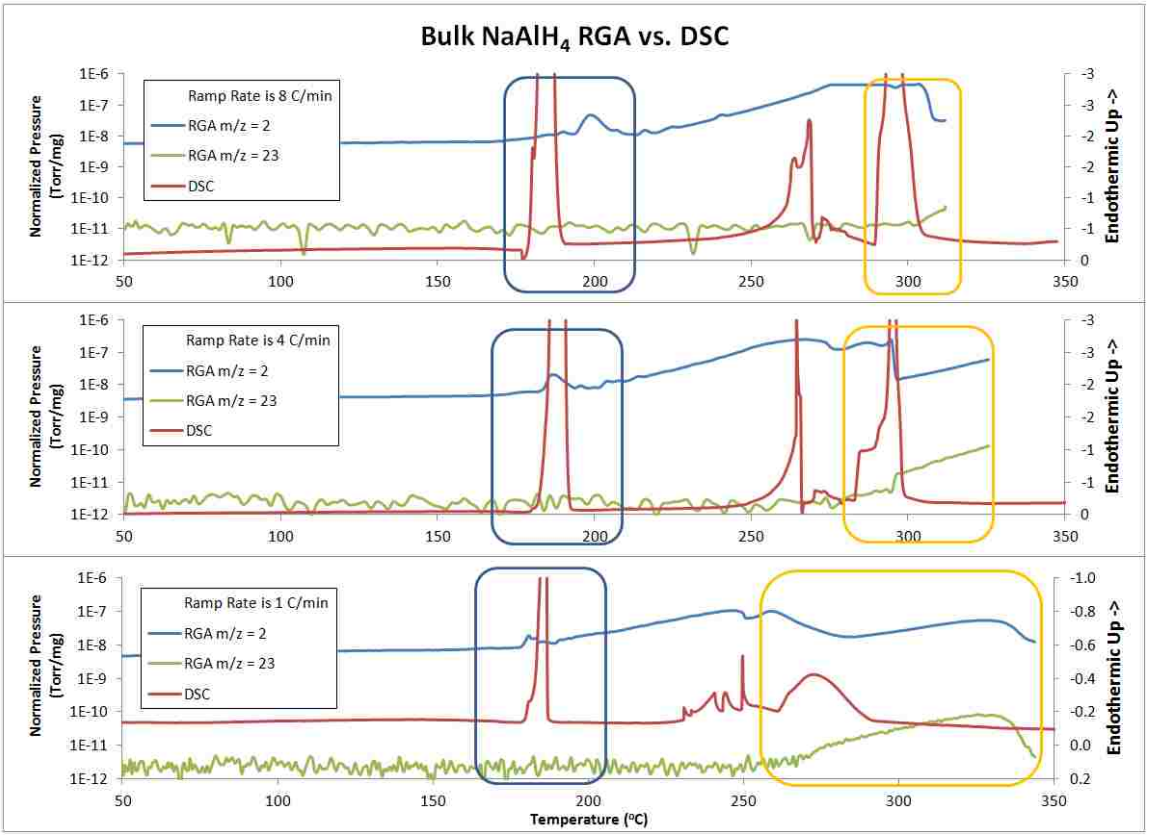

Figure 8.(a). MS-RGA measurements of the thermal decomposition at various ramp rates for bulk $NaAlH_4$. In figures (a)-(c): the top dark line represents the partial pressure of H_2, the bottom dark line represents DSC analysis, and the bottom grey line represents the partial pressure of NaH. Starting from the top chart, the ramp rates are 8, 4, and 1 °C/minute.

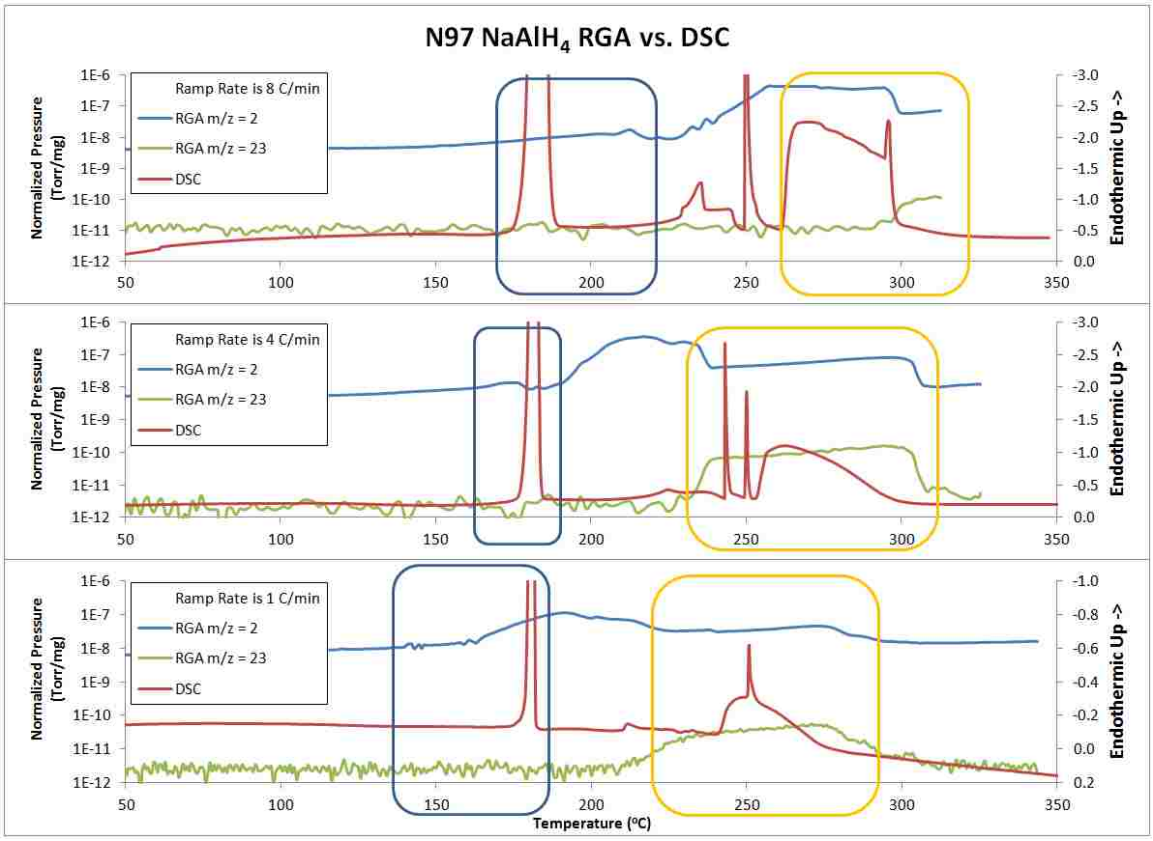

Figure 8.(b). MS-RGA measurements of the thermal decomposition at various ramp rates for high H_2 pressure N97.

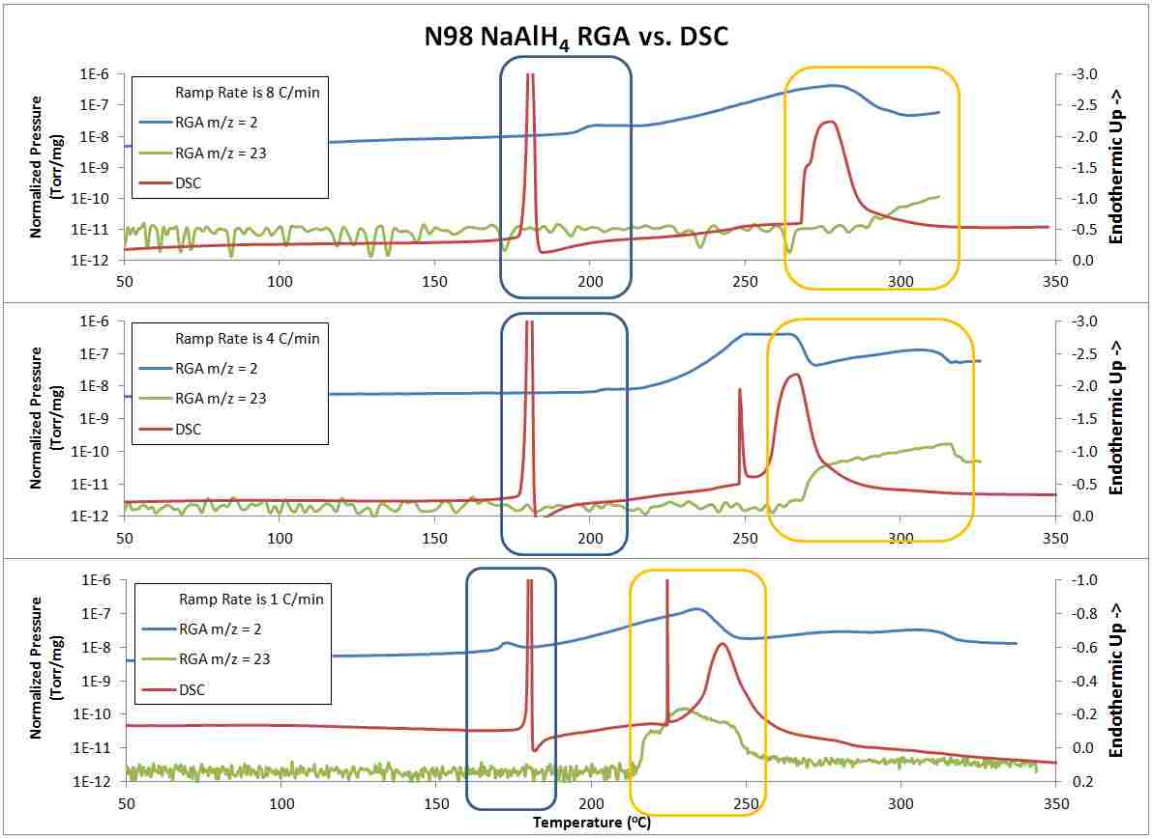

Figure 8.(c). MS-RGA measurements of the thermal decomposition at various ramp rates for the high temperature/pressure phase “S105” N98.

CONCLUSION

Heat and pressure-treated $NaAlH_4$ in the S105 phase has been shown to melt and decompose into Na_3AlH_6 and H_2 gas at a lower temperature than the as prepared bulk material. This would indicate that the effect of pretreating $NaAlH_4$ with a high temperature and H_2 pressure improves this material's ability to store and release H_2 gas at moderate temperatures without the use of catalysts.

ACKNOWLEDGEMENTS

The authors gratefully acknowledge support from DOE Basic Energy Sciences grant DE- FG02-05ER46256.

REFERENCES

[1] "Discovery of a New Al Species in Hydrogen Reactions of $NaAlH_4$" Ivancic, T. M.; Hwang, S-J.; Bowman, R. C., Jr.; Birkmire, D. S.; Jensen, C. M.; Udovic, T. J.; Conradi, M. S., *Phys. Chem. Lett*. 2010, 1, 2412- 2416.

[1] "Mobile Species in $NaAlH_4$" Eric Glenn Sorte, Robert C. Bowman, Eric H. Majzoub, Margriet H.W. Verkuijlen, Terrence J. Udovic, and Mark S. Conradi, *J. Phys. Chem. C*, Just Accepted DOI: 10.1021/ jp401134t.

[2] "General Structure Analysis System (GSAS)" A.C. Larson and R.B. Von Dreele, *Los Alamos National Laboratory Report* LAUR 86-748 (2000).

[3] "Metal-doped sodium aluminium hydrides as potential new hydrogen storage materials" B. Bogdanovic, R.A. Brand, A. Marjanovic, M. Schwicardi, J. Tolle, *J. Alloys and Compounds*, v302, 36, 2000.

II. Controlling the Decomposition Pathway of $LiBH_4$ via Confinement in Highly Ordered Nanoporous Carbon

Xiangfeng Liu, David Peaslee, C. Z. Jost, and E. H. Majzoub
Center for Nanoscience and Department of Physics and Astronomy,
University of Missouri-St. Louis,
One University Boulevard, St. Louis, Missouri 63121
First published in the *Journal of Physical Chemistry C* (August 2010)

The wetting and decomposition behavior of $LiBH_4$ has been investigated in the presence of highly ordered nanoporous hard carbon (NPC) with hexagonally packed 2 nm diameter columnar pores. Calorimetry, X-ray diffraction, and IR spectroscopy measurements confirm that the $LiBH_4$ within the pores is amorphous. The confinement of $LiBH_4$ in such small pores results in the disappearance of the low-temperature structural phase transition, the melting transition, and also the significant decrease of the onset desorption temperature from 460 to 220 °C with respect to bulk $LiBH_4$, a lower temperature than observed in larger pore sizes in the literature. Most importantly, our results suggest that diborane release is suppressed or eliminated in the decomposition of noncrystalline $LiBH_4$. Tight nanoconfinement may therefore mitigate both safety concerns and loss of active material in borohydride-based hydrogen storage systems.

Introduction

Efficient and safe hydrogen storage is one of the most challenging barriers to the widespread commercialization of hydrogen-fueled vehicles [1]. Lithium borohydride ($LiBH_4$) has been extensively studied as a promising hydrogen storage material due to its high gravimetric hydrogen capacity (18.5 wt % H_2) [2]. However, the high desorption temperature (~500 °C), the evolution of toxic diborane (B_2H_6) on decomposition, [3] and inaccessible rehydrogenation conditions of 350 bar of H_2 and 600 °C appear to limit its practical application as a hydrogen storage medium [4]. Some conventional strategies such as the addition of catalysts [5], partial cation substitution [6], and destabilization with metals or hydrides (Mg, Al, Ti, MgH_2, TiH_2, CaH_2, etc.) [7, 8] have been tried to decrease the dehydrogenation temperature and improve the reversibility of $LiBH_4$.

Recent attention has been focused on the nanoscale effect of metal hydrides on the thermodynamics and kinetics [9-12]. Theoretical calculations predict that nanosized metal hydrides will have significantly different thermodynamic properties than their bulk counterparts. First-principle calculations indicate the H_2 desorption enthalpy for MgH_2 may be substantially decreased when the particle size becomes very small (1.3 nm) [13]. Experimental measurements indicate that the onset dehydrogenation temperature of carbon nanofiber supported $NaAlH_4$, with the size of 2-10 nm, was dramatically lowered to 70 °C and that reabsorption of H_2 occurred under relatively low H_2 pressures [14].

This “nanoengineering” strategy has been applied to $LiBH_4$ through the use of nanoscale frameworks which provide support for the hydride [15-17]. Vajo et al.[16] infiltrated $LiBH_4$ into carbon aerogel hosts with average pore sizes of 13 and 25 nm, and demonstrated enhanced desorption kinetics and reversibility. Cahen et al. prepared carbons with an average pore size of 4 nm using mesoporous silica (SBA-15) as a sacrifice template and impregnated the pores through the solution method [17]. The pores of the carbon replica have the shape of the walls of the SBA-15 silica. To better quantify the nanoscale effect it is necessary to control not the average particle size but most importantly the size distribution and the ordered mesostructure of the frameworks. However, the porous carbons used in these studies usually have a large average size and/or a broad size distribution. Here we prepared highly ordered nanoporous carbon by the organic-organic assembly of copolymers PEO-PPO-PEO with resols via an

evaporation induced self-assembly strategy that was well established by Zhao's group [18]. Compared to the carbon that Cahen used our carbon shows a highly ordered hexagonal arrangement of nanopores in addition to the smaller pore size (2.0 nm) and narrower size distribution. In addition, the 4 nm mesoporous carbon was infiltrated through solution techniques that may influence the decomposition process through residual etherates contamination (e.g., the complex between ether and $LiBH_4$) [17]. Although the absence of diborane in the decomposing gas stream in the 4 nm mesoporous carbons is in agreement with our studies, both the calorimetry and structural studies indicate major differences in the structure of the incorporated $LiBH_4$. Taken together, our results shed new light on the possible decomposition pathway of $LiBH_4$ from carbon framework materials.

In this study, we report on the decomposition properties of $LiBH_4$ confined in highly ordered hexagonally packed cylindrical nanoporous carbon (NPC) with an average pore size of 2.0 nm and a very narrow size distribution. The wetting of molten $LiBH_4$ into the nanopores and the decomposition pathway were investigated by using calorimetry and a direct line-of-site residual gas analyzer mass spectrometer (RGA-MS) for decomposing samples for the analysis of gaseous decomposition products. Further characterization of incorporated $LiBH_4$ is provided by X-ray diffraction and IR spectroscopy studies. Our studies indicate that diborane release is mitigated when $LiBH_4$ is incorporated into the 2.0 nm pores of these carbons. A detailed discussion of the possible mechanisms is found below.

Experimental Methods

Nanoporous carbon was prepared by using phenolic resins as carbon precursors and amphiphilic triblock copolymers as soft templates according to referenced literature [18]. Briefly, phenolic resins were first prepared from phenol and formaldehyde with NaOH as the catalyst and dissolved in ethanol after the removal of water. Triblock copolymer F127 (Mw = 12,600, EO_{106}-PO_{70}-EO_{106}, Aldrich) dissolved in ethanol was mixed with the above ethanol solution of phenolic resin. The typical molar ratio of phenol/formaldehyde/NaOH/F127 (1:2:0.1/0.012) was used. The mixed ethanol solution

was poured into dishes and put into an oven for thermopolymerization after the evaporation of ethanol. The powdered products scraped from the dishes were calcinated in a tubular furnace with flowing argon. The furnace was first heated to 350 °C with a rate of 1 deg/min and kept at this temperature for 4 h to remove the triblock copolymer template. Then it was heated to 900 °C with a rate of 1 deg/min and kept at this temperature for 5 h to carbonize.

Before the infiltration of the NPC with $LiBH_4$, it was first dried at 900 °C for 5 h under flowing Ar and then dried at 400 °C under vacuum. In a typical process, 20 mg of $LiBH_4$ (95%, Aldrich) and 180 mg of NPC were ground by hand in an argon-filled glovebox. These physically mixed samples are hereafter referred to as $LiBH_4$/ NPC. Then the mixture was loaded into a sample holder. The sample holder was subsequently attached to a fixed-volume Sievert's-type instrument without exposing the sample to air. The sample holder was heated to 300 °C under about 60 bar of H_2 then kept at this temperature for 30 min. These premelted samples are hereafter referred to as $LiBH_4$@NPC.

Nitrogen adsorption isotherms were measured at 77 K by an SA3100 analyzer (Coulter). Before analysis, the sample of nanoporous carbon was outgassed for 1 h at 300 °C under vacuum. The Brunauer-Emmett-Teller (BET) method was used to calculate the specific surface areas (SBET) using adsorption data in a relative pressure range from 0.05 to 0.2 bar. The total pore volume was estimated from the adsorbed amount at a relative pressure P/P_0 of 0.98 based on the Barrett-Joyner-Halenda (BJH) calculation model. The morphology of the nanoporous carbon was investigated with use of a Philips EM430 high-resolution transmission electron microscopy (TEM). The powder was supported on the copper grid coated by a carbon film. X-ray diffraction (XRD) and small angel X-ray scattering (SAXS) were performed on a Rigaku Ultima IV multipurpose X-ray diffraction (XRD) system with Cu K_α radiation source. Samples containing hydrides were covered with parafilms to prevent the samples from contacting air or moisture during the XRD experiments. FT-IR spectra were collected on a Nicolet 6700. Two KBr polished disks were used to hold the powered samples. DSC analysis was performed on a TQ2000 series analyzer (TA Instruments). About 4 mg of sample was loaded in a Tzero pan in an argon-filled glovebox and crimped with a Tzero lid or Tzero

hermetic lid. The sample was heated to 550 °C at a certain ramping rate under a N_2 flowing rate of 50 mL/min. Thermogravimetric analysis (TGA) was performed on a TGAQ500 Series thermogravimetric analyzer (TA Instruments). In a typical TGA procedure, about 10 mg of sample was loaded in a Tzero pan and crimped with a Tzero hermetic lid in an argon-filled glovebox. A hermetic lid was selected to reduce contamination and a pinhole was made on the top of the lid for the purpose of H_2 release. The sample was heated to 550 °C at a ramping rate of 10 deg/min under a N_2 flowing rate of 100 mL/min.

Mass spectroscopic analysis was performed with an SRS RGA200 residual gas analyzer (RGA) and a high-temperature sample stage. The system is separated into a HV (10^{-8}-10^{-5} Torr) sample chamber and UHV (10^{-9}-10^{-7} Torr) gas analysis chamber. The RGA maintains a line of sight with the sample through a small flow hole to produce the best possible signal. The sample is placed into the system using the same Tzero pans as from the DSC/TGA analysis. An Ar-filled glovebag serves as an ante-chamber for the RGA system. The sample holder is placed into the argon-filled glovebag at which time a small hole is punctured for the later release of gases. The samples are heated to 450 °C at a ramping rate of 4 deg/min. Calibration of the sample temperature was performed by using a sample holder filled with glass beads with the measuring thermocouple in the center of the beads away from the aluminum pan wall. The estimated error between the sample holder temperature and the indicated sample temperature is (15 °C. The maximum partial pressure sensitivity of the RGA using the electron multiplier is 8.8×10^{-7} Torr, and at times the mass to charge ratio (m/z = 2) of the hydrogen pressure is estimated by using m/z = 1 when this partial pressure is exceeded. Cracking-pattern histograms were used to definitively indicate the presence of B_2H_6. The data are presented as the increase in partial pressures from 20 °C up to the peak in B_2H_6. The diborane cracking pattern shows the strongest peak at m/z = 26 (21.1% of the B_2H_6 gas appears at m/z = 26) and the second strongest at m/z = 27 (20.6%) [19]. The mass line at 24, which is 18.9% of the B_2H_6, is very clean with a minimum detectable partial pressure of $\sim 10^{-10}$ Torr. Here, this mass is used to determine the partial pressure of B_2H_6. The signal-to-noise ratio of the baselines is about 17:1 for that of hydrogen (m/z = 2) and

about 2:1 for that of B_2H_6 (m/z = 24). Other stable boranes $(BH_3)_n$ and other gases were not detectable in any of the samples over these temperature ranges.

Results and Discussion

The SAXS pattern shown in Figure 1 of the nanoporous carbon shows two resolved Bragg peaks corresponding to the 10 and 11 planes of a highly ordered 2-D hexagonal mesostructure (space group P6m). TEM micrographs of the porous carbon, shown in Figure 2, show well-defined nanopores in a hexagonal packing arrangement with an average pore size of 2.0 nm viewed from the direction parallel to the pore channels [001] and stripe-like patterns viewed from the direction perpendicular to the pore channels [110], respectively. Combined with the SAXS data showing a d-spacing of about 10 nm (between columns) this morphology was attributed to a 2-D hexagonal packing of nanocolumns in agreement with the previous report [18]. The broad diffracted intensity of the porous carbon in XRD (Figure 3a) indicates the material is amorphous. Figure 4a shows the nitrogen sorption isotherms of neat NPC. The specific surface areas (SBET) of NPC based on the. Brunauer-Emmett-Teller (BET) method and the total pore volume calculated by the Barrett-Joyner-Halenda (BJH) model were 594 m^2/g and 0.35 cm^3/g, respectively, which is in excellent agreement with the previously reported results [18]. After drying the carbon at 400 °C under dynamic vacuum for 6 h, we impregnated the carbon with $LiBH_4$ through melt-infiltration under 60 bar of H_2 at 300 °C.

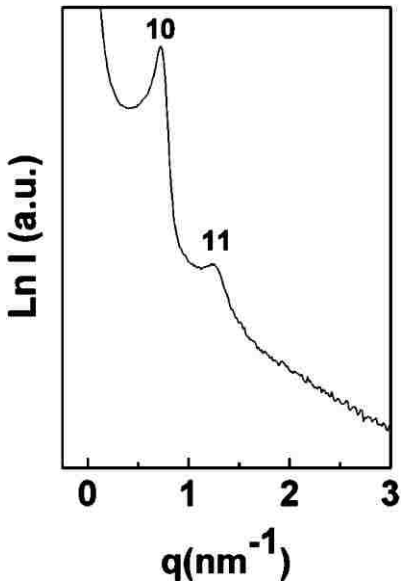

Figure 1. SAXS pattern of the NPC with columnar pores packed in a hexagonal geometry. The (10) and (11) Bragg peaks are prominent and indicate the long-range order in the sample.

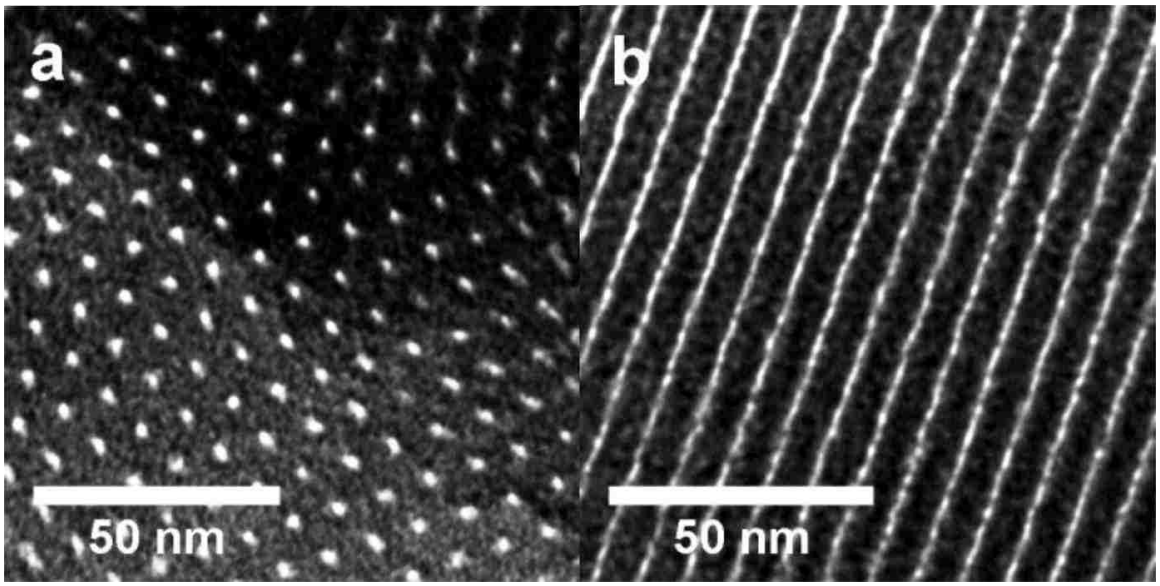

Figure 2. TEM images for NPC of columnar pores packed in a hexagonal geometry, viewed from the directions parallel (a) and perpendicular (b) to the pore channels.

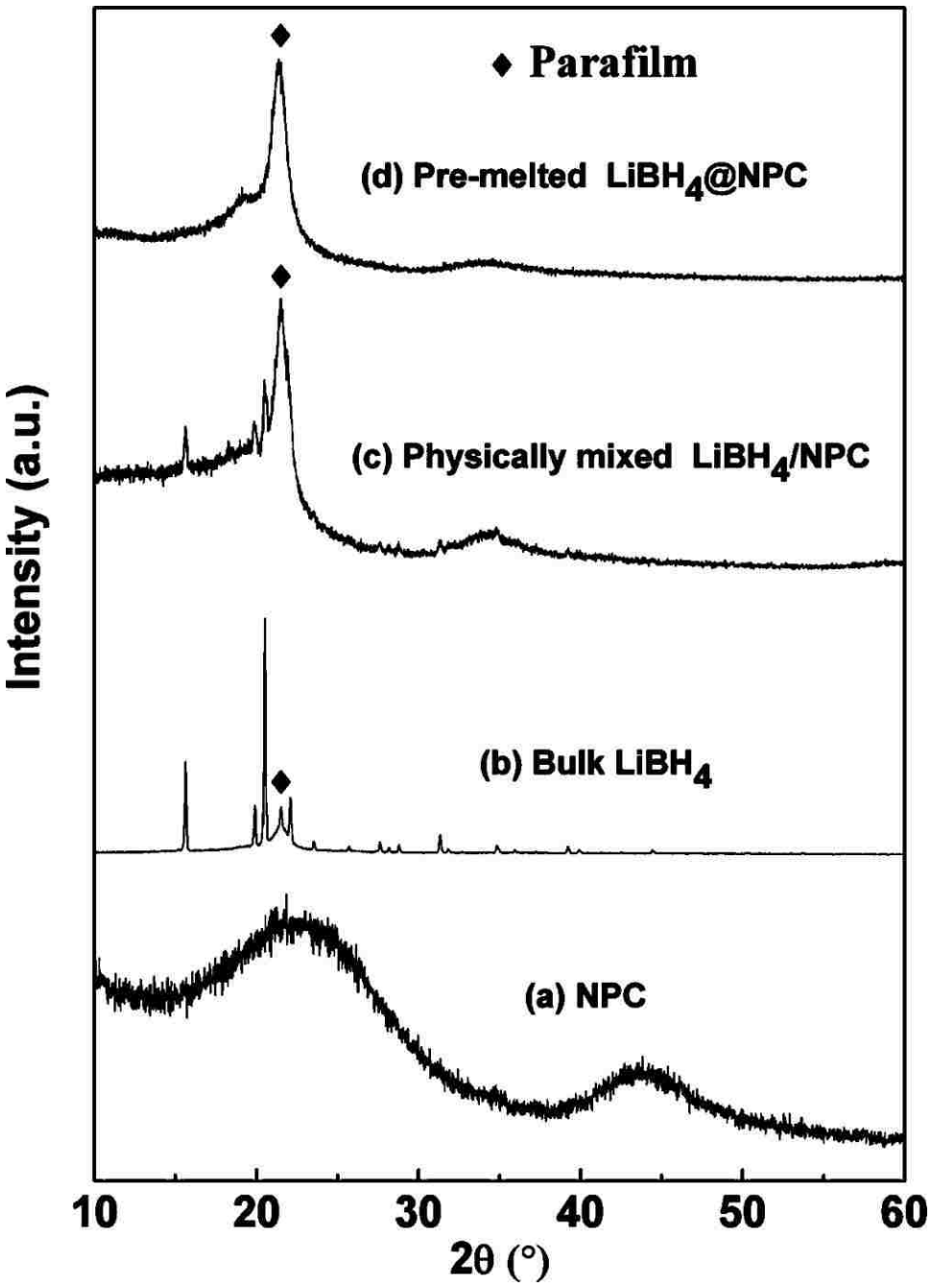

Figure 3. X-ray diffraction of (a) neat NPC, (b) bulk $LiBH_4$, (c) physically mixed $LiBH_4$/NPC, and (d) premelted $LiBH_4$@NPC.

Figure 3 shows the XRD patterns of the physically mixed sample of $LiBH_4$/NPC and the premelted sample of $LiBH_4$@NPC. The XRD pattern of the premelted $LiBH_4$@NPC (Figure 3d) did not show the Bragg peaks of $LiBH_4$ indicating $LiBH_4$

became amorphous after it was confined in the nanopores of NPC through melt infiltration. This is different from what is observed in samples of $LiBH_4$ at carbon aerogels ($LiBH_4$@carbon aerogels) with a pore size of around 25 nm [16]. The diffraction peaks of $LiBH_4$ still exist in the premelted sample of $LiBH_4$@carbon aerogels indicating the existence of crystalline $LiBH_4$ in this nanocomposite system. In comparison to the large pore size and the broader size distribution of carbon aerogels (25 nm), the NPC 2.0 nm pore size and narrow size distribution are likely responsible for the noncrystalline $LiBH_4$ in our carbon. Figure 4b shows the nitrogen sorption isotherms of $LiBH_4$@NPC. SBET and the total pore volume of $LiBH_4$@NPC were reduced to 116 m^2/g and 0.09 cm^3/g, respectively, indicating the filling or blocking of the pores by $LiBH_4$. The total pore volume loss is about 0.26 cm^3/g carbon. The expected volume of the added $LiBH_4$ is about 0.17 cm^3/g carbon. The extra loss of pore volume can be attributed to the blocking of some pores. Calorimetry of these samples, discussed below, indicates filling and rules out simple blocking of the pores. The existence of $[BH_4^-]$ in the premelted sample was confirmed by means of Fourier transform infrared spectroscopy (Figure 5). Figure 5a shows the FT-IR spectra of neat carbon and no significant FT-IR vibration bands were observed indicating the removal of block polymer templates after the formation of the carbon framework. In the premelted sample of $LiBH_4$@NPC (Figure 5b), there exist strong B-H stretching modes at 1100 cm^{-1} and bending modes around 2200-2300 cm^{-1}, confirming the existence of $LiBH_4$.

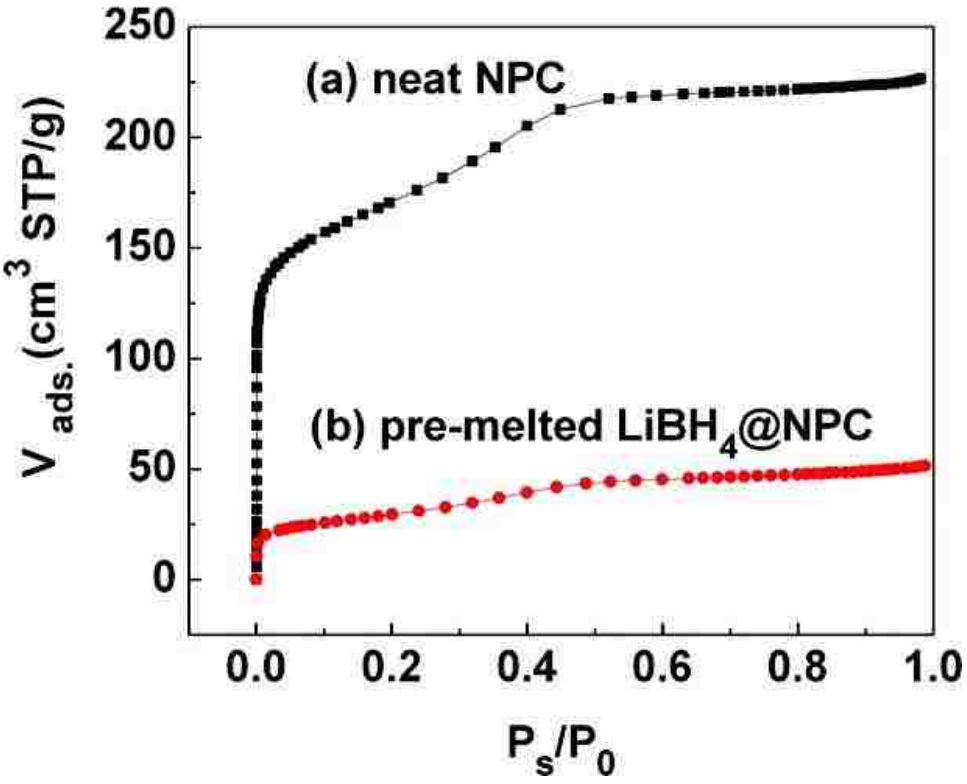

Figure 4. Nitrogen sorption isotherms of (a) NPC with a surface area and pore volume of 594 m^2/g and 0.35 cm^3/g, respectively, and (b) premelted $LiBH_4$@NPC, with a surface area and pore volume of 116 m^2/g and 0.09 cm^3/g, indicating that $LiBH_4$ has infiltrated the pores.

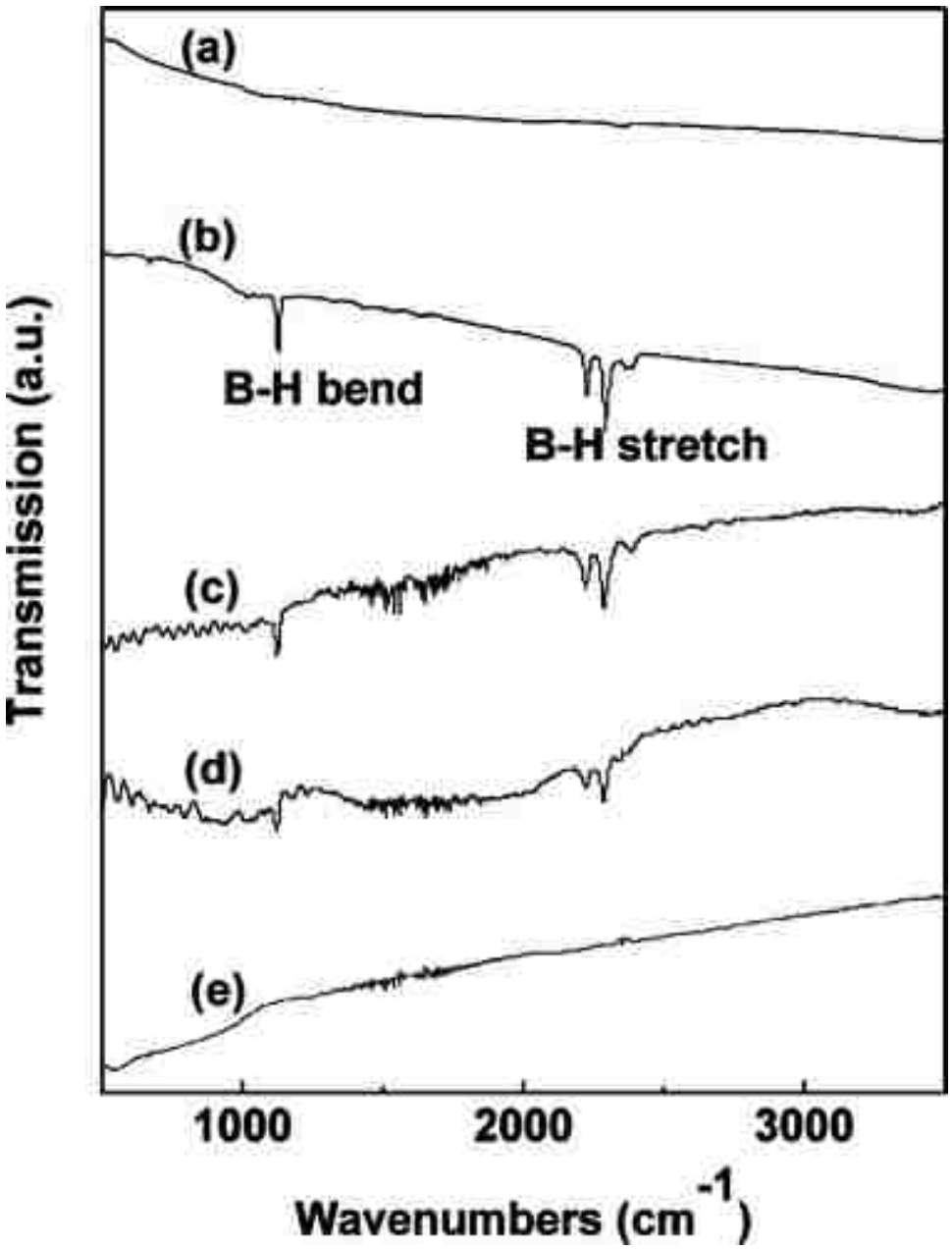

Figure 5. FT-IR spectra of (a) neat NPC, (b) premelted $LiBH_4$@NPC, (c) physically mixed $LiBH_4$/NPC after intermediate DSC stopped just following the melting point, (d) physically mixed $LiBH_4$/NPC after intermediate DSC stopped just following gas escape, and (e) after a full DSC desorption to 550 °C. Spectra b−d show $[BH_4]^-$ bands indicating that $LiBH_4$ is still present in these materials.

Figure 6 shows the DSC plots of bulk $LiBH_4$, a physical mixture of $LiBH_4$/NPC, and $LiBH_4$@NPC. In agreement with bulk $LiBH_4$ the DSC plot of the physical mixture of

$LiBH_4$/ NPC shows the orthorhombic to hexagonal structure transition at a temperature of 115 °C and melting at 284 °C. The decomposition peak of bulk $LiBH_4$ appears around 495 °C. Rapid dehydrogenation after the melting was observed for $LiBH_4$/NPC, and the decomposition peak appeared around 339 °C. In contrast, the premelted sample of $LiBH_4$@NPC did not show the structure transition from orthorhombic to hexagonal and no distinct melting point was observed, indicating that $LiBH_4$ confined in NPC becomes amorphous. This is in agreement with the above XRD result (Figure 3d) but different from what is observed in previous investigations of $LiBH_4$@carbon aerogel [16]. $LiBH_4$@carbon aerogel has a lower, but distinct melting point. We speculate this may be due to lattice strain induced via an interaction between the $LiBH_4$ and the carbon surface. In contrast, from the DSC curve of $LiBH_4$@NPC we can see that $LiBH_4$ confined in NPC begins to decompose below the normal melting point.

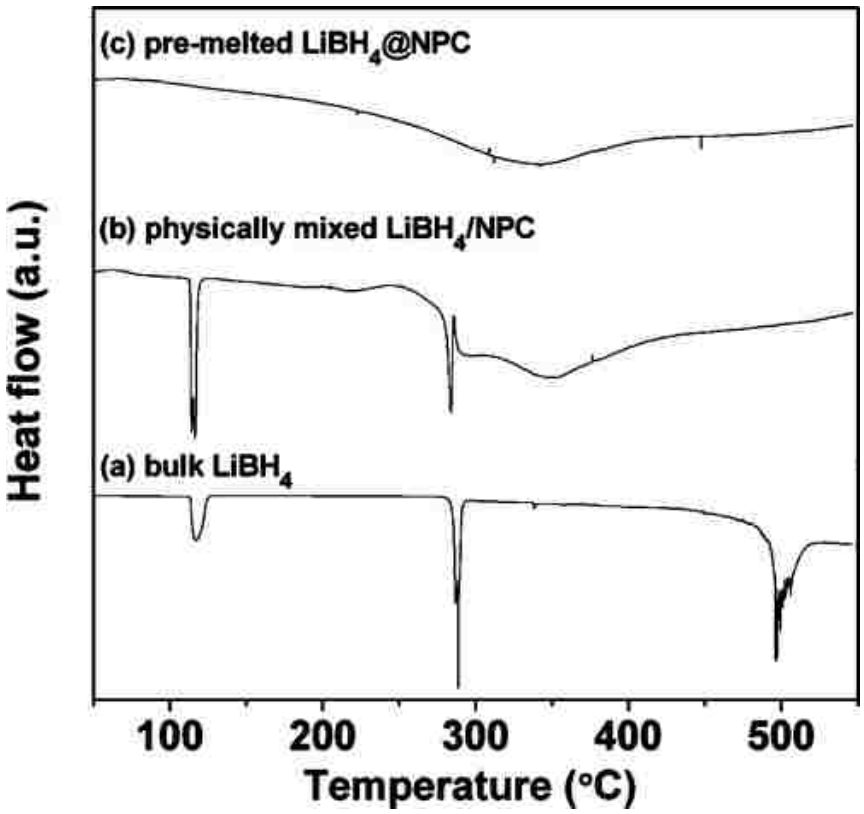

Figure 6. DSC traces of (a) bulk $LiBH_4$, (b) physically mixed $LiBH_4$/NPC, and (c) premelted $LiBH_4$@NPC. The heating rate was 10 deg/min.

Wetting of nanoprous carbons was observed visually in the work by Vajo et al., in carbon aerogels [16]. Evidently, molten $LiBH_4$ is pulled into the nanopores through capillary action. Clearly, the flow rate into the pores will depend on the pore geometry and one would expect a framework with very narrow pores to infiltrate more slowly than one with larger pores. Wetting behavior is most easily observed in calorimetry experiments on infiltration if hydrogen release can be suppressed, as shown in the high-pressure DSC experiments on $NaAlH_4$/C melt-infiltration into nanoporous carbons [20]. If hydrogen gas release cannot be physically suppressed, calorimetry may still be used to qualitatively investigate the wetting process if one uses multiple temperature ramping rates.

To study the process of molten $LiBH_4$ wetting the pores of NPC, hermetic lids were used to cover the sample in a Tzero pan. The Tzero hermetic lid can sustain a nominal pressure of about 3 bar, at which point escaping H_2 or other gases trapped in the pan will result in a large endothermic signature in the DSC scan appearing as a sharp spike. Figure 7 shows DSC curves of a physical mixture of $LiBH_4$/NPC at different heating ramps (2, 5, 10, 20, and 50 deg/min). It is difficult to separate the melting and wetting process when the heating rate is low. This is due to decomposition of the $LiBH_4$ during the wetting process, when the hydrogen overpressure is below the equilibrium pressure, i.e., the sample decomposes on infiltration under vacuum. For instance, $LiBH_4$ decomposed nearly completely during the melting and wetting when the heating rate is 2 deg/min. When the heating rate is increased to 20 deg/min we can clearly see the endothermic peak of melting and a subsequent exothermic peak corresponding to the wetting (and concomitant decomposition) of molten $LiBH_4$ into the pores. The exothermic signature for wetting is most apparent in Figure 7e, with the largest ramping rate of 50 deg/min, where the melting peak clearly precedes the infiltration and wetting of the pores. The following sharp endothermic peak at around 325 °C is due to the escape of H_2 gas resulting from the over pressure inside the DSC pan, and failure of the lid integrity. DSC measurements of the physical mixture of $LiBH_4$/NPC at different intermediate stages (e.g., after melting and before gas escape) were performed, and further indicate that the $LiBH_4$ is indeed inside the pore. For example, the DSC measurement was immediately stopped when the peak of $LiBH_4$ melting appeared as

shown in Figure 8a. While still inside the instrument, it was rapidly cooled to room temperature and then heated again on a second cycle to 550 °C. Both the endothermic structure transition and melting peaks of $LiBH_4$ were again observed but with a reduced enthalpy as shown in Figure 8b, indicating that the molten $LiBH_4$ was not given ample time to completely enter the nanopores. The heat of structure transition calculated from the DSC curve was reduced by about 80% indicating a large part of $LiBH_4$ has become amorphous due to the partial infiltration of molten $LiBH_4$ into the nanopores, or decomposition on melting. If the DSC measurement was immediately stopped when the peak of gas escape appears as shown in Figure 8c, neither the structure transition nor distinct melting peaks appeared when it was reheated; however, there is still a large hydrogen release indicating decomposition of $LiBH_4$. This indicates no $LiBH_4$ exterior to the pores was present. The existence of $LiBH_4$ at the different intermediate stages (after melting and after gas escape) was confirmed by FT-IR. As shown in traces c and d of Figure 5, B-H stretching modes at 1100 cm^{-1} and bending modes around 2200-2300 cm^{-1} were observed.

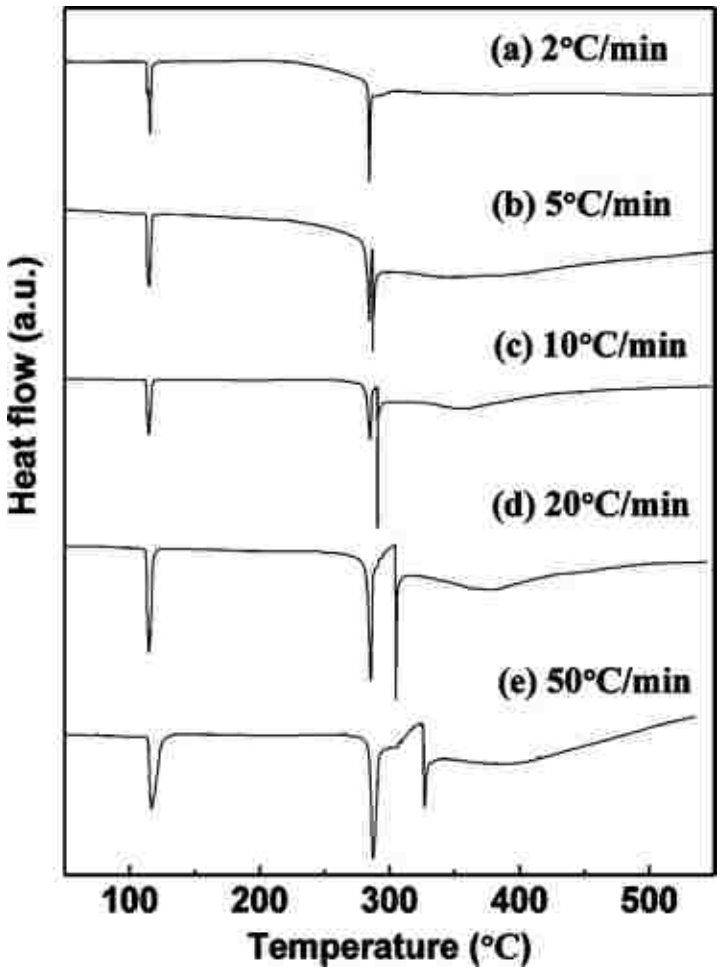

Figure 7. DSC traces of physical mixtures of $LiBH_4$/NPC at different heating ramps of (a) 2, (b) 5, (c) 10, (d) 20, and (e) 50 deg/min. The sharp endothermic spike corresponds to gas escape when the seal integrity is compromised. As the ramping rate is increased the gas escape moves to higher temperatures and indicates that infiltration (and concomitant decomposition) occurs after melting.

The dehydrogenation of bulk $LiBH_4$, physically mixed $LiBH_4$/ NPC, and premelted $LiBH_4$@NPC was measured by thermogravimetric analysis (TGA), as shown in Figure 9. The mass loss of physically mixed $LiBH_4$/NPC and premelted $LiBH_4$@NPC was calculated with respect to $LiBH_4$ content. Bulk $LiBH_4$ only releases a very small amount of H_2 at 284 °C (melting point) with full release following at 485 °C. In contrast, a two-step desorption appeared in the sample of physically mixed $LiBH_4$/NPC. It begins to desorb at around 284 °C followed by a more rapid rate of desorption at 335 °C.

Evidently the molten $LiBH_4$ starts a distinct decomposition during the wetting of the carbon nanopores. Though both the small pore size and the contact between the molten $LiBH_4$ and the carbon contribute to the initial desorption, the latter is mainly responsible for the initial decomposition. After wetting the pores the molten $LiBH_4$ confined in NPC rapidly decomposes at a much lower temperature than in bulk sample, presumably due to the confinement effect. The premelted sample of $LiBH_4$@NPC began to decompose at 220 °C, in excellent agreement with the DSC decomposition onset temperature. It should be noted that the mass loss from the decomposition of $LiBH_4$@NPC is lower than that from the physically mixed $LiBH_4$/NPC sample, which can be attributed to the capacity loss of $LiBH_4$ during melting and wetting. The oxidation of $LiBH_4$, in particular LiH from the decomposition of $LiBH_4$, results in the increase of weight shown in the TGA curves (Figure 9) at higher temperature.

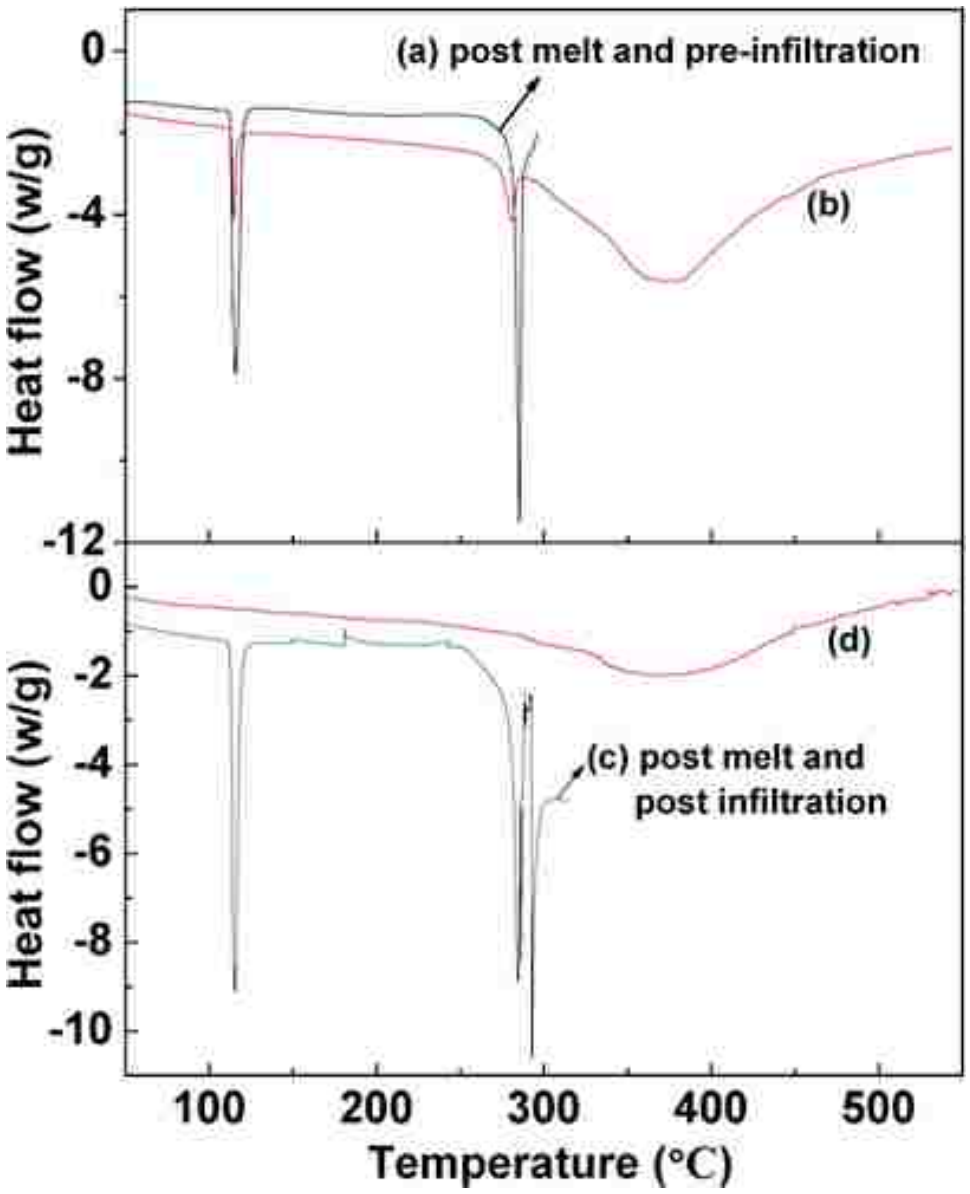

Figure 8. DSC traces of physical mixtures of $LiBH_4$/NPC when the scan was stopped and cooled (a) just following the melting point and (c) just following gas escape. The second cycles are shown in traces b and d. The lack of structural phase transition and melting endotherm in trace d indicate the endothermic spike in trace c corresponds to the gas release during infiltration of the pores, as discussed in the text.

To examine the decomposition pathway, we have observed gaseous decomposition products of bulk $LiBH_4$, a physical mixture of $LiBH_4$/NPC, and premelted samples of $LiBH_4$@NPC, using a direct line-of-site residual gas analyzer and mass

spectrometer (RGA-MS) described above. As noted by Kostka and co-workers [3], the decomposition of bulk $LiBH_4$ is difficult to observe due to the molten sample bubbling caused by a release of hydrogen in the molten material. It is observed in the MS of bulk $LiBH_4$, and the sample of physically mixed $LiBH_4$/NPC, that the decomposition results in the formation of B_2H_6 as shown in Figures 10 and 11. (The H_2 partial pressure exceeded the RGA pressure tolerance in the physical mixture of $LiBH_4$/NPC. The estimation of partial pressure above the flat green segment is based on the linear relationship between the partial pressures of m/z = 1 and 2.) B_2H_6 release data of bulk $LiBH_4$, the physical mixture of $LiBH_4$/NPC, and the premelted $LiBH_4$@NPC were taken at 410, 325, and 382 °C, respectively. The mass spectra cracking pattern of B_2H_6 was taken from the NIST Chemistry Webbook [19]. Interestingly, for the physically mixed sample of $LiBH_4$/NPC, B_2H_6 formed during the initial decomposition of $LiBH_4$, but for the bulk sample B_2H_6 was mainly observed after significant release of H_2. More interestingly, B_2H_6 is not indicated in the premelted sample of $LiBH_4$@NPC. Our diborane release results are largely in agreement with the solution-infiltrated 4 nm carbons of Cahen et al. [17]; however, there are significant differences in our sample preparation techniques and structure transition that may influence these results. First, our carbon framework consists of isolated, geometrically well-defined cylindrical columns with clearly defined pore edges, while the 4 nm carbons of Cahen and coworkers require gas adsorption modeling using a rod-aligned slit-like pore [21]. Second, our 2.0 nm pore diameter carbons result in a loss of both the structural phase transition and melting endotherms in DSC, while retaining the $[BH_4]^-$ bending and stretching modes in FTIR, indicating that $LiBH_4$ confined in NPC is present in the pores but becomes amorphous. In contrast, the 33:67 $LiBH_4$/C composite of the 4 nm mesoporous carbons still indicates the phase transition and melting endotherms, suggesting that either the 4 nm pore diameter is too large to result in X-ray amorphous structure for $LiBH_4$, or that the carbon surface is sufficiently different to allow retention of the crystal structure. We note that the 50:50 $LiBH_4$/C composite of Cahen indicates crystalline $LiBH_4$, perhaps indicating that some $LiBH_4$ is still present outside the pores.

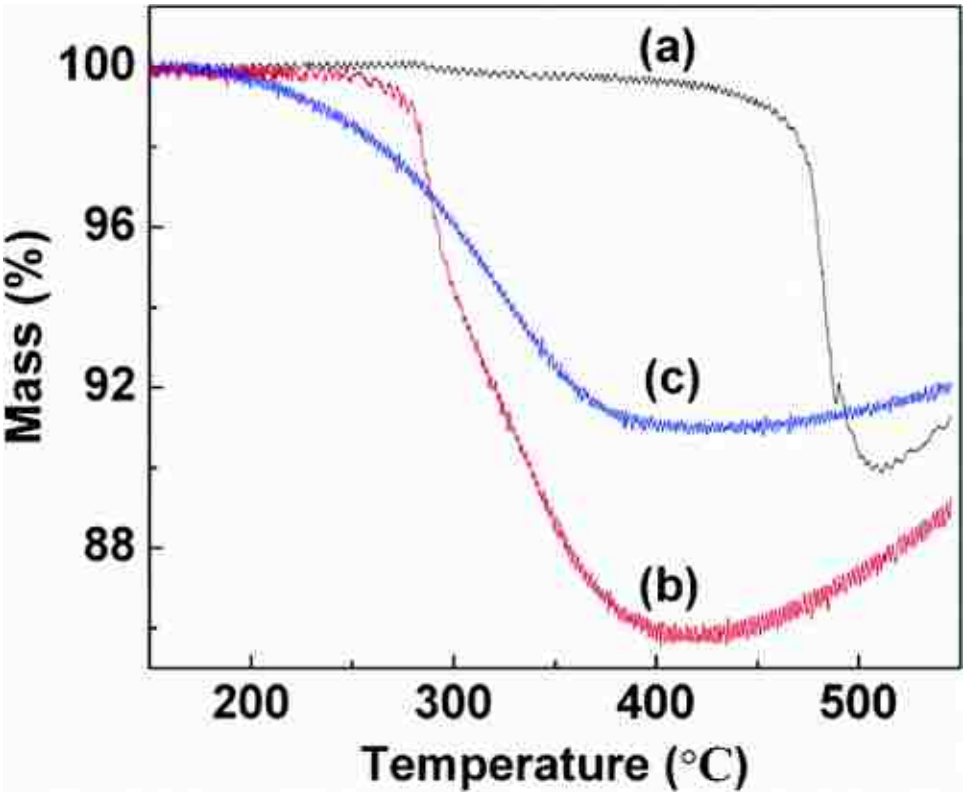

Figure 9. TGA traces of (a) bulk $LiBH_4$, (b) physically mixed $LiBH_4$/NPC, and (c) premelted $LiBH_4$@NPC. A two-step process is suggested by the change in mass loss rate shown in trace b. Combined with calorimetry and RGA data, the first step evidently corresponds to decomposition during infiltration, following melting of the $LiBH_4$.

The diborane release results of Kostka and co-workers of $LiBH_4$ in the presence of mesoporous silica gel materials with different dopants, including Pd-, Ni-, La-, and Ti-chlorides, are difficult to compare with our results due to the framework differences [3]. However, it is noted that the peak diborane release occurs before the peak H_2 release in these materials suggesting clear decomposition pathway differences. Our results indicate that the carbon framework may prevent the formation of B_2H_6 and the decomposition pathway is altered by the presence of the framework through size confinement and/or surface interaction effects as evidenced by the wetting behavior. Alternatively, it may suggest that $LiBH_4$ decomposing from a noncrystalline state cannot produce B_2H_6.

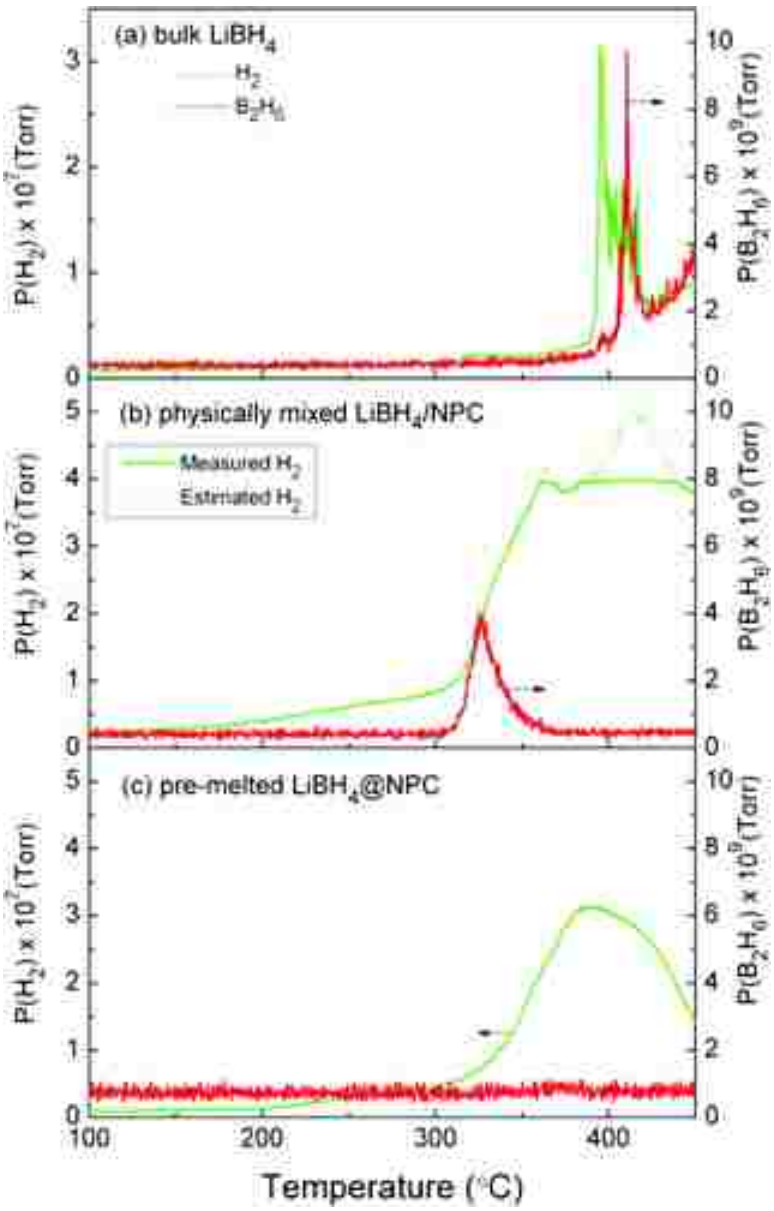

Figure 10. B_2H_6 and H_2 release with increasing temperature for (a) bulk $LiBH_4$, (b) physically mixed $LiBH_4$/NPC, and (c) premelted $LiBH_4$@NPC. The release of diborane is absent in the premelted $LiBH_4$@NPC sample. The H_2 partial pressure exceeded the RGA tolerance in the physical mixture of $LiBH_4$/NPC. The estimation of partial pressure above the flat green segment is based on the linear relationship between the partial pressures of m/z = 1 and 2.

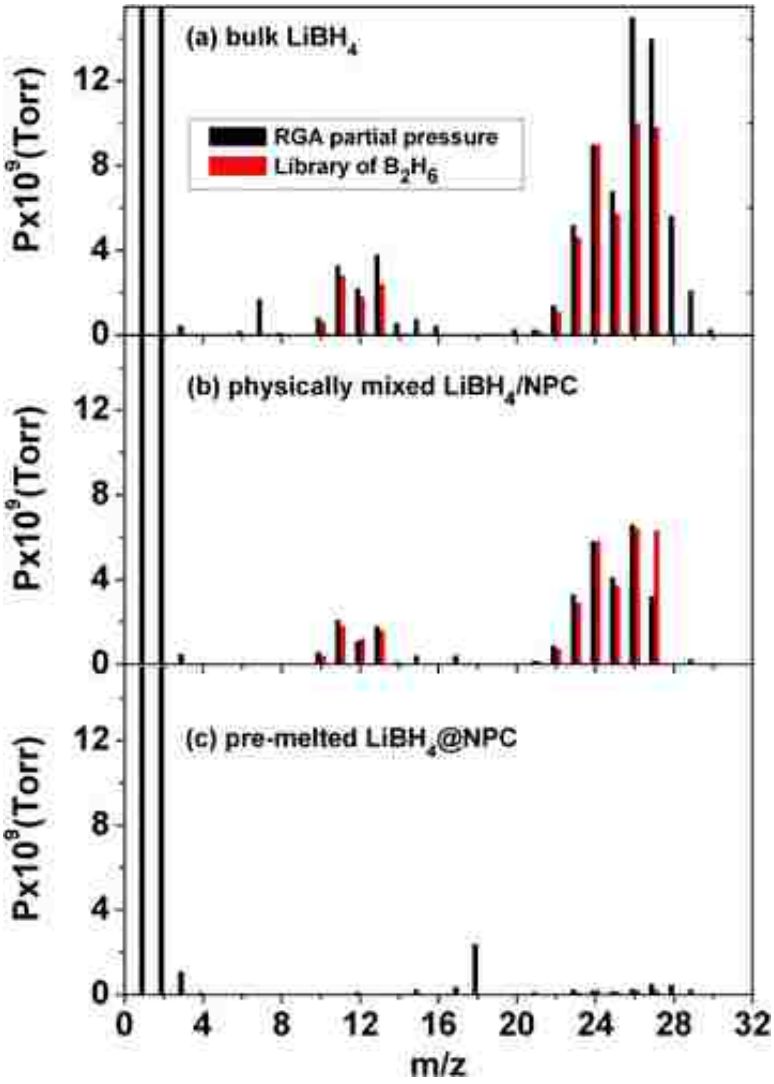

Figure 11. Mass spectra for the decomposition of (a) bulk $LiBH_4$, (b) physically mixed $LiBH_4$/NPC, and (c) premelted $LiBH_4$@NPC. B_2H_6 release data of bulk $LiBH_4$, the physical mixture of $LiBH_4$/NPC, and the premelted $LiBH_4$@NPC were taken at 410, 325, and 382 °C, respectively. The mass spectra cracking pattern of B_2H_6 (*right bars*) was taken from the NIST Chemistry Webbook [19].

The interaction between the infiltrated $LiBH_4$ and the carbon surface, including surface chemistry and structure due to template precursor materials, firing temperatures, and other preparation parameters, plays an important role in our experimental results, and is unfortunately difficult to distinguish from the size effect alone. It would be very difficult to prepare isolated 2 nm $LiBH_4$ particles for comparison without using

templates, due to the sensitivity of $LiBH_4$ to residual water and oxygen, and also particle aggregation. Conventional ball milling, for example, only produces 100-200 nm particles of hydrides and these are usually composite particles with a grain size in the micrometer range. A theoretical understanding of our experimental results will require first-principles calculations of reaction pathways for carbon-supported nanoparticle $LiBH_4$, requiring specifically the energetics of $LiBH_4$ and the decomposition products in contact with either graphene or a more suitable model of the carbon framework.

Conclusion

Highly ordered nanoporous carbon templates with cylindrical pores, with an average pore size of 2.0 nm, templated from amphiphilic triblock copolymers were employed to confine nanoscale $LiBH_4$, resulting in a loss of long-range structural order. Neither the structure transition nor melting point was observed in DSC measurements of the premelted sample of $LiBH_4$@NPC due to its amorphous structure. The hydrogen desorption of $LiBH_4$ is enhanced by incorporation into the framework in agreement with previous studies. The onset desorption temperature of premelted $LiBH_4$@NPC was significantly reduced from 460 to 220 °C. More importantly mass spectra studies of the desorbed gases indicate B_2H_6 is produced in the decomposition of bulk $LiBH_4$ and physical mixtures of $LiBH_4$/NPC but not in premelted samples of $LiBH_4$@NPC. These results indicate the nanoframework alters the decomposition pathway and eliminates the formation of B_2H_6.

Acknowledgment.

This work was funded by the U.S. Department of Energy in the Hydrogen, Fuel Cells, and Infrastructure Technologies Program through the office of Energy Efficiency and Renewable Energy. We are grateful to Dr. David Osborn and Dr. Dan Zhou for assistance with both TEM and SAXS measurements. The authors also thank Dr. Mark Allendorf and Dr. Raghu Bhakta at Sandia National Laboratories for useful discussions and pore size measurements on similarly prepared carbons.

References and Notes

[1] Schlapbach, L.; Zuttel, A. Nature 2001, 414, 353.

[2] Yang, J.; Sudik, A.; Wolverton, C. J. Phys. Chem. C 2007, 111, 19134.

[3] Kostka, J.; Lohstroh, W.; Fichtner, M.; Hahn, H. J. Phys. Chem. C 2007, 111, 14026.

[4] Orimo, S.; Nakamori, Y.; Kitahara, G.; Miwa, K.; Ohba, N.; Towata, S.; Zuttel, A. J. Alloys Compd. 2005, 404-406, 427.

[5] Au, M.; Jurgensen, A. J. Phys. Chem. B 2006, 110, 7062.

[6] Miwa, K.; Ohba, N.; Towata, S.; Nakamori, Y.; Orimo, S. J. Alloys Compd. 2005, 404-406, 140.

[7] Vajo, J. J.; Skeith, S. L.; Mertens, F. J. Phys. Chem. B 2005, 109, 3719.

[8] Mauron, P.; Buchter, F.; Friedrichs, O.; Remhof, A.; Bielmann, M.; Zwicky, C. N.; Zuttel, A. J. Phys. Chem. B 2008, 112, 906.

[9] Zhang, S.; Gross, A. F.; Van Atta, S. L.; Lopez, M.; Liu, P.; Ahn, C. C.; Vajo, J. J.; Jensen, C. M. Nanotechnology 2009, 20, 204027.

[10] Gutowska, A.; Li, L.; Shin, Y.; Wang, C. M.; Li, X. S.; Linehan, G. C.; Smith, R. S.; Kay, B. D.; Schmid, B.; Shaw, W.; Gutowski, M.; Autrey, T. Angew. Chem. 2005, 117, 3644.

[11] Wu, H.; Zhou, W.; Wang, K.; Udovic, T. J.; Rush, J. J.; Yildirim, T.; Bendersky, L. A.; Gross, A. F.; Van Atta, S. L.; Vajo, J. J.; Pinkerton, F. E.; Meyer, M. S. Nanotechnology 2009, 20, 204002.

[12] Fichtner, M. Nanotechnology 2009, 20, 204009.

[13] Wagemans, R. W. P.; van Lenthe, J. H.; de Jongh, P. E.; Jos van Dillen, A.; de Jong, K. P. J. Am. Chem. Soc. 2005, 127, 16675.

[14] Balde, C. P.; Hereijgers, B. P. C.; Bitter, J. H.; de Jong, K. P. J. Am. Chem. Soc. 2008, 130, 6761.

[15] Zhang, Y.; Zhang, W. S.; Wang, A. Q.; Sun, L. X.; Fan, M. Q.; Chu, H. L.; Sun, J. C.; Zhang, T. Int. J. Hydrogen Energy 2007, 32, 3976.

[16] Gross, A. F.; Vajo, J. J.; Van Atta, S. L.; Olson, G. L.; Skeith, S. L.; Mertens, F. J. Phys. Chem. C 2008, 112, 5651.

[17] Cahen, S.; Eymery, J. B.; Janot, R.; Tarascon, J. M. J. Power Sources 2009, 189, 902.

[18] Meng, Y.; Gu, D.; Zhang, F.; Shi, Y.; Cheng, L.; Feng, D.; Wu, Z.; Chen, Z.; Wan, Y.; Stein, A.; Zhao, D. Chem. Mater. 2006, 18, 4447.

[19] Seehttp://webbook.nist.gov/chemistry.

[20] Adelhelm, P.; Gao, J.; Verkuijlen, M. H. W.; Rongeat, C.; Herrich, M.; van Bentum, P. J. M.; Gutfleisch, O.; Kentgens, A. P. M.; deJong, K. P.; de Jongh, P. E. Chem. Mater. 2010, 22, 2233.

[21] Parmentier, J.; Saadhallah, S.; Reda, M.; Gibot, P.; Roux, M.; Vidal, L.; Vix-Guterl, C.; Patarin, J. J. Phys. Solids 2004, 65, 139.

III. Systematic Pore-Size Effects of Nanoconfinement of $LiBH_4$: Elimination of Diborane Release and Tunable Behavior for Hydrogen Storage Applications

Xiangfeng Liu[†], David Peaslee[†], Christopher Z. Jost[†], Theodore F. Baumann[‡], and Eric H. Majzoub[*,†]

[†]*Center for Nanoscience and Department of Physics and Astronomy, University of Missouri-St. Louis, One University Boulevard, St. Louis, Missouri 63121, United States*

[‡]*Lawrence Livermore National Laboratory, Livermore, California, United States*

First published in the *Chemistry of Materials* (February 2011)

ABSTRACT

The effects of nanoconfinement on the structural phase transition, H_2 release and uptake, and the emission of toxic diborane (B_2H_6) on desorption of $LiBH_4$ have been comprehensively investigated in the presence of various porous hard carbon templates at a variety of pore sizes. Calorimetry signatures of both the structural phase transition and melting of nanoconfined $LiBH_4$ shifted to a lower temperature with respect to the bulk, finally vanishing below a pore size around 4 nm. The desorption of $LiBH_4$ confined in these nanoporous carbons shows a systematic and monotonic decrease in the desorption temperature and concomitantly, mass spectroscopic analysis indicated a gradual reduction of the partial pressure of B_2H_6 with decreasing pore size, suggesting that formation of stable closoborane salts may be avoided by interrupting the reaction pathway. This represents a major breakthrough in the reversibility of boron-based hydrogen storage systems, where capacity is lost in the formation of stable B-H species on cycling. Different carbon preparation techniques suggest that the confinement size, and not solely surface interactions, may be used to tune the properties of complex hydrides for kinetic and reaction pathway improvements for hydrogen storage applications.

INTRODUCTION

Hydrogen storage is one of the key technical barriers to the widespread commercialization of hydrogen-fueled vehicles [1, 2]. Among the current hydrogen storage technologies [3-5], complex metal hydrides have received wide attention due to their high gravimetric H_2 capacity.[6]. Bulk lithium borohydride ($LiBH_4$) has a gravimetric capacity of 18.5 wt %, but its poor hydrogen release/uptake kinetics and impractical reversibility conditions restrict its application as hydrogen storage medium. $LiBH_4$ decomposes at around 500 °C and the dehydrided products can be rehydrided at 350 bar H_2 and 600 °C [7]. In addition, the evolution of diborane (B_2H_6) accompanying H_2 release during the decomposition of $LiBH_4$ results in capacity loss on each cycle, and is also a safety concern [8-11]. A few approaches have been applied to improve the dehydrogenation kinetics and the reversibility of $LiBH_4$ such as the addition of catalysts or destabilizers [12-16]. Vajo et al. found the addition of MgH_2 to $LiBH_4$ lowered the hydrogenation/dehydrogenation enthalpy by 25 kJ/(mol of H_2) compared with pure $LiBH_4$ and improved the reversibility [12]. However, this destabilization strategy relies on the formation of the very stable compound MgB_2 on decomposition, limiting reversibility to high temperatures. Yang et al. studied the destabilization of $LiBH_4$ by adding metals (Mg, Al, Ti, V, Cr, or Sc) or metal hydrides like MgH_2, TiH_2, or CaH_2 [13]. Au et al. improved the reversibility of $LiBH_4$ by ball milling with some transition metal oxides or chlorides and moderated the rehydrogenation conditions to 873 K and 7 MPa [14]. But the rehydrogenation temperature is still too high for practical applications. The formation of diborane during the decomposition of the composite systems remains a persistent problem, and cannot be understated. One of the largest obstacles to the use of boron-based hydrogen storage systems is the formation of stable "sinks" of, for example, closoborane $[B_{10}H_{10}]^{2-}$ and $[B_{12}H_{12}]^{2-}$ salts [9, 10], that decrease capacity as boron is lost to these compounds on each cycle. Hwang et al. confirmed the presence of intermediate $Li_2B_{12}H_{12}$ on the decomposition of $LiBH_4$ by ^{11}B NMR [9]. A more recent study showed that $Li_2B_{12}H_{12}$ and possibly $Li_2B_{10}H_{10}$ resulted from the reaction of the released B_2H_6 with the remaining $LiBH_4$ on decomposition [17]. We show below that the intermediates needed for the formation of the closoboranes are not

produced if the confinement size is small enough, representing a breakthrough in the utilization of boron-based hydrogen storage systems.

Recently, nanoconfinement of hydrides has proven beneficial in hydrogen storage materials and may provide new insights and solutions to current hydrogen storage technology [18-22], Theoretical calculations and preliminary experiments show that nanosized metal hydrides have significantly different thermodynamic and kinetic properties with respect to their bulk counterparts. First-principles density functional theory (DFT) calculations indicate the H_2 desorption enthalpy for MgH_2 may be substantially decreased when the particle size becomes very small (≈1.3 nm) [23]. Paskevicius et al. investigated the thermodynamic properties of magnesium hydride nanoparticles (≈7 nm in size) and found only a small decrease in the decomposition reaction enthalpy of about 3 kJ/mol H_2 [24]. However, the complex hydride $NaAlH_4$ embedded in microporous carbon fiber shows a dramatic change in the resulting pressure−composition−isotherm suggesting large changes in thermodynamic properties and perhaps the reaction pathway [25]. Gao et al. also reported that the confinement of $NaAlH_4$ in porous carbons with 2−3 nm pores improved both the kinetics and thermodynamics of hydrogen sorption [26].

The improved kinetics and perhaps thermodynamics of nanoconfined hydrides have attracted increasing interest in improving the properties of $LiBH_4$ [27-30]. Vajo and co-workers enhanced the dehydrogenation kinetics and reversibility through infiltrating $LiBH_4$ into carbon aerogels (CA). The reported desorption rate at 300 °C of $LiBH_4$ confined in the CA host was 50 times faster than bulk and the dehydrided sample was rehydrided at 100 bar H_2 and 400 °C [27]. More recently, Jensen's group reported the hydrogen storage properties of nanoconfined MgH_2 and $LiBH_4/MgH_2$ in carbon aerogels (D_{max}≈ 21 nm) [31]. These nanoconfined systems showed significantly enhanced desorption kinetics and possibly improved thermodynamic properties. In a recent publication, our group reported the decomposition properties of nanoconfined $LiBH_4$ in highly ordered hexagonally packed cylindrical nanoporous carbon (NPC) with an average pore size of 2.0 nm and a very narrow size distribution [32]. The nanoconfined $LiBH_4$ in such small pores resulted in the disappearance of the low temperature structural phase transition, the melting transition, and also the significant decrease of the onset desorption

temperature from 460 to 220 °C with respect to bulk $LiBH_4$. Most importantly, diborane release of $LiBH_4$ confined in the highly ordered nanoporous carbon was suppressed or eliminated in the decomposition indicating a changed decomposition pathway. However, the studies above lack a direct set of systematic measurements of these properties on pore, and ultimately, particle size of the hydride. In this report, we present a comprehensive study of the effects of nanoconfinement size on the calorimetry, diborane emission and reversibility of $LiBH_4$ through a series of experiments on both CAs and highly ordered nanoporous carbons with a pore size distribution from 2 to 15 nm.

EXPERIMENTAL SECTION

Highly ordered porous carbons were prepared according to a well-established method [33]. The preparation conditions of NPC-2 nm also can be found in an earlier publication [32]. The preparation method of NPC-4 nm was similar to NPC-2 nm except that NPC-4 nm was calcinated at 600 °C under a flowing O_2/N_2 (O_2: 2.5 vol %). NPC-L represents the NPC with lower surface area. The preparation of NPC-L is similar to NPC-2 nm except that it was not crushed to powders before calcination. The CAs used in this study were prepared through carbonization of organic aerogels derived from resorcinol and formaldehyde. Resorcinol (99%), formaldehyde (37% in water) and sodium carbonate monohydrate reagents were purchased from Aldrich Chemical Co. and used without further purification. For the synthesis of the CA with 9 nm pores, resorcinol (12.35 g, 112 mmol) and 37% formaldehyde solution (17.9 g, 224 mmol) were dissolved in distilled water (32 mL), followed by the addition of sodium carbonate monohydrate (0.069 g, 0.55 mmol). The same reactant ratio was employed for the synthesis of the CA scaffold with 15 nm pores with the exception that a larger volume of distilled water (62 mL) was used in the reaction. These reaction mixtures were then transferred to cylindrical glass molds and cured at 80 °C for 72 h. The resultant organic hydrogels were washed with acetone to remove the water from the pores of the gel and then dried with supercritical CO_2 (T_c = 31.1 °C, P_c = 7.4 MPa). The organic aerogels were subsequently carbonized at 1050 °C (ramp rate: 2 °C/min) for 3 h under an N_2 atmosphere, affording the CAs as black cylindrical monoliths. The porous carbon templates were first dried at

900 °C for 5 h under flowing Ar and then dried at 400 °C under vacuum. Subsequently, the dried carbons were impregnated with $LiBH_4$ by a melting method. In a typical process, a 200 mg mixture of $LiBH_4$ (95%, Aldrich) and carbon template was loaded into a sample holder in an argon-filled glovebox. The sample holder was subsequently attached to a fixed-volume Sievert's-type instrument without exposing the sample to air. The sample holder was heated to 300 °C under about 60 bar H_2 then kept at this temperature for 30 min. These premelted samples are hereafter referred to as $LiBH_4$@CA-x or $LiBH_4$@NPC-x (x: the values at the pore size distribution peaks.).

Textural properties of carbon aerogels were determined using N_2 adsorption−desorption techniques (ASAP 2010 Surface Area Analyzer, Micromeritics). Brunauer−Emmett−Teller (BET) and Barrett−Joyner−Halenda (BJH) methods were used to calculate surface areas and pore size distributions using desorption data, respectively. An SA3100 analyzer (Coulter) was used to measure nitrogen adsorption isotherms for NPC carbons at 77 K. Before analysis, the sample of porous carbon was outgassed for 1 h at 300 °C under a vacuum. The BET method was used to calculate the specific surface areas (S_{BET}) using adsorption data in a relative pressure range from 0.05 to 0.2 bar. The total pore volume was estimated from the adsorbed amount at a relative pressure P/P_0 of 0.98 based on the BJH model. The morphology of the nanoporous carbon was investigated using a Philips EM430 high-resolution transmission electron microscopy (TEM). The powder was supported on the copper grid coated by a carbon film. X-ray diffraction (XRD) was performed on a Rigaku Ultima IV multipurpose X-ray diffraction (XRD) system with CuK_a radiation source. Samples containing hydrides were covered with parafilms to prevent the samples from contacting air or moisture during the XRD experiments. FT-IR spectra were collected using Nicolet 6700. Two KBr polished discs were used to hold the powered samples. Differential scanning calorimetry (DSC) analysis was performed on a TQ2000 series analyzer (TA Instruments). About 4 mg of sample was loaded in a Tzero pan in an argon-filled glovebox and crimped with a Tzero lid. The sample was heated to 550 °C at a ramping rate of 10 °C/min under a N_2 flowing rate of 50 mL/min. Thermogravimetric analysis (TGA) was performed on a TGAQ500 Series thermogravimetric analyzer (TA Instruments). In a typical TGA procedure, about 10 mg of sample was loaded in a Tzero pan and crimped with a Tzero hermetic lid in an argon-

filled glovebox. A hermetic lid was selected to reduce contamination and a pinhole was made on the top of the lid for the purpose of H_2 release. The sample was heated to 550 °C at a ramping rate of 10 °C/min under a N_2 flowing rate of 100 mL/min. Mass spectroscopic analysis was performed using an SRS RGA200 residual gas analyzer (RGA) and a high temperature sample stage. The system is separated into a HV (1×10^{-8} to 1×10^{-5} Torr) sample chamber and UHV (1×10^{-9} to 1×10^{-7} Torr) gas analysis chamber. The species partial pressure per gram of $LiBH_4$ was used for comparisons. The details of the measurement can be found in an earlier publication [32].

RESULTS AND DISCUSSION

TEM was used to characterize the pore structure. Figure 1 shows TEM images of columnar pores packed in a hexagonal geometry for NPC-4 nm (a, b) and NPC-L (c, d) viewed from the directions parallel (a, c) and perpendicular (b, d) to the pore channels. From TEM images, we can clearly see the highly ordered hexagonally packed pores viewed from the direction parallel to the pore channels [001] and stripe-like patterns viewed from the direction perpendicular to the pore channels [110], respectively, in good agreement with the previously reported pore morphology [32, 33].

Figure 2 shows the pore size distributions of CA-15 nm, CA-9 nm and NPC-4 nm. The pore size of 15, 9, and 4 nm correspond to the values at the pore size distribution peaks. The two carbon aerogels both have a slightly wider pore size distribution in comparison with the ordered porous carbon. The surface area and the total pore volumes are summarized in Table 1.

Table 1. Surface Areas and the Total Pore Volumes of Different Carbon Templates

samples	CA-15 nm	CA-9 nm	NPC-4 nm	NPC-2 nm	NPC-L
BET surface area (m^2/g)	652	706	730	594	241
total pore volume (cm^3/g)	2.3	1.5	0.53	0.35	0.13

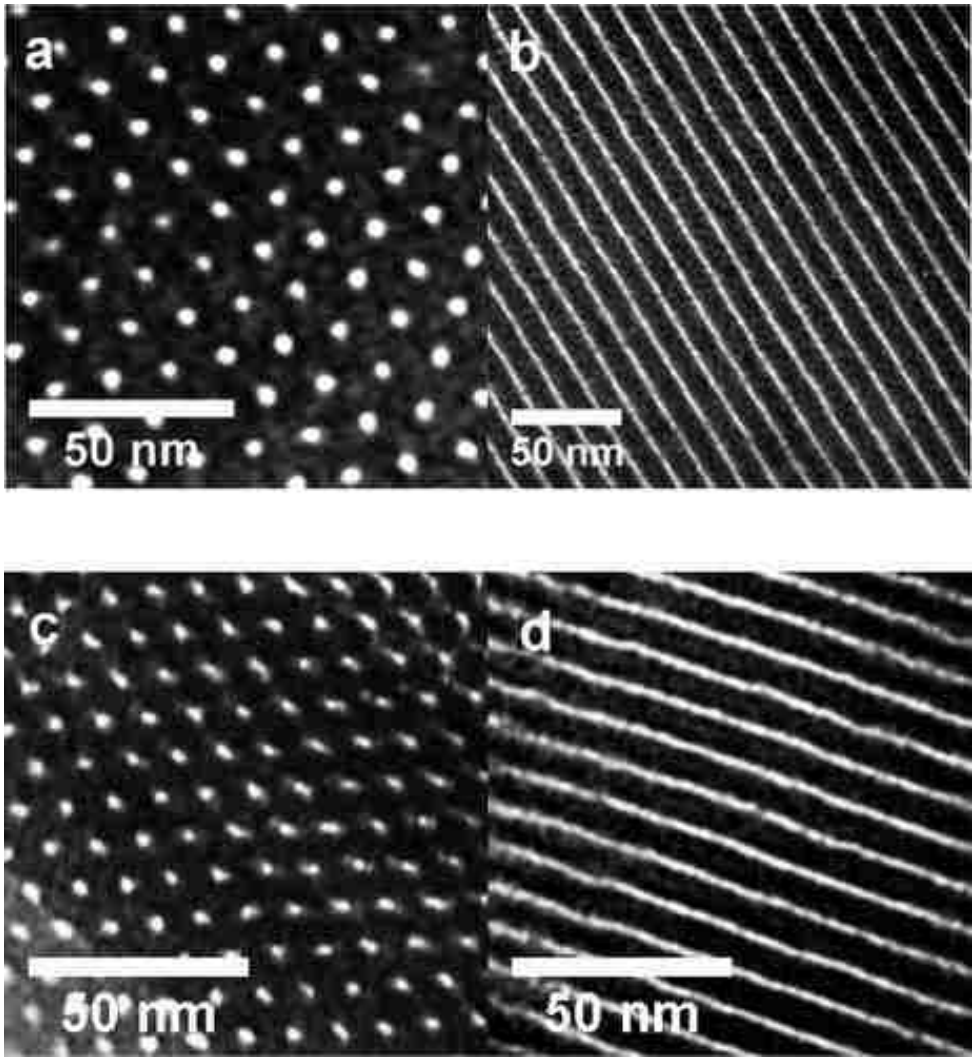

Figure 1. TEM images of columnar pores packed in a hexagonal geometry for (a, b) NPC-4 nm and (c, d) NPC-L viewed from the directions parallel (a, c) and perpendicular (b, d) to the pore channels.

The specific surface areas (S_{BET}) of NPC-4 nm based on the BET method and the total pore volume calculated by the BJH model were 730 m^2/g and 0.53 cm^3/g, respectively. S_{BET} and the total pore volume of $LiBH_4$@NPC-4 nm were reduced to 292 m^2/g and 0.23 cm^3/g, respectively, indicating the filling or blocking of the pores by $LiBH_4$ (see Figure S1 in the Supporting Information).

In an earlier publication we have shown that $LiBH_4$ confined in NPC-2 nm is amorphous and shows no Bragg peaks of $LiBH_4$ [32]. Similarly, the XRD pattern of the

premelted $LiBH_4$@NPC-4 nm also does not show Bragg peaks of $LiBH_4$, indicating the hydride became amorphous after melt-infiltration in the 4 nm nanopores (see Figure S2 in the Supporting Information). In contrast, the XRD pattern of $LiBH_4$@CA-9 nm shows peaks indicating the existence of crystalline $LiBH_4$. However, the confinement of the hydride in 9 nm pores still results in broad and diffuse Bragg peaks. Fourier transform infrared spectroscopy was further used to confirm the existence of $[BH_4^-]$ in the infiltrated sample of $LiBH_4$@NPC-4 nm. The spectra indicate B−H bending modes at 1100 cm^{-1} and stretching modes around 2200−2300 cm^{-1} of $[BH_4^-]$ (see Figure S3 in the Supporting Information).

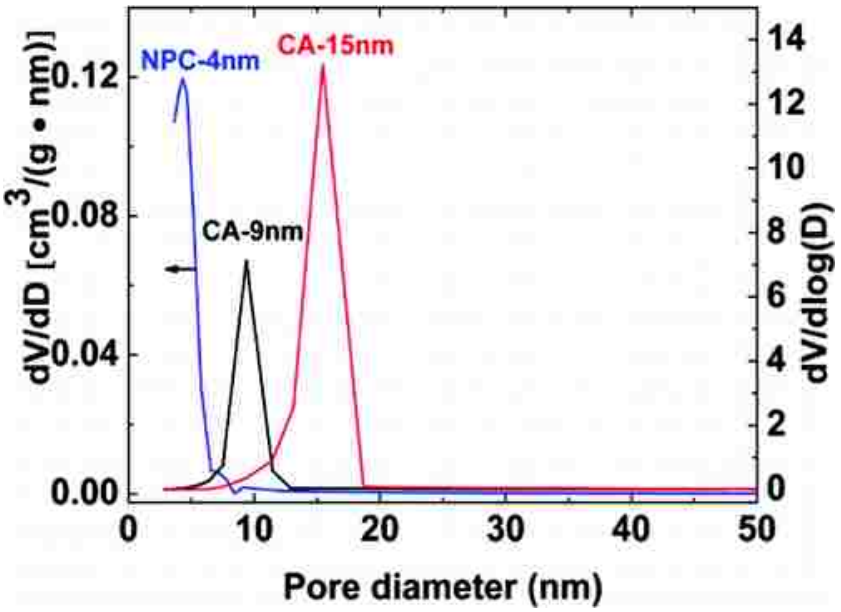

Figure 2. Pore-size distributions of NPC-4 nm, CA-9 nm, and CA-15 nm. Pore-size distributions of carbon aerogels were analyzed by ASAP 2010 surface area analyzer (Micromeritics) based on the desorption data. Pore-size distribution of NPC was analyzed by SA3100 analyzer (Coulter) based on adsorption isotherms.

DSC plots of bulk $LiBH_4$ and nanoconfined $LiBH_4$@NPC or $LiBH_4$@CA are shown in Figure 3. The DSC plot of bulk $LiBH_4$ shows the orthorhombic to hexagonal structure transition at a temperature of about 115 °C, melting at 284 °C and a decomposition peak around 495 °C. Both the structural phase transition and the melting

transition of the nanoconfined $LiBH_4$ in carbon aerogels (CA-9 nm and CA-15 nm) still appeared but the transition peaks became broader and shifted to a lower temperature with decreasing pore size. The DSC trace of the structural phase transition is broader in bulk $LiBH_4$ than in infiltrated samples. (If we assume the phase transition proceeds by a nucleation and growth process, and if the nucleation is heterogeneous and more likely to occur on the large surface area of the templates, it would take a shorter time to complete the phase transition in the infiltrated samples, in agreement with the experimental results.) The appearance of the structural phase transition and the melting transition indicates the existence of crystalline $LiBH_4$ in agreement with XRD analysis. The broadness and temperature shift of the transition peaks is attributed to the decreasing coherence length within the incorporated material from nanoconfinement effects. In contrast, neither the structural transition or melting peak appeared in $LiBH_4$@NPC (2 or 4 nm) indicating $LiBH_4$ confined in the ordered NPC becomes amorphous as indicated in XRD analysis. We note that two small broad endothermic peaks appeared at about 80 and 200 °C when the loading of $LiBH_4$ in NPC-4 nm was increased to 20 wt %, where about 70% of the pore volume was filled, and may be due to incomplete infiltration of the $LiBH_4$ into the pores (see Figure 5 below).

Figure 4 shows the temperature of maximum hydrogen release rate, as determined from both TGA and DSC measurements, versus pore size. In comparison with the bulk $LiBH_4$ the dehydrogenation temperature of $LiBH_4$ confined in the carbon templates tends to decrease more with the decrease of the pore size. Note that the dehydrogenation temperature does not decrease linearly with the decreasing pore size; there is a sharp decrease in desorption temperature when the pore size is reduced from 9 to 4 nm, which may be attributed to the fact that $LiBH_4$ confined in 4 nm templates becomes amorphous.

Thermogravimetric analysis (TGA) was further used to study the dehydrogenation behaviors of the samples and is shown in the Supporting Information. Figure S4a shows the thermogravimetric and the corresponding DSC plots of $LiBH_4$@NPC-4 nm, which starts to decompose below the melting point. The fastest dehydrogenation appeared around 342 °C in agreement with the endothermic peak in DSC. Figure S4b compares the thermogravimetric plots of $LiBH_4$@NPC-4 nm and $LiBH_4$@CA-9 nm, indicating $LiBH_4$@NPC-4 nm has a lower dehydrogenation temperature.

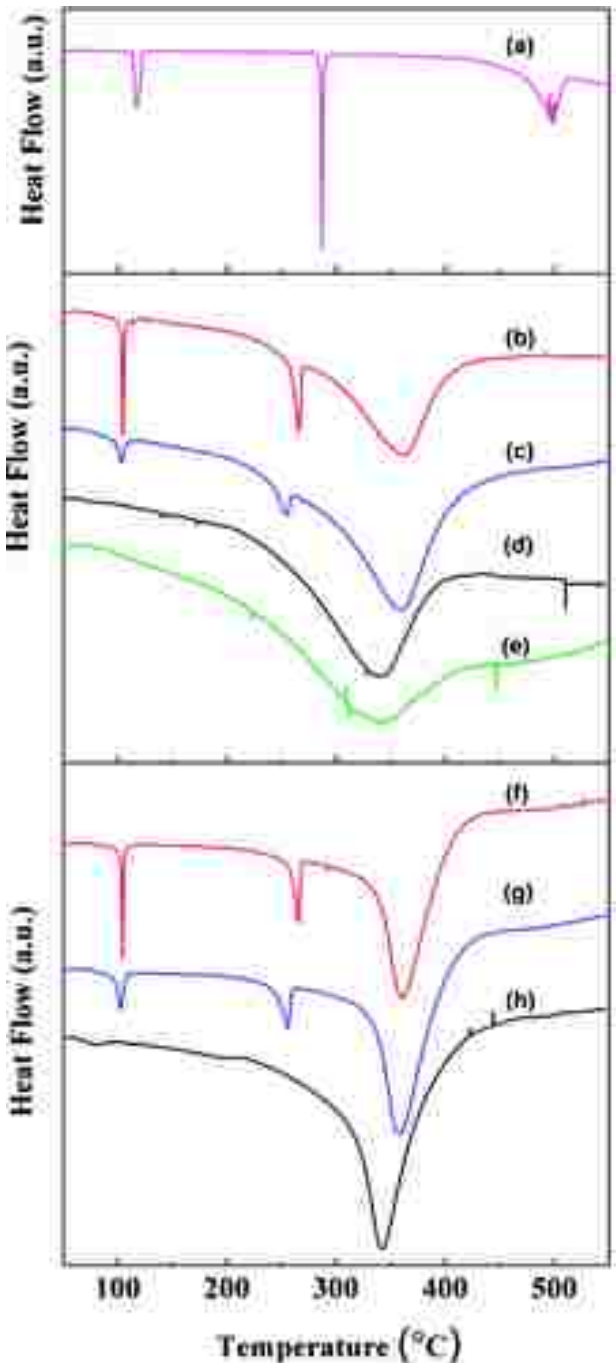

Figure 3. DSC plots of bulk $LiBH_4$ and nanoconfined $LiBH_4$@NPC or $LiBH_4$@CA: (a) bulk $LiBH_4$; (b) $LiBH_4$@CA-15 nm with a loading of 10 wt %; (c) $LiBH_4$@CA-9 nm with a loading of 10 wt %; (d) $LiBH_4$@NPC-4 nm with a loading of 10 wt %; (e) $LiBH_4$@NPC-2 nm with a loading of 10 wt %; (f) $LiBH_4$@CA-15 nm with a loading of 20 wt %; (g) $LiBH_4$@CA-9 nm with a loading of 20 wt %; (h) $LiBH_4$@NPC-4 nm with a loading of 20 wt %.

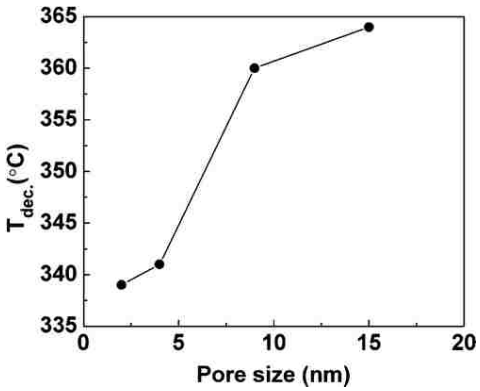

Figure 4. Pore-size dependence of dehydrogenation temperature of nanoconfined $LiBH_4$ in different carbon templates with a loading of 10 wt %. The lines connecting the points are only a guide for the eye.

The extent to which the pore volume can be filled while retaining the benefits of confinement was studied by varying the filling factor of $LiBH_4$ in the pores. We denote by Q the filling factor of the pores with $LiBH_4$, with Q = 100% corresponding to a maximum loading of 26 wt % (for $LiBH_4$@NPC-4 nm), based on the pore volume and density of crystalline orthorhombic $LiBH_4$. Figure 5 shows the DSC plots of $LiBH_4$@NPC-4 nm with different Q. When the content of $LiBH_4$ in NPC was 10 wt % (Q = 31%) no structural transition or melting transition appeared. When the loading was increased to 30 wt % (Q = 120%), and the template was significantly overfilled, both the structural, and melting transition appeared, indicating lack of available pore space. At Q = 70%, small endothermic signatures are present, indicating that some $LiBH_4$ may be exterior to the pores, and may represent the practical limit of pore loading in this NPC.

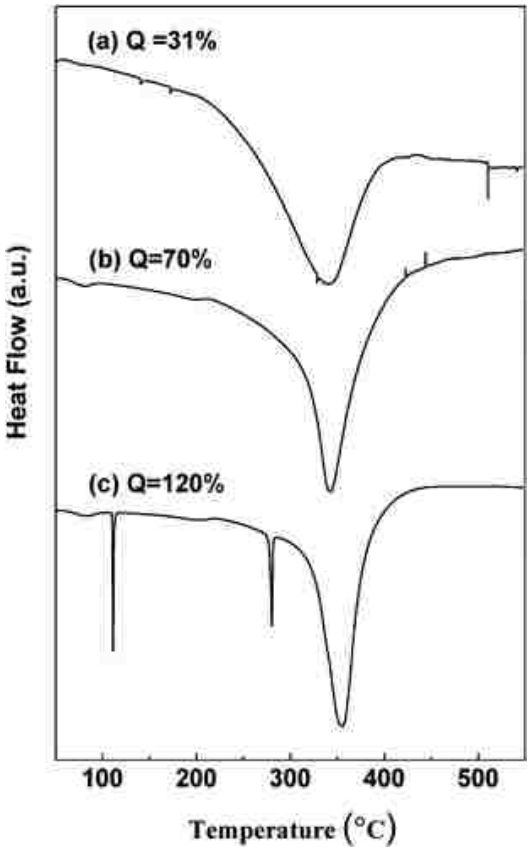

Figure 5. Comparisons of DSC plots for $LiBH_4$@NPC-4 nm with different filling degree. Q represents the filling degree of the pore by $LiBH_4$. $Q = V_{hydride}/V_{total}$ ($V_{hydride}$ and V_{total} represent the volume of hydrides and total pore volume, respectively).

Nanoconfinement is thought to improve the reversibility of hydrides due to limitation of the diffusion of the decomposing species [19]. Although bulk $LiBH_4$ can be rehydrided at 350 bar H_2 and 600 °C [7], nanoconfined $LiBH_4$ in carbon aerogels with a pore size of 13 and 25 nm can be rehydrided at significantly lower temperatures and pressures of 100 bar H_2 and 400 °C [27]. As discussed in the section below, $LiBH_4$@NPC-4 nm desorbs and also absorbs under moderate conditions below the melting point.

Figure 6 shows the hydrogen desorption curves of $LiBH_4$@NPC-4 nm. The measurements were performed using a fixed-volume Sieverts-type apparatus. We performed a series of absorption/desorption cycles at different temperatures to demonstrate that the incorporated $LiBH_4$ may be rehydrided at temperatures lower than

400 °C. All desorptions were performed at 350 °C into an initial static vacuum of 1×10^{-5} bar. Prior to each desorption, the sample was cooled to room temperature. The following sequence was performed: (1) Initial desorption at 350 °C. (2) Rehydriding at 350 °C and 60 bar H_2. (3) Second desorption at 350 °C. (4) Rehydriding at 300 °C and 60 bar H_2. (5) Third desorption at 350 °C. (6) Rehydriding at 250 °C and 60 bar H_2. (7) Fourth desorption at 350 °C. (8) Rehydriding at 350 °C and cooled to RT under 60 bar H_2. (8) Fifth desorption at 350 °C. (9) Rehydriding at 350 °C and 60 bar H_2. (10) Sixth desorption at 350 °C. As shown in Figure 6, the H_2 capacity of the sample decreased gradually with increasing cycles, and is attributed to two causes. Clearly, the lower rehydriding temperatures reduces the rate at which the sample can absorb hydrogen due to slower kinetics, and therefore the capacity fades with increasing cycling numbers. Additional capacity loss is perhaps due to sequestration of boron to the framework or simple segregation of boron. It is evident in desorption cycles 5 and 6, that upon returning to higher temperatures, the sample regains some of the capacity loss. These results indicate that the reversibility of $LiBH_4$ is kinetically inhibited at lower temperatures, and that the equilibrium hydrogen overpressure at 250 °C is still below 60 bar. Perhaps most importantly, the results demonstrate that nanoconfined $LiBH_4$ in highly ordered nanoporous carbon (NPC-4 nm) can be rehydrided at significantly improved conditions of 250 °C (below the melting point of bulk sample) and 60 bar H_2.

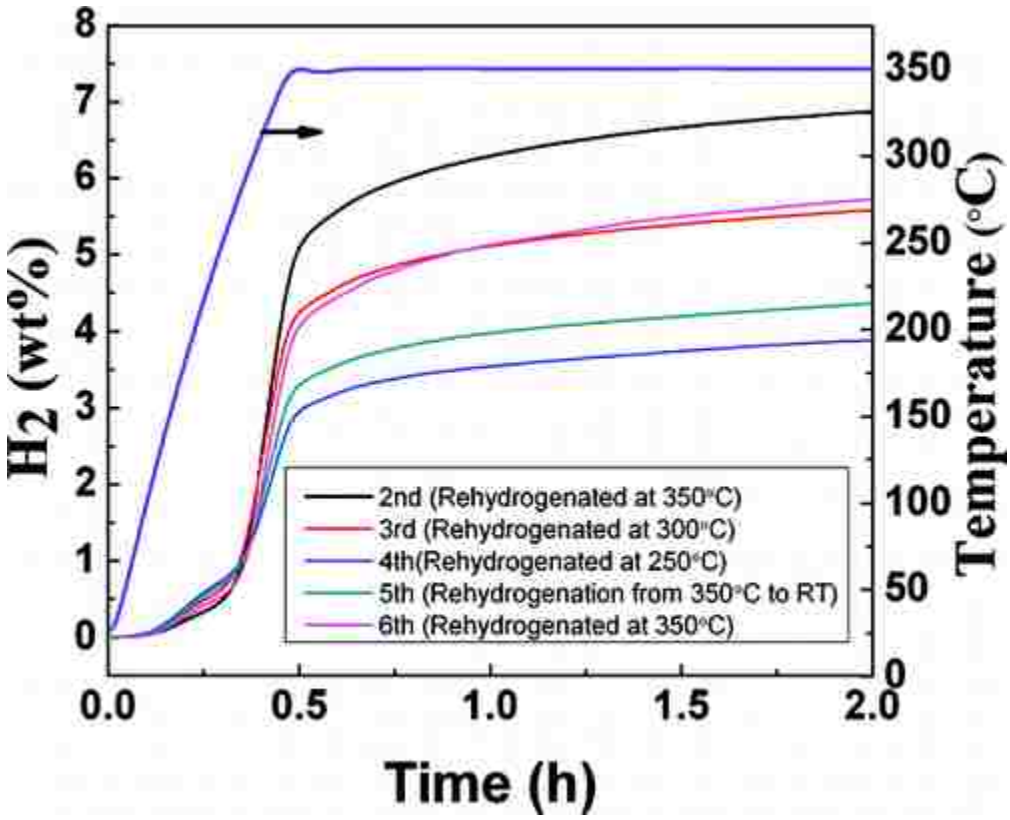

Figure 6. Desorption curves of nanoconfined $LiBH_4$@NPC-4 nm with an initial loading of 20 wt % (Q = 70%) (*order of curves at 2 hours: 2nd, 6th, 3rd, 5th, 4th*).

Finally, we address the critical issue surrounding the formation of diborane and higher borane species in the decomposition of nanoconfined $LiBH_4$. The H_2 and B_2H_6 release, per gram of infiltrated $LiBH_4$, on decomposition in different carbon templates was analyzed using a direct line-of-site residual gas analyzer mass spectrometer (RGA-MS). Figure 7 compares the B_2H_6 release and H_2 release of $LiBH_4$@CA-15 nm, $LiBH_4$@CA-9 nm and $LiBH_4$@NPC-4 nm. As indicated in the figure, more B_2H_6 is released from the decomposition of $LiBH_4$@CA-15 nm than $LiBH_4$@CA-9 nm and $LiBH_4$@NPC-4 nm. The decomposition of $LiBH_4$@NPC-4 nm shows only small release of B_2H_6. In our previous study, no measurable B_2H_6 is produced during the decomposition of $LiBH_4$@NPC-2 nm [32].

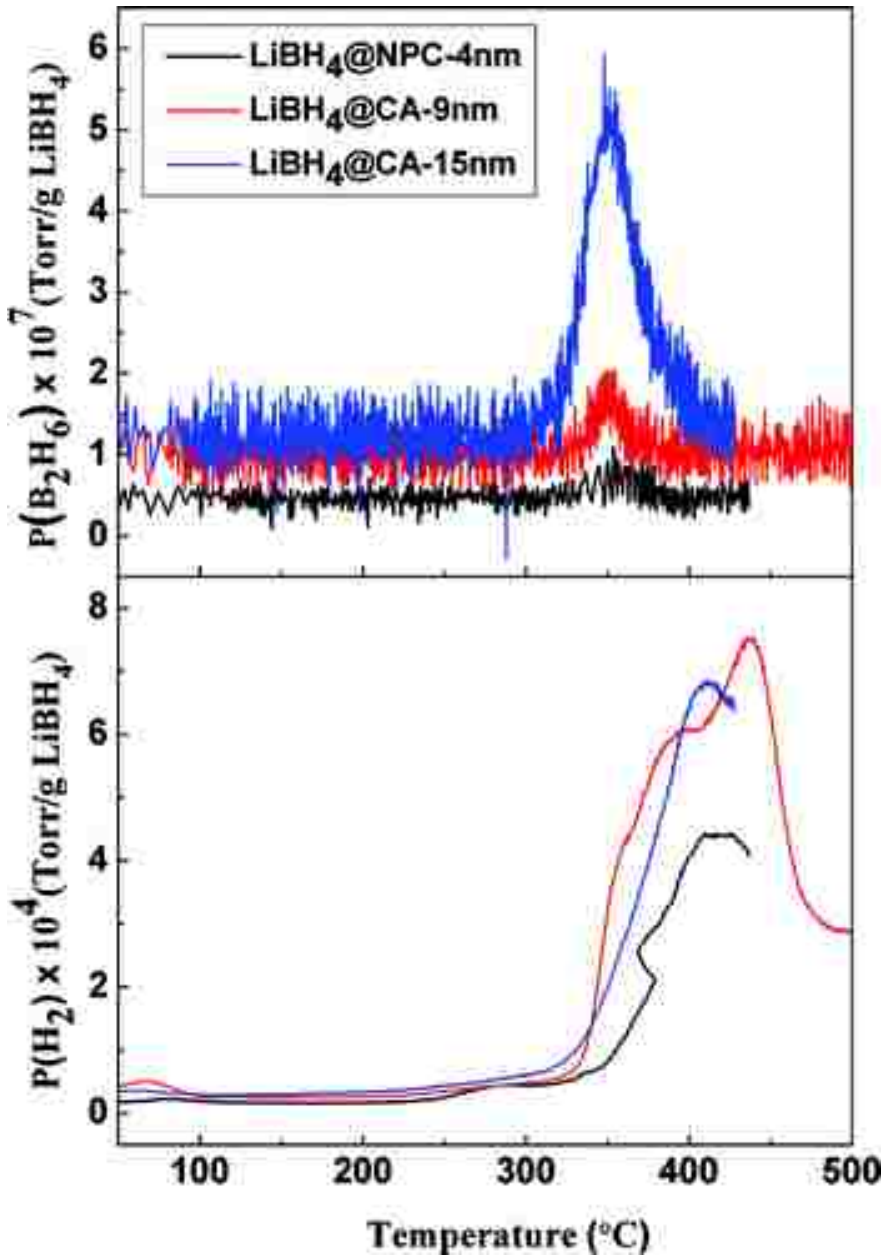

Figure 7. B_2H_6 and H_2 release with increasing temperature for $LiBH_4$@NPC-4 nm, $LiBH_4$@CA-9 nm, and $LiBH_4$@CA-15 nm. The loading of each sample is 10 wt %. (*For the first figure highest to lowest: 15 nm, 9 nm, 4 nm. For the second figure highest to lowest: 9 nm, 15 nm, 4 nm*).

Although the peak rate of desorption of diborane is lower than that of hydrogen, the onset of diborane and hydrogen desorption is very close. Once hydrogen desorption is well underway and the sample chemistry changes, the chemical concentrations and

interactions that result in early diborane formation are evidently changed enough to reduce the amount of diborane produced. The partial pressures, per gram of infiltrated hydride, indicate the amount of diborane released during the decomposition of $LiBH_4$ decreases with decreasing pore size, and nanoconfinement can suppress or eliminate the reaction path that produces B_2H_6. These results suggest that the formation of the very stable $[B_{12}H_{12}]$-based closoborane salts, which represent thermodynamic sinks and significantly reduce the capacity and reversibility of borohydride-based materials [9, 10] can be largely mitigated through the use of nanoconfinement of the hydride. It is difficult to determine the primary cause for the change in reaction pathway, but the loss of crystallinity of the $LiBH_4$ with decreasing particle size corresponds to the changes in calorimetry and the lower temperature of decomposition onset. Without knowing the energetics of the $LiBH_4$/C interaction, we speculate this might play a role in changing the reaction pathway.

CONCLUSION

The calorimetry, H_2 release and uptake behavior, and the emission of toxic B_2H_6 have been investigated in the desorption of $LiBH_4$ confined in several pore-size carbon aerogel and highly ordered nanoporous carbon templates. In contrast to the $LiBH_4$ in carbon aerogels (CA-9 nm and CA-15 nm) $LiBH_4$ confined in the highly ordered NPC (NPC-2 nm and NPC-4 nm) did not show Bragg peaks of the crystallized $LiBH_4$, the structural or melting transition, due to the smaller pore size and subsequently induced amorphization. Nanoconfined $LiBH_4$ desorbs hydrogen at a much lower temperature with respect to bulk $LiBH_4$ and the dehydrogenation temperature decreases monotonically with the reduction of pore size. The reversibility of $LiBH_4$ was demonstrated at 60 bar H_2 and 250 °C, and may be slowly reversible under even more moderate conditions. Most importantly, mass spectroscopic analysis indicates nanoconfinement can suppress or eliminate diborane release, implying that the reaction pathway leading to higher borane species by decomposing borohydrides may be controlled. This represents a major breakthrough in the reversibility of borohydrides for hydrogen storage, as the formation of very stable closoborane species, such as $B_{12}H_{12}$ salts may be interrupted, and removed

from the reaction pathway, opening the door to lightweight, reversible, boron-based hydrogen storage systems.

ACKNOWLEDGMENT.

This work was funded by the U.S. Department of Energy in the Hydrogen, Fuel Cells, and Infrastructure Technologies Program through the office Energy Efficiency and Renewable Energy under Contract DE-AC04-94AL85000. We are grateful to Dr. David Osborn and Dr. Dan Zhou for assistance with TEM measurement.

REFERENCES.

[1] Schlapbach, L.; Züttel, A. Nature 2001, 414, 353

[2] Ritter, J. A.; Ebner, A. D.; Wang, J.; Zidan, R. Mater. Today 2003, 6, 18

[3] Mandal, T. K.; Gregory, D. H. Annu. Rep. Prog. Chem., Chem., Sect. A 2009, 105, 21

[4] Graetz, J. Chem. Soc. Rev. 2009, 38, 73

[5] Chen, P.; Zhu, M. Mater. Today 2008, 12, 36

[6] Orimo, S.; Nakamori, Y.; Eliseo, J. R.; Züttel, A.; Jensen, C. M. Chem. Rev. 2007, 107, 4111

[7] Orimo, S.; Nakamori, Y.; Kitahara, G.; Miwa, K.; Ohba, N.; Towata, S.; Züttel, A. J. Alloys.Compd. 2005, 404−406, 427

[8] Kostka, J.; Lohstroh, W.; Fichtner, M.; Hahn, H. J. Phys. Chem. C 2007, 111, 14026

[9] Hwang, S. J.; Bowman, R. C., Jr.; Reiter, J. W.; Rijssenbeek, J.; Soloveichik, G. L.; Zhao, J. C.; Kabbour, H.; Ahn, C. C. J. Phys. Chem. C 2008, 112, 3164

[10] Ozolins, V.; Majzoub, E. H.; Wolverton, C. J. Am. Chem. Soc. 2009, 131, 230

[11] Au, M.; Jurgensen, A. R.; Spencer, W. A.; Anton, D. L.; Pinkerton, F. E.; Hwang, S. J.; Kim, C.; Bowman, R. C., Jr. J. Phys. Chem. C 2008, 112, 18661

[12] Vajo, J. J.; Skeith, S. L.; Mertens, F. J. Phys. Chem. B 2005, 109, 3719

[13] Yang, J.; Sudik, A.; Wolverton, C. J. Phys. Chem. C 2007, 111, 19134

[14] Au, M.; Jurgensen, A. J. Phys. Chem. B 2006, 110, 7062

[15] Mauron, P.; Buchter, F.; Friedrichs, O.; Remhof, A.; Bielmann, M.; Zwicky, C. N.; Züttel, A. J. Phys. Chem. B 2008, 112, 906

[16] Miwa, K.; Ohba, N.; Towata, S.; Nakamori, Y.; Orimo, S. J. Alloys Compd. 2005, 404- 406, 140

[17] Friedrichs, O.; Remhof, A.; Hwang, S. J.; Züttel, A. Chem. Mater. 2010, 22, 3265

[18] Zhang, S.; Gross, A. F.; Van Atta, S. L.; Lopez, M.; Liu, P.; Ahn, C. C.; Vajo, J. J.; Jensen, C. M. Nanotechnology 2009, 20, 204027

[19] Fichtner, M. Nanotechnology 2009, 20, 204009

[20] Adelhelm, P.; Gao, J.; Verkuijlen, M. H. W.; Rongeat, C.; Herrich, M.; van Bentum, P. J. M.; Gutfleisch, O.; Kentgens, A. P. M.; deJong, K. P.; de Jongh, P. E. Chem. Mater. 2010, 22, 2233

[21] Nielsen, T. K.; Manickam, K.; Hirscher, M.; Besenbacher, F.; Jensen, T. R. ACS Nano 2009, 3, 3521

[22] Gutowska, A.; Li, L.; Shin, Y.; Wang, C. M.; Li, X. S.; Linehan, G. C.; Smith, R. S.; Kay, B. D.; Schmid, B.; Shaw, W.; Gutowski, M.; Autrey, T. Angew. Chem. 2005, 117, 3644

[23] Wagemans, R. W. P.; van Lenthe, J. H.; de Jongh, P. E.; Jos van Dillen, A.; de Jong, K. P. J. Am. Chem. Soc. 2005, 127, 16675

[24] Paskevicius, M.; Sheppard, D. A.; Buckley, C. E. J. Am. Chem. Soc. 2010, 132, 5077

[25] Lohstroh, W.; Roth, A.; Hahn, H.; Fichtner, M. ChemPhysChem. 2010, 11, 789

[26] Gao, J.; Adelhelm, P.; Verkuijlen, M. H. W.; Rongeat, C.; Herrich, M.; van Bentum, P. J. M.; Gutfleisch, O.; Kentgens, A. P. M.; de Jong, K. P.; de Jongh, P. E. J. Phys. Chem. C 2010, 114, 4675

[27] Gross, A. F.; Vajo, J. J.; Van Atta, S. L.; Olson, G. L. J. Phys.Chem. C 2008, 112, 5651

[28] Ngene, P.; Adelhelm, P.; Beale, A. M.; de Jong, K. P.; de Jongh, P. E. J. Phys. Chem. C 2010, 114, 6163

[29] Cahen, S.; Eymery, J. B.; Janot, R.; Tarascon, J. M. J. Power Sources 2009, 189, 902

[30] Shane, D. T.; Corey, R. L.; McIntosh, C.; Rayhel, L. H.; Bowman, R. C., Jr.; Vajo, J. J.; Gross, A. F.; Conradi, M. S. J. Phys. Chem. C 2010, 114, 4008

[31] Nielsen, T. K.; Bösenberg, U.; Gosalawit, R.; Dornheim, M.; Cerenius, Y.; Besenbacher, F.; Jensen, T. R. ACS Nano 2010, 4, 3903

[32] Liu, X.; Peaslee, D.; Jost, C. Z.; Majzoub, E. H. J. Phys. Chem. C 2010, 114, 14036

[33] Meng, Y.; Gu, D.; Zhang, F.; Shi, Y.; Cheng, L.; Feng, D.; Wu, Z.; Chen, Z.; Wan, Y.; Stein, A.; Zhao, D. Chem. Mater. 2006, 18, 4447

SUPPORTING INFORMATION

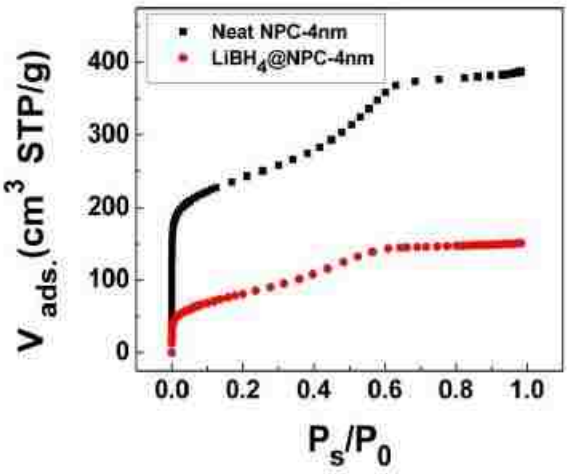

Figure S1. Nitrogen sorption isotherms of (a) NPC-4nm with a surface area and pore volume of 730 m^2/g, and 0.53 cm^3/g respectively, and (b) pre-melted $LiBH_4$@NPC-4nm, with a surface area and pore volume of 292 m^2/g and 0.23 cm^3/g, indicating that $LiBH_4$ has infiltrated the pores.

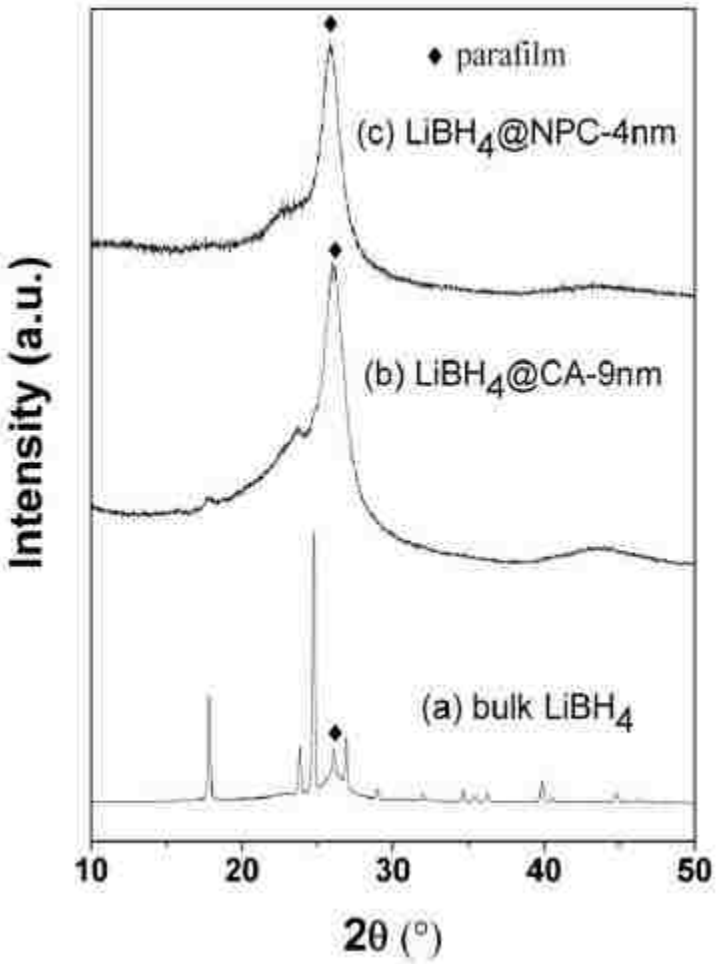

Figure S2. X-ray diffraction patterns of (a) bulk $LiBH_4$, (b) $LiBH_4$@CA-9nm, and (c) $LiBH_4$@NPC-4nm, respectively. The loading of $LiBH_4$ in each sample is 20 wt%.

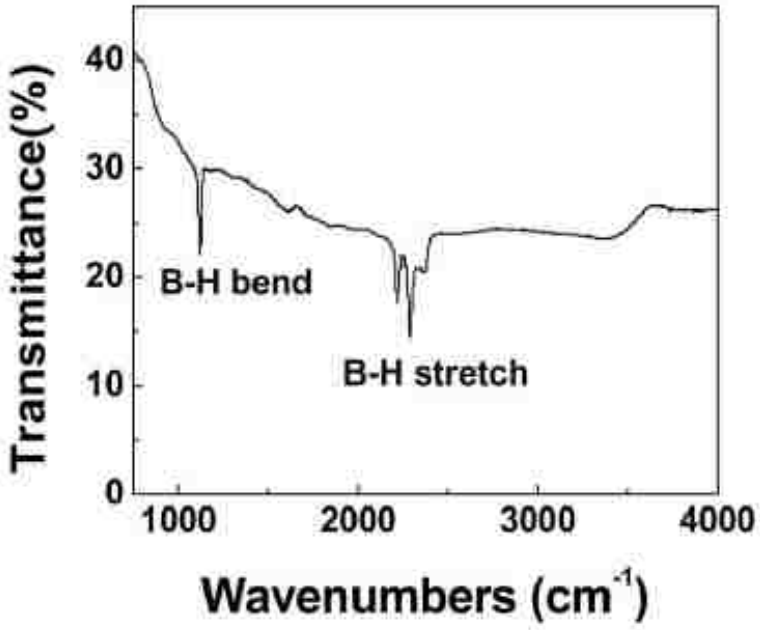

Figure S3. FT-IR spectra of pre-melted $LiBH_4$@NPC-4nm (20 wt%). $[BH_4]^-$ bands indicate the existence of $LiBH_4$ in nanoconfined $LiBH_4$@NPC-4nm system.

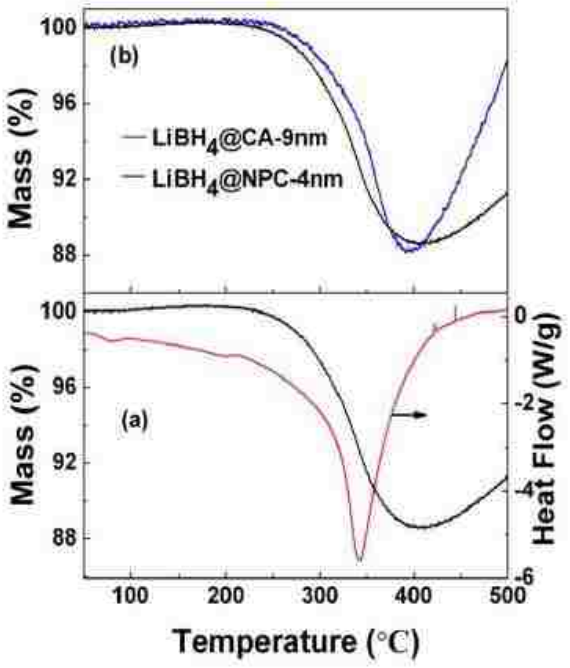

Figure S4. The DSC and TGA plots of $LiBH_4$@NPC-4nm (a) and TGA comparison of $LiBH_4$@NPC-4nm and $LiBH_4$@CA-9nm. The loading of $LiBH_4$ is 20 wt%.

IV. Tailoring the hydrogen storage properties of $Li_4BN_3H_{10}$ by confinement into highly ordered nanoporous carbon

Xiangfeng Liu*[ab], David Peaslee[a] and E. H. Majzoub*[a]

[a]Center for Nanoscience, and Department of Physics and Astronomy, University of Missouri-St. Louis, One University Blvd., St. Louis, MO 63121, USA. [b]College of Materials Science and Opto-Electronic Technology, University of Chinese Academy of Sciences, Beijing, 10049, P. R. China.

First published in the *Journal of Materials Chemistry A* (January 2013)

The effects of nanoconfinement on the H_2 release and uptake, and the emission of toxic ammonia (NH_3) and diborane (B_2H_6) during the decomposition of quaternary phase $Li_4BN_3H_{10}$ have been comprehensively investigated. $Li_4BN_3H_{10}$ confined in highly ordered nanoporous carbon ($Li_4BN_3H_{10}$@NPC) with cylindrical pores and an average pore size of 4.4 nm (NPC-4.4 nm) did not show Bragg peaks or melting of the $Li_4BN_3H_{10}$ due to nanoconfinement-induced amorphization. $Li_4BN_3H_{10}$ confined in NPC starts to decompose at 110 °C, lower by more than 160 °C with respect to bulk and the dehydrogenation kinetics was significantly enhanced. More importantly, in comparison with the *exothermic* decomposition of bulk $Li_4BN_3H_{10}$, a distinct two-step *endothermic* decomposition process was observed in the nanoconfined $Li_4BN_3H_{10}$ system indicating the decomposition pathway was altered by nanoconfinement. A direct line-of-site residual gas analyzer mass-spectrometer (RGA-MS) analysis indicated NH_3 was released earlier than H_2 during the decomposition of nanoconfined $Li_4BN_3H_{10}$ but it evolved slowly and the overall emissions of NH_3 and B_2H_6 were significantly suppressed by nanoconfinement. More interestingly, some other possible gases, diimine (N_2H_2) and triborane or heavier species, produced during the decomposition of $Li_4BN_3H_{10}$ or its constituent parts ($LiBH_4$ and $LiNH_2$), were identified by RGA-MS for the first time. The observation of diimine in the reaction product may provide insight into the reaction mechanisms for rehydriding of compounds in the $LiNH_2$ and Li_2NH systems as well.

Introduction

Hydrogen storage technology is one of the main challenges in the progress of a hydrogen-based energy economy [1, 2]. Hydrogen storage technologies have been widely explored and the current hydrogen storage technologies can be classified into compressed hydrogen tanks, metal hydrides (conventional metal hydrides and complex metal hydrides), high-surface-area adsorbents and chemical hydrogen storage materials [3–5]. Among the hydrogen storage technologies, complex metal hydrides have received wide attention due to their high gravimetric H_2 capacity [6–8]. For example, $NaAlH_4$ [9,10], $LiAlH_4$ [11,12], $LiBH_4$ [13,14], $Mg(BH_4)_2$ [15,16], $Ca(BH_4)_2$ [17,18], M–N–H [19–21] and ammine metal borohydrides systems [22] have been extensively studied. Recently, a quaternary hydride phase $Li_4BN_3H_{10}$ has attracted an increasing interest because of its high hydrogen capacity (*ca.* 11 wt%) [23–25]. But the irreversibility and the significant evolution of ammonia (NH_3) and diborane (B_2H_6) accompanying H_2 release during the decomposition of $Li_4BN_3H_{10}$ restricts its application as a practical hydrogen storage medium. Pinkerton and Meyer investigated the dehydrogenation behavior of nickel chloride-catalyzed stoichiometric $Li_4BN_3H_{10}$ and found that the addition of $NiCl_2$ lowered the H_2 release temperature by 122 °C [26]. They also showed that reducing the H_2 release temperature of $Li_4BN_3H_{10}$ can suppress NH_3 cogeneration during the dehydrogenation process. A recent study from Chen's group shows that the addition of LiH and cobalt-catalyst lowered the H_2 release (9.6 wt%) temperature by 110 °C and NH_3 concentration in hydrogen was dramatically decreased from 12 mol% to 0.008 mol% [27].

Recently, the effects of nanoconfinement on the kinetics, thermodynamics and reversibility of metal hydrides have attracted increasing attention [28–33]. Schueth *et al.* first reported a study on nanoconfinement effect of complex hydride and they found that the desorption temperature of $NaAlH_4$ confined in mesoporous carbon was lowered by 40 K [28]. A theoretical calculation shows that nanosized metal MgH_2 has significantly different thermodynamic properties and the H_2 desorption enthalpy may be substantially decreased when the particle size becomes very small (■1.3 nm) [34]. Vajo and coworkers enhanced the dehydrogenation kinetics and reversibility of $LiBH_4$ by infiltrating into carbon aerogels [35]. The reported desorption rate at 300 °C of

nanoconfined $LiBH_4$ in the carbon aerogel host was 50 times faster than the bulk sample and the dehydrided sample was rehydrided at 100 bar H_2 and 400 °C. Gao *et al.* also reported that the confinement of $NaAlH_4$ in porous carbons with 2–3 nm pores improved both the kinetics and thermodynamics of hydrogen sorption [36]. Jensen *et al.* reported the hydrogen storage properties of nanoconfined MgH_2 and $LiBH_4/MgH_2$ in carbon aerogels (D_{max} ■21 nm) [37]. These nanoconfined systems showed significantly enhanced desorption kinetics and possibly improved thermodynamic properties. In a recent study, our group reported the structural phase transition, H_2 release and uptake, and the emission of toxic diborane (B_2H_6) of $LiBH_4$ confined in highly ordered hexagonally packed cylindrical nanoporous carbon (NPC) [38,39]. $LiBH_4$ confined in highly ordered NPC becomes amorphous and releases H_2 at much lower temperature (220 °C). More importantly, the reversibility was improved and the release of B_2H_6 on the decomposition of $LiBH_4$ was suppressed or eliminated by the nanoconfinement. Wu *et al.* studied the dehydrogenation behaviors and reversibility of nanoscaffolded $Li_3BN_2H_8$ [40]. The infiltration of $Li_3BN_2H_8$ into 13 nm carbon aerogel improved the reversibility but resulted in increased emission of NH_3 compared to bulk sample.

In this study, the quaternary hydride $Li_4BN_3H_{10}$ was infiltrated into a 4.4 nm pore size highly ordered nanoporous carbon template and the effects of nanoconfinement on the dehydrogenation kinetics, the H_2 release, NH_3 or B_2H_6 emission and the reversibility will be comprehensively discussed.

Experimental section

$Li_4BN_3H_{10}$ was prepared by mechanical milling of a 2.0 g mixture of $LiBH_4$ (95%, Aldrich) + $3LiNH_2$ (95%, Aldrich) according to reported literature [41]. The sample was milled with 6 WC balls in a WC milling pod for about 30 minutes under 0.1 MPa Ar, and subsequently annealed at 100 °C under 5 bar H_2 for 12 hours.

Highly ordered porous carbons (NPC) were prepared through an evaporation induced self-assembly strategy [42]. The preparation of nanoporous carbon used in this study was similar to the material we prepared previously [38]. Here we used a calcination temperature of 800 °C. Before infiltration, the prepared nanoporous carbon templates

were first dried at 900 °C for 5 hours under flowing Ar and then dried at 450 °C under vacuum. Subsequently, 20 wt% of $Li_4BN_3H_{10}$ was infiltrated into the dried nanoporous carbon under 240 °C and 60 bar H_2. The pre-melted sample is hereafter referred to as $Li_4BN_3H_{10}$@NPC. Nitrogen adsorption isotherms of the nanoporous carbon were measured using a SA3100 analyzer (Coulter). Brunauer–Emmett–Teller (BET) and Barrett–Joyner–Halenda (BJH) methods were used to calculate the surface areas and pore size distributions, respectively, using adsorption data. X-ray diffraction (XRD) was performed on a Rigaku Ultima IV multipurpose X-ray diffraction (XRD) system with a CuK_α radiation source. The samples containing hydrides were covered with the parafilms to prevent the samples from contacting air or moisture during the XRD experiments. Differential scanning calorimetry (DSC) analysis was performed on a TQ2000 series analyzer (TA instrument). The gas desorption species were measured by a direct line-of-site residual gas analyzer mass-spectrometer (RGA-MS). The details of the measurement can be found in an earlier publication [38].

Results and discussion

Fig. 1(a) shows the nitrogen sorption isotherms of neat NPC and nanoconfined $Li_4BN_3H_{10}$@NPC. The specific surface areas (S_{BET}) of neat NPC and the total pore volume calculated by the BJH model were 1012 $m^2\ g^{-1}$ and 0.65 $cm^3\ g^{-1}$, respectively. After the infiltration of hydride, the specific surface area and the total pore volume of $Li_4BN_3H_{10}$@NPC were considerably reduced to 97 $m^2\ g^{-1}$ and 0.10 $cm^3\ g^{-1}$, respectively, indicating the filling or blocking of the pores by $Li_4BN_3H_{10}$. The pore size distribution before and after the infiltration of $Li_4BN_3H_{10}$ is shown in Fig. 1(b). We can see that the distribution peak shifted to the small size area after infiltration of hydride into NPC and the value at the pore size distribution peak is reduced from 4.4 nm to 4.0 nm due to the filling of the pores.

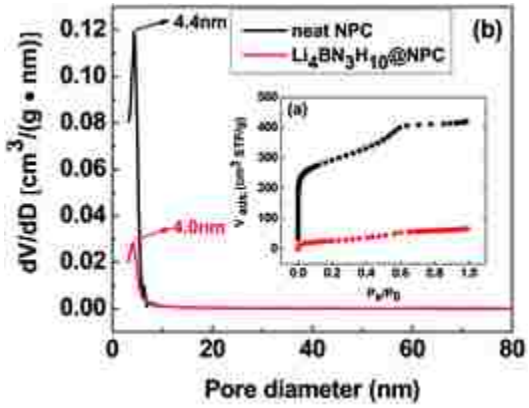

Figure 1. (a) Nitrogen adsorption isotherms of neat NPC (*top line*) with a surface area and pore volume of 1012 m^2 g^{-1} and 0.65 cm^3 g^{-1} respectively, and pre-melted $Li_4BN_3H_{10}$@NPC (*bottom line*) with a surface area and pore volume of 97 m^2 g^{-1} and 0.10 cm^3 g^{-1}, respectively and (b) pore size distribution of neat NPC and pre-melted $Li_4BN_3H_{10}$@NPC.

Fig. 2 shows XRD patterns of as prepared $Li_4BN_3H_{10}$ and the pre-melted $Li_4BN_3H_{10}$@NPC. In our earlier publications, $LiBH_4$ confined in NPC-2 nm or NPC-4 nm both become amorphous and show no Bragg peaks of $LiBH_4$. However, the confinement of the $LiBH_4$ in 9 nm pores still results in broad and diffuse Bragg peaks [38,39]. Similarly, the XRD pattern of the pre-melted $Li_4BN_3H_{10}$@NPC-4.4 nm also does not show Bragg peaks of $Li_4BN_3H_{10}$, indicating the hydride becomes amorphous after melt-infiltration in the 4.4 nm nanopores. This is different from what is observed in $Li_3BN_2H_8$@carbon aerogel-13 nm [40]. The XRD pattern of $Li_3BN_2H_8$@carbon aerogel-13 nm still shows Bragg peaks of $Li_3BN_2H_8$, indicating the existence of crystalline $Li_3BN_2H_8$.

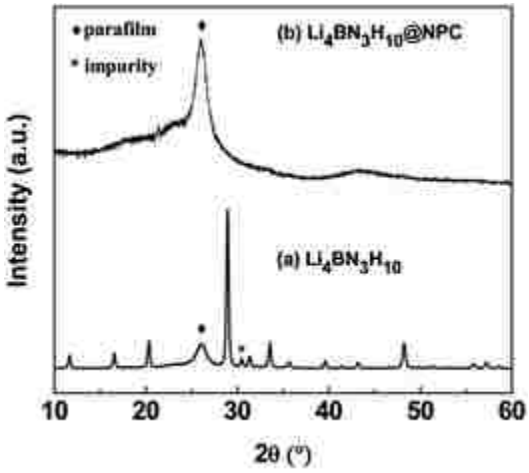

Figure 2. X-ray diffraction of (a) as prepared $Li_4BN_3H_{10}$, and (b) pre-melted $Li_4BN_3H_{10}$@NPC.

The thermal decomposition behaviors of bulk $Li_4BN_3H_{10}$ and nanoconfined $Li_4BN_3H_{10}$@NPC were analyzed by DSC. As shown in Fig. 3, the DSC plot of bulk $Li_4BN_3H_{10}$ shows a sharp *endothermic* peak at 218 °C (melting point) and a broad *exothermic* peak around 340 °C due to the decomposition of $Li_4BN_3H_{10}$, which is in excellent agreement with calorimetry measurements by Zheng *et al.*[27]. In contrast, the DSC plot of the nanoconfined $Li_4BN_3H_{10}$@NPC shows a much broader *endothermic* peak around 200 °C and another *endothermic* peak at 342 °C. The disappearance of the sharp melting peak indicates the nanoconfined hydride became amorphous in agreement with the XRD analysis. RGA analysis of nanoconfined $Li_4BN_3H_{10}$@NPC indicates the first broad *endothermic* peak around 200 °C can be largely attributed to the initial NH_3 release from the dissociation of $Li_4BN_3H_{10.}$ The second *endothermic* peak at 342 °C can be attributed to the further decomposition of the resultant intermediate hydride phase and the further evolution of NH_3 and H_2. More interestingly, in contrast to the *exothermic* decomposition signal of the bulk $Li_4BN_3H_{10}$ the decomposition reactions of $Li_4BN_3H_{10}$ nanoconfined in NPC become *endothermic* indicating the decomposition pathway was completely altered through the nanoconfinement. The strong endothermic change also suggests that the decomposition products may interact more strongly with the NPC framework than does $Li_4BN_3H_{10}$.

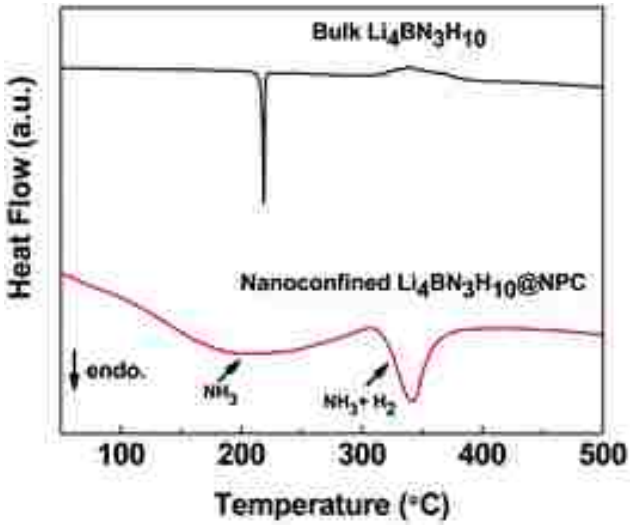

Figure 3. DSC curves of bulk $Li_4BN_3H_{10}$ (*top*) and nanoconfined $Li_4BN_3H_{10}$@NPC (*bottom*). The heating rate is 5 °C min^{-1}.

Fig. 4 shows temperature-programmed desorption (TPD) curves of $Li_4BN_3H_{10}$ and nanoconfined $Li_4BN_3H_{10}$@NPC. The measurements were performed using a fixed-volume Sieverts-type apparatus. We performed a series of absorption–desorption cycles for the as prepared $Li_4BN_3H_{10}$ and nanoconfined $Li_4BN_3H_{10}$@NPC to test the decomposition kinetics and reversibility. As shown in Fig. 4, the as prepared $Li_4BN_3H_{10}$ starts to decompose at about 270 °C and the nanoconfined material starts to decompose at about 110 °C. The onset decomposition temperature of nanoconfined $Li_4BN_3H_{10}$@NPC is lowered by more than 160 °C indicating the dehydrogenation kinetics is significantly improved by nanoconfinement. The decomposed samples were placed under 60 bar of hydrogen at 400 °C for 12 hours and then decomposed at the same conditions as the originally prepared samples. As shown in Fig. 4, $Li_4BN_3H_{10}$ cannot be rehydrided under this condition. The nanoconfined sample has a little higher cycling capacity than bulk $Li_4BN_3H_{10}$ but the nanoconfinement has not significantly improved the reversibility of $Li_4BN_3H_{10}$. More interestingly, the nanoconfined sample indicates two-step decomposition in comparison with the overall single step decomposition of the bulk $Li_4BN_3H_{10}$ indicating a different decomposition pathway induced by nanoconfinement, in agreement with the DSC analysis.

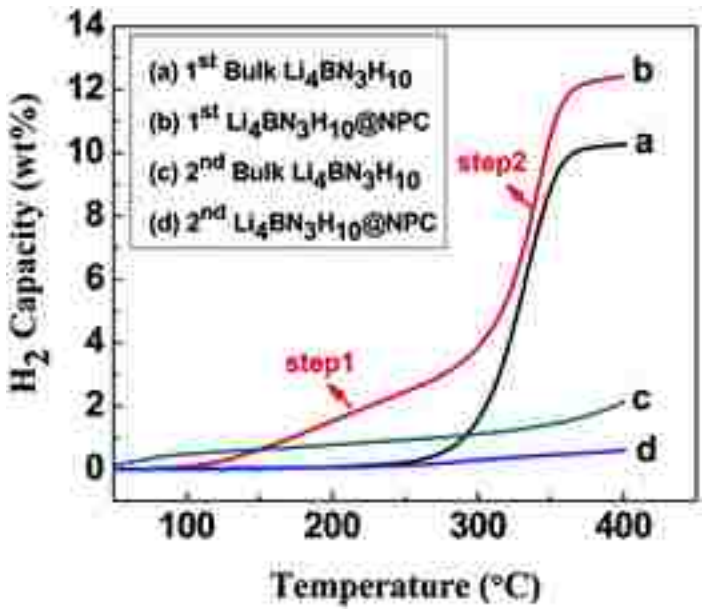

Figure 4.Temperature-programmed desorption (TPD) curves of as prepared $Li_4BN_3H_{10}$ and pre-melted $Li_4BN_3H_{10}$@NPC with an initial loading of 20 wt%. (a) 1st desorption of as prepared $Li_4BN_3H_{10}$; (b) 1st desorption of pre-melted $Li_4BN_3H_{10}$@NPC; (c) 2nd desorption of rehydrided $Li_4BN_3H_{10}$; (d) 2nd desorption of rehydrided $Li_4BN_3H_{10}$@NPC. Note that some of the desorbed gas is NH_3, especially in the bulk sample (a).

Finally, the evolution of ammonia, diborane and other possible gaseous products in the decomposition of bulk $Li_4BN_3H_{10}$ and nanoconfined $Li_4BN_3H_{10}$@NPC will be addressed. The H_2, NH_3, and B_2H_6 release, of $LiBH_4$, $LiNH_2$, and $Li_4BN_3H_{10}$, on decomposition was analyzed using a direct line-of-site residual gas analyzer mass spectrometer (RGA-MS). In order to better understand the decomposition pathway of $Li_4BN_3H_{10}$ its constituent parts ($LiBH_4$, $LiNH_2$) were analyzed separately by RGA-MS. Fig. 5 compares the ammonia production between $LiNH_2$ and $Li_4BN_3H_{10}$. More details of RGA cracking patterns and gas evolution for $LiBH_4$, $LiNH_2$, $Li_4BN_3H_{10}$ and nanoconfined $Li_4BN_3H_{10}$@NPC can be found in the supporting file (Fig. S1–4). In Fig. 5a the ammonia production for $Li_4BN_3H_{10}$ is seen to precede the ammonia production of $LiNH_2$ by 40 °C. Additionally, the reaction that generates the NH_3 is completed in $Li_4BN_3H_{10}$ by 410 °C, but has not finished in $LiNH_2$ by 450 °C (the end of the measurement). This data has been normalized with respect to mass of hydride. The data in Fig. 5b represents the respective peaks in the ammonia production. The figure

shows that both $LiNH_2$ and $Li_4BN_3H_{10}$ materials generate an unidentified gas with similar cracking patterns. The pattern of NH_3 (from published cracking patterns [43]), as well as a smaller unidentified signal at a *m*/*z* ratio of 28 and 30 (in the blue circle area) is present in the decomposition of $LiNH_2$ and $Li_4BN_3H_{10}$. This smaller signal may represent the cracking pattern of diimine (N_2H_2), which has not been previously reported. It appears that the ratio of diimine to ammonia is consistent between the decomposition of $LiNH_2$, $Li_4BN_3H_{10}$, and the $Li_4BN_3H_{10}$@NPC as can be seen in the cracking patterns of the supporting files. The cogeneration of diimine with ammonia suggests an intermediate compound that is part of the mechanism of dehydrogenation or rehydrogenation in the $LiNH_2$ and $Li_4BN_3H_{10}$ systems. Its observation may suggest reaction pathways or intermediates in the decomposition and rehydriding of the nitrogen-containing complex hydride compounds.

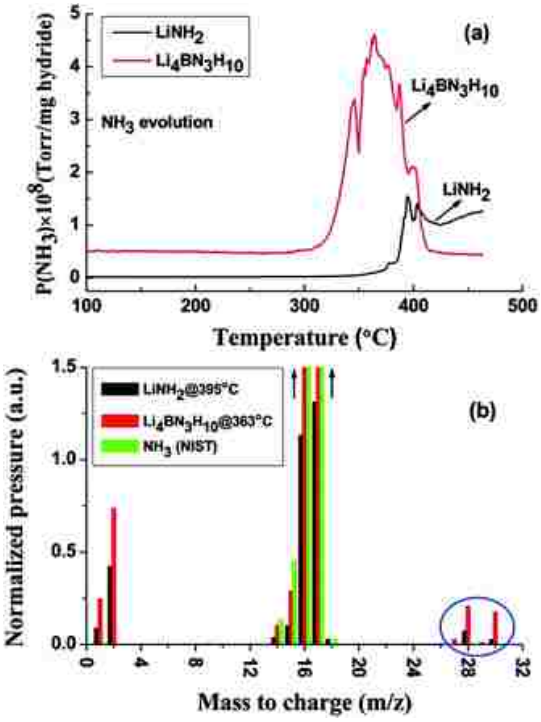

Figure 5. (a) RGA analyses of ammonia in bulk $LiNH_2$ and $Li_4BN_3H_{10}$ samples and (b) the cracking pattern of the sample at the main ammonia peaks with the published ammonia cracking pattern. The blue-circled area may indicate the presence of diimine (N_2H_2).

Fig. 6 represents a similar comparison between $Li_4BN_3H_{10}$ and $LiBH_4$. As can be seen in Fig. 6a, in bulk $LiBH_4$ there is a fair amount of diborane (B_2H_6) produced at a temperature of 405 °C, but in $Li_4BN_3H_{10}$ there is a much smaller amount of this gas at a temperature of 425 °C. It should be noted that the amount of diborane produced is much smaller in comparison to the ammonia. In Fig. 6b, the cracking patterns of diborane are shown (from published cracking patterns [43]), where all the data has been normalized for comparison. Fig. S1 and S3 show the direct line-of-sight RGA cracking patterns and gas evolution of $LiBH_4$ and $Li_4BN_3H_{10}$, respectively. With bulk $LiBH_4$, most of the pattern shown is similar to that of diborane, but when compared to $Li_4BN_3H_{10}$ there is a small range of masses (*m*/*z* of 38 to 44) that appears in both samples with similar ratios, but dominates the pattern in $Li_4BN_3H_{10}$. This is a previously unidentified product that may represent more complicated triboranes, or even B–N–H species discussed below in more detail. B_3H_8 is a borane with a mass of 41. The possible formation of polyborane intermediate species (B_3H_8) in the dehydrogenation of $Mg(BH_4)_2$ was proposed in a recent study [44]. The masses 27 through 31 in the spectrum may also be an unidentified B–N–H species present in similar mass ratios.

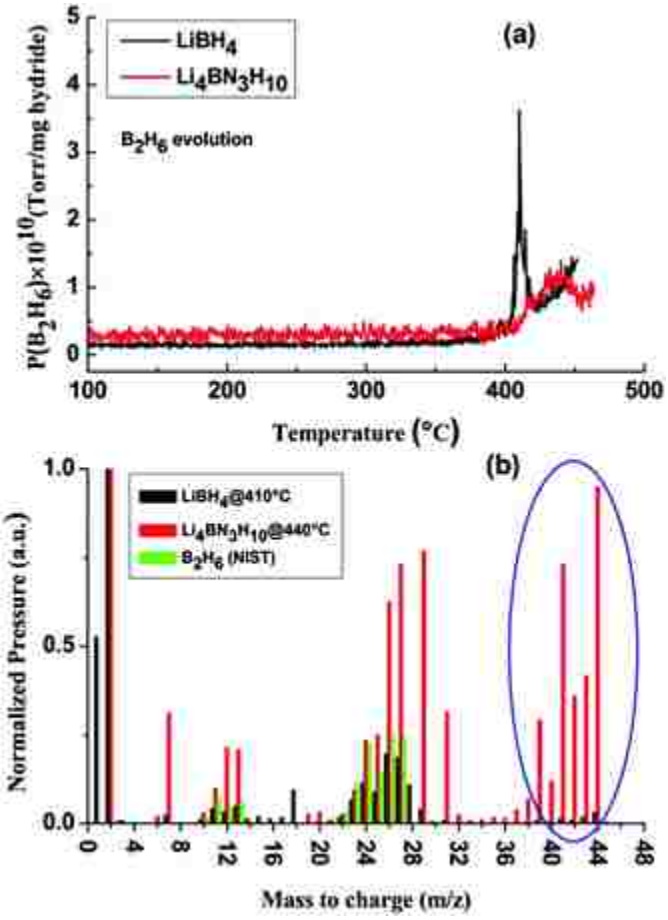

Figure 6. (a) Normalized RGA traces of diborane in bulk $LiBH_4$ (*with strong peak*) and $Li_4BN_3H_{10}$ (*no strong peak*) samples and (b) the cracking pattern of the sample at the main diborane peaks with published diborane cracking pattern. The blue-circled area indicates the presence of a heavier mass species that may be triborane, or even B–N–H species such as BH_2NH_2, for example.

Fig. 7 compares the NH_3, B_2H_6 and H_2 releases between bulk $Li_4BN_3H_{10}$ and nanoconfined $Li_4BN_3H_{10}$@NPC. As indicated in Fig. 7, NH_3 evolves slowly and less NH_3 is released from the decomposition of nanoconfined $Li_4BN_3H_{10}$@NPC in comparison with bulk $Li_4BN_3H_{10}$. The gasses associated with NH_3 emission (such as N_2H_2) follow a similar ratio to that of bulk and since the ammonia is drastically reduced they are difficult to observe in the nanoconfined system. This is different from what was observed in Wu's nanoscaffolded $Li_3BN_2H_8$ system [40]. Wu *et al.* reported that the infiltration of $Li_3BN_2H_8$ into 13 nm carbon aerogel resulted in an increased emission of

NH_3 compared to bulk sample [40]. The differences might come from the following facts. In this study, the highly ordered nanoporous carbon templates with an average pore size of 4.4 nm were employed and the nanoconfined $Li_4BN_3H_{10}$ became amorphous. In contrast, 13 nm carbon aerogel was used in Wu's study and crystalline $Li_3BN_2H_8$ still exists. In addition, in comparison with $Li_4BN_3H_{10}$ no measurable B_2H_6 is produced during the decomposition of nanoconfined $Li_4BN_3H_{10}$@NPC. The results indicate nanoconfinement at the 4.4 nm pore size can suppress or eliminate the decomposition reaction path of $Li_4BN_3H_{10}$ that produces more NH_3 or B_2H_6. The suppression on the formation of B_2H_6 by nanoconfinement was also observed in our previous studies on nanoconfined $LiBH_4$ [39,40]. In addition, as shown in Fig. S3, for bulk $Li_4BN_3H_{10}$, the evolution of triborane or larger species (possibly even nitrogen containing boranes such as BNH_2 or BNH_3, for example) [45] is evident from the masses between *m*/*z* of 39–44 and groups centered at 56 and 69. In contrary, as shown in Fig. S4, the cracking pattern of nanoconfined $Li_4BN_3H_{10}$@NPC is absent any strong signal of larger species indicating the suppression of their evolution. More interestingly, in Pinkerton's $NiCl_2$-catalyzed $Li_4BN_3H_{10}$ system, NH_3 is evolved in a separate decomposition at higher temperature [26]. In contrast to the $NiCl_2$-catalyzed $Li_4BN_3H_{10}$ system, our samples show a little amount of NH_3 starts to release earlier than H_2 at lower temperature in the nanoconfined $Li_4BN_3H_{10}$@NPC system. Because of the amorphous product XRD does not provide any information about the phases, the detailed decomposition mechanism study of the nanoconfined system is still in progress and needs to be further confirmed by solid state NMR or neutron scattering techniques.

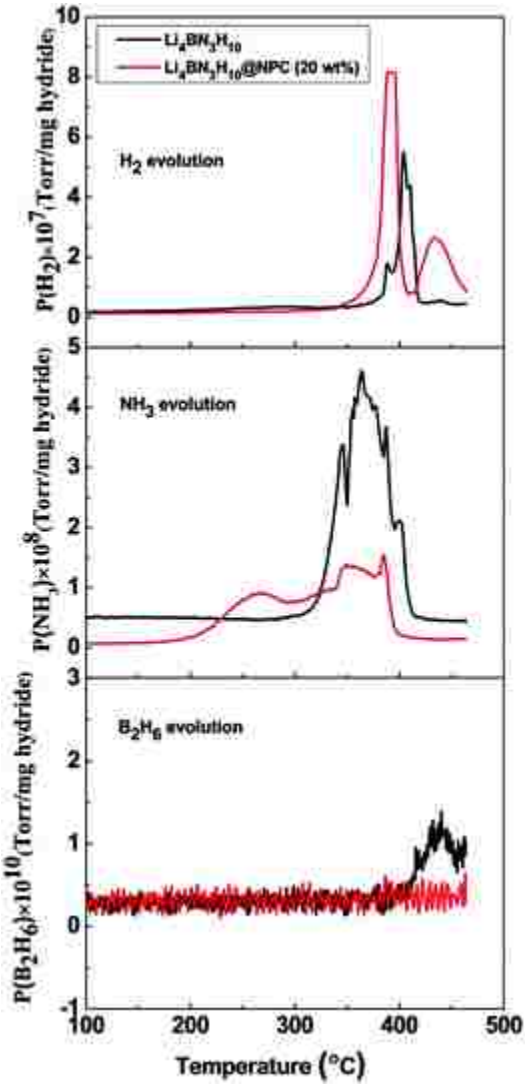

Figure 7. RGA-MS traces showing H_2, NH_3, and B_2H_6 release with increasing temperature for as prepared $Li_4BN_3H_{10}$ and nanoconfined $Li_4BN_3H_{10}$@NPC. (*Bulk $Li_4BN_3H_{10}$ is the lower curve in the first figure,and the higher curve in the second and third figures*)

The decomposed $Li_4BN_3H_{10}$@NPC was placed under 60 bar of hydrogen at 400 °C for 12 hours. RGA-MS was used to analyze the decomposed gas phases of the rehydrided sample. Fig. 8 shows H_2, NH_3, and B_2H_6 releases with increasing temperature for the rehydrided $Li_4BN_3H_{10}$@NPC. Interestingly, H_2 and NH_3 released but showed a different decomposition behavior from the original $Li_4BN_3H_{10}$@NPC indicating some different hydride might form during the rehydriding process. The detailed study of the

rehydrided sample is still in progress. It should be also noticed that no detectable B_2H_6 was emitted on the decomposition of the rehydrided sample.

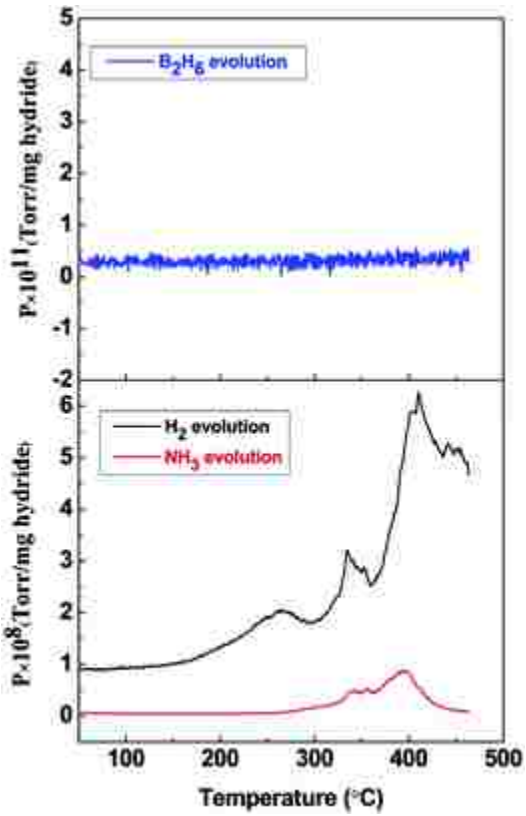

Figure 8. RGA-MS traces showing H_2, NH_3 (*bottom curve in lower figure*), and B_2H_6 releases with increasing temperature for the rehydrided $Li_4BN_3H_{10}$@NPC.

Conclusion

The H_2 release and uptake behavior, and the emission of toxic NH_3 and B_2H_6 on the decomposition of nanoconfined $Li_4BN_3H_{10}$ in highly ordered nanoporous carbon template have been investigated. $Li_4BN_3H_{10}$ confined in the highly ordered NPC (NPC-4.4 nm) did not show Bragg peaks in XRD or melting in calorimetry, indicating the nanoconfinement resulted in amorphization. In contrast with bulk $Li_4BN_3H_{10}$ starting to decompose at 270 °C in a single step *exothermic* decomposition pathway, the nanoconfined $Li_4BN_3H_{10}$ started to decompose at a much lower temperature (*ca.* 110 °C) with a two-step

endothermic decomposition pathway indicating the change of the decomposition pathway by the nanoconfinement. Mass spectroscopic analysis indicates NH_3 starts to release earlier than H_2 at a lower temperature but nanoconfinement suppressed the overall NH_3 release and eliminated B_2H_6 evolution. Some possible gases diimine (N_2H_2) and triborane or heavier species released during the decomposition of $Li_4BN_3H_{10}$ and its constituent parts ($LiBH_4$, $LiNH_2$) were identified by RGA-MS, and may indicate possible reaction mechanisms in the nitrogen-containing complex hydrides. H_2 and NH_3 released for the rehydrided $Li_4BN_3H_{10}$@NPC composite but showed a different decomposition behavior indicating some different hydride might form during the rehydriding process.

Acknowledgements

This work was funded by the U.S. Department of Energy in the Hydrogen, Fuel Cells, and Infrastructure Technologies Program through the office Energy Efficiency and Renewable Energy under Contract no. DE-AC04-94AL85000. The authors also thank Dr Mark Allendorf and Dr Raghu Bhakta at Sandia National Laboratories for useful discussions. Xiangfeng Liu also would like to thank the Chinese Academy of Sciences for “Hundred Talents Project”.

References

[2] L. Schlapbach and A. Züttel, *Nature*, 2001, 414, 353–358.

[3] P. Chen and M. Zhu, *Mater. Today*, 2003, 6, 36–43

[4] J. Graetz, *Chem. Soc. Rev.*, 2009, 38, 73–82.

[5] G. S. Walker, M. Abbas, D. M. Grant and C. Udeh, *Chem. Commun.*, 2011, 47, 8001–8003.

[6] T. K. Mandal and D. H. Gregory, *Annu. Rep. Prog. Chem., Sect. A: Inorg. Chem.*, 2009, 105, 21–54.

[7] U. Eberle, M. Felderhoff and F. Schuth, *Angew. Chem., Int. Ed.*, 2009, 48, 6608–6630.

[8] S. Orimo, Y. Nakamori, J. R. Eliseo, A. Züttel and C. M. Jensen, *Chem. Rev.*, 2007, 107, 4111–4132.

[9] W. Grochala and P. P. Edwards, *Chem. Rev.*, 2004, 104, 1283–1315.

[10] B. Bogdanović and M. Schwickardi, *J. Alloys Compd.*, 1997, 253, 1–7.

[11] P. Wang and C. M. Jensen, *J. Phys. Chem. B*, 2004, 108, 15827–15829.

[12] J. Graetz, J. Wegrzyn and J. J. Reillly, *J. Am. Chem. Soc.*, 2008, 130, 17790–17794.

[13] X. Liu, G. S. McGrady, H. W. Langmi and C. M. Jensen, *J. Am. Chem. Soc.*, 2009, 131, 5032–5033.

[14] S. Orimo, Y. Nakamori, G. Kitahara, K. Miwa, N. Ohba, S. Towata and A. Züttel, *J. Alloys Compd.*, 2005, 427, 404–406.

[15] J. Shao, X. Xiao, L. Chen, X. Fan, S. Li, H. Ge and Q. Wang, *J. Mater. Chem.*, 2012, 22, 20764–20772.

[16] G. L. Soloveichik, Y. Gao, J. Rijssenbeek, M. Andrus, S. Kniajanski, R. C. Bowman, Jr, S. J. Hwang and J. C. Zhao, *Int. J. Hydrogen Energy*, 2009, 34, 916–928.

[17] M. D. Riktor, M. H. Sørby, K. Chłopek, M. Fichtner, F. Buchter, A. Züttel and B. C. Hauback, *J. Mater. Chem.*, 2007, 17, 4939–4942.

[18] E. Ronnebro and E. H. Majzoub, *J. Phys. Chem. B*, 2007, 111, 12045–12047.

[19] C. Rongeat, V. D'Ann, H. Hagemann, A. Borgschulte, A. Züttel, L. Schultz and O. Gutfleisch, *J. Alloys Compd.*, 2010, 493, 281–287.

[20] P. Chen, Z. T. Xiong, J. Z. Luo, J. Y. Lin and K. L. Tan, *Nature*, 2002, 420, 302–304.

[21] J. Wang, J. Hu, Y. Liu, Z. Xiong, G. Wu, H. Pan and P. Chen, *J. Mater. Chem.*, 2009, 19, 2141–2146.

[22] H. Y. Leng, T. Ichikawa, S. Hino, N. Hanada, S. Isobe and H. Fujii, *J. Phys. Chem. B*, 2004, 103, 8763–8765.

[23] G. Xia, Q. Gu, Y. Guo and X. Yu, *J. Mater. Chem.*, 2012, 22, 7300–7307.

[24] Y. E. Filinchuk, K. Yvon, G. P. Meisner, F. E. Pinkerton and M. P. Balogh, *Inorg. Chem.*, 2006, 45, 1433–1435.

[25] J. P. Singer, M. S. Meyer, R. M. Speer, Jr, J. E. Fischer and F. E. Pinkerton, *J. Phys. Chem. C*, 2009, 113, 18927–18934.

[26] H. Wu, W. Zhou, T. J. Udovic, J. J. Rush and T. Yildirim, *Chem. Mater.*, 2008, 20, 1245–1247.

[27] F. E. Pinkerton and M. S. Meyer, *J. Phys. Chem. C*, 2009, 113, 11172–11176.

[28] X. Zheng, Z. Xiong, Y. Lim, G. Wu, P. Chen and H. Chen, *J. Phys. Chem. C*, 2011, 115, 8840–8845.

[29] F. Schueth, A. Taguchi, S. Kounosu and B. Bogdanovic, 2004, DE Patent Specification 10332438.

[30] Gutowska, L. Li, Y. Shin, C. M. Wang, X. S. Li, G. C. Linehan, R. S. Smith, B. D. Kay, B. Schmid, W. Shaw, M. Gutowski and T. Autrey, *Angew. Chem., Int. Ed.*, 2005, 44, 3578–3582.

[31] P. E. de Jonghand and P. Adelhelm, *ChemSusChem*, 2010, 3, 1332–1348.

[32] R. Xiong, G. Sang, X. Yan, G. Zhang and X. Ye, *J. Mater. Chem.*, 2012, 22, 17183–17189.

[33] M. Fichtner, *Nanotechnology*, 2009, 20, 204009.

[34] T. K. Nielsen, F. Besenbacher and T. R. Jensen, *Nanoscale*, 2011, 3, 2086–2098.

[35] R. W. P. Wagemans, J. H. van Lenthe, P. E. de Jongh, A. Jos van Dillen and K. P. de Jong, *J. Am. Chem. Soc.*, 2005, 127, 16675–16680.

[36] F. Gross, J. J. Vajo, S. L. Van Atta and G. L. Olson, *J. Phys. Chem. C*, 2008, 112, 5651–5657.

[37] J. Gao, P. Adelhelm, M. H. W. Verkuijlen, C. Rongeat, M. Herrich, P. J. M. van Bentum, O. Gutfleisch, A. P. M. Kentgens, K. P. de Jong and P. E. de Jongh, *J. Phys. Chem. C*, 2010, 114, 4675–4682.

[38] T. K. Nielsen, U. Bösenberg, R. Gosalawit, M. Dornheim, Y. Cerenius, F. Besenbacher and T. R. Jensen, *ACS Nano*, 2010, 4, 3903–3908.

[39] X. Liu, D. Peaslee, C. Z. Jost and E. H. Majzoub, *J. Phys. Chem. C*, 2010, 114, 14036–14041.

[40] X. Liu, D. Peaslee, C. Z. Jost, T. F. Baumann and E. H. Majzoub, *Chem. Mater.*, 2011, 23, 1331–1336.

[41] H. Wu, W. Zhou, K. Wang, T. J. Udovic, J. J. Rush, T. Yildirim, L. A. Bendersky, A. F. Gross, S. L. Van Atta, J. J. Vajo, F. E. Pinkerton and M. S. Meyer, *Nanotechnology*, 2009, 20, 204002.

[42] M. Matsuo, A. Remhof, P. Martelli, R. Caputo, M. Ernst, Y. Miura, T. Sato, H. Oguchi, H. Maekawa, H. Takamura, A. Borgschulte, A. Zuttel and S. Orimo, *J. Am. Chem. Soc.*, 2009, 131, 16389–16391.

[43] Y. Meng, D. Gu, F. Zhang, Y. Shi, L. Cheng, D. Feng, Z. Wu, Z. Chen, Y. Wan, A. Stein and D. Zhao, *Chem. Mater.*, 2006, 18, 4447–4464.

[44] http://webbook.nist.gov.

[45] M. Chong, A. Karkamkar, T. Autrey, S. Orimo, S. Jalisatgi and C. M. Jensen, *Chem. Commun.*, 2011, 47, 1330–1332.

[46] F. Baitalow, J. Baumann, G. Wolf, K. Jaenicke-Roßler and G. Leitner, *Thermochim. Acta*, 2002, 391, 159–168.

Supporting information

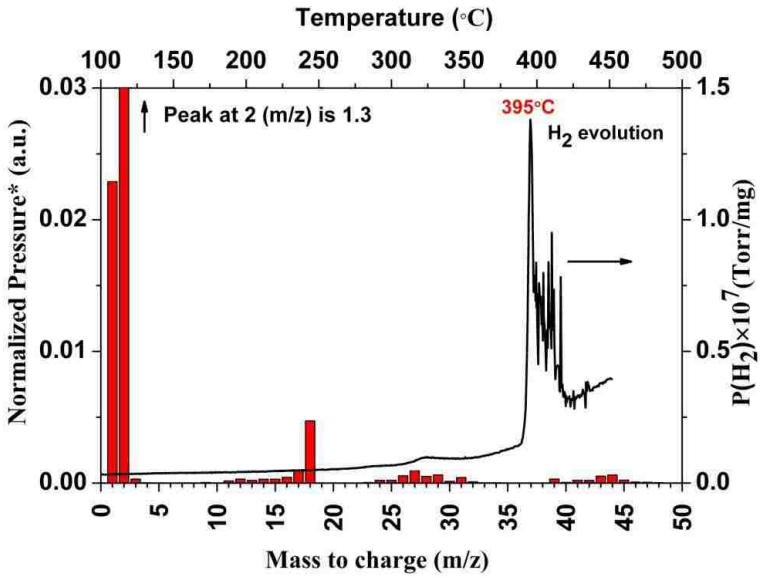

(a)

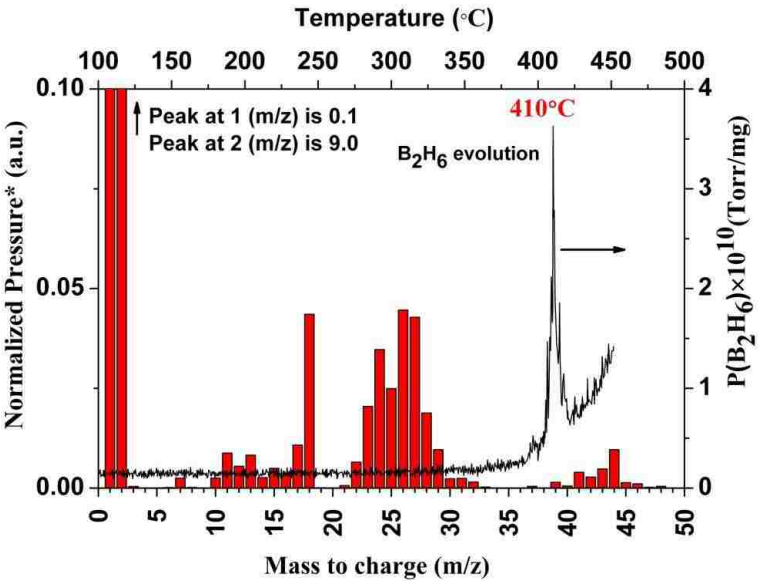

(b)

Figure S1. Direct line-of-sight RGA cracking patterns and gas evolution of $LiBH_4$. (a) shows the evolution of H_2 (m/z=2) as well as the cracking pattern taken at 395°C; (b) shows the evolution of B_2H_6 (m/z=24) as well as the cracking pattern taken at 410°C. *All mass spectra bar graphs have been background subtracted. All arbitrary units (a.u.) are with respect to the partial pressure of the corresponding gas evolution.

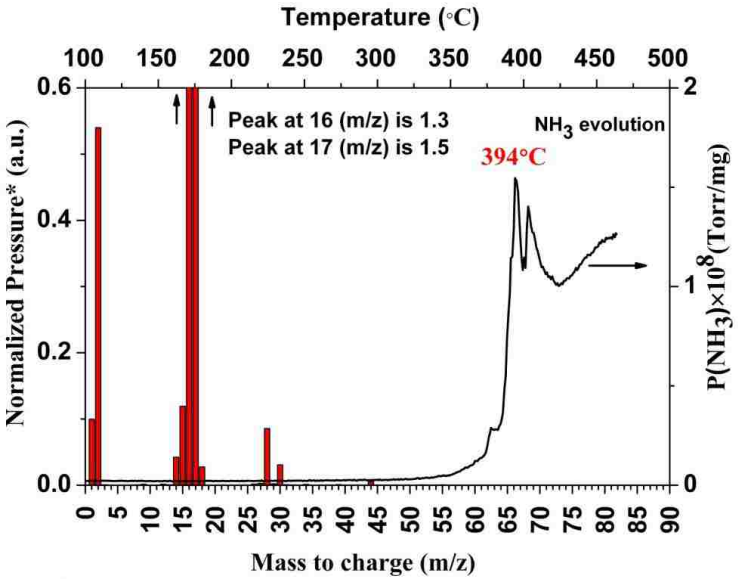

(a)

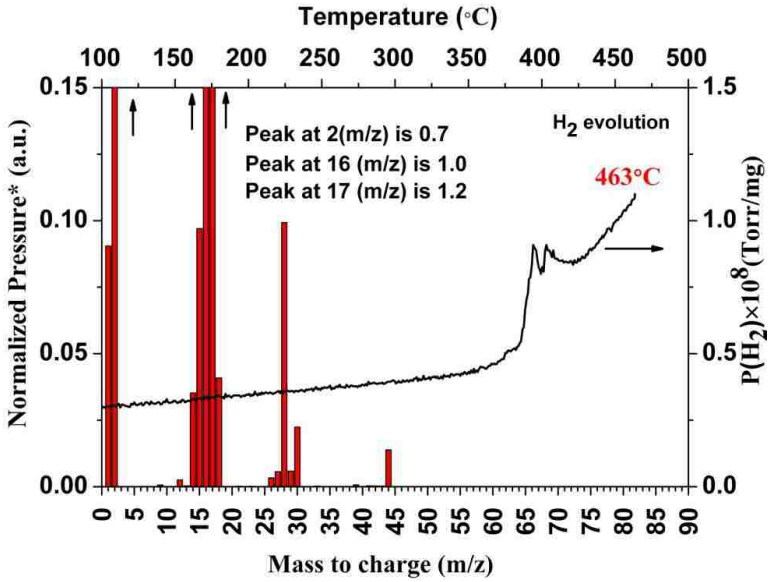

(b)

Figure S2. Direct line-of-sight RGA cracking patterns and gas evolution of $LiNH_2$. (a) shows the evolution of NH_3 (m/z=17) as well as the cracking pattern taken at 394°C; (b) shows the evolution of H_2 (m/z=2) as well as the cracking pattern taken at 463°Cwhich is the near the maximum process temperature. The evolution of hydrogen continues beyond 475°C, but the peaks shown in the hydrogen curve more than likely are hydrogen release associated with the release of ammonia. Present in the ammonia and hydrogen cracking patterns are N_2H_2 (m/z = 28and 30 at similar ratios).

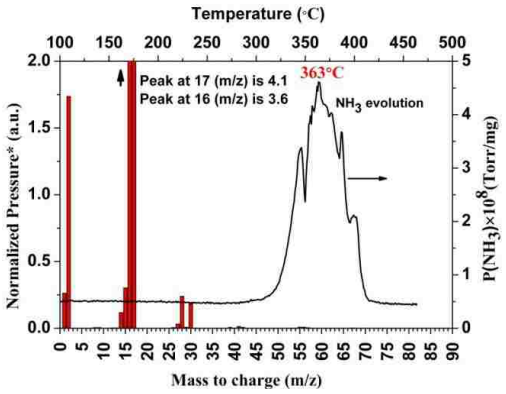

(a)

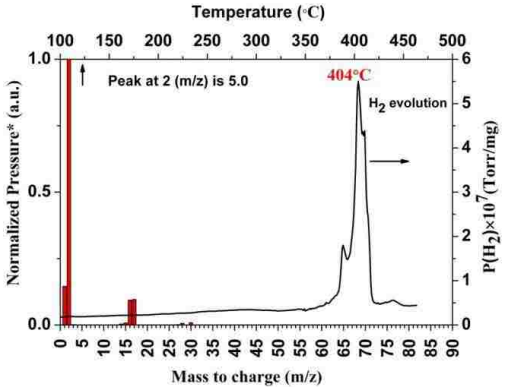

(b)

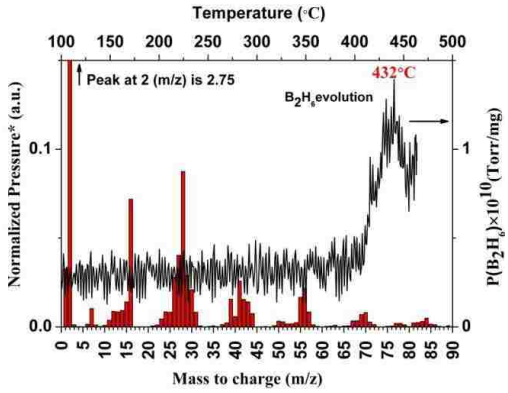

(c)

Figure S3. Direct line-of-sight RGA cracking patterns and gas evolution of $Li_4BN_3H_{10}$. (a) shows the evolution of NH_3 (m/z=17) as well as the cracking pattern taken at 363°C; (b) shows the evolution of H_2 (m/z=2) as well as the cracking pattern taken at 404°C; (c) shows the evolution of B_2H_6 (m/z=24) as well as the cracking pattern taken at 432°C. The evolution of triborane or larger species (possibly even nitrogen containing boranes such as BNH_2 or BNH_3, for example) is evident from the masses between m/z of 39-44 and groups centered at 56 and 69.

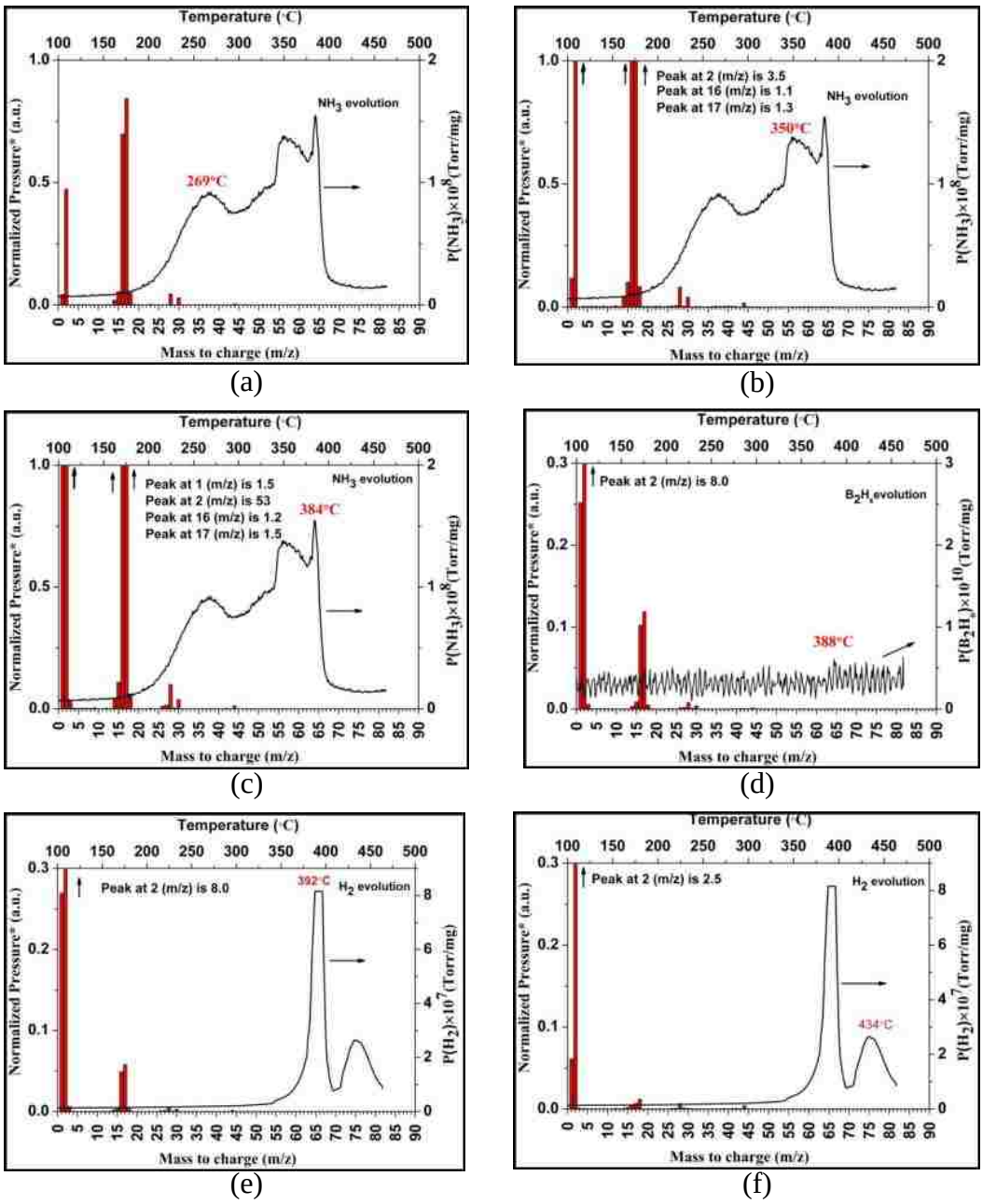

Figure S4. Direct line-of-sight RGA cracking patterns and gas evolution of $Li_4BN_3H_{10}$@NPC. (a,b,c) shows the evolution of NH_3 (m/z=17) as well as the cracking pattern taken at the three peaks at 269 °C, 350 °C, 384 °C respectively; (d) shows the evolution of B2H6 (m/z=24) as well as the cracking pattern taken at 388 °C. This cracking pattern is absent any strong signal of triborane or larger species, especially diborane; (e,f) shows the evolution of H_2 (m/z=2) as well as the cracking pattern taken at the peaks of 392 °C and 434 °C respectively.

V. Decomposition Behaviors of Eutectic $LiBH_4$-$Mg(BH_4)_2$ and Confinement Effects in Ordered Nanoporous Carbon

David Peaslee[1], Xiangfeng Liu[2], T. Patrick Sheehan[1], and Eric H. Majzoub[1,*]

[1]*Center for Nanoscience, and Department of Physics and Astronomy*

University of Missouri-St. Louis

One University Blvd., St. Louis, MO 63121, USA

[2]*College of Materials Science and Opto-Electronic Technology, University of Chinese Academy of Sciences, Beijing, 10049, P. R. China*

ABSTRACT

The crystal structure, diborane (B_2H_6) and triborane (B_3H_n) evolution, and dehydrogenation kinetics, of both bulk and nanoconfined $Li/Mg(BH_4)_3$ in highly ordered nanoporous carbon template have been comprehensively investigated. The bimetallic borohydride $Li/Mg(BH_4)_3$ mainly forms a eutectic structure similar to that of α-$Mg(BH_4)_2$. The decomposition temperature of $Li/Mg(BH_4)_3$ lies between that of $LiBH_4$ and $Mg(BH_4)_2$. A direct line-of-site residual gas analyzer mass spectrometer (RGA-MS) shows that very little diborane and no detectable triborane are released during the decomposition of $Li/Mg(BH_4)_3$, which is quite different from $Mg(BH_4)_2$ or $LiBH_4$ indicating that the dual-cation borohydride undergoes a different decomposition pathway, and that the reaction pathway related to diborane or triborane formation was suppressed. The nanoconfined $Li/Mg(BH_4)_3$ shows a higher cycling capacity as well as a lower decomposition temperature but produces more diborane and triborane in comparison with bulk $Li/Mg(BH_4)_3$.

INTRODUCTION

Safe and efficient hydrogen storage is the key challenge for the widespread commercialization of hydrogen-powered vehicles [1-2]. Among the various hydrogen storage approaches (i.e. compressed hydrogen tanks, metal hydrides, high-surface-area adsorbents and chemical hydrogen storage materials) [3-5] complex metal hydrides have received wide attention due to their high gravimetric H_2 capacity [6-9] Borohydrides such as $LiBH_4$ and $Mg(BH_4)_2$ have attracted a great interest owing to the high H_2 capacity (For examples, 18.5wt% for $LiBH_4$ and 15 wt% for $Mg(BH_4)_2$) [10-14]. But the poor hydrogen release/uptake kinetics and impractical reversibility conditions hinder their use in practical applications for hydrogen storage. $LiBH_4$ has a high desorption temperature (~500°C) and inaccessible rehydrogenation conditions of 350 bar H_2 and 600°C [10]. It was reported that the multi-step dehydrogenations of $Mg(BH_4)_2$, each with different enthalpies, makes the rehydrogenation very difficult [11]. A possible intermediate compound, $MgB_{12}H_{12}$, might form after rehydrogenation under 543K and 400bar H_2 [13]. Tuning the thermodynamic and kinetics properties is the key for the application of borohydrides as high performance hydrogen storage materials. A few approaches have been applied to improve the dehydrogenation kinetics and the reversibility of complex hydrides such as the addition of catalysts or destabilizers and the nanosizing of hydrides [15-19]. Vajo et al. found that the addition of MgH_2 to $LiBH_4$ lowered the hydrogenation/dehydrogenation enthalpy by 25 kJ/(mol of H_2) in comparison with pure $LiBH_4$ and significantly improved the reversibility [15]. Recently, the tuning of the kinetics and the possible thermodynamics through nanoconfinement of complex hydrides have attracted increasing interest [20-25]. Vajo et al. reported that the dehydrogenation kinetics and reversibility of $LiBH_4$ were greatly enhanced by infiltrating $LiBH_4$ into carbon aerogels [20]. The desorption rate at 300°C of nanoconfined $LiBH_4$ in the carbon aerogel host was 50 times faster than the bulk sample and the dehydrided sample was rehydrided at 100 bar H_2 and 400 °C; reduced from 350 bar H_2 and 600°C. Fichtner et al. also reported that the confinement of $Mg(BH_4)_2$ in microporous carbon with a pore diameter of <2 nm improved the desroption kinetics [25].

Another promising method to tune the kinetics and thermodynamic properties of borohydrides is the preparation of bimetallic borohydrides [26-29]. Nakamori et al. has

discovered the relationship between electronegativity of metal cation and the thermal stability of metal borohydrides and the decomposition temperature decreased with the increase of electronegativity [30]. The thermodynamic stability of $LiBH_4$ might be tuned by mixing with other metal boronhydrides, $M(BH_4)_n$, (M: alkali- or alkaline-earth-metal or transition-metal). Both theoretical and experimental studies show that the kinetics and thermodynamic properties can be tuned by the formation of bimetallic borohydrides [31-33]. Nickels et al. first reported the synthesis, crystal structure determination and decomposition temperature of a mixed alkali metal borohydride, $LiK(BH_4)_2$ [31] They found that $LiK(BH_4)_2$ crystallizes in a structure closely related to that of orthorhombic $LiBH_4$ and the decomposition temperature lies between that of $LiBH_4$ and KBH_4. Xiao et al. studied the structure and thermodynamic property of $LiK(BH_4)_2$ using a first-principles density functional theory (DFT) approach and found that the decomposition temperature of $LiK(BH_4)_2$ lies between that of the constituent phases [32]. Fang et al. synthesized the dual-cation (Li, Mg) borohydride through mechanical milling of 1:1 $LiBH_4/Mg(BH_4)_2$ mixture and a subsequent heating process and found that the dual-cation borohydride exhibited a lower melting point (~183°C) and lower onset dehydrogenation temperature than the constituent phases [34]. A different mechanistic pathway was suggested in comparison with the constituent phase $LiBH_4$ or $Mg(BH_4)_2$. Recently, Fichtner et al. systematically investigated the possible formation of $xLiBH_4/(1-x)Mg(BH_4)_2$ and found that high-energy ball milling of a mixture of $LiBH_4$ and $Mg(BH_4)_2$ leads to the formation of a physical mixture of the components rather than a new compound [35]. But a eutectic composition was found to exist at $0.50 < x < 0.60$ exhibiting melting at 180°C and lower dehydrogenation temperature than those of the pure metal borohydrides. This group also found that with the higher mixing ratio of $x = 0.60$, and under H_2 pressures the $LiBH_4$ would decompose at a lower temperature while in the presence of MgH_2, which is produced in an earlier decomposition step [36].

In addition to poor thermodynamics and kinetics, the evolution of diborane accompanying H_2 release during the decomposition of $LiBH_4$ or $Mg(BH_4)_2$ is also a critical issue [37-38]. The evolution of toxic diborane accompanying H_2 release during the decomposition of borohydrides not only results in capacity loss on each cycle due to the loss of boron but also a safety concern. Reducing diborane release plays a critical role

for metal borohydrides as a real hydrogen storage medium. The additions of some suitable catalysts such as $LaCl_3$ and $TiCl_3$ have been found to reduce the concentration of diborane release upon the decomposition of $LiBH_4$ [37]. The release of diborane also can be suppressed or eliminated through controlling the dehydrogenation pathway by nanoconfinement of $LiBH_4$ [38]. In comparison with $LiBH_4$ or $Mg(BH_4)_2$ the dual-cation borohydride $Li/Mg(BH_4)_3$ is expected to have some differences in the evolution of diborane due to the possible change of the decomposition pathways. In this study, we will investigate the releases of diborane and H_2 in the decomposition of the dual-cation borohydride, $Li/Mg(BH_4)_3$, using a direct line-of-site residual gas analyzer mass-spectrometer (RGA-MS) as well as crystal structure determination. The bimetallic borohydride $Li/Mg(BH_4)_3$ was successfully infiltrated into a highly ordered nanoporous hard carbon by melt infiltration. The effects of nanoconfinement on the de/re-hydrogenation and diborane/triborane release will also be studied for the first time.

EXPERIMENTAL SECTION

$Mg(BH_4)_2$ (95%, Aldrich) was heat treated under 200 °C and 60 bar H_2 for 4 hours to remove any remaining solvents. Bimetallic borohydride, $Li/Mg(BH_4)_3$, was prepared by a mechanical milling of $LiBH_4$ (95%, Aldrich) and heat-treated $Mg(BH_4)_2$ and a subsequent annealing. In a typical procedure, 1.0g mixture of $LiBH_4/Mg(BH_4)_2$ (molar ratio=1:1) was milled with 6 WC balls in a WC milling pod for about 60 minutes under 0.1MPa Ar, and subsequently annealed at 150°C under 60 bar H_2 for 12 hours.

Highly ordered porous carbons (NPC) were prepared according to a well established method [38-39]. The preparation method of nanoporous carbon used in this study was similar to NPC-4nm except that the calcination temperature was 800°C [38]. Before infiltration, the prepared nanoporous carbon templates were first dried at 900°C for 5 hours under flowing Ar and then dried at 450°C under vacuum. Subsequently, the dried nanoporous carbon was impregnated with $Li/Mg(BH_4)_3$ by a melt infiltration method. In a typical process, a 200 mg mixture of $Li/Mg(BH_4)_3$ and carbon template (hydride: 20 wt%) was loaded into a sample holder in an argon-filled glove box. The sample holder was subsequently attached to a fixed-volume Sievert's-type instrument

without exposing the sample to air. The sample holder was heated to 200ºC under about 60 bar H_2 then kept at this temperature for 30 min. The pre-melted sample was hereafter referred to as Li/$Mg(BH_4)_3$@NPC.

X-ray diffraction (XRD) was performed on a Rigaku Ultima IV multipurpose X-ray diffraction (XRD) system with Cu K_α radiation source. Samples containing hydrides were covered with parafilms to prevent the samples from contacting air or moisture during the XRD experiments. FT-IR spectra were collected using Nicolet 6700. Two KBr polished discs were used to hold the powered samples. A direct line-of-site RGA-MS was used to characterize gas desorption species. The RGA-MS system is separated into a HV (10^{-8}~10^{-5} Torr) sample chamber and UHV (10^{-9}~10^{-7} Torr) gas analysis chamber. The species partial pressure per gram of Li/$Mg(BH_4)_3$ was used for comparisons. The details of the measurement can be found in an earlier publication [23]. SA3100 analyzer (Coulter) was used to measure nitrogen adsorption isotherms for NPC carbons at 77 K. Before analysis, the sample of porous carbon was out gassed for 1 h at 300°C under vacuum. Using adsorption data, Brunauer-Emmett-Teller (BET) and Barrett-Joyner-Halenda (BJH) methods were used to calculate surface areas and pore size distributions. The BET method was used to calculate the specific surface areas (S_{BET}) using adsorption data in a relative pressure range from 0.05 to 0.2 bar. The total pore volume was estimated from the adsorbed amount at a relative pressure *P/P*0 of 0.98 based on the BJH calculation model.

RESULTS AND DISCUSSION

The Phase Formation of Dual-cation Borohydride Li/$Mg(BH_4)_3$. Figure 1 show XRD patterns of as received $LiBH_4$ (a), as received $Mg(BH_4)_2$ (b), heat treated $Mg(BH_4)_2$ (c), ball milled mixture of $LiBH_4$/$Mg(BH_4)_2$ (d), and ball milled/heat-treated $LiBH_4$/$Mg(BH_4)_2$ (e). As shown in Figure 1, the as received $Mg(BH_4)_2$ is the γ-phase reported in an earlier publication [40]. Mass spectrometer analysis shows that as received $Mg(BH_4)_2$ produces a significant amount of diborane at a lower decomposition temperature (~240°C), as shown in Figure S1. The γ-phase is evidently not the ground state [41]. To obtain the β-phase, the as received $Mg(BH_4)_2$ was heated at 200 °C under

60 bar H_2, and then it was cooled to room temperature. After the treatment it transformed to β-$Mg(BH_4)_2$ (high temperature phase), as shown in Figure 1(c). The heat treated $Mg(BH_4)_2$ was used for the following experiments. After ball milling the mixture of $LiBH_4$/$Mg(BH_4)_2$ and a subsequent annealing at 150°C under 60 bar H_2 the main phase becomes α-$Mg(BH_4)_2$ with a minority of β-$Mg(BH_4)_2$. This indicates that $LiBH_4$ was dissolved into $Mg(BH_4)_2$ and Li/$Mg(BH_4)_3$ mainly formed a eutectic structure similar to that of α-$Mg(BH_4)_2$. This is similar to what was observed in Bardaji's study, which showed that after ball milling and annealing of $LiBH_4$/$Mg(BH_4)_2$ the Bragg peaks can be indexed to α-$Mg(BH_4)_2$ or β-$Mg(BH_4)_2$ [35]. They also proposed that Li/$Mg(BH_4)_3$ was not a new compound but formed a eutectic phase with a low melting point (~180°C). A similar study about the eutectic composition of $LiBH_4$/$Ca(BH_4)_2$ was also reported by Lee [27]. Therefore, we note that the compound studied here is a physical mixture of $LiBH_4$ and $Mg(BH_4)_2$, and is denoted Li/$Mg(BH_4)_3$.

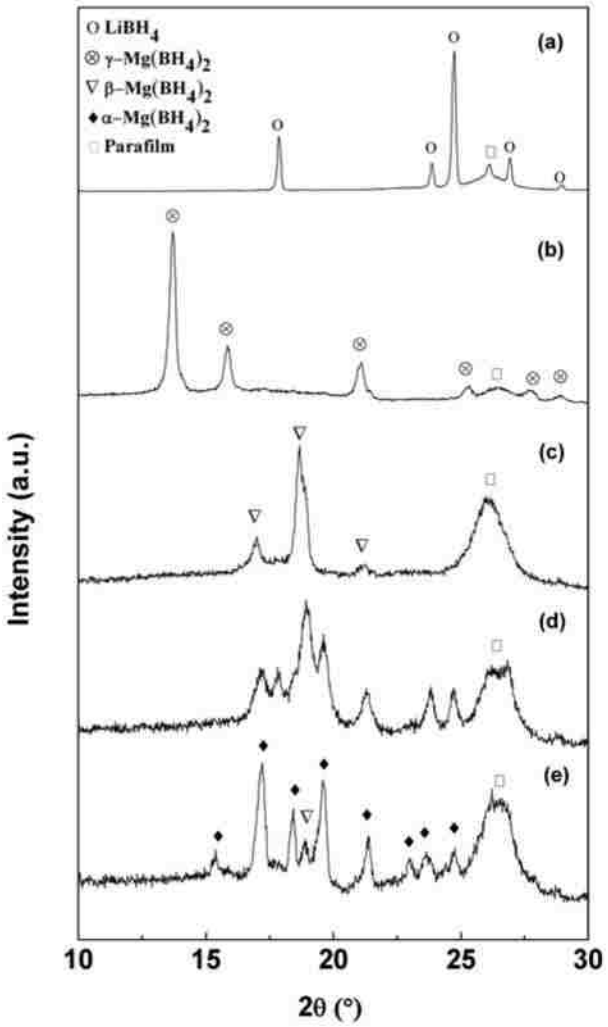

Figure 1. XRD patterns of as received $LiBH_4$ (a), as received $Mg(BH_4)_2$ (b), heat-treated $Mg(BH_4)_2$ (c), ball milled mixture of $LiBH_4/Mg(BH_4)_2$ (d), and ball milled/heat-treated $LiBH_4/Mg(BH_4)_2$ (e).

The Decomposition Behavior and Diborane/Triborane Release of the Dual-cation Borohydride $Li/Mg(BH_4)_3$. Figure 2 shows the desorption curves of as received $LiBH_4$, heat treated $Mg(BH_4)_2$ and $Li/Mg(BH_4)_3$, respectively. The measurements were performed using a fixed volume Sieverts-type apparatus. The samples were heated to 400°C under an initial static vacuum of 1×10^{-5}bar. As shown in Figure 2, the decomposition temperature of $Li/Mg(BH_4)_3$ is between that of $LiBH_4$ and $Mg(BH_4)_2$. This is similar to what was observed in the previous study about $LiK(BH_4)_2$. The decomposition temperature of $LiK(BH_4)_2$ was between that of $LiBH_4$ and KBH_4.

Different from $LiBH_4$ and $Mg(BH_4)_2$, the decomposition curve of $Li/Mg(BH_4)_3$ shows two obvious steps. The first step and the second step start at 230°C and 310°C, respectively.

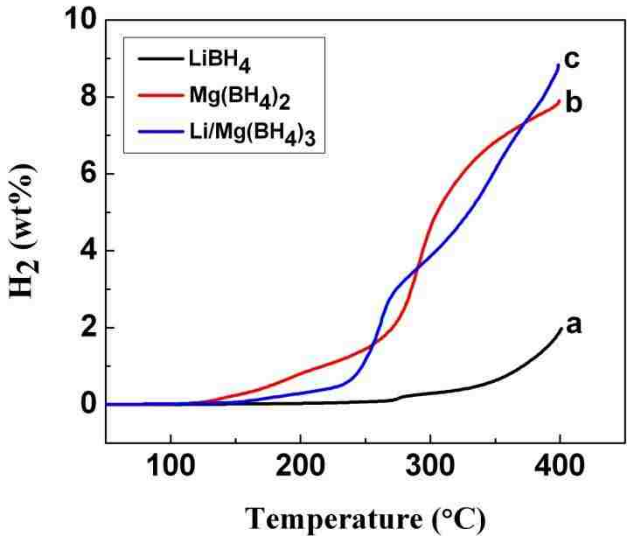

Figure 2. Desorption curves of as received $LiBH_4$ (a), as received $Mg(BH_4)_2$ (b), and $Li/Mg(BH_4)_3$ (c).

The H_2 and diborane or triborane release, per gram of $Li/Mg(BH_4)_3$, on decomposition were analyzed using a direct line-of-site RGA-MS. We assume that the masses from m/z=39-43 in RGA-MS data represent the triborane ions, which have masses in this range [42]. Figure 3 compares the H_2, diborane and triborane releases of as received $LiBH_4$, heat-treated $Mg(BH_4)_2$ and as prepared $Li/Mg(BH_4)_3$, respectively. As shown in Figure 3, a large quantity of diborane is emitted during the decomposition of $Mg(BH_4)_2$ and $LiBH_4$.

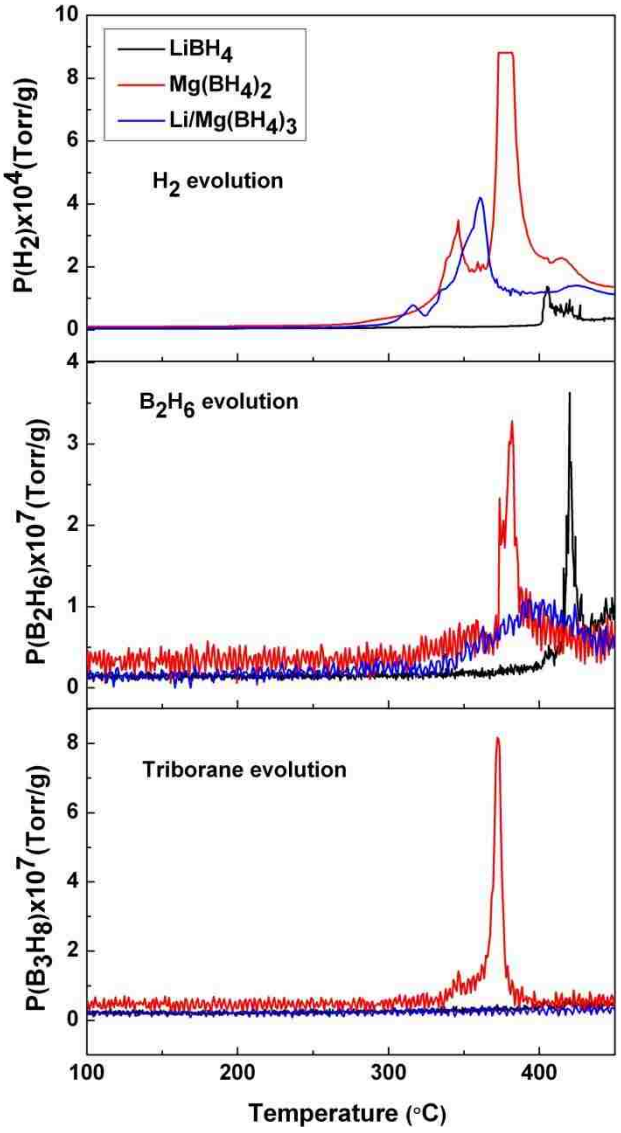

Figure 3. H_2, diborane and triborane release of as received $LiBH_4$ (*lowest of first and third figures*), $Li/Mg(BH_4)_3$,and heat treated $Mg(BH_4)_2$ (*tallest peak in fist and third, and first peak in second*), respectively.

Figure 4 shows the cracking pattern of $Li/Mg(BH_4)_3$ at the peak of diborane release. Interestingly, much less diborane and no detectable triborane is released during the decomposition of $Li/Mg(BH_4)_3$ indicating the reaction pathway relating to diborane or triborane formation was suppressed. From the H_2 release plots we can see that $Li/Mg(BH_4)_3$ mainly has two H_2 release peaks at 316°C and 360°C. This is in agreement with the two step dehydrogenations measured by Sieverts-type apparatus. The

temperature differences are a result of the pressure differences between the two measurement systems, with the RGA-MS measurement being under higher vacuum. Soloveichik et al. studied the decomposition of $Mg(BH_4)_2$ using thermal desorption, calorimetry, in situ X-ray diffraction, and solid state NMR [40]. They proposed a four-stage decomposition pathway and suggested hydrogen release from $Mg(BH_4)_2$ occurred in at least four steps via the formation of several polyborane intermediate species (B_nH_m). Triborane formation during the dehydrogenation process of $Mg(BH_4)_2$ was also reported in a recent publication [43]. Using RGA-MS we did detect diborane as well as some other possible polyborane species (B_nH_m, possibly B_2H_7 and B_3H_8) during the decomposition of $Mg(BH_4)_2$. Figures 5a and 5b shows the cracking patterns of $Mg(BH_4)_2$ at the diborane evolution peaks (377°C and 382°C respectively) with the published diborane cracking pattern (NIST) as a reference [44]. Figure 5a shows the end of the evolution of triborane with the beginning of the evolution of diborane. While Figure 5b shows that the production of triborane has ended and that the diborane has continued to evolve. The evolution of triborane is accompanied by the masses in the spectrum 15, 16 and 26 through 29 which may be a previously unidentified species diborane(7) (B_2H_7). In a first principles computational paper by Fichtner et al. diborane(7) appears as H_3BHBH_3 [45]. As can be seen in Figure 6, this mass is present in the cracking pattern of the diborane release of $LiBH_4$ with similar mass ratios, but is not nearly as abundant as it is in $Mg(BH_4)_2$, and so has not been previously reported. Earlier results failed to mention this peak at m/z = 28 since it also corresponds with CO and N_2 spectra, but in Figure S2 it can be seen that it evolves in the temperature range of diborane production in the pure as well as mixed materials. This may be the ion $(B_2H_6)^+$ which could be produced when B_2H_7 loses an H^- during electron impact ionization.. We also compared the H_2, diborane and triborane releases of heat treated $Mg(BH_4)_2$ measured at different ramps with 16, 8, 4 and 1°C/min, respectively. As shown in Figure S3, diborane and triborane were both emitted under the different ramps. When the ramp is 16°C/min most of $Mg(BH_4)_2$ has not decomposed which is responsible for the small H_2 and borane releases.

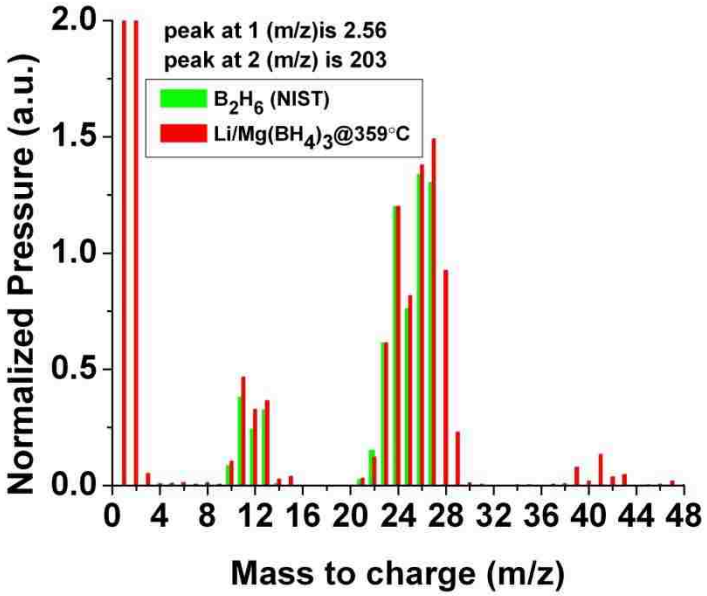

Figure 4. The cracking patterns of heated $Li/Mg(BH_4)_3$ at the B_2H_6 release peak (359°C) with the published diborane cracking pattern (*left bars*) [44].

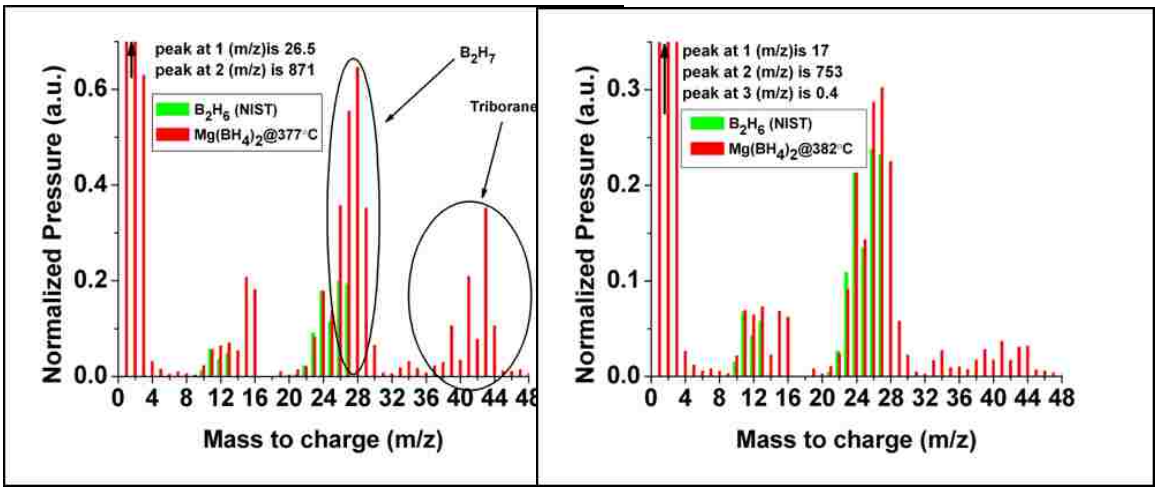

Figure 5. The standard cracking pattern of B_2H_6 (*left bars*) shown with those of (left) $Mg(BH_4)_2$ at 377°C, indicating species larger than B_2H_6, and (right) decomposition at 382°C, where only B_2H_6 is evident.

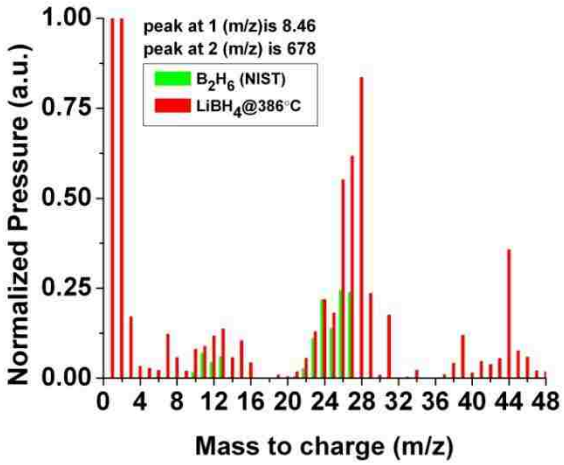

Figure 6. The cracking patterns of heated $LiBH_4$ at the B_2H_6 release peak at 386°C with the published diborane cracking pattern (*left bars*).

The Effects of Nanoconfinement on the Decomposition and H_2 / Diborane Releases of $Li/Mg(BH_4)_3$. Two earlier studies both reported that the melting point of $Li/Mg(BH_4)_3$ was around 180 °C [34-35]. In this study, the as synthesized $Li/Mg(BH_4)_3$ was infiltrated into nanoporous carbon under 200°C and 60 bar H_2. Brunauer-Emmett-Teller (BET) and Barrett-Joyner-Halenda (BJH) methods were used to analyze texture structures of neat porous carbon template and the impregnated carbon. Figure 7 (a) shows the nitrogen sorption isotherms of neat NPC and pre-melted $Li/Mg(BH_4)_3$@NPC. The specific surface areas (S_{BET}) of neat NPC and the total pore volume calculated by the BJH model were 1012 m^2/g and 0.65 cm^3/g respectively. After the infiltration of $Li/Mg(BH_4)_3$, the specific surface area and the total pore volume of $Li/Mg(BH_4)_3$@NPC were considerably reduced to 461 m^2/g and 0.32cm^3/g respectively, indicating the filling or blocking of the pores by $Li/Mg(BH_4)_3$. The pore size distribution before and after the infiltration of $Li/Mg(BH_4)_3$ are shown in Figure 7 (b). The distribution peak has a slight shift to the small size area after the infiltration of hydride into NPC and the value at the pore size distribution peak is reduced from 4.4 nm to 4.2nm due to the filling of the pores. The pore size distribution peak after the infiltration is still narrow indicating a possibly homogenous filling.

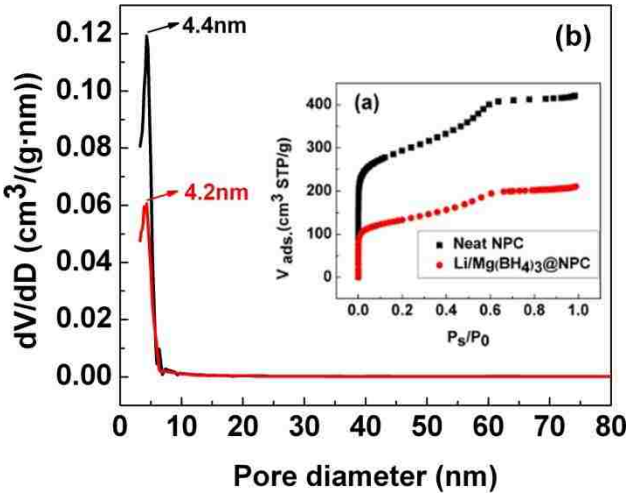

Figure 7. Inset (a) nitrogen sorption isotherms of neat NPC (*top curves*) with a surface area and pore volume of 1012 m^2/g and 0.65 cm^3/g respectively, and nanoconfined $Li/Mg(BH_4)_3$@NPC with a surface area and pore volume of 461 m^2/g and 0.32 cm^3/g, respectively; (b) pores size distribution of neat NPC and pre-melted $Li/Mg(BH_4)_3$@NPC.

Figure 8 compares the X-ray diffraction patterns of $Li/Mg(BH_4)_3$ before and after infiltration. In comparison with the as synthesized $Li/Mg(BH_4)_3$ the nanoconfined $Li/Mg(BH_4)_3$ in highly ordered nanoporous carbon ($Li/Mg(BH_4)_3$@NPC) does not show Bragg peaks of $Li/Mg(BH_4)_3$ indicating that $Li/Mg(BH_4)_3$ becomes amorphous after infiltration into NPC. $LiBH_4$ also becomes amorphous after infiltration into the highly ordered nanoporous carbon [38]. Fourier transform infrared spectroscopy was used to confirm the existence of $[BH_4^-]$ in the pre-melted sample of $Li/Mg(BH_4)_3$@NPC. As shown in Figure 9, the spectra indicate B-H bending modes at 1100 cm^{-1} and stretching modes around 2200-2300 cm^{-1} of $[BH_4^-]$,respectively, indicating the existence of $[BH_4^-]$.

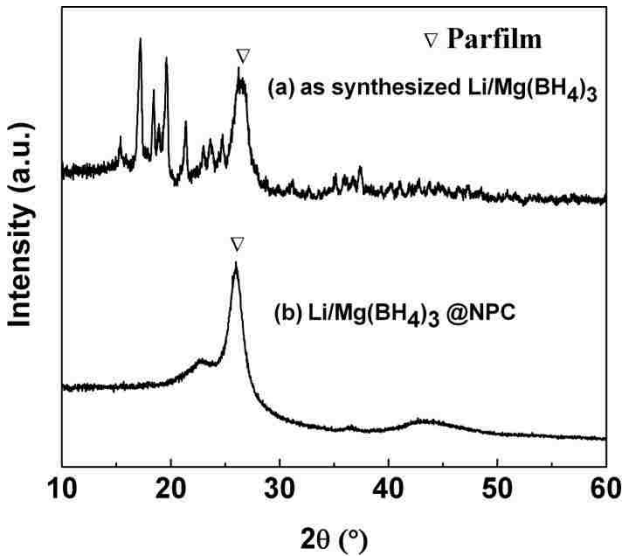

Figure 8. X-ray diffraction patterns of $Li/Mg(BH_4)_3$ before and after infiltration into NPC.

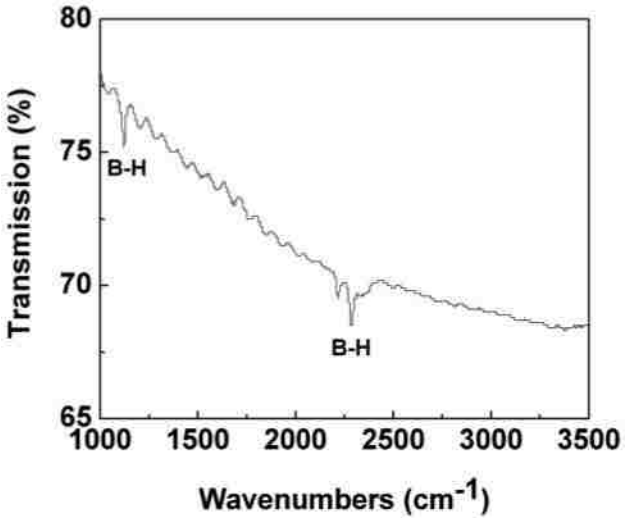

Figure 9. FT-IR spectra of pre-melted $LiBH_4$@NPC. $[BH_4]$- bands indicates the existence of $Li/Mg(BH_4)_3$.

The absorption/desorption cycles of $Li/Mg(BH_4)_3$ and $Li/Mg(BH_4)_3$@NPC were performed using a fixed-volume Sieverts-type apparatus. $Li/Mg(BH_4)_3$ and $Li/Mg(BH_4)_3$@NPC were heated up to 400°C and 350°C at the same temperature ramp. As shown in Figure 10, the $Li/Mg(BH_4)_3$@NPC shows an improved kinetics and the

decomposition temperature of $Li/Mg(BH_4)_3$@NPC was about 70°C lower than that of bulk $Li/Mg(BH_4)_3$. The decomposed sample was subsequently rehydrided under 60 bar H_2 and 350°C.

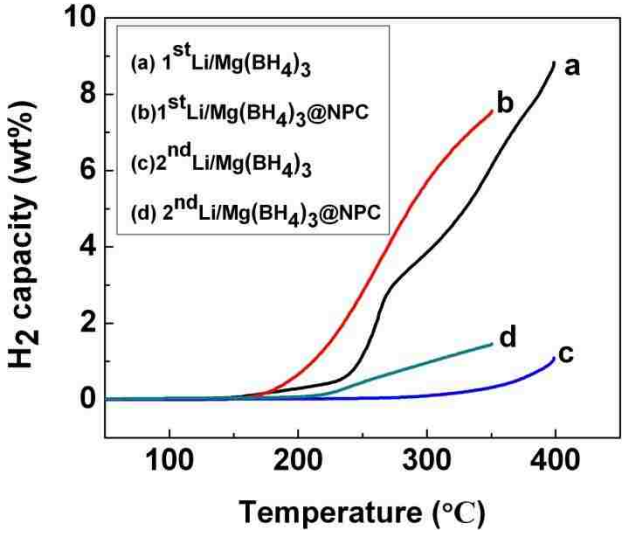

Figure 10. Desorption curves of as prepared $Li/Mg(BH_4)_3$ and the pre-melted $Li/Mg(BH_4)_3$@NPC with an initial loading of 20wt%.

Figure 11 compares the H_2, diborane and triborane releases of $Li/Mg(BH_4)_3$ and $Li/Mg(BH_4)_3$@NPC, per gram of $Li/Mg(BH_4)_3$, during the decomposition. Interestingly, $Li/Mg(BH_4)_3$@NPC has *more* diborane release than bulk $Li/Mg(BH_4)_3$. This is in stark contrast to what is observed in our previous study of nanoconfined $LiBH_4$. In that study, the release of diborane was *suppressed* through nanoconfinement of $LiBH_4$ in highly ordered nanoporous carbon. From the H_2 release plot we can see that $Li/Mg(BH_4)_3$@NPC has a lower H_2 release temperature than $Li/Mg(BH_4)_3$. But the H_2 was released in a different way indicating that the decomposition pathway of $Li/Mg(BH_4)_3$ was changed by nanoconfinement.

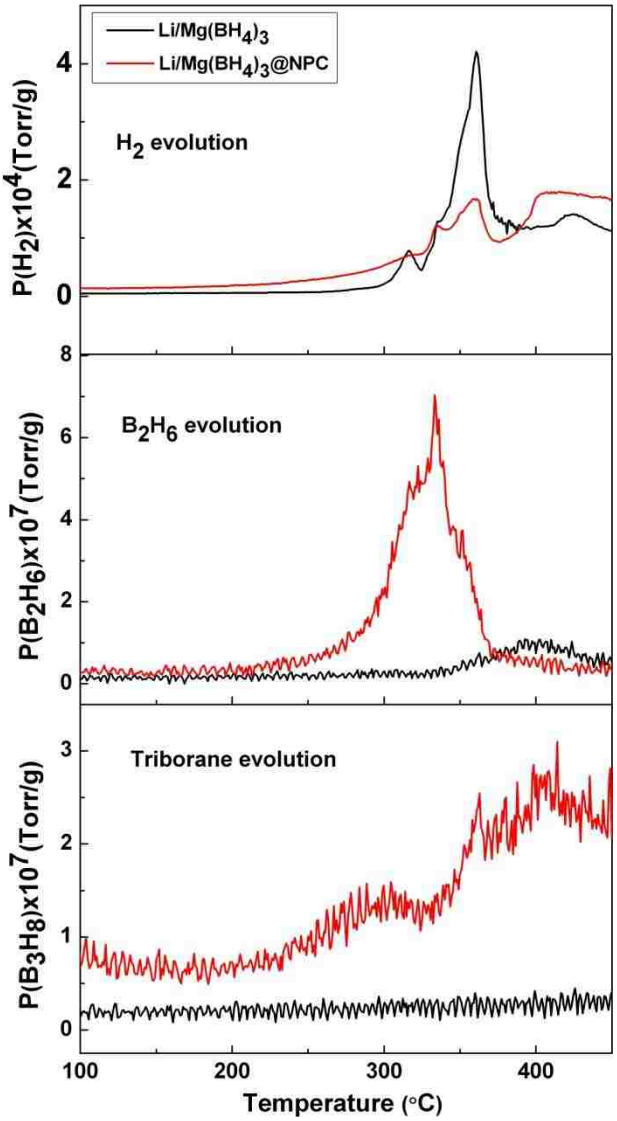

Figure 11. H_2, diborane and triborane release with increasing temperature for as prepared Li/$Mg(BH_4)_3$ (*top peak in first figure and bottom curve in next 2 figures*) and nanoconfined Li/$Mg(BH_4)_3$@NPC.

CONCLUSION

Li/$Mg(BH_4)_3$ mainly forms an eutectic structure similar to that of α-$Mg(BH_4)_2$ and the decomposition temperature of Li/$Mg(BH_4)_3$ lies between that of $LiBH_4$ and $Mg(BH_4)_2$. The diborane release analysis by a direct line-of-site residual gas analyzer mass spectrometer (RGA-MS) indicates that in comparison with $LiBH_4$ and $Mg(BH_4)_2$ less diborane and no detectable triborane released during the decomposition of

$Li/Mg(BH_4)_3$. $Li/Mg(BH_4)_3$ was successfully infiltrated into the highly ordered nanoporous carbon by melt method and the nanoconfined $Li/Mg(BH_4)_3$ shows a lower decomposition temperature as well as a higher cycling capacity but releases a little higher amount of diborane in comparison with the as-prepared $Li/Mg(BH_4)_3$.

ACKNOWLEDGMENT.

This work was funded by the U.S. Department of Energy in the Hydrogen, Fuel Cells, and Infrastructure Technologies Program through the office Energy Efficiency and Renewable Energy under Contract No. DE-AC04-94AL85000. Funding also provided by "Hundred Talents Project" of the Chinese Academy of Sciences and the National Basic Research Program of China (973 Program, 2010CB833101).

REFERENCES

[1] Schlapbach, L.; Züttel, A. *Nature* 2001, *414*, 353.

[2] Ritter, J. A.; Ebner, A. D.; Wang, J.; Zidan, R. *Materials Today* 2003, *6*, 18.

[3] Mandal, T. K.; Gregory, D. H. Annu. Rep. Prog. Chem., Chem., Sect. A, 2009, 105, 21.

[4] Graetz,J. *Chem. Soc. Rev.*, 2009, *38*, 73.

[5] Eberle, U.; Felderhoff, M.; Schuth, F. Angew. *Chem. Int. Ed.* 2009, *48*, 6608.

[6] Orimo, S.; Nakamori, Y.; Eliseo, J. R.; Züttel, A.; Jensen, C. M. *Chem. Rev*. 2007, *107*, 4111.

[7] Felderhoff, M., Weidenthaler, C., von Helmolt, R., Eberle, U. *Phys Chem Chem Phys*, 2007, 9, 2643.

[8] Grochala, W.; Edwards, P. P. *Chem. Rev.* 2004, 104, 1283.

[9] Bogdanović, B.; Schwickardi, M. *J. Alloys Compd.* 1997, 253, 1.

[10] Orimo, S.; Nakamori, Y.; Kitahara, G.; Miwa, K.; Ohba, N.; Towata,S.; Züttel, A. *J.Alloys.Compd.* 2005, *404-406*, 427.

[11] Soloveichika, G. L.; Gao,Y.; Rijssenbeek, J.; Andrus,M.; Kniajanski, S.; Bowman, Jr. R. C.; Hwang, S.; Zhao, J. C. *J. International Journal of Hydrogen Energy*. 2009, *34*, 916.

[12] Severa,G.; Ronnebrow, E.; Jensen, C. M. *Chem. Commun.* 2010, *46*, 421.

[13] Li, H. W.; Kikuchi,K.; Nakamori, Y.; Ohba, N.; Miwa, K.; Towata, S.; Orimo, S. *Acta Materialia* 2008,56, 1342.

[14] Au, M.; Jurgensen, A. R.; Spencer, W. A.; Anton, D. L.; Pinkerton, F. E.; Hwang, S. J.; Kim, C.; Bowman, Jr., R. C. *J. Phys. Chem. C* 2008,*112*, 18661.

[15] Vajo, J. J.; Skeith, S. L.; Mertens, F. *J. Phys. Chem. B* 2005, *109*, 3719.

[16] Yang, J.; Sudik, A.; Wolverton, C. *J. Phys. Chem. C* 2007,*111*, 19134.

[17] Au, M.; Jurgensen, A. *J. Phys. Chem. B* 2006, *110*, 7062.

[18] Mauron, P.; Buchter, F.; Friedrichs, O.; Remhof, A.; Bielmann, M.; Zwicky, C. N.; Züttel, A. *J. Phys. Chem. B* 2008, *112*, 906.

[19] Newhouse, R. J.; Stavila,V.; Hwang, S. J.; Klebanoff, L. E.; Zhang, J. Z. *J. Phys. Chem. C* 2010,*114*, 5224.

[20] Gross, A. F.; Vajo, J. J.; Van Atta, S. L.; Olson, G. L. *J. Phys.Chem. C* 2008, *112*, 5651.

[21] Ngene, P.; Adelhelm, P.; Beale, A. M.; de Jong, K. P.; de Jongh, P. E. *J. Phys. Chem. C* 2010, *114*, 6163.

[22] Gao, J.; Adelhelm,P.; Verkuijlen, M. H. W.; Rongeat, C.; Herrich, M.; van Bentum, P. J. M.; Gutfleisch,O.; Kentgens, A. P. M.; de Jong,K. P.; de Jongh, P. E. *J. Phys. Chem. C* 2010, *114*, 4675.

[23] Liu, X.; Peaslee, D.; Jost, C. Z.; Majzoub, E. H. *J. Phys. Chem. C* 2010, *114*, 14036.

[24] Nielsen, T. K.; Bösenberg, U.; Gosalawit, R.; Dornheim,M.; Cerenius,Y.; Besenbacher, F.; Jensen, T. R. *ACS Nano* 2010, *4*, 3903.

[25] Fichtner, M.; Zhao-Karger, Z.; Hu,J.; Roth, A.; Weidler, P. *Nanotechnology* 2009, *20*, 204029.

[26] Cerny, R.; Kim, K. C.; Penin,N.; D'Anna,V.; Hagemann,H.; Sholl, D. S. *J. Phys. Chem. C* 2010, *114*, 19127

[27] Lee, J.; Ravnsbæk, D.; Lee,Y. S.; Kim,Y.; Cerenius,Y.; Shim, J. K.; Jensen,T. R.; Hur, N. H.; Cho. Y. W. *J. Phys. Chem. C* 2009, *113*, 15080.

[28] Seballos, L.; Zhang, J. Z.; Ronnebro, E.; Herberg, J. L.; Majzoub, E. H. *Journal of Alloys and Compounds* 2009,*476*, 446.

[29] Cerny,R.; Severa,G.; Ravnsbæk,D. B.; Filinchuk, Y.; D'Anna,V.; Hagemann,H.; Haase, D.; Jensen, C. M.; Jensen, T. R. *J. Phys. Chem. C* 2010, *114*, 1357.

[30] Nakamori, Y.; Li, H. W.; Matsuo, M.; Miwa, K.;Towata,S.; Orimo, S. *Journal of Physics and Chemistry of Solids* 2008, *69*, 2292.

[31] Nickels, E. A.; Jones, M. O.; David,W. I. F.; Johnson, S. R.; Lowton, R. L.; Sommariva, M.; Edwards, P. P. *Angew. Chem. Int. Ed.* 2008, *47*, 2817.

[32] Xiao, X. B.; Yu, W. Y.; Tang, B. Y. *J. Phys.: Condens. Matter* 2008, *20*, 445210.

[33] Fang, Z. Z.; Kang, X. D.; Luo, J. H.; Wang, P.; Li, H. W.; Orimo, S. *J. Phys. Chem. C* 2010, *114*, 22736.

[34] Fang, Z. Z.; Kang, X. D.; Wang, P.; Li, H. W.; Orimo, S. *Journal of Alloys and Compounds* 2010, *491*, L1.

[35] Bardaji,E. G.; Zhao-Karger,Z.; Boucharat,N.; Nale,A.; van Setten,M. J.; Lohstroh,W.; Rohm,E.; Catti,M.; Fichtner, M. *J. Phys. Chem. C* 2011, *115*, 6095.

[36] Nale, A.; Catti, M; Bardajı´, E.G.; Fichtner, M. *International Journal of Hydrogen Energy.* 2011, *36*, 13676.

[37] Kostka, J.; Lohstroh,W.; Fichtner, M.; Hahn, H. *J. Phys. Chem. C* 2007, *111*, 14026.

[38] Liu, X.; Peaslee, D.; Jost, C. Z.; Baumann, T. F.; Majzoub, E. H. *Chem. Mater*. 2011, *23*, 1331.

[39] Meng, Y.; Gu, D.; Zhang, F.; Shi, Y.; Cheng, L.; Feng, D.; Wu, Z.; Chen, Z.; Wan, Y.; Stein, A.; Zhao, D. *Chem. Mater*. 2006, *18*, 4447.

[40] Soloveichika, G. L.; Andrus, M.; Gao,Y.; Rijssenbeek, J.; Zhao, J. C.; Kniajanski, S. *J. International Journal of Hydrogen Energy*. 2009, *34*, 2144.

[41] Filinchuk, Y.; Richter, B.; Jensen, T. R.; Dmitriev, V.; Chernyshov, D.; Hagemann, H. *Angew. Chem. Int. Ed.* 2011, 50, 11162.

[42] Greenwood, N. N.; Greatrex, R. *Pure and Applied Chemistry*. 1987, 59, 857.

[43] Chong, M.; Karkamkar, A.; Autrey, T.; Orimo, S.; Jalisatgi, S.; Jensen, C. M. *Chem. Commun.* 2011, *47*, 1330.

[44] Linstrom, P. J.; Mallard, W.G. NIST Chemistry WebBook, NIST Standard Reference Database Number 69. http://webbook.nist.gov, (retrieved April 5, 2012)

[45] van Setten, M. J.; Lohstrohb, W.; Fichtner, M. *J. Mater. Chem.* 2009, 19, 7081.

SECTION

4. CONCLUSIONS

The Temperature Programmed Decomposition Mass Spectrum Residual Gas Analyzer was used in conjunction with other characterization techniques, to identify key issues affecting various hydrogen storage systems. The most critical of which is the production of unwanted gasses during decomposition. This enabled us to gain insight into the specific effect that modifications had on a particular metal hydride.

For instance, with $NaAlH_4$ we showed that the high H_2 pressure pretreatment does have an effect on lowering the decomposition temperature, as well as potentially reducing the total amount of NaH lost as a gas. Additionally, the primary decomposition step shows that there may be a secondary interaction that releases more hydrogen. This may be due to oxygen impurities, or potentially a side interaction with $NaAlH_4$ and Na_3AlH_6. Further studies could focus on tests of purity to compare the stated theoretical results with measurements.

For infiltrated nanoporous carbons, we have shown similar improvements in the materials of $LiBH_4$, $Li/Mg(BH_4)_3$, and $Li_4BN_3H_{10}$. Our highly ordered hexagonally packed carbons have been thoroughly characterized. This provides us with an accurate knowledge of just how much hydride is in the system.

For $LiBH_4$, we have successfully infiltrated 20 wt. % by mass into the 4 nm NPC. This corresponds to a potential hydrogen capacity of 3.6% for total decomposition and 2.7% for partial decomposition to LiH, B, and H_2. Potentially this exceeds the DOE specified goals for 2015. We have also shown that the co-generation of diborane is related to pore size, and can be effectively eliminated in the decomposition of $LiBH_4$. Nanoconfinement has also led to a lowered decomposition temperature and a loss of observable crystallinity in the material.

To characterize the metal hydride $Li_4BN_3H_{10}$, we have extensively studied its precursors $LiBH_4$ and $LiNH_2$. The results are interesting in that the decomposition temperature is reduced by almost 75 °C from $LiNH_2$. Unfortunately, much more

ammonia is released in the reaction than in the $LiNH_2$ alone. Less diborane is formed, but other gasses have been identified that had not previously been reported, such as N_2H_2. We have shown that nanoconfinement greatly improves the kinetics of this material. In the 4 nm NPC the rate of H_2 evolution seems to have increased, the temperature of evolution has decreased by ~50 °C, and the diborane has been eliminated from the decomposition pathway. Unfortunately, although the ammonia production has also been reduced, the temperature at which it evolves has been lowered by ~100 °C. Nanoconfinement may have drastically affected the decomposition pathway here, as multiple distinct hydrogen and ammonia decomposition peaks are observed, when in bulk form, there are mainly single peaks.

$Li/Mg(BH_4)_3$, the amalgamation of two borohydrides, has shown similar promising results. When studied alone, each material generates an unwanted gas, but when physically combined and decomposed, the amalgamated material shows a reduction in both of the gases diborane and triborane. Here, nanoconfinement does reduce the decomposition temperature, but for some reason the release of the byproduct gasses actually increases. This may be due to surface interactions with the carbon, that for the other materials do not manifest. Further studies on the pore size effect on this material may shed some light into the decomposition pathways that are taken here.

Future improvements to the MS-RGA may include a calibration technique that would enable us to measure the exact rate of gas evolution. One aspect that we have not yet used is the QCM measurement abilities built into the system. As this work progresses, and we are able to lower the temperature of decomposition significantly, this calibration will be enabled through the use of the QCM. Decomposition paths, reaction rates, activation energies, and heats of formation, could all be better understood with an accurate measurement of the change in mass as it relates to the partial pressures of the generated gasses.

APPENDIX A.
THERMODYNAMIC APPROXIMATIONS FOR THE MS-RGA SYSTEM

Table A.1. Volume and Surface Area Approximations for MS-RGA Components.

Upper Chamber	Volume in m^3	Area in m^2
RGA Tube	1.8279E-04	0.0208
TP adapter	2.5805E-05	0.0028
Turbo Pump	1.9639E-04	0.0156
4 Way Cross	5.3501E-04	0.0255
Valve	8.5822E-04	0.0944
Ion Gauge	2.1561E-04	0.0228
Nipple	1.3548E-04	0.0146
Adapter	2.5805E-05	0.0039
Total	2.1751E-03	0.2004
Lower Chamber	Volume in m^3	Area in m^2
6 Way Cross	5.2896E-03	0.1877
Adapter	2.5805E-05	0.0028
Ion Gauge	2.1561E-04	0.0228
Adapter	7.0686E-04	0.0283
Turbo Pump	1.7671E-03	0.0707
Total	8.0050E-03	0.3122
Grand Total	1.0180E-02	0.5126

The thermodynamics describing the flow through the small orifice between the upper UHV and the lower HV chambers can be approximated by assuming that the pressures are low enough so that no molecular interactions occur. The pressures in the lower HV chamber range from 10^{-7} to 10^{-5} Torr. The pressures in the upper UHV system range from 10^{-8} to 10^{-6} Torr. The pressure ratio P_L/P_H for the two chambers range from 0.39 to 0.04, with the lower ratio occurring during sample decomposition.

With these pressure differences the throughput *Q* ranges from $6x10^{-4}$ to $1x10^{-5}$ N-m^3/s according to Equation 1 below. This is on the order of 300 l/s for the maximum mass flow (*C*) through the hole with the gas mass of 2 amu and at 300 K.

$$Q = \frac{1}{4} \nu_{average} \cdot A \cdot (P_1 - P_2) \tag{1}$$

$$C = \frac{Q}{(P_1 - P_2)} \tag{2}$$

$$\nu_{average} = \sqrt{3kT/m} \tag{3}$$

Actual results may vary according to the temperature of the molecule in question, but the upper UHV pump is rated at 48 l/s for H_2. These approximations may give insight into the amount of gas coming from a sample, especially if it could be calibrated to measure an exact mass flow as a function of the pressure in the two chambers.

APPENDIX B.

TEMPERATURE CALIBRATION OF THE HIGH TEMPERATURE SAMPLE STAGE

Appendix B outlines the process for the temperature correction of the high temperature (HT) sample stage of the TPDMSRGA.

The sample chamber is wired with 2 thermocouples (TC) through the electrical feedthroughs on the 6" CFF holding the HT stage. One TC is mounted to the heater block, and measures the temperature at a point on the sample holder approximately 0.1255" from the center of the sample. The second TC is not used during normal operation, but can be used as a reference TC during temperature calibration.

Calibration of the reference TC was done using 2 reference temperatures. All reference measurements were made with the reference TC connected from the USB Temp-AI data logger to the electrical feedthroughs of the CFF, finally into a liquid bath. The first reference temperature was 100 °C, where the reference TC was placed in a bath of boiling water. The second reference temperature was at 290 °C, where the reference TC was placed in a bath of boiling Glycerol.

After calibrating the reference TC, a sample of glass beads in a Tzero pan was prepared. A hole was pierced large enough to insert the TC through the pan lid and into the glass beads. Conduction from the pan to the TC wires was assumed to be negligible. The system was then pumped down for 2 hours to simulate the conditions of a sample run. 4 ramp rates were chosen as the standard ramp rates for the system: 60 °C per hour, 120 °C per hour, 240 °C per hour and 480 °C per hour. For each ramp rate the temperature controller monitored and controlled the ramp rate (as with normal operation), while the data logger monitored the temperature of the sample. The 2 time series were correlated and the corresponding series were charted and curve fitted to produce Figure B.1. The curve fittings are 4th order polynomials in order to minimize errors. These polynomials are used in the MATLAB RGA data analysis software (Appendix C), for temperature calibration.

The sources of error most likely stem from the limited physical contact between the Tzero pan – the sample holder – and the TC of the controller. Therefore with negligible convection it is assumed that the heat transfer occurs by radiative heat transfer and a limited amount of heat conduction. The following settings are general settings which work best for the CalControl 3300 in the RGA system.

Device details

Opc Server = CALControls.CALogixServer

Initial setup

Process units = Deg C

Sensor type = K

Display resolution = 1

Setpoint 1

Setpoint value = 400

Tune mode = PARK

Proportional cycle time mode = Variable

Proportional cycle time value = 0.2

Proportional band = 24

Integral time = 10

Derivative time = 23

Derivative approach control = 3

Derivative sensitivity = 1

Setpoint manual power = OFF

Power level = 0

Power limit = 0

Offset = 0

Set point lock = OFF

Minimum scale value = 0

Maximum scale value = 1200

Programmer

Program Mode = OFF

Program ramp rate = 800

Soak interval = Infinite

Calibration adjustment

Zero offset adjustment = 0

Span offset adjustment. = 0

Output configuration

Setpoint 1 burnout output state = Upscale

Setpoint 2 burnout output state = Upscale

Setpoint 1 output mode = Reversed

Setpoint 2 output mode = Direct

Setpoint 1 indicator state = Non Inverted

Setpoint 2 indicator state = Non Inverted

Diagnosis and settings

Display averaging = 6

Auto tune settings (CT1) = 0

Auto tune settings (CT2) = 0

Auto tune settings (CT3) = 0

Auto tune settings (CT4) = 0

Auto tune settings (CTA) = 0

Auto tune settings (CTB) = 0

Auto tune settings (OS1) = 0

Auto tune settings (OS2) = 0

Auto tune settings (US) = 0

SoftwareVersion = 3300/9300 Version 2

Level lock = None

Program auto exit = Auto

Display communications activity = OFF

Communications settings

MODBUS address = 1

Baud rate = 9600

Data format = 1 Start bit 1 Stop bit 8 Data bits

No Parity

I. Initial Settings

1. Thermocouple type: inPt = K
2. Temperature units: unit = C
3. Relay type: SP1.d = Ssd
4. Tuning tunE = ParK

(Automatic, Park means no power, never set this to on)

II. Communications Settings

1. Unit address Addr = 1
2. Baud rate bAud = 9600
3. Data format dAtA = 18n1

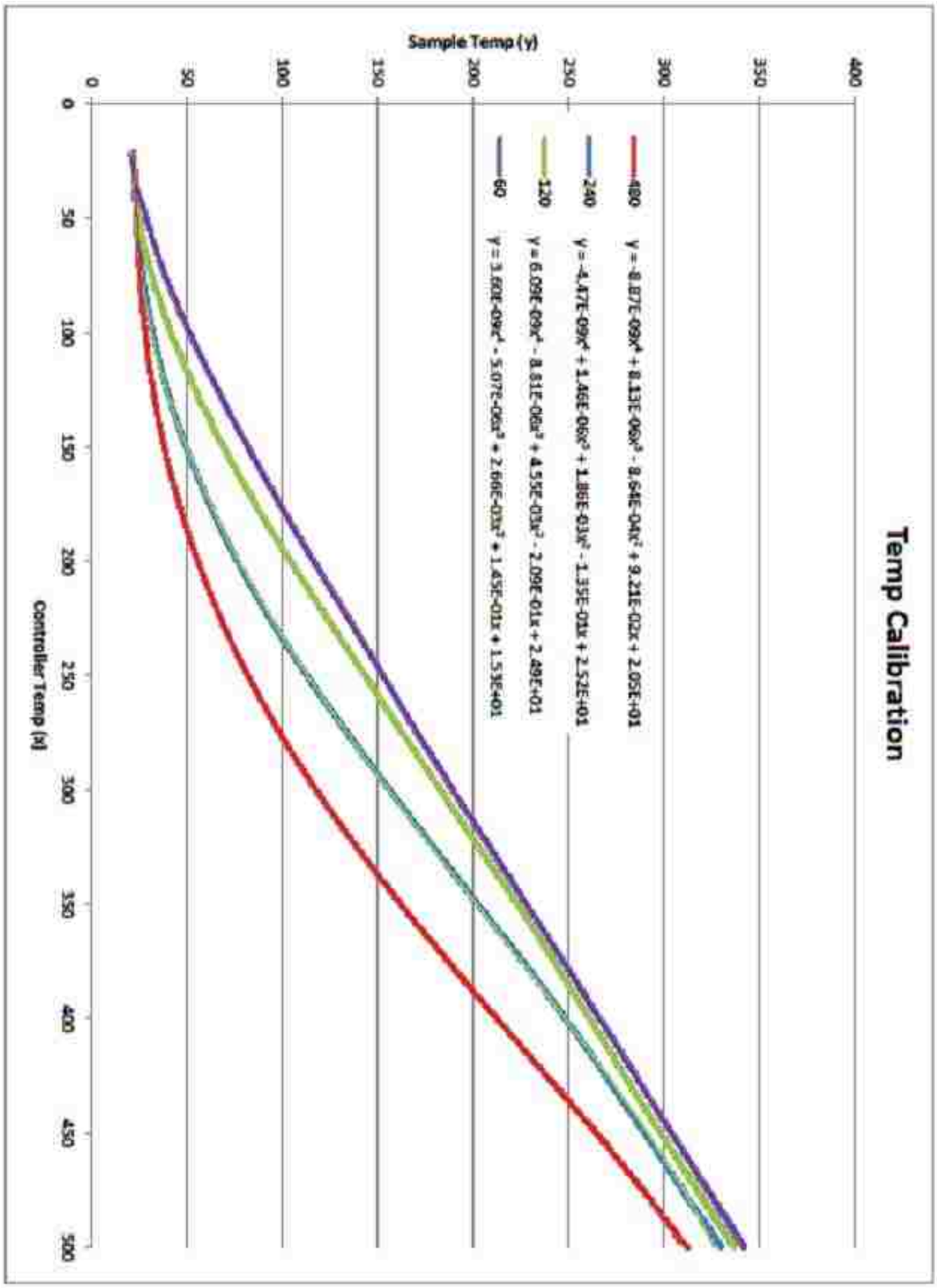

Figure B.1. The temperature calibration curves of 4 different ramp rates. Lines from top to bottom are 60 °C per hour, 120 °C per hour, 240 °C per hour and 480 °C per hour.

APPENDIX C.

OUTLINE OF MATLAB CODE FOR ANALYSIS OF MS-RGA DATA

The RGA analysis software is written using MATLAB R2012b. T. Patrick Sheehan was the major contributor to the code. The software is written to aid in the coloration of the temperature, pressure, and RGA-MS data. The first function inputGUI correlates the time stamped data, applies the temperature correction and outputs a .mat file. This file is then passed to the second function viewerGUI. The second function has various plotting tools available in the GUI (Figure C.1). Figures C.2 and C.3 show the GUIs used in the peak finding algorithm. Figure C.4 shows the output for a background subtracted bar graph at a specified temperature.

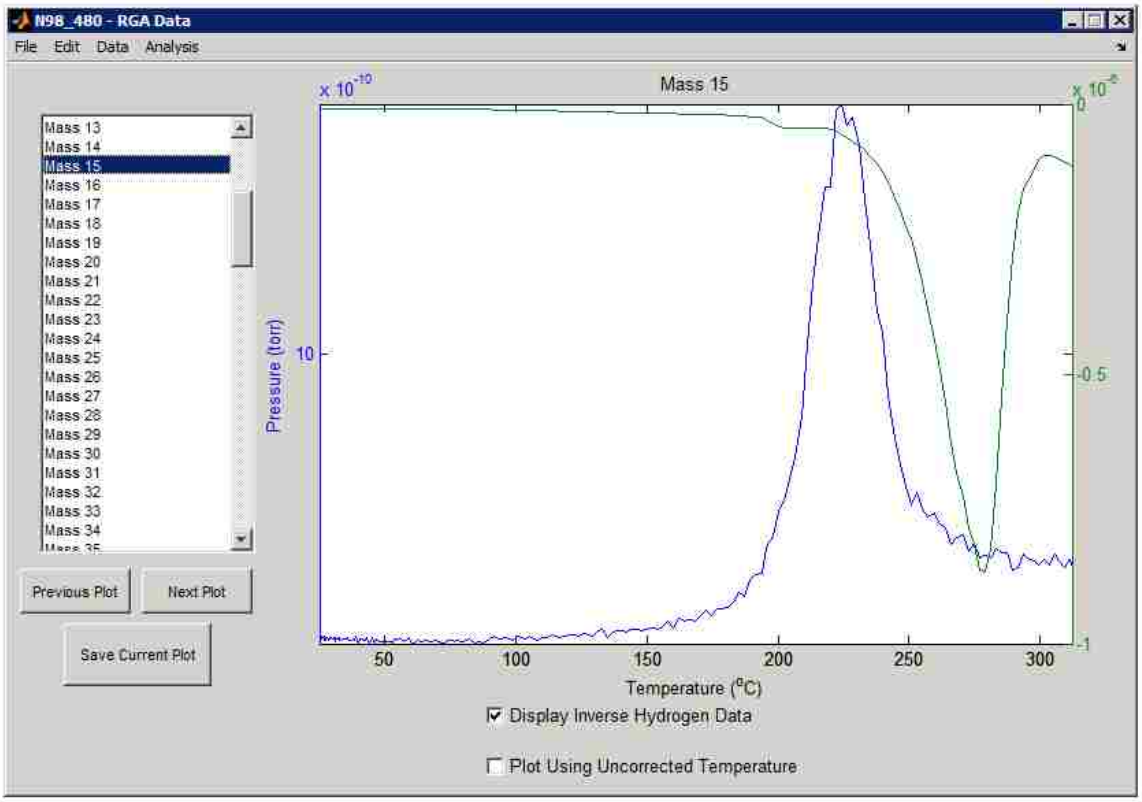

Figure C.1. Output of viewerGUI showing inverse hydrogen data.

```
function varargout = inputGUI(varargin)
% INPUTGUI M-file for inputGUI.fig
%      INPUTGUI, by itself, creates a new INPUTGUI or raises the existing
%      singleton*.
%
%      H = INPUTGUI returns the handle to a new INPUTGUI or the handle to
%      the existing singleton*.
```

```
%
%      INPUTGUI('CALLBACK',hObject,eventData,handles,...) calls the local
%      function named CALLBACK in INPUTGUI.M with the given input arguments.
%
%      INPUTGUI('Property','Value',...) creates a new INPUTGUI or raises the
%      existing singleton*.  Starting from the left, property value pairs are
%      applied to the GUI before inputGUI_OpeningFcn gets called.  An
%      unrecognized property name or invalid value makes property application
%      stop.  All inputs are passed to inputGUI_OpeningFcn via varargin.
%
%      *See GUI Options on GUIDE's Tools menu.  Choose "GUI allows only one
%      instance to run (singleton)".
%
% See also: GUIDE, GUIDATA, GUIHANDLES

% Edit the above text to modify the response to help inputGUI

% Last Modified by GUIDE v2.5 06-Feb-2013 15:03:04

% Begin initialization code - DO NOT EDIT
gui_Singleton = 1;
gui_State = struct('gui_Name',       mfilename, ...
    'gui_Singleton',  gui_Singleton, ...
    'gui_OpeningFcn', @inputGUI_OpeningFcn, ...
    'gui_OutputFcn',  @inputGUI_OutputFcn, ...
    'gui_LayoutFcn',  [] , ...
    'gui_Callback',   []);
if nargin && ischar(varargin{1})
    gui_State.gui_Callback = str2func(varargin{1});
end

if nargout
    [varargout{1:nargout}] = gui_mainfcn(gui_State, varargin{:});
else
    gui_mainfcn(gui_State, varargin{:});
end
% End initialization code - DO NOT EDIT

 % --- Executes just before inputGUI is made visible.
function inputGUI_OpeningFcn(hObject, eventdata, handles, varargin)
% This function has no output args, see OutputFcn.
% hObject    handle to figure
% eventdata  reserved - to be defined in a future version of MATLAB
% handles    structure with handles and user data (see GUIDATA)
% varargin   command line arguments to inputGUI (see VARARGIN)

% Choose default command line output for inputGUI
handles.output = hObject;

set(handles.delete_file,'Enable','off');
set(handles.read_data,'Enable','off');
set(handles.figure1,'Name','Data Wizard');

 if exist('Analyzed Data','dir') ~= 7
    mkdir('Analyzed Data');
end

% Update handles structure
guidata(hObject, handles);

% --- Outputs from this function are returned to the command line.
function varargout = inputGUI_OutputFcn(hObject, eventdata, handles)
% varargout  cell array for returning output args (see VARARGOUT);
% hObject    handle to figure
% eventdata  reserved - to be defined in a future version of MATLAB
% handles    structure with handles and user data (see GUIDATA)

% Get default command line output from handles structure
varargout{1} = handles.output;
```

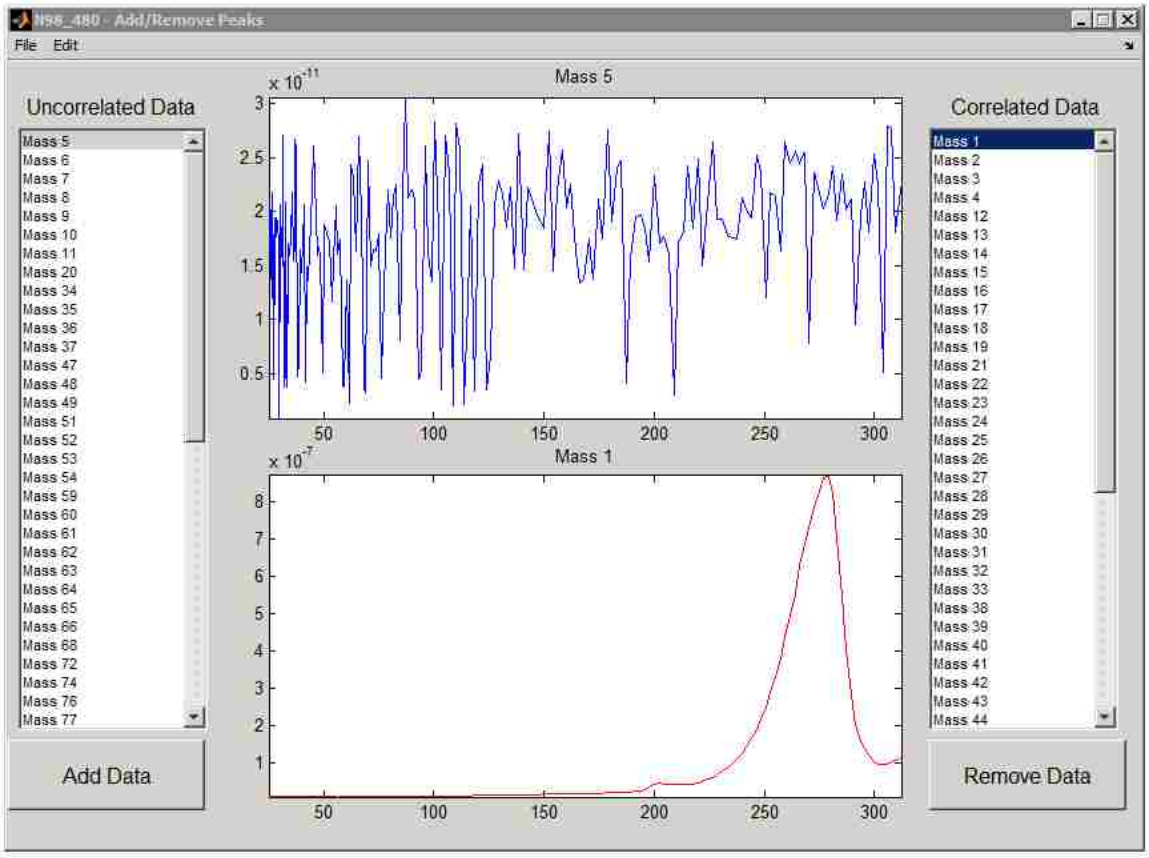

Figure C.2. Output of add_removeGUI used to pick specific RGA masses used in the peak finding algorithm.

```
% --------------------------------------------------------------------
% -------------------- CREATE FUNCTIONS ------------------------------
% --------------------------------------------------------------------

% --- Executes during object creation, after setting all properties.
function file_list_CreateFcn(hObject, eventdata, handles)
if ispc && isequal(get(hObject,'BackgroundColor'), get(0,'defaultUicontrolBackgroundColor'))
   set(hObject,'BackgroundColor','white');
end

% --------------------------------------------------------------------
% -------------------- CALLBACK FUNCTIONS ----------------------------
% --------------------------------------------------------------------

% --- Executes on selection change in file_list.
function file_list_Callback(hObject, eventdata, handles)
% hObject    handle to file_list (see GCBO)
% eventdata  reserved - to be defined in a future version of MATLAB
% handles    structure with handles and user data (see GUIDATA)
% Hints: contents = cellstr(get(hObject,'String')) returns file_list contents as cell array
%        contents{get(hObject,'Value')} returns selected item from file_list

if isempty(cellstr(get(hObject,'String')))
```

```
    set(handles.delete_file,'Enable','off');
    set(handles.read_data,'Enable','off');
end

% --- Executes on button press in add_file.
function add_file_Callback(hObject, eventdata, handles)
%gets input file(s) from user
[input_file,handles.pathname] = uigetfile( ...
    {'*.txt', 'Notepad (*.txt)';...
    '*.*', 'All Files (*.*)'}, ...
    'Select files', ...
    'MultiSelect', 'on');

%if file selection is cancelled, handles.pathname should be zero
%and nothing should happen
if handles.pathname == 0
    return
end
%gets the current data file names inside the listbox
inputFileNames = get(handles.file_list,'String');
%if they only select one file, then the data will not be a cell
%if more than one file selected at once,
%then the data is stored inside a cell
if iscell(input_file) == 0
    %add the most recent data file selected to the cell containing
    %all the data file names
    inputFileNames{end+1} = fullfile(handles.pathname,input_file);
    %else, data will be in cell format
else
    %stores full file path into inputFileNames
    for n = 1:length(input_file)
        %notice the use of {}, because we are dealing with a cell here!
        inputFileNames{end+1} = fullfile(handles.pathname,input_file{n});
    end
end
%updates the gui to display all filenames in the listbox
set(handles.file_list,'String',inputFileNames);
%make sure first file is always selected so it doesn't go out of range
%the GUI will break if this value is out of range
set(handles.file_list,'Value',1);
set(handles.delete_file,'Enable','on');
set(handles.read_data,'Enable','on');
% Update handles structure
guidata(hObject, handles);

% --- Executes on button press in delete_file.
function delete_file_Callback(hObject, eventdata, handles)
inputFileNames = get(handles.file_list,'String');
%get the values for the selected file names
option = get(handles.file_list,'Value');
%is there is nothing to delete, nothing happens
if (isempty(option) == 1 || option(1) == 0 || isempty(inputFileNames))
    return
end
%erases the contents of highlighted item in data array
inputFileNames(option) = [];
%updates the gui, erasing the selected item from the listbox
set(handles.file_list,'String',inputFileNames);
if isempty(get(handles.file_list,'String'))
    set(handles.delete_file,'Enable','off');
    set(handles.read_data,'Enable','off');
end
%moves the highlighted item to an appropiate value or else will get error
if option(end) > length(inputFileNames)
    set(handles.file_list,'Value',length(inputFileNames));
end
% Update handles structure
guidata(hObject, handles);
```

```
% --- Executes on button press in read_data.
function read_data_Callback(hObject, eventdata, handles)
% hObject    handle to read_data (see GCBO)
% eventdata  reserved - to be defined in a future version of MATLAB
% handles    structure with handles and user data (see GUIDATA)

% get list of file names and call presort routine
inputFileNames = get(handles.file_list,'String');
% inputFileNames = presortFileNames(inputFileNames);

% initialize variables
n = length(inputFileNames);

nMasses = numel(textread(inputFileNames{1},'%1c%*[^\n]'))-18;
data = zeros(nMasses,n);
massTimes = zeros(1,n);

 % bring in data from files in list
for i = 1:n
   scanfile = inputFileNames{i};

   massTimes(i) = datenum(strrep(strrep(scanfile,handles.pathname,'')...
      ,'.txt',''),'mmm_dd_yyyy__HH-MM-SS_AM');

   % bring in data
   data(:,i) = dlmread(scanfile,',',22,1);
end

prompt = {'Please Open TempChart and Pressure File Location',...
   'Sample Name','RGA scan rate'};
name = 'User Input';
numlines = 1;
delim = strfind(handles.pathname,'\');
defaultName = handles.pathname(delim(end-2)+1:delim(end-1)-1);
if ~isempty(strfind(defaultName,'\'))
   defaultName = 'New Sample';
else
   numPeriods = strfind(defaultName,'.');
   for i = 1:length(numPeriods)
      defaultName(numPeriods(i)) = '_';
   end
end

defaultanswer = {handles.pathname(1:delim(end-1)),defaultName,'32'};
options.Resize='on';
options.WindowStyle='modal';
answer = inputdlg(prompt,name,numlines,defaultanswer,options);

if ~isempty(answer)
   try
      dataFileNames = {'TempChart.csv','Pressure.csv'};
   catch
      dataFileNames = {'TempChart.csv','pressure.csv'};

   end

   handles = temp_correction_Callback(hObject, eventdata, handles);
   dataFilePaths = strcat(answer(1,1),dataFileNames);
   sampleName = answer{2,1};
   dataStruct(1,1) = importdata(dataFilePaths{1,1});
   dataStruct(1,2) = importdata(dataFilePaths{1,2});
   scanRate = str2double(answer{3,1});
   startDate=min(massTimes);

   numTemps = length(dataStruct(1,1).textdata);
   temps = zeros(3,numTemps);
   flag = false;
   d=1;
```

```
    for i = 1:numTemps

        try
            temps(1,i)=datenum(...
                strcat(datestr(startDate, 'mmm_dd_yyyy'),...
                dataStruct(1,1).textdata{i,1}), 'mmm_dd_yyyyHH MM SS')+ flag;
            temps(2,i)= dataStruct(1,1).data(d,2);
            temps(3,i)= dataStruct(1,1).data(d,4);
            d=d+1;

                if (~flag && (i>1) && (temps(1,i)<temps(1,i-1)))
            temps(1,i)=temps(1,i)+1;
            flag = true;
        end
        catch err

        end

    end

    numPres= length(dataStruct(1,2).textdata);
    Presures = zeros(5,numPres);
    flag = false;
    d = 1;

    for i = 1:numPres
        try
            Presures(1,i)=datenum(...
                strcat(datestr(startDate, 'mmm_dd_yyyy'),...
                dataStruct(1,2).textdata{i,1}),...
                'mmm_dd_yyyyHH:MM:SS')+flag;
            Presures(2:5,i)= dataStruct(1,2).data(d,1:4);
            d=d+1;

            if (~flag && (i>1) && (Presures(1,i)<Presures(1,i-1)))
                Presures(1,i)=Presures(1,i)+1;
                flag = true;
            end
        catch err
          if d > 1
             d = d+1;
          end
        end

    end

    RGAdata = dataSorter(massTimes,data,temps,Presures,handles.fixT,scanRate);
    powerLimits = find_power_limit(RGAdata{1,1}(4,:));

    close(inputGUI);
    RGAdata = formatData(RGAdata);
    date = datestr(startDate, 'mmmdd,yyyy');
    viewerGUI(RGAdata,sampleName,date,powerLimits);
end

% --------------------------------------------------------------------
function handles = temp_correction_Callback(hObject, eventdata, handles)
% hObject    handle to temp_correction (see GCBO)
% eventdata  reserved - to be defined in a future version of MATLAB
% handles    structure with handles and user data (see GUIDATA)

% handles = guidata(hObject);

rampRates = {'60','120','240','480','Old','Custum'};
[s,~]=listdlg('PromptString','Select a ramp rate:',...
    'SelectionMode','single','ListString',rampRates);

if( s == 1 ) % 60 ramp rate
    %    tempCorrection = '3.60E-09*T^4 - 5.07E-06*T^3 + 2.66E-03*T^2 + 1.45E-01*T + 1.53E+01';
```

```
    handles.fixT = '3.60E-09*T^4 - 5.07E-06*T^3 + 2.66E-03*T^2 + 1.45E-01*T + 1.53E+01' ;
elseif(s == 2) % 120 ramp rate
    %     tempCorrection = '6.09E-09*T^4 - 8.81E-06*T^3 + 4.55E-03*T^2 - 2.09E-01*T + 2.49E+01';
    handles.fixT = '6.09E-09*T^4 - 8.81E-06*T^3 + 4.55E-03*T^2 - 2.09E-01*T + 2.49E+01' ;
elseif(s == 3) % 240 ramp rate
    %     tempCorrection = '-4.47E-09*T^4 + 1.46E-06*T^3 + 1.86E-03*T^2 - 1.35E-01*T + 2.52E+01';
    handles.fixT = '-4.47E-09*T^4 + 1.46E-06*T^3 + 1.86E-03*T^2 - 1.35E-01*T + 2.52E+01';
elseif(s == 4) % 480 ramp rate
    %     tempCorrection = '-8.87E-09*T^4 + 8.13E-06*T^3 - 8.64E-04*T^2 + 9.21E-02*T + 2.05E+01';
    handles.fixT = '-8.87E-09*T^4 + 8.13E-06*T^3 - 8.64E-04*T^2 + 9.21E-02*T + 2.05E+01' ;
elseif(s == 5) % old ramp rate
    %     tempCorrection = 'T*0.91+0.56';
    handles.fixT = 'T*0.91+0.56' ;
elseif(s == 6) % custum ramp rate
    prompt = 'Change Temperature Correction Formula';
    name = 'Temperature Correction';
    numlines = 1;
    defaultanswer = {handles.defStr};
    answer = inputdlg(prompt,name,numlines,defaultanswer);
    if ischar(answer{1,1})
        val = strfind(answer{1,1},'T');
        if isempty(val)
            error = errordlg('T is not included as an independent variable!!!');
            uiwait(error);
            temp_correction_Callback(hObject, eventdata, handles);
        else
            %           tempCorrection = answer{1,1};
            handles.fixT = inline(answer{1,1},'T');
        end
    end
else
    return
end

handles.defStr = handles.fixT;
save tempCorrection
guidata(hObject, handles)

% --------------------------------------------------------------------
function file_menu_Callback(hObject, eventdata, handles)
% hObject    handle to file_menu (see GCBO)
% eventdata  reserved - to be defined in a future version of MATLAB
% handles    structure with handles and user data (see GUIDATA)

 % --------------------------------------------------------------------
function mat_import_Callback(hObject, eventdata, handles)
% hObject    handle to mat_import (see GCBO)
% eventdata  reserved - to be defined in a future version of MATLAB
% handles    structure with handles and user data (see GUIDATA)
[filename,pathname] = uigetfile('*mat');
if pathname == 0
    return
end
close(inputGUI);
fname = strcat(pathname,filename);
viewerGUI(fname);

% --------------------------------------------------------------------
% -------------------- SUPPORT FUNCTIONS ----------------------------
% --------------------------------------------------------------------

function [RGAdata] = dataSorter(timeData,massData,tempData,presData,Tfnc,scanRate)
% sortedTimes{1} = Recorded Temperature Times
% sortedTimes{2} = Recorded Pressure Times
%massTimes,data,temps,Presures,handles.fixT,scanRate

[m,n]=size(massData);
mergedData = zeros(m+10,n);
```

```
dataHeader(1:8,1) = {'Time','Temp','Corrected Temp','Power'...
   'Upper Ion', 'Lower Ion', 'Upper Cnv', 'Lower Cnv'};
for i = 1:m
   dataHeader{i+8,1}= ['Mass ', num2str(i)];
end

scanRate = scanRate/60/60/24;

for i=1:n
   [val1,place1]= min(abs(tempData(1,:)-timeData(i)));
   [val2,place2]= min(abs(presData(1,:)-timeData(i)));
   if (val1 < 1/2*scanRate && val2 < 1/2*scanRate)
      %record RGA time
      mergedData(1,i)=timeData(i);

      %record initial temp
      mergedData(2,i)=tempData(2,place1);
      %record corrected temp
      mergedData(3,i)=correctTemp(tempData(2,place1),Tfnc);
      %record power
      mergedData(4,i)=tempData(3,place1);

      %record RGA Pressures
      mergedData(9:m+8,i)=massData(1:m,i);

      %record initial pressures
      mergedData(5:8,i)=presData(2:5,place2);

   end
   mergedData(m+9,i)=val1*60*60*24;
   mergedData(m+10,i)=val2*60*60*24;
end
RGAdata{1,1} = transpose(sortrows(transpose(mergedData),1));

RGAdata{1,1}(:,1:(find(RGAdata{1,1}(1,:),1)-1))=[];

RGAdata{1,2} = dataHeader;

function limits = find_power_limit(powerVals)

% maxStep = length(powerVals);
limits = zeros(1,2);
limits(1) = find(powerVals,1);
limits(2) = find(powerVals==max(powerVals),1);

function returnCell = formatData(dataArray)
[m,n]=size(dataArray{1,1});
returnCell = cell(2,m-4);

returnCell{1,1} = 'Time';
returnCell{1,2} = 'Temperature';
returnCell{1,3} = 'Original Temperature';
returnCell{1,4} = 'Up Ion Gauge';
returnCell{1,5} = 'Lower Ion Gauge';
returnCell{1,6} = 'Total RGA Pressure';
for i = 1:(m-10)
   returnCell{1,i+6} = dataArray{1,2}{8+i,1};
end

returnCell{2,1} = dataArray{1,1}(1,:);
returnCell{2,2} = dataArray{1,1}(3,:);
returnCell{2,3} = dataArray{1,1}(2,:);
returnCell{2,4} = dataArray{1,1}(5,:);
returnCell{2,5} = dataArray{1,1}(6,:);

for i = 1:n
   returnCell{2,6}(1,i) = sum(dataArray{1,1}(9:m-2,i));
end
```

```
for i = 1:(m-10)
   returnCell{2,i+6} = dataArray{1,1}(8+i,:);
end

% --- Executes when user attempts to close figure1.
function figure1_CloseRequestFcn(hObject, eventdata, handles)
% hObject    handle to figure1 (see GCBO)
% eventdata  reserved - to be defined in a future version of MATLAB
% handles    structure with handles and user data (see GUIDATA)

% Hint: delete(hObject) closes the figure
delete(hObject);
```

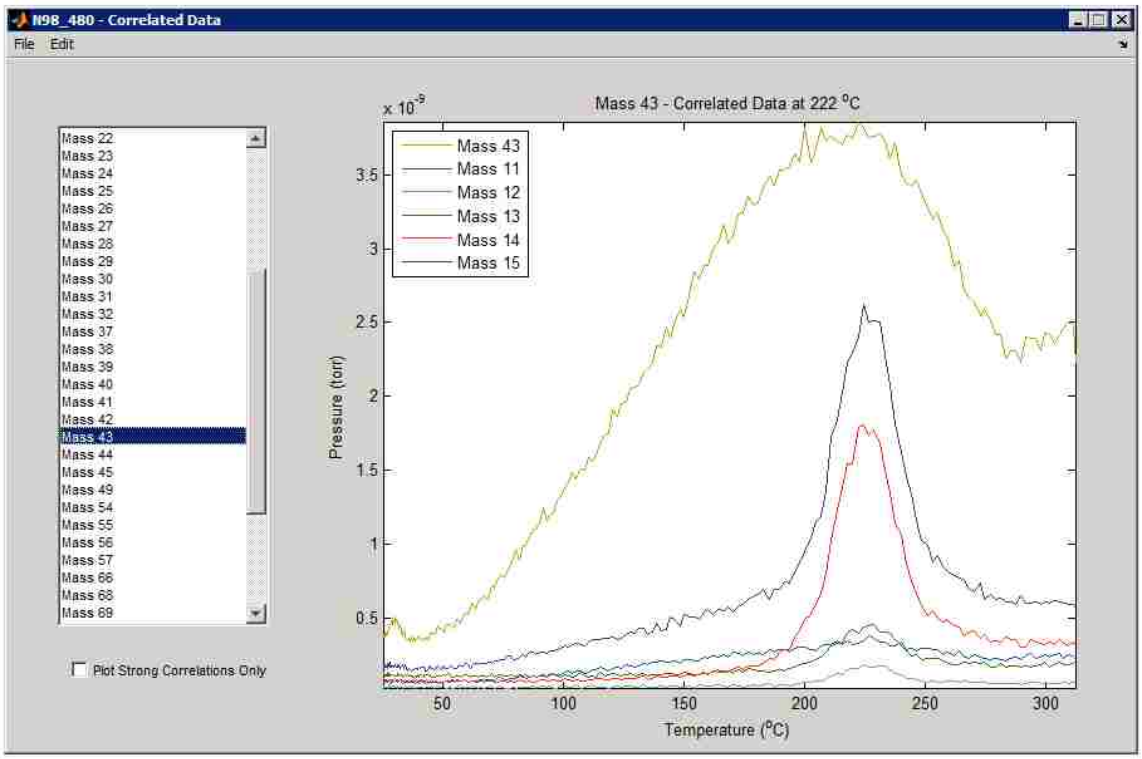

Figure C.3. Output of viewPeaksGUI which displays correlated peaks.

```
function varargout = viewerGUI(varargin)
% VIEWERGUI M-file for viewerGUI.fig
%      VIEWERGUI, by itself, creates a new VIEWERGUI or raises the existing
%      singleton*.
%
%      H = VIEWERGUI returns the handle to a new VIEWERGUI or the handle to
%      the existing singleton*.
%
%      VIEWERGUI('CALLBACK',hObject,eventData,handles,...) calls the local
%      function named CALLBACK in VIEWERGUI.M with the given input arguments.
%
%      VIEWERGUI('Property','Value',...) creates a new VIEWERGUI or raises the
%      existing singleton*.  Starting from the left, property value pairs are
%      applied to the GUI before viewerGUI_OpeningFcn gets called.  An
```

```
%     unrecognized property name or invalid value makes property application
%     stop.  All inputs are passed to viewerGUI_OpeningFcn via varargin.
%
%     *See GUI Options on GUIDE's Tools menu.  Choose "GUI allows only one
%     instance to run (singleton)".
%
% See also: GUIDE, GUIDATA, GUIHANDLES

% Edit the above text to modify the response to help viewerGUI

% Last Modified by GUIDE v2.5 28-Feb-2013 01:30:48

% Begin initialization code - DO NOT EDIT
gui_Singleton = 1;
gui_State = struct('gui_Name',       mfilename, ...
   'gui_Singleton',  gui_Singleton, ...
   'gui_OpeningFcn', @viewerGUI_OpeningFcn, ...
   'gui_OutputFcn',  @viewerGUI_OutputFcn, ...
   'gui_LayoutFcn',  [] , ...
   'gui_Callback',   []);
if nargin && ischar(varargin{1})
   gui_State.gui_Callback = str2func(varargin{1});
end

if nargout
   [varargout{1:nargout}] = gui_mainfcn(gui_State, varargin{:});
else
   gui_mainfcn(gui_State, varargin{:});
end
% End initialization code - DO NOT EDIT


% --- Executes just before viewerGUI is made visible.
function viewerGUI_OpeningFcn(hObject, eventdata, handles, varargin)

if numel(varargin) ~= 0
   if ischar(varargin{1})
      [handles.data,handles.SampleName,handles.date] = load_mat_file(varargin);
   else
      handles.data = varargin{1};
      handles.SampleName = varargin{2};
      handles.date = varargin{3};
      handles.pwrLimits = varargin{4};
      try
         save(strcat(pwd,'\Analyzed Data\',handles.SampleName,...
            ' Raw Data - ',handles.date,'.mat'),'-struct','handles','data');
      catch
         save(strcat(pwd,'\Analyzed Data\',handles.SampleName,...
            ' Raw Data.mat'),'-struct','handles','data');
      end
   end
elseif ~isfield(handles,'data')
   [filename,pathname] = uigetfile('*mat');
   if pathname == 0
      return
   end
   fname = strcat(pathname,filename);
   [handles.data,handles.SampleName,handles.date] = load_mat_file(fname);
else
   return
end
set(handles.undo_smooth,'Enable','off');
set(handles.figure1,'Name',strcat(handles.SampleName,...
   ' - RGA Data'));
set(handles.plotList,'String',handles.data(1,4:end));
handles.smoothed = 0;
handles.mData = size(handles.data)-5;
handles.item_selected = 1;
handles.state = 0;
```

```
handles.normalized = 0;
handles.cleaned = 0;
set(handles.plotList,'Value',handles.item_selected);
set(handles.time_chbk,'Value',handles.state);
set(handles.clean_temp_range,'Enable','On');

plot_Callback(hObject,eventdata,handles);

warning('off','MATLAB:polyfit:RepeatedPoints');

handles.output = hObject;
% Update handles structure
guidata(hObject,handles);


% --- Outputs from this function are returned to the command line.
function varargout = viewerGUI_OutputFcn(hObject, eventdata, handles)

varargout{1} = handles.output;


% --- Executes when user attempts to close figure1.
function figure1_CloseRequestFcn(hObject, eventdata, handles)

exit_program_Callback(hObject, eventdata, handles)


% ------------------------------------------------------------------
% ------------------- CREATE FUNCTIONS -----------------------------
% ------------------------------------------------------------------

% --- Executes during object creation, after setting all properties.
function plotList_CreateFcn(hObject, eventdata, handles)

if ispc && isequal(get(hObject,'BackgroundColor'), get(0,'defaultUicontrolBackgroundColor'))
   set(hObject,'BackgroundColor','white');
end


% ------------------------------------------------------------------
% ------------------- CALLBACK FUNCTIONS ---------------------------
% ------------------------------------------------------------------

% --- Executes on selection change in plotList.
function plotList_Callback(hObject, eventdata, handles)

handles.item_selected = get(hObject,'Value');
guidata(hObject,handles);
plot_Callback(hObject, eventdata, handles);


% --- Executes on button press in plotButton.
   function plot_Callback(hObject, eventdata, handles)

      y = smoothCheck(handles);
      PString ='Pressure (torr)';

      if (handles.normalized && handles.sampleMass ~= 1)
         PString = 'Pressure (torr/mg)';
      end

      list = get(handles.plotList,'String');
      str = list{handles.item_selected};

      if ~get(handles.time_chbk,'Value')

         if get(handles.H_Data,'Value')
            [AX,H1,H2] = plotyy(handles.data{2,2},y{1},handles.data{2,2},-handles.data{2,8});
            xlabel('Temperature (^oC)');
```

```
            ylabel(PString);

            linkaxes(AX, 'x');
            axis tight;

        else
            plot(handles.axes1,handles.data{2,2},y{1},'-');
            xlabel('Temperature (^oC)');
            ylabel(PString);
            axis tight;

        end

    else

        if get(handles.H_Data,'Value')

            [AX,H1,H2] = plotyy(handles.data{2,3},y{1},handles.data{2,3},-handles.data{2,8});
            xlabel('Temperature (^oC)');
            ylabel(PString);
            linkaxes(AX, 'x');
                    axis tight;

        else
            plot(handles.axes1,handles.data{2,3},y{1},'-');
            xlabel('Temperature (^oC)');
            ylabel(PString);
            axis tight
        end

    end
    title(str);


% --- Executes on button press in nextPlot.
function nextPlot_Callback(hObject, eventdata, handles)

handles.item_selected = handles.item_selected + 1;
if handles.item_selected > handles.mData(2) - 3
   handles.item_selected = 1;
end
set(handles.plotList,'Value',handles.item_selected);
guidata(hObject,handles);
plot_Callback(hObject, eventdata, handles);

% --- Executes on button press in backPlot.
function backPlot_Callback(hObject, eventdata, handles)

handles.item_selected = handles.item_selected - 1;
if handles.item_selected == 0
   mList = size(get(handles.plotList,'String'));
   handles.item_selected = mList(1);
end
set(handles.plotList,'value',handles.item_selected);
guidata(hObject,handles);
plot_Callback(hObject, eventdata, handles);

% --- Executes on button press in savePlot.
function savePlot_Callback(hObject, eventdata, handles)

list = get(handles.plotList,'String');
str = list{handles.item_selected};
sample = get(handles.figure1,'Name');
str = strcat({sample},{' ('},{str},{')'});
savePlotWithinGUI(handles.axes1,str{1});

% --------------------------------------------------------------------
function file_menu_Callback(hObject, eventdata, handles)
```

```
% --------------------------------------------------------------------
function save_as_Callback(hObject, eventdata, handles)

[filename, path] = uiputfile({'*.csv','Comma Separated Values (*.csv)';...
   '*.xls','Excel File (*.xls)'},'Save as',strcat(handles.SampleName,...
   ' - RGA Data'));
if isequal(filename,0) || isequal(path,0)
   return
else
   guidata(hObject,handles);
end
str = filename(end-3:end);
fname = strcat(path,filename);
if strcmp(str,'xls')
   xlswrite(fname,handles.data);
else
   fid = fopen(fname,'wt');
   RGAdata = handles.data;
   [~,maxStep] = size(RGAdata);
   [~,cols] = size(RGAdata{2,1});
   fprintf(fid,'Sample Name: %s, Date: %s\n',handles.SampleName,handles.date);
   for i = 1:maxStep
      for j = 1:2
         if j == 1
            fprintf(fid,'%s, ',RGAdata{1,i});
         else
            for k = 1:cols
               if k ~= cols
                  fprintf(fid,'%g, ',RGAdata{2,i}(k));
               else
                  fprintf(fid,'%g\n',RGAdata{2,i}(k));
               end
            end
         end
      end
   end
end
fclose all;

% --- Executes on button press in time_chbk.
function time_chbk_Callback(hObject, eventdata, handles)

handles.state = get(hObject,'Value');
guidata(hObject,handles);
plot_Callback(hObject,eventdata,handles);

% --- Executes on button press in H_Data.
function H_Data_Callback(hObject, eventdata, handles)

  [~, ~, limits] = cleanTemp(handles.data);

for i = 1:size(handles.data,2);
   handles.data{2,i} = handles.data{2,i}(limits(1):limits(2));
end

set(handles.clean_temp_range,'Enable','Off');

handles.cleaned = 1;

guidata(hObject,handles);

plot_Callback(hObject,eventdata,handles);

% --------------------------------------------------------------------
function analysis_menu_Callback(hObject, eventdata, handles)

% --------------------------------------------------------------------
```

```
function plot_parameters_Callback(hObject, eventdata, handles)
% hObject    handle to plot_parameters (see GCBO)
% eventdata  reserved - to be defined in a future version of MATLAB
% handles    structure with handles and user data (see GUIDATA)

if isfield(handles,'pwrLimits')
   [cleanTemps, pressures, ~] = cleanTemp(handles.data,handles.pwrLimits);
else
   [cleanTemps, pressures, ~] = cleanTemp(handles.data);
end

plot_overlay_menu(cleanTemps,pressures,handles.SampleName,'single');

% --------------------------------------------------------------------
function compare_parameters_Callback(hObject, eventdata, handles)
% hObject    handle to compare_parameters (see GCBO)
% eventdata  reserved - to be defined in a future version of MATLAB
% handles    structure with handles and user data (see GUIDATA)


if isfield(handles,'pwrLimits')
   [temperatures.data1, pressures.data1, ~] = cleanTemp(handles.data,...
      handles.pwrLimits);
else
   [temperatures.data1, pressures.data1, ~] = cleanTemp(handles.data);
end
[temperatures.data1, pressures.data1, ~] = cleanTemp(handles.data);

sampleName.data1 = handles.SampleName;
date.data1 = handles.date;

[filename,pathname] = uigetfile('*mat');
if pathname == 0
   return
end
fname = strcat(pathname,filename);
[data,sampleName.data2,date.data2] = load_mat_file(fname);
[temperatures.data2, pressures.data2, ~] = cleanTemp(data);

plot_overlay_menu(temperatures,pressures,sampleName,'double');


% --------------------------------------------------------------------
function analyze_data_Callback(hObject, eventdata, handles)

choice = questdlg('Would you like to calibrate the peak finder?', ...
   'Peak Finder Calibration','Yes','No','Yes');

switch choice
   case 'Yes'
      h = multiMenuGUI(handles.data,'calibration');
      waitfor(h);
      s = load('New Peak Detection Values.mat');
   otherwise
      s = load('Peak Detection Defaults.mat');
end


if isfield(handles,'pwrLimits')
   [cleanTemps, pressures, ~] = cleanTemp(handles.data,handles.pwrLimits);
else
   [cleanTemps, pressures, ~] = cleanTemp(handles.data);
end
maxStep = size(pressures,2);
testVar = zeros(1,maxStep);
for i = 1:maxStep
   testVar(i) = var(smooth(pressures{i}));
end
```

```
index = 1;
test = ceil(log10(median(testVar)));
ySig = struct('data',[],'name',{},'peaks',[]);
for i = 1:maxStep
   if ( log10(testVar(i)) > test  && ...
         mean(pressures{i})/std(pressures{i})< 11)
      ySig(index).data = pressures{i};
      ySig(index).name = handles.data{1,5+i};
      index = index + 1;
   end
end

for i = 1:index-1
   ySig(i).peaks = getPeaks(cleanTemps,ySig(i).data,s.slope,...
      s.amp*std(smooth(ySig(i).data)),s.smoothwidth,s.group);
   if (numel(ySig(i).peaks(:,1)) > 20)
      k1 = numel(ySig(i).peaks(:,1));
      k2 = numel(getPeaks(cleanTemps,smooth(ySig(i).data),s.slope,...
         2*std(smooth(ySig(i).data)),s.smoothwidth,s.group))/4;
      if k1 == k2
         ySig(i).noise = 'Noise';
      end
   elseif ySig(i).peaks == 0
      ySig(i).peaks = [];
   end
end

ySig = correlatePeaks(ySig);
save('New Peak Detection Values.mat','s');

guidata(hObject,handles);
viewPeaksGUI(ySig,cleanTemps,handles.SampleName,handles.date);


% --------------------------------------------------------------------
function get_new_data_Callback(hObject, eventdata, handles)
close(viewerGUI);
inputGUI;

function Open_New_Callback(hObject, eventdata, handles)
close(viewerGUI);
viewerGUI;

% --------------------------------------------------------------------
function edit_sample_name_Callback(hObject, eventdata, handles)

prompt = {'Enter Sample Name: '};
name='Sample Name';
numlines=1;
defaultanswer={handles.SampleName};
options.Resize='on';
options.WindowStyle='modal';
answer=inputdlg(prompt,name,numlines,defaultanswer,options);
handles.SampleName = answer{:};
set(handles.figure1,'Name',handles.SampleName);

% --------------------------------------------------------------------
function historgram_plot_Callback(hObject, eventdata, handles)
% hObject    handle to historgram_plot (see GCBO)
% eventdata  reserved - to be defined in a future version of MATLAB
% handles    structure with handles and user data (see GUIDATA)

multiMenuGUI(handles.data,'histogram');


% --------------------------------------------------------------------
function edit_menu_Callback(hObject, eventdata, handles)
% hObject    handle to edit_menu (see GCBO)
% eventdata  reserved - to be defined in a future version of MATLAB
```

```
% handles    structure with handles and user data (see GUIDATA)


% --------------------------------------------------------------------
function smooth_data_Callback(hObject, eventdata, handles)
% hObject    handle to smooth_data (see GCBO)
% eventdata  reserved - to be defined in a future version of MATLAB
% handles    structure with handles and user data (see GUIDATA)
handles.smoothed = handles.smoothed + 1;
set(handles.undo_smooth,'enable','on');
guidata(hObject,handles);
plot_Callback(hObject,eventdata,handles);

% --------------------------------------------------------------------
function undo_smooth_Callback(hObject, eventdata, handles)
% hObject    handle to undo_smooth (see GCBO)
% eventdata  reserved - to be defined in a future version of MATLAB
% handles    structure with handles and user data (see GUIDATA)
handles.smoothed = handles.smoothed - 1;
if handles.smoothed == 0
   set(handles.undo_smooth,'enable','off');
end
guidata(hObject,handles);
plot_Callback(hObject,eventdata,handles);




% --------------------------------------------------------------------
function data_menu_Callback(hObject, eventdata, handles)
% hObject    handle to data_menu (see GCBO)
% eventdata  reserved - to be defined in a future version of MATLAB
% handles    structure with handles and user data (see GUIDATA)


% --------------------------------------------------------------------
function normalize_data_Callback(hObject, eventdata, handles)
% hObject    handle to normalize_data (see GCBO)
% eventdata  reserved - to be defined in a future version of MATLAB
% handles    structure with handles and user data (see GUIDATA)

prompt = {'Enter sample Mass (mg):'};
name = 'Normalize Data';
numlines = 1;
defaultanswer = {''};
options.Resize = 'On';
options.WindowStyle = 'normal';

answer=inputdlg(prompt,name,numlines,defaultanswer,options);

if handles.normalized
   for i = 6:size(handles.data,2)
      handles.data{2,i} = handles.data{2,i}.*handles.sampleMass;
   end
else
   handles.normalized = 1;
end

[handles.sampleMass status] = str2num(answer{1});
if ~status
   % Handle empty value returned for unsuccessful conversi
   handles.sampleMass = 1;
else
   % val is a scalar or matrix converted from the first input

   for i = 6:size(handles.data,2)
      handles.data{2,i} = handles.data{2,i}./handles.sampleMass;
   end
end
```

```
guidata(hObject,handles);

plot_Callback(hObject,eventdata, handles);


% --------------------------------------------------------------------
function clean_temp_range_Callback(hObject, eventdata, handles)
% hObject    handle to clean_temp_range (see GCBO)
% eventdata  reserved - to be defined in a future version of MATLAB
% handles    structure with handles and user data (see GUIDATA)


if isfield(handles,'pwrLimits')
   [~, ~, limits] = cleanTemp(handles.data,handles.pwrLimits);
else
   [~, ~, limits] = cleanTemp(handles.data);
end
for i = 1:size(handles.data,2);
   handles.data{2,i} = handles.data{2,i}(limits(1):limits(2));
end

set(handles.clean_temp_range,'Enable','Off');
handles.cleaned = 1;

guidata(hObject,handles);
plot_Callback(hObject,eventdata,handles);

% --------------------------------------------------------------------
function exit_program_Callback(hObject, eventdata, handles)

delete(gcf)



% --------------------------------------------------------------------
% ------------------- SUPPORT FUNCTIONS ----------------------------
% --------------------------------------------------------------------

% --- Executes on key press with focus on figure1 and none of its controls.
function figure1_KeyPressFcn(hObject, eventdata, handles)

mData = handles.mData;
if ( strcmp(eventdata.Key,'leftarrow') || strcmp(eventdata.Key,'uparrow') )
   handles.item_selected = handles.item_selected - 1;
   if handles.item_selected == 0
      handles.item_selected = mData(2) - 3;
   end
   set(handles.plotList,'value',handles.item_selected);
   plot_Callback(hObject, eventdata, handles);
elseif ( strcmp(eventdata.Key,'rightarrow') || strcmp(eventdata.Key,'downarrow') )
   handles.item_selected = handles.item_selected + 1;
   if handles.item_selected > mData(2) - 3
      handles.item_selected = 1;
   end
   set(handles.plotList,'value',handles.item_selected);
   plot_Callback(hObject, eventdata, handles);
end
pause(.1);
guidata(hObject,handles);

function savePlotWithinGUI(axesObject,str)
[filename, pathname] = uiputfile({ '*.png','Portable Network Graphic (*.png)';...
   '*.emf','Enhanced Meta File (*.emf)';'*.bmp','Bitmap (*.bmp)';...
   '*.fig','Figure (*.fig)'},'Save picture as',str);
%if user cancels save command, nothing happens
if isequal(filename,0) || isequal(pathname,0)
   return
end
```

```
%create a new figure
newFig = figure;
%get the units and position of the axes object
axes_units = get(axesObject,'Units');
axes_pos = get(axesObject,'Position');
%copies axesObject onto new figure
axesObject2 = copyobj(axesObject,newFig);
%realign the axes object on the new figure
set(axesObject2,'Units',axes_units);
set(axesObject2,'Position',[15 5 axes_pos(3) axes_pos(4)]);
%adjusts the new figure accordingly
set(newFig,'Units',axes_units);
set(newFig,'Position',[15 5 axes_pos(3)+30 axes_pos(4)+10]);
%saves the plot
saveas(newFig,fullfile(pathname, filename))
%closes the figure
close(newFig)

function [y] = smoothCheck(handles)
y = cell(1,2);
if handles.smoothed > 0
    for i = 1:handles.smoothed
        if i == 1
            y{1} = smooth(handles.data{2,3+handles.item_selected});
        else
            y{1} = smooth(y{1});
        end
    end
else
    y{1} = handles.data{2,3+handles.item_selected};
end

function [values,SampleName,date] = load_mat_file(argin)

if iscell(argin)
    load(argin{1});
    numSlashs = strfind(argin{1},'\');
    numSpaces = strfind(argin{1},' ');
    SampleName = argin{1}(numSlashs(end)+1:numSpaces(2)-1);
    date = argin{1}(numSpaces(end)+2:strfind(argin{1},'.')-1);
else
    load(argin);
    numSlashs = strfind(argin,'\');
    numSpaces = strfind(argin,' ');
    SampleName = argin(numSlashs(end)+1:numSpaces(2)-1);
    date = argin(numSpaces(end)+2:strfind(argin,'.')-1);
end

values = data;


% --------------------------------------------------------------------
```

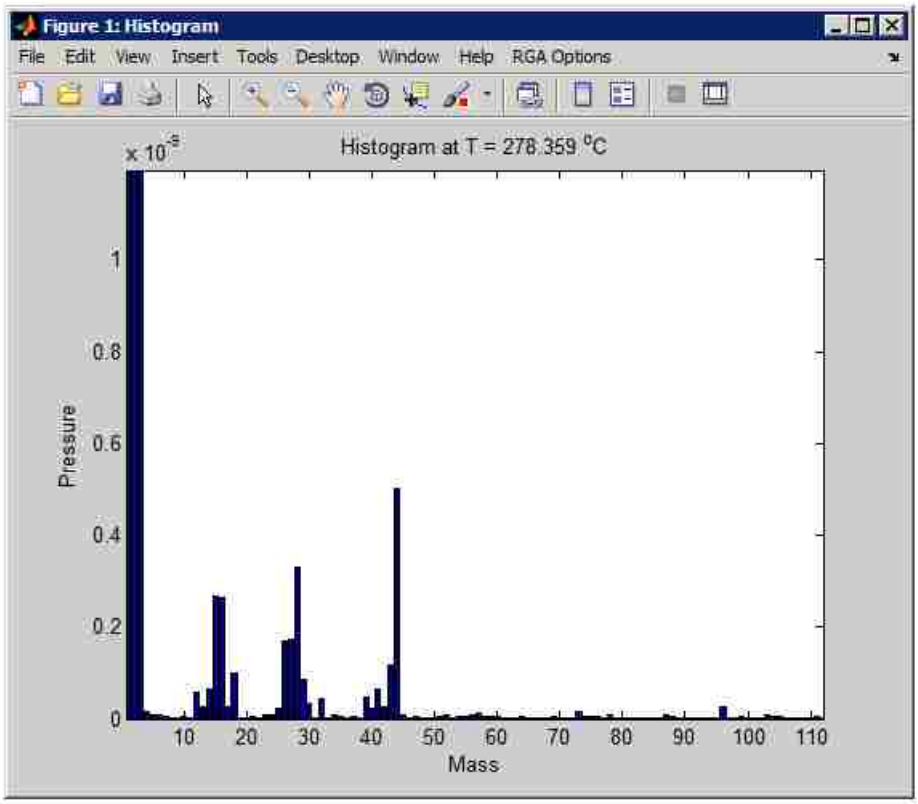

Figure C.4. Bargraph of background subtracted RGA data.

APPENDIX D.

OUTLINE OF VISUAL BASIC CODE FOR RECORDING PRESSURE FROM XGS -600

The XGS – 600 control software connects the Varian XGS-600™ gauge controller through serial communication with the computer. This software can control various types of pressure sensors as well as record the data at various sampling rates. Timothy Mason helped with the serial communication protocol. Figures D.1 and D.2 show the important GUI interfaces for this software. The software was created using the student edition of Microsoft Visual Studio 2008. The output of the software is a .csv file containing time stamped entries for each pressure gauge.

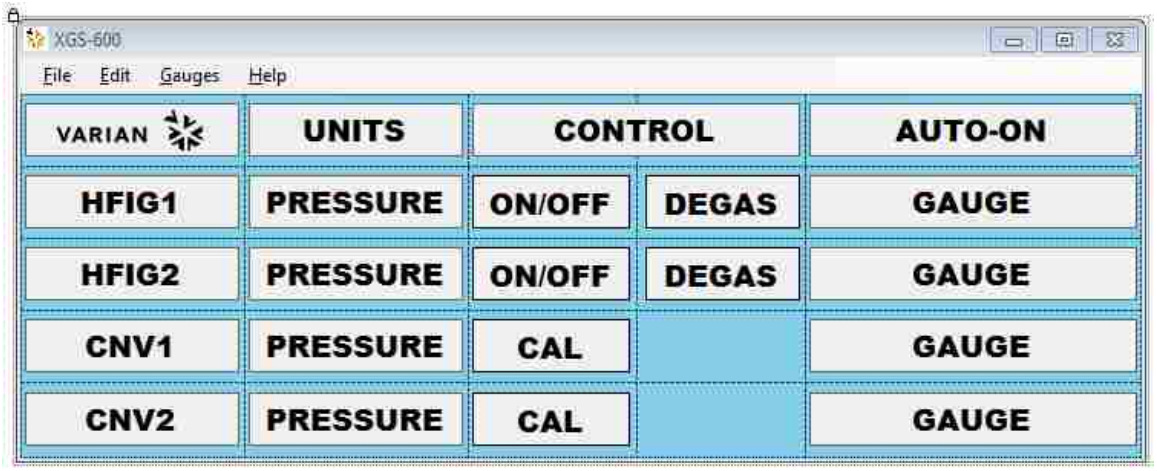

Figure D.1. XGS -600 Control Interface

```
Imports System.IO
Imports System.String
Imports System.Threading
Public Class Form1

#Region "Constants"
    Dim ComPort As Object
    Dim Units As String
    Public Pressure(12) As String
    Public GaugeSet As New Collection
    Dim Frequency As Object = 8
    Dim Frequency_input As Object
    Dim myStream As String
    Dim myFileName As String
    Dim IonOpt = New String() {"Emission ON", "Emission OFF", "Degas ON", "Degas OFF"}
    Dim IMGOpt = New String() {"OFF", "ON"}
    Dim CNVOpt = New String() {"Calibrate"}
    Dim cntrl As Control
#End Region

#Region "Gauges"
```

```
    Public HFIG1 As New Gauge
    Public HFIG2 As New Gauge
    Public HFIG3 As New Gauge
    Public HFIG4 As New Gauge
    Public CNV1 As New Gauge
    Public CNV2 As New Gauge
    Public CNV3 As New Gauge
    Public CNV4 As New Gauge
    Public CNV5 As New Gauge
    Public CNV6 As New Gauge
    Public CNV7 As New Gauge
    Public CNV8 As New Gauge
    Public CNV9 As New Gauge
    Public CNV10 As New Gauge
    Public CNV11 As New Gauge
    Public CNV12 As New Gauge
    Public IMG1 As New Gauge
    Public IMG2 As New Gauge
    Public IMG3 As New Gauge
    Public IMG4 As New Gauge
    Public IMG5 As New Gauge
    Public item As Gauge

    Public IonArray() As Gauge = {HFIG1, HFIG2, HFIG3, HFIG4}

    Public CnvArray() As Gauge = {CNV1, CNV2, CNV3, CNV4, CNV5, CNV6, _
                                  CNV7, CNV8, CNV9, CNV10, CNV11, CNV12}
    Public ImgArray() As Gauge = {IMG1, IMG2, IMG3, IMG4, IMG5}
#End Region

#Region "Functions"

    Public Function Wait() As Integer
        Return 0
    End Function

    Public Function TxRx(ByVal input As String) As String

        While SerialPort1.IsOpen
            MsgBox("Port is open")
        End While

        Dim incoming As String = ""
        Using SerialPort1 As IO.Ports.SerialPort = My.Computer.Ports.OpenSerialPort(ComPort)

            SerialPort1.NewLine = vbCr

            Try
                SerialPort1.WriteLine(input & vbCr)
                incoming = SerialPort1.ReadLine()

            Catch ex As TimeoutException

            End Try

            SerialPort1.Close()
        End Using

        Return Mid(incoming, 2)

    End Function

    Public Function ReadContents() As Object()

        Dim Cont As String
        Dim Position(6) As String
        Dim i As Integer = 0

        Cont = TxRx("#0001")
```

```
    For i = 1 To 6
        Position(i - 1) = Mid(Cont, (2 * i) - 1, 2)
    Next i

    Return Position

End Function

Public Function LoadCard() As Integer

    'generate buttons

    Return 0
End Function

Public Function GaugeList() As Integer

    'go through card list and
    'add gauge to collection
    'assign gauge a position
    'assign gauge an option array
    'assign gauge a type
    'assign gauge a name

    Dim h As Integer = 1
    Dim i As Integer
    Dim j As Integer = 1
    Dim k As Integer = 1
    Dim l As Integer = 1

    Dim cardlistIn As Object()

    cardlistIn = ReadContents()
    For i = 1 To 6
        Select Case cardlistIn(i - 1)
            Case "FE"
                'empty

            Case "10"
                'HFIG
                IonArray(j - 1).Options = IonOpt
                IonArray(j - 1).Position = "I" & h
                IonArray(j - 1).UserName = NameRead(IonArray(j - 1).Position)
                IonArray(j - 1).Type = ReadType(IonArray(j - 1).Position)
                GaugeSet.Add(IonArray(j - 1), "HFIG" & j)
                j += 1
                h += 1

            Case "3A"
                'IMG
                ImgArray(k - 1).Options = IMGOpt
                ImgArray(k - 1).Position = "I" & h
                ImgArray(k - 1).UserName = NameRead(ImgArray(k - 1).Position)
                ImgArray(k - 1).Type = ReadType(ImgArray(k - 1).Position)
                GaugeSet.Add(ImgArray(k - 1), "IMG" & k)
                k += 1
                h += 1

            Case "40"
                'CNV X 2
                CnvArray(l - 1).Options = CNVOpt
                CnvArray(l - 1).Position = "T" & l
                CnvArray(l - 1).UserName = NameRead(CnvArray(l - 1).Position)
                CnvArray(l - 1).Type = ReadType(CnvArray(l - 1).Position)
                GaugeSet.Add(CnvArray(l - 1), "CNV" & l)
                l += 1
                CnvArray(l - 1).Options = CNVOpt
                CnvArray(l - 1).Position = "T" & l
```

```
            CnvArray(l - 1).UserName = NameRead(CnvArray(l - 1).Position)
            CnvArray(l - 1).Type = ReadType(CnvArray(l - 1).Position)
            GaugeSet.Add(CnvArray(l - 1), "CNV" & l)
            l += 1

        Case Else
            MsgBox("Error in GaugeList")
    End Select
  Next i

  Return 0

End Function

Public Function Version() As Object

  Return TxRx("0005")

End Function

Public Function PressDump() As Object

  Return TxRx("#000F")

End Function

Public Function SetUnits(ByVal unit As String) As Integer

  If unit = "Torr" Then
    TxRx("#0010")
  ElseIf unit = "mBarr" Then
    TxRx("#0011")
  ElseIf unit = "Pascal" Then
    TxRx("#0012")
  End If

  Return 0

End Function

Public Function ReadUnits() As String

  Dim SC As Object
  SC = TxRx("#0013")

  If SC = "00" Then
    Return "Torr"
  ElseIf SC = "01" Then
    Return "mBarr"
  ElseIf SC = "02" Then
    Return "Pascal"
  Else : Return "Error"
  End If

End Function

Public Function Rename(ByVal Name As String, ByVal Pos As String) As Integer

  TxRx("#0014" & Pos & Mid(Name, 1, 5))

  Return 0

End Function

Public Function NameRead(ByVal Name As String) As String

  Return TxRx("#0015" & Name)

End Function
```

```
Public Function ReadLO() As Boolean

   'Check to see if Locked Out
   Dim LO As String

   LO = TxRx("#0022")

   If LO = "00" Then
      Return False    'Not Locked
   ElseIf LO = "01" Then
      Return True     'Locked
   Else
      Return True     'Locked

   End If

End Function

Public Function IonSet(ByRef Ion As Gauge, ByVal Switch As String) As String

   Select Case Switch
      Case "Emission ON"
         If Not Ion.Status(0) Then
            TxRx("#0031" & Ion.Position)
            Return "Emission ON"
         End If
      Case "Emission OFF"
         TxRx("#0040" & Ion.Position)

         TxRx("#0030" & Ion.Position)
         Return "Emission OFF"
      Case "Degas ON"
         If Ion.Status(0) AndAlso Not Ion.Status(1) Then
            TxRx("#0041" & Ion.Position)
            Return "Degas ON"
         End If
      Case "Degas OFF"
         If Ion.Status(1) Then
            TxRx("#0040" & Ion.Position)
            Return "Degas OFF"
         End If
   End Select

   Return 0

End Function

Public Function CNVCalibrate(ByVal address As String) As Integer

   TxRx("#00A1" & address)

   Return 0

End Function

Public Function IonStatus(ByVal Address As String) As Boolean()

   Dim Status(2) As Boolean
   Dim Emission As String = TxRx("#0032" & Address)

   If Emission = "01" Then
      Status(0) = True
   Else : Status(0) = False
   End If

   Dim Degas As String = TxRx("#0042" & Address)
   If Degas = "01" Then
      Status(1) = True
```

```
    Else : Status(1) = False
    End If

    Return Status

End Function

Private Function LockOutProcedures(ByVal LO As Boolean) As Integer

    'Lock out disables all changes except for renaming gauges and control options
    'if not locked
    If Not LO Then
        GaugesToolStripMenuItem.Enabled = True
        ToolStripComboBox1.Enabled = True
        LockOutToolStripMenuItem.Enabled = True
        IonGaugeToolStripMenuItem.Enabled = True
        ConvectionGaugeToolStripMenuItem.Enabled = True
        IMGToolStripMenuItem.Enabled = True
    End If

    LockOutToolStripMenuItem.Checked = LO

    Return 0
End Function

Public Function EssentialRenew() As Integer

    '6 Calls to TXRX


    HFIG1.Status = IonStatus(HFIG1.Position) '2x
    If HFIG1.Status(0) AndAlso HFIG1.Status(1) Then
        Button1.Text = "ON/off"
        Button1.BackColor = Color.Gold
        Button1.FlatStyle = FlatStyle.Popup
        Button2.BackColor = Color.Gold
        Button2.FlatStyle = FlatStyle.Popup
    ElseIf HFIG1.Status(0) AndAlso Not HFIG1.Status(1) Then
        Button1.Text = "ON/off"
        Button1.BackColor = Color.Gold
        Button1.FlatStyle = FlatStyle.Popup
        Button2.BackColor = DefaultBackColor
        Button2.FlatStyle = FlatStyle.Flat
    Else
        Button1.Text = "OFF/on"
        Button1.BackColor = DefaultBackColor
        Button1.FlatStyle = FlatStyle.Flat
        Button2.BackColor = DefaultBackColor
        Button2.FlatStyle = FlatStyle.Flat
    End If

    HFIG2.Status = IonStatus(HFIG2.Position) '2x
    If HFIG2.Status(0) AndAlso HFIG2.Status(1) Then
        Button3.Text = "ON/off"
        Button3.BackColor = Color.Gold
        Button3.FlatStyle = FlatStyle.Popup
        Button4.BackColor = Color.Gold
        Button4.FlatStyle = FlatStyle.Popup
    ElseIf HFIG2.Status(0) AndAlso Not HFIG2.Status(1) Then
        Button3.Text = "ON/off"
        Button3.BackColor = Color.Gold
        Button3.FlatStyle = FlatStyle.Popup
        Button4.BackColor = DefaultBackColor
        Button4.FlatStyle = FlatStyle.Flat
    Else
        Button3.Text = "OFF/on"
        Button3.BackColor = DefaultBackColor
        Button3.FlatStyle = FlatStyle.Flat
        Button4.BackColor = DefaultBackColor
```

```
            Button4.FlatStyle = FlatStyle.Flat
        End If
        Pressure = ReadPressure() '1x
        Label6.Text = Pressure(0)
        Label7.Text = Pressure(1)
        Label8.Text = Pressure(2)
        Label9.Text = Pressure(3)

        Return 0
    End Function

    Public Function NonEssentialRenew() As Integer

        '6x
        Label5.Text = ReadUnits()
        ToolStripComboBox1.Text = Label5.Text

        Label1.Text = NameRead(GaugeSet(1).Position)
        Label2.Text = NameRead(GaugeSet(2).Position)
        Label3.Text = NameRead(GaugeSet(3).Position)
        Label4.Text = NameRead(GaugeSet(4).Position)

        LockOutProcedures(ReadLO)

        Return 0
    End Function

    Public Function ReadPressure() As String()

        Dim pressuredump As String = PressDump()

        Return Strings.Split(pressuredump, ",", 12)

    End Function

    Public Function ReadType(ByVal Address As String) As String

        Return TxRx("#0017" & Address)
    End Function

#End Region

#Region "Controls"

    Private Sub Form1_Load(ByVal sender As System.Object, ByVal e As System.EventArgs) Handles MyBase.Load
        ToolStripComboBox1.Items.Add("Torr")
        ToolStripComboBox1.Items.Add("mBarr")
        ToolStripComboBox1.Items.Add("Pascal")
        FrequencyOfSampleToolStripMenuItem.Text = "Frequency: " & Frequency

    End Sub

    Private Sub AboutToolStripMenuItem_Click(ByVal sender As System.Object, ByVal e As System.EventArgs) Handles
ToolStripMenuItem1.Click

        My.Forms.HelpInfo.ShowDialog()

    End Sub

    Private Sub CommSetUpToolStripMenuItem_Click(ByVal sender As System.Object, ByVal e As System.EventArgs) Handles
CommSetUpToolStripMenuItem.Click

        Dim objForm As New CommControl()
        If (objForm.ShowDialog() = DialogResult.OK) Then
            ComPort = objForm.Form2Value
        End If
        objForm = Nothing

        If ComPort <> "" Then
```

```
            ComSellectedToolStripMenuItem.Text = ComPort
            MsgBox("Communications is Set at: " & vbCrLf & ComPort, MsgBoxStyle.Information)
            CommSetUpToolStripMenuItem.Enabled = False

            GaugeList()

            'enable renew timer once comport has been enabled
            EssentialRenew_timer.Enabled = True
            NonEssentialRenew()
            NonEssentialRenew_timer.Enabled = True

            FirmwareVersionToolStripMenuItem.Enabled = True
            DisplayContentsToolStripMenuItem.Enabled = True

            'For Each cntrl In TableLayoutControlCollection
            '    cntrl.Enabled = True
            'Next

        End If

        'Turn on Frequency Select
        If myFileName <> "" AndAlso ComPort <> "" Then
            FrequencyToolStripMenuItem.Enabled = True
            FrequencyToolStripMenuItem.Text = "Start"
        End If

    End Sub

    Private Sub UnitsComboBox1_Click(ByVal sender As System.Object, ByVal e As System.EventArgs) Handles
ToolStripComboBox1.DropDownClosed

        SetUnits(ToolStripComboBox1.SelectedItem)
        Label5.Text = ToolStripComboBox1.SelectedItem

    End Sub

    Private Sub DisplayContentsToolStripMenuItem_Click(ByVal sender As System.Object, ByVal e As System.EventArgs) Handles
DisplayContentsToolStripMenuItem.Click

        For Each item In GaugeSet
            MsgBox("Name:  " & item.UserName & vbCr & "Type:  " & item.Type _
                & vbCr & "Position:  " & item.Position, MsgBoxStyle.Information)
        Next

    End Sub

    Private Sub QuitToolStripMenuItem_Click(ByVal sender As System.Object, ByVal e As System.EventArgs) Handles
QuitToolStripMenuItem.Click
        If (MsgBox("Are you sure you want to quit?", MsgBoxStyle.OkCancel, "Exit") = MsgBoxResult.Ok) Then
            RecordTimer.Enabled = False
            SerialPort1.Close()

            End
        End If

    End Sub

    Private Sub FirmwareVersionToolStripMenuItem_Click(ByVal sender As System.Object, ByVal e As System.EventArgs) Handles
FirmwareVersionToolStripMenuItem.Click

        MsgBox("Firmware version is: " & TxRx("#0005"), MsgBoxStyle.Information)

    End Sub

    Private Sub FrequencyToolStripMenuItem_Click(ByVal sender As System.Object, ByVal e As System.EventArgs) Handles
FrequencyToolStripMenuItem.Click

        If FrequencyToolStripMenuItem.Text = "Stop" Then
            RecordTimer.Enabled = False
```

```
            FrequencyToolStripMenuItem.Text = "Start"

        ElseIf FrequencyToolStripMenuItem.Text = "Start" Then
            RecordTimer.Enabled = True
            FrequencyToolStripMenuItem.Text = "Stop"

        End If

    End Sub

    Private Sub FrequencyOfSampleToolStripMenuItem_Click(ByVal sender As System.Object, ByVal e As System.EventArgs)
Handles FrequencyOfSampleToolStripMenuItem.Click

        Frequency_input = InputBox("Enter a sampling rate in seconds greater than or equal to 1 seconds.", "Sample Rate", "8")

        If IsNumeric(Frequency_input) AndAlso Frequency_input >= 1 Then
            Frequency = Frequency_input
            My.Computer.FileSystem.WriteAllText(myFileName, "Timer Interval Changed:  " & Frequency & vbCrLf, True)

        End If

        FrequencyOfSampleToolStripMenuItem.Text = "Frequency: " & Frequency
        RecordTimer.Interval = Frequency * 1000

    End Sub

    Private Sub SaveAsToolStripMenuItem_Click(ByVal sender As System.Object, ByVal e As System.EventArgs) Handles
SaveAsToolStripMenuItem.Click

        If SaveFileDialog1.ShowDialog() = DialogResult.OK Then
            myFileName = SaveFileDialog1.FileName

            FileOpen(1, myFileName, OpenMode.Output)
            PrintLine(1, "Timer Interval:  " & Frequency & vbCrLf & My.Computer.Clock.LocalTime & vbCrLf _
                    & myFileName & vbCrLf _
                    & "Time,      " & Label1.Text & ",   " & Label2.Text & ",  " & Label3.Text & ",   " & Label4.Text)
            FileClose(1)

            FileNameToolStripMenuItem1.Text = myFileName
        End If

        'Turn on Frequency Select
        If myFileName <> "" AndAlso ComPort <> "" Then
            FrequencyToolStripMenuItem.Enabled = True
            FrequencyToolStripMenuItem.Text = "Start"
        End If

    End Sub

    Private Sub OpenTextToolStripMenuItem_Click(ByVal sender As System.Object, ByVal e As System.EventArgs) Handles
OpenTextToolStripMenuItem.Click

    End Sub

    Private Sub Label1_Click(ByVal sender As System.Object, ByVal e As System.EventArgs) Handles Label1.Click

        If LockOutToolStripMenuItem.Enabled Then
            Dim newName As String
            newName = InputBox("5 Letters Only")
            If newName <> "" Then
                Label1.Text = newName.ToUpper
                Rename(newName.ToUpper(), HFIG1.Position)
            End If
        End If

    End Sub

    Private Sub Label2_Click(ByVal sender As System.Object, ByVal e As System.EventArgs) Handles Label2.Click
```

```
    If LockOutToolStripMenuItem.Enabled Then
        Dim newName As String
        newName = InputBox("5 Letters Only")
        If newName <> "" Then
            Label2.Text = newName.ToUpper
            Rename(newName.ToUpper(), HFIG2.Position)
        End If
    End If

End Sub

Private Sub Label3_Click(ByVal sender As System.Object, ByVal e As System.EventArgs) Handles Label3.Click

    If LockOutToolStripMenuItem.Enabled Then
        Dim newName As String
        newName = InputBox("5 Letters Only")
        If newName <> "" Then
            Rename(newName.ToUpper(), CNV1.Position)
            Label3.Text = newName.ToUpper
        End If
    End If

End Sub

Private Sub Label4_Click(ByVal sender As System.Object, ByVal e As System.EventArgs) Handles Label4.Click

    If LockOutToolStripMenuItem.Enabled Then
        Dim newName As String
        newName = InputBox("5 Letters Only")
        If newName <> "" Then
            Rename(newName.ToUpper(), CNV2.Position)
            Label4.Text = newName.ToUpper
        End If
    End If

End Sub

Private Sub Button1_Click(ByVal sender As System.Object, ByVal e As System.EventArgs) Handles Button1.Click

    'toggle on HFIG1
    If Button1.Text = "ON/off" Then
        Button1.BackColor = Color.Red
        IonSet(HFIG1, HFIG1.Options(1))
    ElseIf Button1.Text = "OFF/on" Then
        Button1.BackColor = Color.Red
        IonSet(HFIG1, HFIG1.Options(0))
    End If

    PictureBox1.Select()

End Sub

Private Sub Button3_Click(ByVal sender As System.Object, ByVal e As System.EventArgs) Handles Button3.Click

    'toggle on HFIG2
    If Button3.Text = "ON/off" Then
        Button3.BackColor = Color.Red
        IonSet(HFIG2, HFIG2.Options(1))
    ElseIf Button3.Text = "OFF/on" Then
        Button3.BackColor = Color.Red
        IonSet(HFIG2, HFIG2.Options(0))
    End If

    PictureBox1.Select()

End Sub

Private Sub Button2_Click(ByVal sender As System.Object, ByVal e As System.EventArgs) Handles Button2.Click
```

```
        'Degas toggle for HFIG1
        If Button2.FlatStyle = FlatStyle.Flat Then
            Button2.BackColor = Color.Red
            IonSet(HFIG1, HFIG1.Options(2))
        ElseIf Button2.FlatStyle = FlatStyle.Popup Then
            Button2.BackColor = Color.Red
            IonSet(HFIG1, HFIG1.Options(3))
        End If

        PictureBox1.Select()

    End Sub

    Private Sub Button4_Click(ByVal sender As System.Object, ByVal e As System.EventArgs) Handles Button4.Click

        'Degas toggle for HFIG2
        If Button4.FlatStyle = FlatStyle.Flat Then
            Button4.BackColor = Color.Red
            IonSet(HFIG2, HFIG2.Options(2))
        ElseIf Button4.FlatStyle = FlatStyle.Popup Then
            Button4.BackColor = Color.Red
            IonSet(HFIG2, HFIG2.Options(3))
        End If

        PictureBox1.Select()

    End Sub

    Private Sub Button5_Click(ByVal sender As System.Object, ByVal e As System.EventArgs) Handles Button5.Click
        CNVCalibrate(CNV1.Position)
    End Sub

    Private Sub Button6_Click(ByVal sender As System.Object, ByVal e As System.EventArgs) Handles Button6.Click
        CNVCalibrate(CNV2.Position)
    End Sub

    Private Sub EssentialRenew_timer_Tick(ByVal sender As System.Object, ByVal e As System.EventArgs) Handles
EssentialRenew_timer.Tick

        EssentialRenew()

    End Sub

    Private Sub NonEssentialRenew_timer_Tick(ByVal sender As System.Object, ByVal e As System.EventArgs) Handles
NonEssentialRenew_timer.Tick

        NonEssentialRenew()

    End Sub

    Private Sub RecordTimer_Tick(ByVal sender As System.Object, ByVal e As System.EventArgs) Handles RecordTimer.Tick

        myStream = TimeString & ",   " & PressDump() & vbCrLf
        My.Computer.FileSystem.WriteAllText(myFileName, myStream, True)

    End Sub

    Private Sub InstructionManualToolStripMenuItem_Click(ByVal sender As System.Object, ByVal e As System.EventArgs) Handles
InstructionManualToolStripMenuItem.Click

        pdfViewer.Start()

    End Sub
#End Region


    Public Sub New()

        ' This call is required by the Windows Form Designer.
```

```
        InitializeComponent()

        ' Add any initialization after the InitializeComponent() call.

    End Sub
End Class
```

Figure D.2. Initial Serial Communication Interface

```
Imports System.IO

Public Class CommControl
    Private MyVal As Object


    Private Sub CommControl_Load(ByVal sender As System.Object, ByVal e As System.EventArgs) Handles MyBase.Load

        For Each sp As String In My.Computer.Ports.SerialPortNames
            ComboBox1.Items.Add(sp)
        Next
    End Sub
    Public Property Form2Value() As Object
        Get
            Return MyVal
        End Get
        Set(ByVal Value As Object)
            MyVal = Value
        End Set
    End Property

    Private Sub Button1_Click(ByVal sender As System.Object, ByVal e As System.EventArgs) Handles Button1.Click
        If Me.Form2Value = "" Then
            MsgBox("A Communications Port Must be selected")
            Me.DialogResult = DialogResult.Abort
```

```
        Else
            Me.DialogResult = DialogResult.OK
        End If

    End Sub

    Private Sub Button3_Click(ByVal sender As System.Object, ByVal e As System.EventArgs) Handles Button3.Click
        Dim incoming As String = ""
        Try
            Using SerialPort1 As IO.Ports.SerialPort = My.Computer.Ports.OpenSerialPort(Me.Form2Value)

                SerialPort1.NewLine = vbCr

                SerialPort1.WriteLine("#00" & vbCr)
                incoming = SerialPort1.ReadLine()

                SerialPort1.Close()
            End Using
        Catch ex As IO.IOException
        Catch ex As TimeoutException
        Catch ex As ArgumentException

        End Try

        If (incoming = "?FF") Then
            MsgBox("Connection successful to " & Me.Form2Value)
        Else : MsgBox("Connection Failed" & ErrorToString(), MsgBoxStyle.DefaultButton1, "Error")
        End If
    End Sub

    Private Sub Button2_Click(ByVal sender As System.Object, ByVal e As System.EventArgs) Handles Button2.Click
        Me.DialogResult = DialogResult.Cancel
    End Sub

    Private Sub ComboBox1_SelectedIndexChanged(ByVal sender As System.Object, ByVal e As System.EventArgs) Handles
ComboBox1.SelectedIndexChanged
        Me.Form2Value = ComboBox1.SelectedItem
    End Sub
End Class
```

APPENDIX E.

DRAWINGS OF MS-RGA PARTS AND ASSOCIATED TOOLS

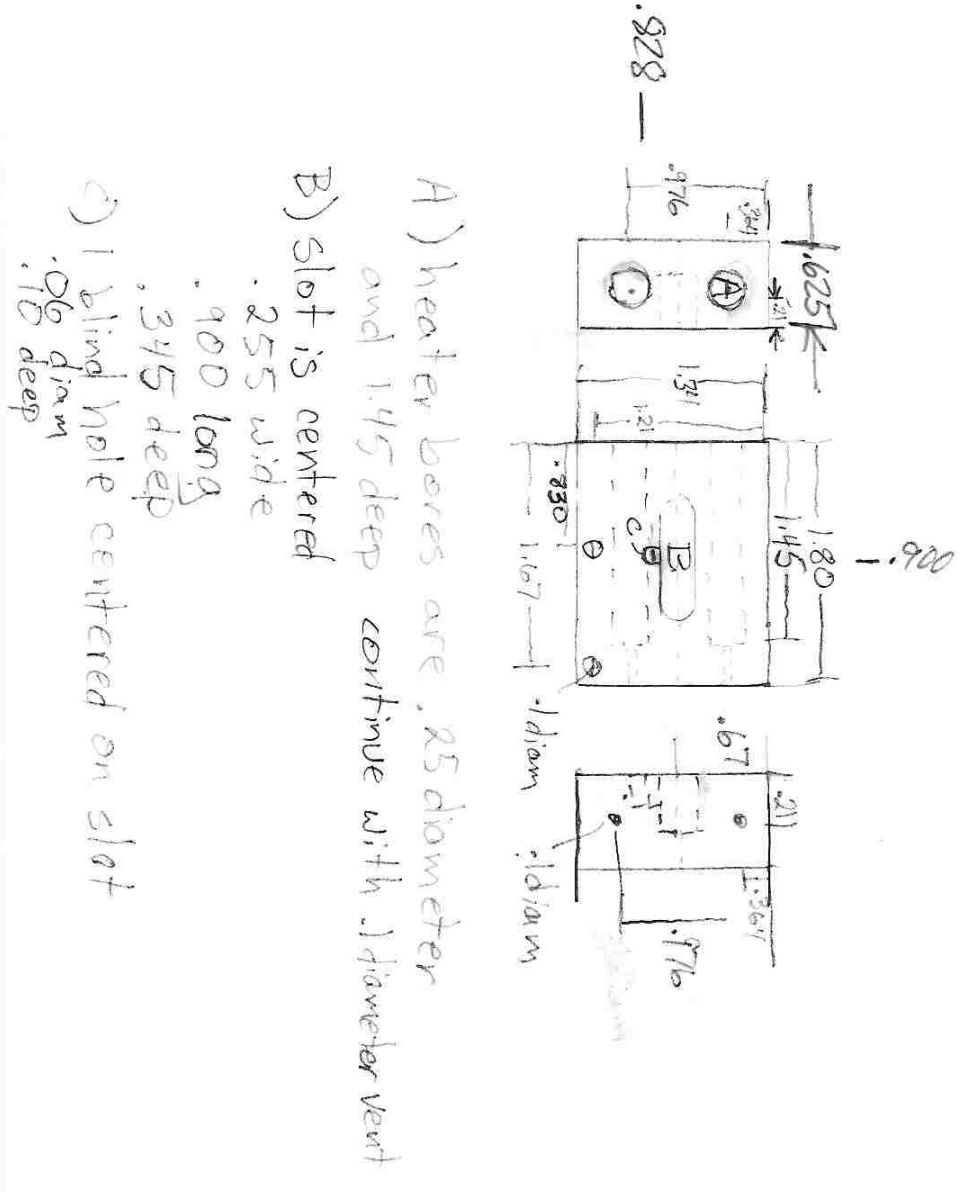

Figure E.1. The sample heater block, constructed from stainless steel. A) 0.25" diameter bores for heater, B) trough for sample holder, C) indentation for thermocouple insertion. Parts machined by B. A. Burkeen in the University of Missouri – St. Louis's Machine Shop.

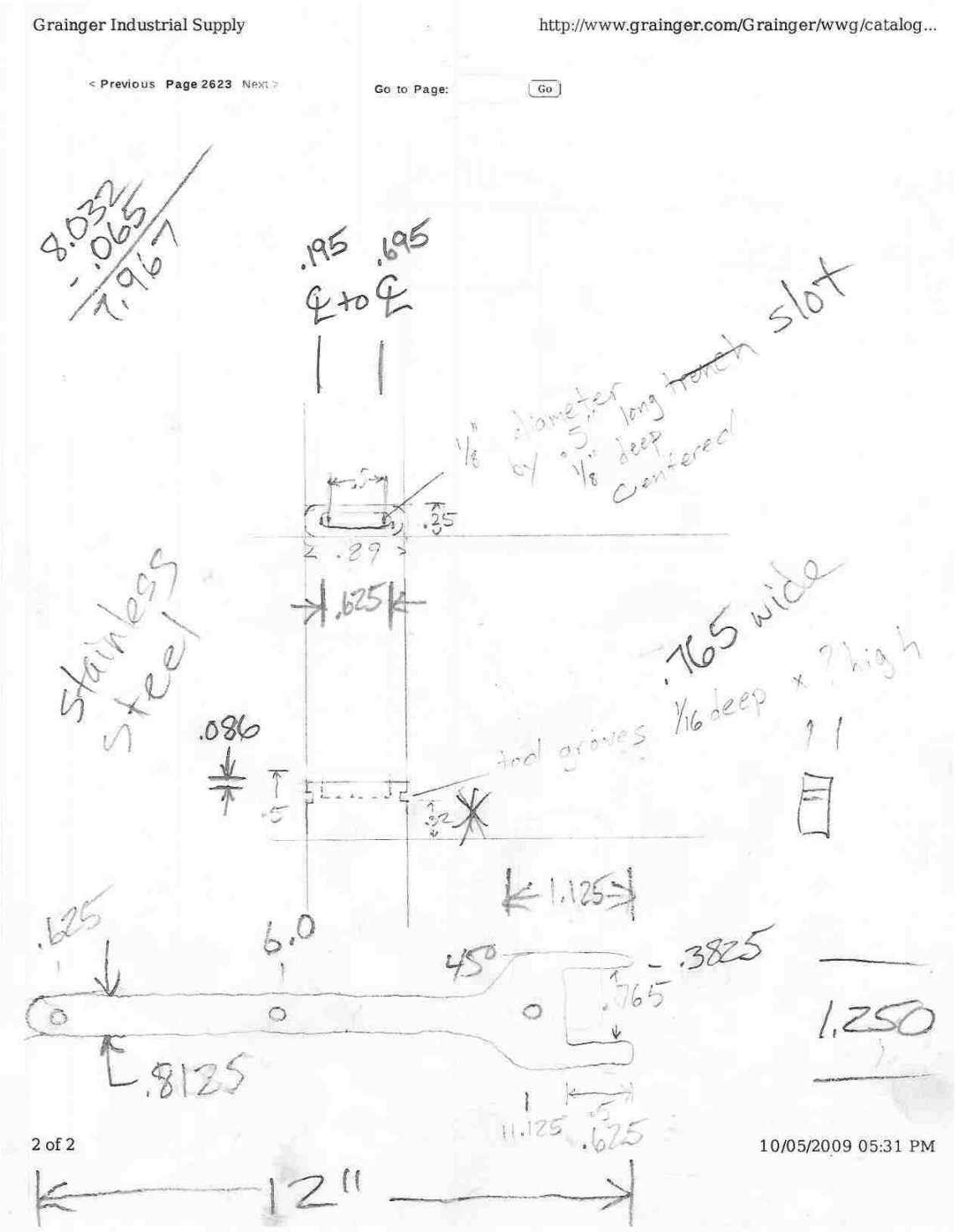

Figure E.2. The sample holder (top), constructed from stainless steel. There are 2 versions of the sample holder. The 1st is for bulk samples, and the 2nd is machined to take Tzero Sample pans. The fork/wrench (bottom). The fork end is for inserting the sample holder into the heater block, and the wrench end is for loosening the nuts which fasten the glass viewport to the main sample chamber. Parts machined by B. A. Burkeen in the University of Missouri – St. Louis's Machine Shop.

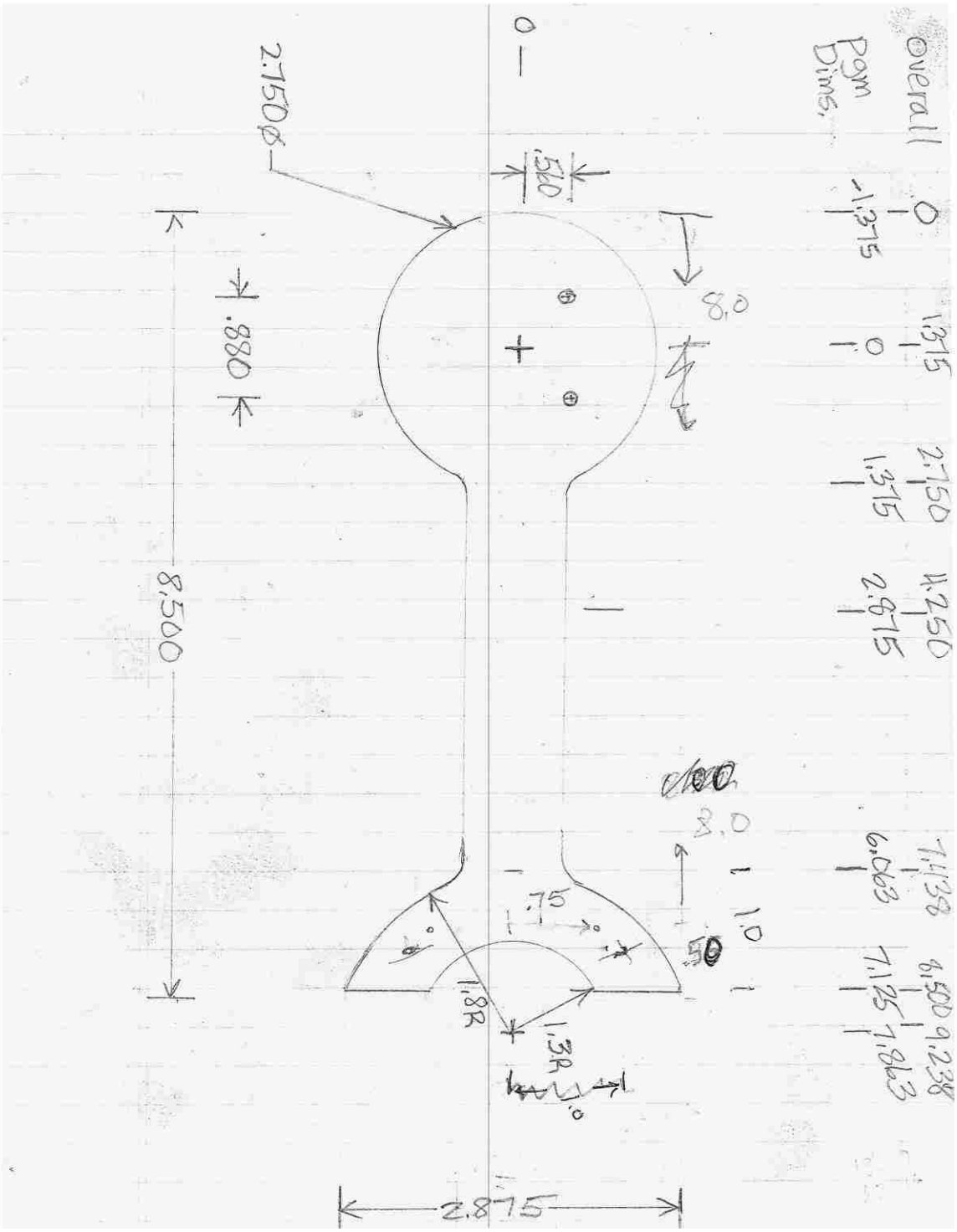

Figure E.3. The mounting bracket for the high temperature sample stage. Parts machined by B. A. Burkeen in the University of Missouri – St. Louis's Machine Shop.

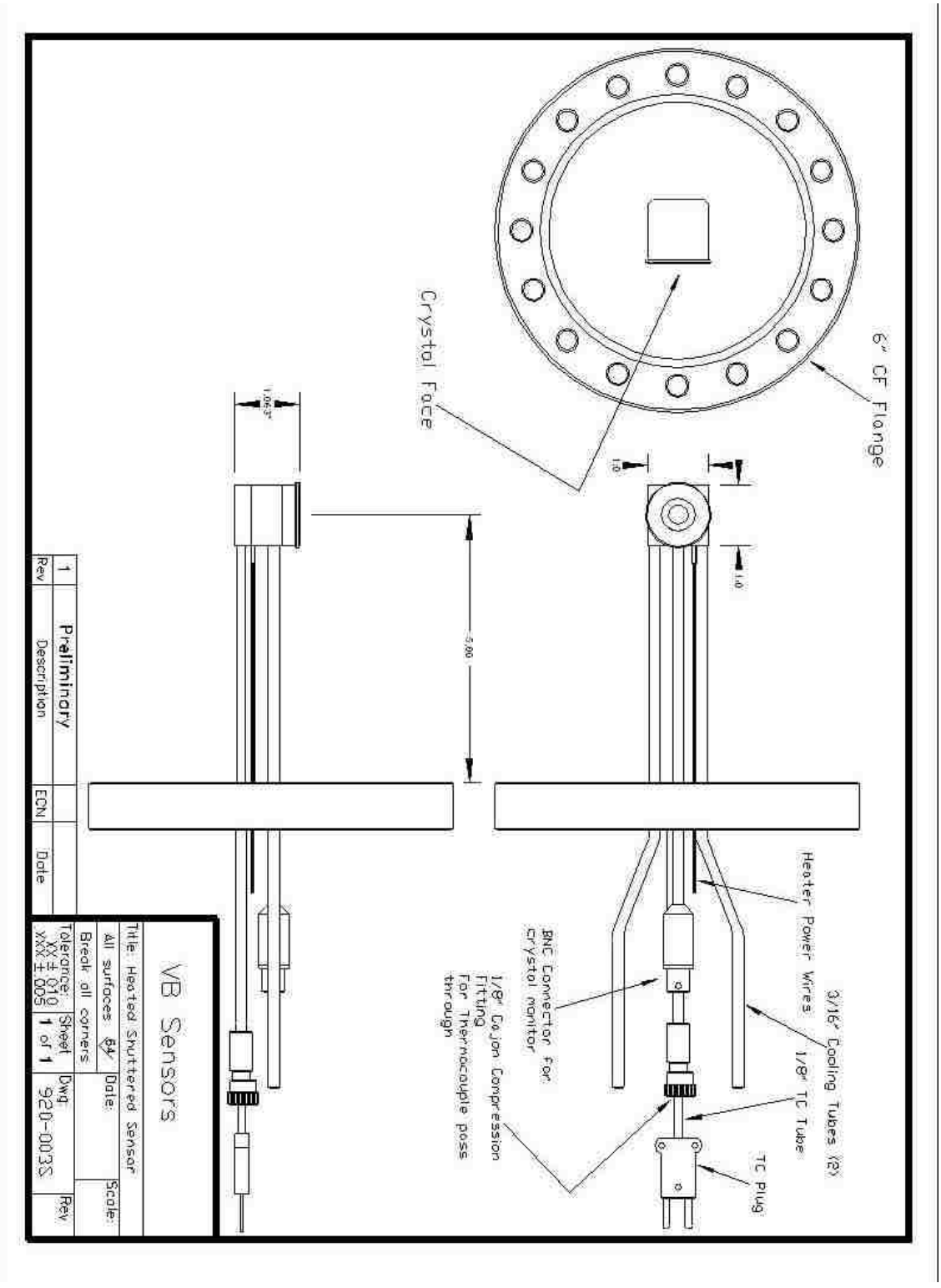

Figure E.4. QCM sample stage showing 6" CFF and associated parts. Reprinted here with permission from Scott Grimshaw, Tangidyne Corporation on 9/12/2013.

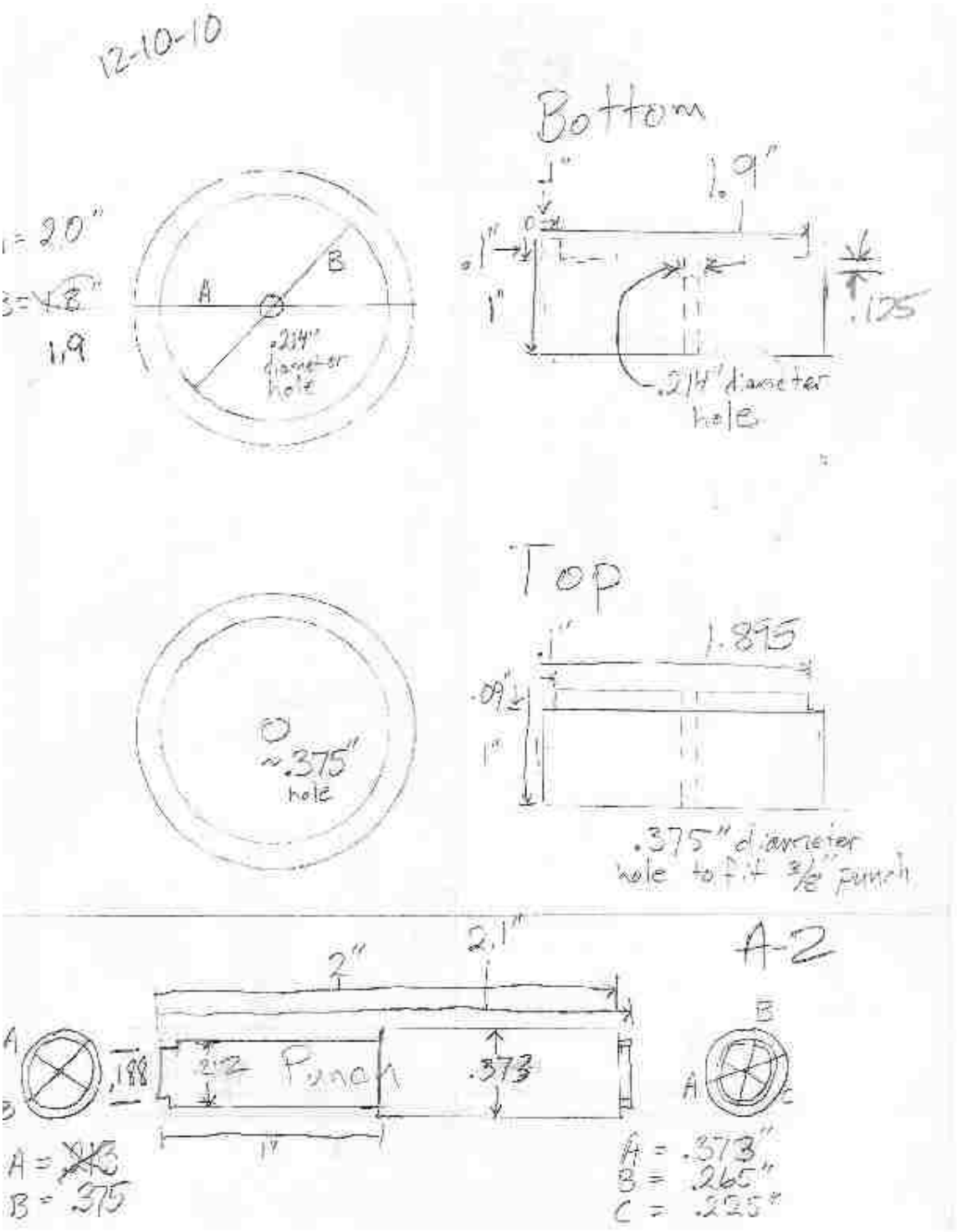

Figure E.5. Drawing of the Tzero Hermitic Seal Press. The body of the press (top) is 2 pieces. The bottom piece is hold the sample pan and lid, while the top piece is to guide the punch for sealing the lid. The punch (bottom) is designed to seal the Tzero pan as well as to remove the sample from the press. Parts machined by B. A. Burkeen in the University of Missouri – St. Louis's Machine Shop.

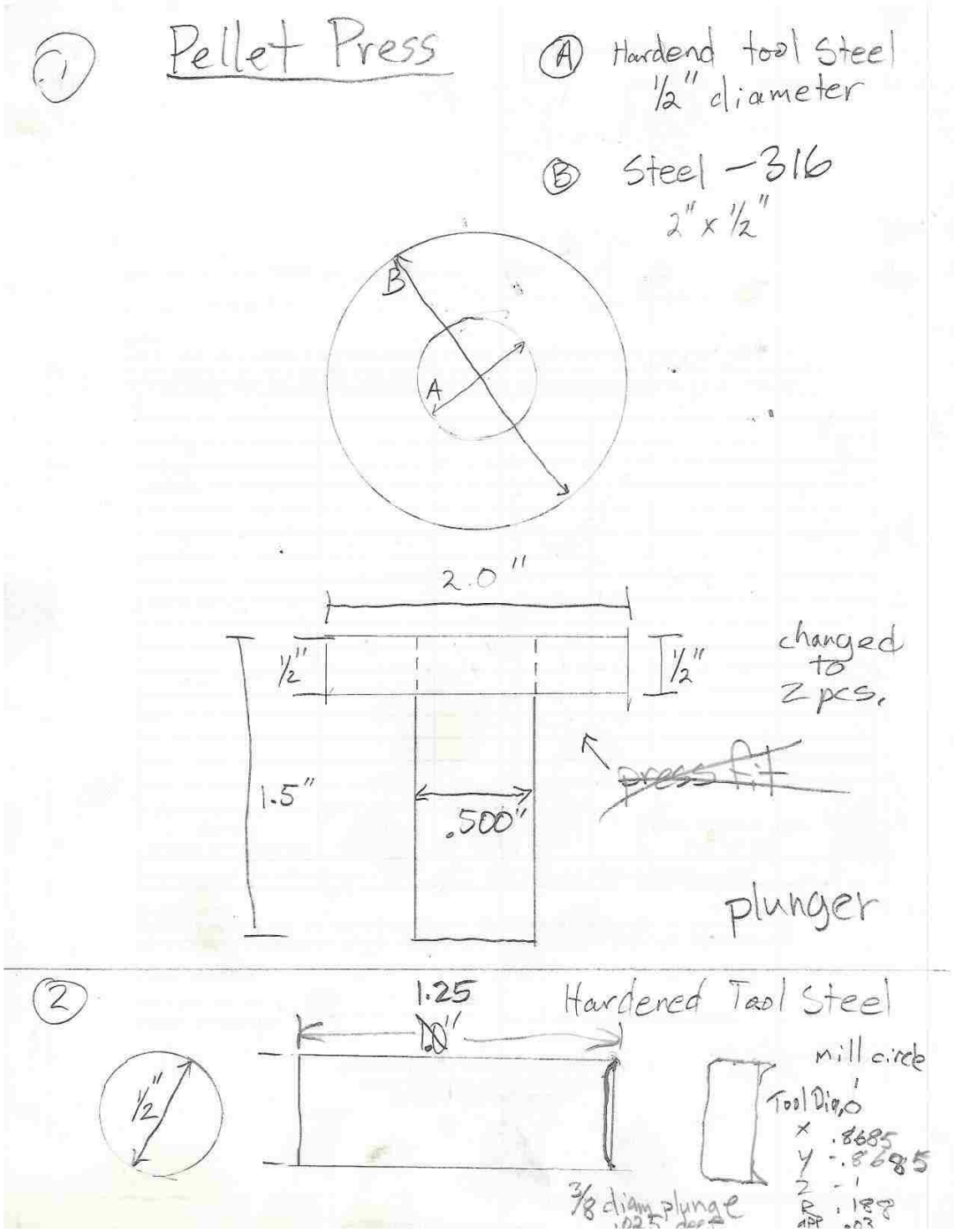

Figure E.6. Drawing of the pellet press used for pressing NPC into electrodes.

REFERENCES

[1] Goodenough, J. B., Abruna, H. D., Buchanan, M. V. "Basic Research Needs for Electrical Energy Storage" *BES Sciences, Office of Science, DOE.* 2007.

[2] Chen, H., Cong, T., Yang, W., Tan, C., Li, Y., Ding, Y. *Progress in Natural Science* 19 (2009) 291-312.

[3] Beaudin, M., Zareipour, H. Schellenberglabe, A., Rosehart, W., *Energy for Sustainable Development* 14 (2010) 302-314.

[4] Maxwell Technologies: http://www.maxwell.com, retrieved from *Wikipedia.org* (2013).

[5] Energy.gov

[6] "Energy Storage Program Planning Document" *U.S. Dept. of Energy, Office of Electricity Delivery & Energy Reliability* 2011.

[7] Satyapal, S., Petrovic, J., Read, C., Thomas, G., Ordaz, G., *Catalysis Today* 120 (2007) 247-256.

[8] "The Department of Energy Hydrogen and Fuel Cells Program Plan" *U.S. Dept. of Energy* 2011.

[9] "Fuel Cell Technologies Office Multi-Year Research, Development and Demonstration Plan" *Fuel Cell Technologies Office, Office of Energy Efficiency and Renewable Energy, U.S. Dept. of Energy* 2012.

[10] Seayad, A. M., Antonelli, D. M., *Adv. Mater.* 2004**,** 16 9-10.

[11] Fakioglu, e., Yurum, Y., Veziroglu, T. N. *Int J. of Hydrogen Energy*, 29 (2004) 1371-1376.

[12] Gao., J., Adelhelm, P., Verkuijlen, M. H. W., et al. *J. Phys Chem. C* 2010, 114, 4675-4682.

[13] Ahluwalia, R. K., *Int. J. of Hydrogen Energy* 32 (2007) 1251-1261.

[14] Mauron. P., Buchter, F. Friedrichs, O., Remhof, A., Bielmann, M., Zwicky, C. N., Zuttel, A., *J. Phys. Chem. B* 112, 3, 2008.

[15] Kostka, J,. Lohstroh, W., Fichtner, M., Hahn, H., *J. Phys. Chem. C* 2007, 111, 14026-14029.

[16] Nale, A., Catti, M., Bardaji, E. G., Fichtner, M. *Int. J. of Hydrogen Energy* 36 (2011) 12676-13682.

[17] Fang, ZZ., Kang, XD., Wang, P., Li, HW., Orimo, SI., *J. of Alloys and Compounds* 491 (2010) L1-L4.

[18] Zheng, X., Xiong, Z., Lim, Y., Wu, G., Chen, P., Chen, H., *J. Phys. Chem. C*, 2011, 115, 8840-8844.

[19] Pinkerton, F. E., Meyer, M. S., *J. Phys. Chem. C* 2009, 113, 11172-11176.

[20] Elliott, J. A. W., Ward, C. A., *J. Chem Phys.* 106, 5677 (1997).

[21] Sandrock, G. Gross, K., Thomas, G., Jensen, C., Meeker, D. Takara, S., *J. Alloys and Compounds* 330-332 (2002) 696-701.

[22] Graetz, J. Reilly, J. J., *J. Phys. Chem. B* 2005, 109, 22181-22185.

[23] Berube, V., Radtke, G., Dresselhaus, M., Chen, G., *Int. J. Energy Res.* 2007, 31:637-663.

[24] Meng, Y., Gu, D., Zhang, F., Shi, Y., Cheng, L., Feng, D., Wu, Z., Chen, Z., Wan, Y., Stein, A., Zhao, D. *Chem. Mater.* 2006, 18, 447-4464.

[25] Behrens, R., *Rev. Sci. Instrum.* 58, 451 (1987).

[26] R. Jayaram. *Mass Spectrometry.* Plenum Press, New York, NY, 1966.

a. J. B. Robertson. *Mass Spectrometry*. John Wiley & Sons Inc., New York, NY (1954).

[27] S. R. Shrader. *Introductory Mass Spectrometry*. Allyn and Bacon, Inc., Boston, MA (1971).

[28] *Operating Manual and Programming Reference: Models RGA100, RGA200, and RGA300 Residual Gas Analyzer.* Stanford Research Systems, Sunnyvale, CA (2009).

[29] *Operating Manual: CAL 3300 and 9300 Autotune Temperature Controllers.* CAL Controls, Libertyville, IL, (1997).

[30] *Operation and Service Manual: QCM200 Quartz Crystal Microbalance Digital Controller.* Stanford Research Systems, Sunnyvale, CA (2009).

[31] *XGS-600™ Gauge Controller: Instruction Manual.* Varian Vacuum Technologies, Lexington, MA (2008).

[32] *USB-TEMP-AI: Temperature and Voltage Measurement User's Guide.* Measurement Computing, Norton, MA (2013).

[33] NIST. (2011). Mass Spectrometry Data Center Collection. Retrieved from Webbook.nist.gov.

[34] D. P. Stevenson, J. A. Hipple. *Phys. Rev.* 62, 237-240 (1942).

[35] D. R. Lide (ed), *CRC Handbook of Chemistry and Physics*, 84th Edition. CRC Press. Boca Raton, Florida, (2003).

[36] NIST. (2013). Electron-Impact Cross Sections for Ionization and Excitation. Retrieved from http://physics.nist.gov/PhysRefData/Ionization/molTable.html.

[37] R. Basner and M. Schmidt. *J. Chem. Phys.* 118, 5 (2003)

[38] Stein, Z. Wang, M.A. Fierke., "Functionalization of Porous Carbon Materials with Designed Pore Architecture," *Adv. Materials*, 21, 265 (2009).

[39] Xiangfeng Liu, David Peaslee, C. Z. Jost, E. H. Majzoub "Controlling the Decomposition Pathway of LiBH4 via Confinement in Highly Ordered Nanoporous Carbon," *The Journal of Phys.Chem. C* 114, 14036 -14041(2010).

[40] Patrice Simon, Yury Gogotsi, "Charge Storage Mechanism in Nanoporous Carbons and its Consequence for Electrical Double Layer Capacitors," *Phil. Trans. R. Soc. A* 368 3457-3467 (2010).

[41] J. Rouquerol, D. Avnir, C. W. Fairbridge, D. H. Everett, J. H. Haynes, N. Pernicone, J. D. F. Ramsay, K. S. W. Sing, K. K. Unger, "Recommendations for the Characterization of Porous Solids," *Pure & Appl. Chem.* 66 (8) , 1739 - 1758 (1994).

[42] Meng, Y.; Gu, D.; Zhang, F.; Shi, Y.; Cheng, L.; Feng, D.; Wu, Z.; Chen, Z.; Wan, Y.; Stein, A.; Zhao, D. *Chem. Mater.*, 18, 4447 (2006).

[43] Xiangfeng Liu, David Peaslee, Christopher Z. Jost, Theodore F. Baumann, Eric H. Majzoub, "Systematic Pore-Size Effects of Nanoconfinement of LiBH4: Elimination of Diborane Release and Tunable Behavior for Hydrogen Storage Applications" *Chemistry of Materials* 23 (5), 1331-1336 (2011).

[44] Anyuan Cao, Cailu Xu, Ji Liang, Dehai Wu, Bingqing Wei, "X-ray diffraction characterization on the alignment degree of carbon nanotubes," *Chemical Physics Letters*, 344, (1-2), 13-17 (2001).

[45] Xray Diffraction Table (1997-2010 by David Barthelmy) [Xray Diffraction Data Analysis, May 11, 2011] Minerals Arranged by X-Ray Powder Diffraction, Retrieved from http://webmineral.com/MySQL/xray.php

[46] Rasband, W.S., ImageJ, U. S. National Institutes of Health, Bethesda, Maryland, USA, http://imagej.nih.gov/ij/, 1997-2012

VITA

David Peaslee is a California native. He graduated *Cum Laude* with a B.S. in Physics and a B.A. in Mathematics in 2007 while attending the University of Missouri - St. Louis. While there, he earned his M.S. in Physics in 2008 and his M.A. in Mathematics in 2012. In December, 2013, he received his Ph.D. in Physics which was jointly awarded by Missouri University of Science and Technology and the University of Missouri-St. Louis.

He joined Dr. Eric Majzoub's energy storage materials research group in 2007. While working in this group he collaborated on 3 peer reviewed journal articles. In 2011 he was selected to receive a NASA fellowship from the Jenkins Predoctoral Fellowship Project, where he worked as an intern at NASA – Ames in the Advanced Studies Laboratory under the direction of Dr. Bin Chen.

David was elected to be a member of Sigma Xi, The Scientific Research Society, for winning first place overall in the graduate research fair in 2011 at the University of Missouri - St. Louis. In 2011 he also presented "Direct line-of-site gas desorption study of $LiBH_4$ in nanoporous carbons" at the Hydrogen Storage in Materials Symposium during the TMS Annual Meeting & Exhibition. He received graduate research fellowships from the NASA Missouri Space Grant Consortium and the University of Missouri - St. Louis from 2007 to 2011. David also won the first annual Andalafte Mathematical Competition at the University of Missouri - St. Louis in 2006.

David’s hobbies include: large scale kinetic sculptures, interactive robotics, and teaching.